

**Modeling effects of diffusion and gravity drainage on oil  
recovery in naturally fractured reservoirs under gas injection**

By

Ahmad Jamili

Submitted to the graduate degree program in Chemical and Petroleum  
Engineering and the graduate faculty of The University of Kansas School of  
Engineering in partial fulfillment of the requirements for the degree of  
Doctor of Philosophy

-----  
Co-Chairperson: Dr. G. Paul Willhite

-----  
Co-Chairperson: Dr. Don W. Green

-----  
Dr. Jenn-Tai Liang

-----  
Dr. John H. Doveton

-----  
Dr. Jyun Syung Tsau

Date defended: -----

The dissertation committee for Ahmad Jamili certifies that

this is the approved version of the following Dissertation:

**Modeling effects of diffusion and gravity drainage on oil  
recovery in naturally fractured reservoirs under gas injection**

Committee:

-----  
Co-Chairperson: Dr. G. Paul Willhite

-----  
Co-Chairperson: Dr. Don W. Green

-----  
Dr. Jenn-Tai Liang

-----  
Dr. John H. Doveton

-----  
Dr. Jyun Syung Tsau

Date approved: -----

## **Abstract**

Gas injection in naturally fractured reservoirs maintains the reservoir pressure, and increases oil recovery primarily by gravity drainage and to a lesser extent by mass transfer between the flowing gas in the fracture and the porous matrix. Although gravity drainage has been studied extensively, there has been limited research on mass-transfer mechanisms between the gas flowing in the fracture and fluids in the porous matrix.

This dissertation presents a mathematical model which describes the mass transfer between a gas flowing in a fracture and a horizontal matrix block. The model accounts for diffusion and convection mechanisms in both gas and liquid phases in the porous matrix. The injected gas diffuses into the porous matrix through gas and liquid phases causing the vaporization of oil in the porous matrix which is transported by convection and diffusion to the gas flowing in the fracture. Compositions of equilibrium phases are computed using the Peng-Robinson EOS.

The mathematical model was validated by comparing calculations to two sets of experimental data reported in the literature (Morel et. al. (1990) and Le Romancer et. al. (1994)), one involving nitrogen flow in the fracture and the second with carbon dioxide flow. The matrix was a chalk. The resident fluid in the porous matrix was a mixture of methane and pentane. In the nitrogen injection experiments, liquid and vapor phases were initially present, while in the carbon dioxide experiment the matrix was saturated with a liquid phase.

Calculated results match the experimental data, including recovery of each component, saturation profile, and pressure gradient between matrix and fracture. The simulation revealed the presence of countercurrent flow inside the block. Diffusion was the main mass-transfer mechanism between matrix and fracture during nitrogen injection. In the carbon dioxide experiment, diffusion and convection were both important.

Studies in 2-D were conducted to investigate the effect  $\text{CO}_2$  on recovery from a matrix block. It was found that the scaling capillary pressure with interfacial tension increased  $\text{CO}_2$  from the fracture to the matrix and therefore enhanced gravity drainage from the matrix block. Diffusion was the main recovery mechanism between matrix and fracture.

## **Acknowledgments**

I would like to express my gratitude and sincere appreciation to my advisers Dr. Willhite and Dr. Green for guidance, assistance, and continued encouragement for completion of this dissertation.

My gratitude is also extended to my dissertation committee members: Dr. Lian, Dr. Tsau, and Dr. Doveton for reviewing the dissertation manuscript and providing valuable comments and suggestions.

I would like to thank Dr. Kazemi from Colorado School of Mines who furthered my understanding of reservoir simulation.

**Dedicated to**

**my wife, Pooneh, and**

**my son, Ali,**

**for the moral support and continued encouragement**

**to finish this work.**

## Contents

Abstract.....	ii
Acknowledgments.....	iv
List of tables.....	x
List of figures .....	xv
Chapter 1. Introduction .....	1
Chapter 2. Literature review.....	3
2.1. Laboratory studies .....	3
2.2. Simulation studies.....	15
2.3. Literature summary.....	24
Chapter 3. Mathematical model .....	25
3.1. Dual-continuum approach.....	26
3.2. Mass transfer mechanisms .....	26
3.2.1. Convection (Bulk flow).....	26
3.2.2. Molecular diffusion .....	27
3.3. Governing equations in the model.....	28
3.4. Initial and boundary conditions .....	30
3.4.1. Initial conditions.....	30
3.4.2. Matrix boundary conditions.....	31

3.4.2.1 Matrix sealed boundary conditions .....	32
3.4.2.2 Matrix-fracture boundary conditions .....	32
3.5. Numerical solution .....	36
3.5.1. Discertization of the flow equations .....	37
3.5.1. Numerical solution scheme .....	40
Chapter 4. Rock properties, phase behavior , and fluid properties .....	54
4.1. Rock properties .....	54
4.1.1. Porosity .....	54
4.1.2. Absolute permeability .....	55
4.1.2. Relative permeability .....	55
4.1.3. Capillary pressure .....	58
4.1.4. Tortuosity.....	59
4.2. Phase behavior and fluid properties .....	60
4.2.1. Equations of State (EOS) .....	61
4.2.2. Flash calculation.....	64
4.2.3. Density .....	68
4.2.4. Volume translation (or Volume shift) .....	68
4.2.5. Viscosity .....	72
4.2.6. Molecular diffusion .....	74



4.2.7. Interfacial tension (IFT).....	77
Chapter 5. Preliminary testing of the model .....	78
5.1. Phase behavior.....	78
5.2. Testing the model with 1-dimension and 2-dimension flow problems versus CMG .....	85
5.3. Summary .....	86
Chapter 6. Validation of the proposed model.....	108
6.1. Introduction.....	108
6.2. Measurement of local gas saturation along the core .....	109
6.3. Nitrogen injection experiment .....	111
6.3.1. Description of the nitrogen injection experiment.....	111
6.3.2. Simulation of 1-D nitrogen injection experiment .....	113
6.3.2. Summary .....	117
6.4. Carbon dioxide injection experiment.....	118
6.4.1. Description of the carbon dioxide injection experiment .....	118
6.4.2. Simulation of 1-D carbon dioxide injection experiment.....	120
6.4.3. Summary .....	128
Chapter 7. Simulation of CO <sub>2</sub> injection in a fracture in .....	163
2-dimension .....	163

7.1. Introduction .....	163
7.2. Simulation results .....	163
7.2.1. Example 1: Simulation of CO <sub>2</sub> injection in a short matrix block .....	164
7.2.2. Example 2: Simulation of CO <sub>2</sub> injection in a tall matrix block.....	166
7.3. Summary .....	171
Chapter 8. Conclusions and recommendations .....	195
8.1. Conclusions .....	195
8.2. Recommendations.....	196
Nomenclatures.....	197
References .....	207
Appendix A. Derivation of the multiphase flow equations .....	213
Appendix B. Discretizing the flow equations .....	218
Appendix C. Newton-Raphson method.....	226

## List of tables

Table 2.1: Description of 1-dimension diffusion experiments by Morel et al. (1990) .....	5
Table 2.2: Description of 1-dimension diffusion experiment by Le Romancer et al. (1994a, 1994b) .....	10
Table 2.3: Description of Le Gallo et al. (1997) 1-dimension diffusion experiment .....	12
Table 2.4: Simulation examples of Hoteit and Firoozabadi (2006).....	21
Table 4.1: Shift parameter for hydrocarbons (Jhaveri and Youngren (1988)) .....	72
Table 4.2: Shift parameter correlation coefficients for hydrocarbons heavier than hexane (Jhaveri and Youngren (1988)) .....	72
Table 5.1: Overall composition and critical properties of C <sub>1</sub> -nC <sub>4</sub> -C <sub>10</sub> mixture for flash calculations at p=1000 psi and T=160°F (McCain (1990)) .....	79
Table 5.2: Binary interaction coefficients of C <sub>1</sub> -nC <sub>4</sub> -C <sub>10</sub> mixture (McCain (1990)) .....	80
Table 5.3: Comparison of oil and gas phases properties Flash calculations from this work and flash calculations of McCain (1990) at p=1000 psi and T=160°F .....	81
Table 5.4: Comparison of oil and gas phases composition Flash calculations from this work and the experimental data of Sage et al. (1950) at p=1000 psi and T=160°F .....	82

Table 5.5: Compositions of oil and gas phases at critical point ( $p=1653$ psi, $T=539^{\circ}\text{F}$ ) from this work .....	83
Table 5.6: Comparison of bubble-point pressure calculations between this work and Hashem (1998) .....	84
Table 5.7: Reservoir properties (Hashem (1998)).....	88
Table 5.8: Overall composition and critical properties of $\text{C}_1\text{-nC}_4\text{-C}_{10}$ mixture from WinProp (CMG) .....	89
Table 5.9: Binary interaction coefficients of $\text{C}_1\text{-nC}_4\text{-C}_{10}$ mixture from WinProp (CMG).....	89
Table 5.10: Pressure output for 1-D flow problem (CMG).....	90
Table 5.11: Pressure output for 1-D flow problem (This work).....	91
Table 5.12: Oil saturation output for 1-D flow problem (CMG) .....	92
Table 5.13: Oil saturation output for 1-D flow problem (This work) .....	93
Table 5.14: Gas saturation output for 1-D flow problem (CMG).....	94
Table 5.15: Gas saturation output for 1-D flow problem (This work).....	95
Table 5.16: Pressure output for 2-D flow problem (CMG).....	96
Table 5.16: Pressure output for 2-D flow problem (CMG), Cont. ....	97
Table 5.17: Pressure output for 2-D flow problem (This work).....	98
Table 5.17: Pressure output for 2-D flow problem (This work), Cont. ....	99
Table 5.18: Oil saturation output for 2-D flow problem (CMG) .....	100
Table 5.18: Oil saturation output for 2-D flow problem (CMG), Cont.....	101
Table 5.19: Oil saturation output for 2-D flow problem (This work) .....	102

Table 5.19: Oil saturation output for 2-D flow problem (This work), Cont.....	103
Table 5.20: Gas saturation output for 2-D flow problem (CMG).....	104
Table 5.20: Gas saturation output for 2-D flow problem (CMG), Cont. ....	105
Table 5.21: Gas saturation output for 2-D flow problem (This work).....	106
Table 5.21: Gas saturation output for 2-D flow problem (This work), Cont. ....	107
Table 6.1: Model inputs for simulation of the nitrogen injection experiment.....	130
Table 6.2: Relative permeabilities and capillary pressure (Hua et. al. (1991)) ..	130
Table 6.3: Critical properties of N <sub>2</sub> , C <sub>1</sub> , C <sub>5</sub> , and CO <sub>2</sub> .....	131
Table 6.4: Compositions and densities of oil and gas phases for tie-lines 1 and 2 of methane-pentane-nitrogen ternary diagram at 1479 psi and 38.5°C from Morel et. al. (1990).....	131
Table 6.5: Compositions and densities of oil and gas phases for tie-lines 1 and 2 of methane-pentane-nitrogen ternary diagram at 1479 psi and 38.5°C from this work .....	131
Table 6.6: Model inputs for simulation of the CO <sub>2</sub> injection experiment .....	131
Table 6.7: Binary interaction coefficients for methane-pentane-carbon dioxide mixture .....	132
Table 6.8: Phase behavior calculations for C <sub>1</sub> -C <sub>5</sub> tie-line of Fig. 6.24.....	132
Table 6.9: Phase behavior calculations for CO <sub>2</sub> -C <sub>5</sub> tie-line of Fig. 6.24 .....	133
Table 6.10: Phase behavior calculations for tie-line 1 of Fig. 6.24.....	133
Table 6.11: Phase behavior calculations for tie-line 2 of Fig. 6.24.....	134
Table 6.12: Phase behavior calculations for tie-line 3 of Fig. 6.24.....	134

Table 6.13: Phase behavior calculations for tie-line 4 of Fig. 6.24 .....	135
Table 6.14: Phase behavior calculations for tie-line 5 of Fig. 6.24 .....	135
Table 6.15: Phase behavior calculations for tie-line 6 of Fig. 6.24 .....	136
Table 6.16: Phase behavior calculations for tie-line 7 of Fig. 6.24 .....	136
Table 6.17: Phase behavior calculations for tie-line 8 of Fig. 6.24 .....	137
Table 6.18: Phase behavior calculations for tie-line 9 of Fig. 6.24 .....	137
Table 6.19: Calculating initial total mole of methane and pentane in the core in CO <sub>2</sub> injection experiment .....	138
Table 6.20 : Calculating total mole of methane and pentane in the core at 95 days in CO <sub>2</sub> injection experiment .....	138
Table 6.21: Calculating average oil and gas saturation at 95 day in CO <sub>2</sub> injection experiment when highest value of density used for oil and gas .....	138
Table 6.22: Calculating average oil and gas saturation at 95 day in CO <sub>2</sub> injection experiment when lowest value of density used for oil and gas .....	139
Table 7.1: Model inputs in simulation of 2D CO <sub>2</sub> injection (Example 1) .....	173
Table 7.2: Calculated local oil pressure inside the matrix at t=715 day for Example 1-Case A .....	173
Table 7.3: Calculated local oil pressure inside the matrix at t=600 day for Example 1-Case B .....	174
Table 7.4: Calculated local oil pressure inside the matrix at t=600 day for Example 1-Case C .....	174
Table 7.5: Model inputs in simulation of 2D CO <sub>2</sub> injection (Example 2) .....	175

Table 7.6: Calculated local oil pressure inside the matrix at t=160 day for Example 2-Case B (without scaling capillary pressure with interfacial tension).....	175
Table 7.7: Comparing calculated local IFT inside the matrix at t=200 day for Example 2-Case C (with and without scaling capillary pressure with interfacial tension).....	176
Table 7.8: Comparing calculated local CO <sub>2</sub> mole fraction in oil phase inside the matrix at t=200 day for Example 2-Case C (with and without scaling capillary pressure with interfacial tension) .....	177
Table 7.9: Comparing calculated local oil density inside the matrix at t=200 day for Example 2-Case C (with and without scaling capillary pressure with interfacial tension).....	178
Table 7.10: Comparing calculated local oil pressure inside the matrix at t=200 day for Example 2-Case C (with and without scaling capillary pressure with interfacial tension).....	179
Table 7.11: Comparing calculated local gas saturation inside the matrix at t=200 day for Example 2-Case C (with and without scaling capillary pressure with interfacial tension).....	180
Table 7.12: Comparing calculated local oil viscosity inside the matrix at t=200 day for Example 2-Case C (with and without scaling capillary pressure with interfacial tension).....	181

## List of figures

Fig. 2.1: Diffusion experiment layout (Morel et al. (1990)) .....	4
Fig. 2.2: Methane-pentane-nitrogen ternary phase diagram at 10.1 Mpa and 38.5°C (Morel et al. (1990)) .....	4
Fig. 2.3: Gas saturation profile along the core for experiment No. M6 of Table 2.1 (Morel et al. (1990)) .....	6
Fig. 2.4: Schematic of diffusion experiment (Chukwuma (1983) and Renner (1988)) .....	8
Fig. 2.5: Experiment setup of Thiebot and Sakthikumar (1991), Darvish et al. (2006), and Karimaie (2007) .....	9
Fig. 2.6: Effect of diffusing gas type on pentane recovery (Le Romancer et al. (1994a)) .....	10
Fig. 2.7: Schematic of high pressure experimental cell (Riazi et al. (1994)) .....	11
Fig. 2.8: 2-D cross section with different fracture intensities: a) 100mx10m matrix blocks, b) 10mx10m matrix blocks, and c) 10mx5m matrix blocks (Hoteit and Firoozabadi (2006)) .....	22
Fig. 3.1: Model layout.....	27
Fig. 3.2: flow chart of Implicit Pressure Explicit Saturation Composition (IMPESC) numerical technique.....	53
Fig. 5.1: Grid numbering in 1-dimension and 2-dimension flow problems.....	87
Fig. 6.1: Diffusion experiment layout (Morel et al. (1990)) .....	139
Fig. 6.2: Ternary diagram for methane-pentane-nitrogen at 1479 psi and 38.5°C	



(Morel et al. (1990)) .....	140
Fig. 6.3: Calculated and experimental $C_1$ and $C_5$ recoveries in $N_2$ injection experiment.....	141
Fig. 6.4: Gas saturation at $t = 4$ day in $N_2$ injection experiment .....	141
Fig. 6.5: Gas saturation at $t = 8$ day in $N_2$ diffusion experiment .....	142
Fig. 6.6: Gas saturation at $t = 16$ day in $N_2$ diffusion experiment .....	142
Fig. 6.7: Calculated $N_2$ mass-transfer rates at fracture-matrix surface in $N_2$ injection experiment.....	143
Fig. 6.8: Calculated $C_1$ mass-transfer rates at fracture-matrix surface in $N_2$ injection experiment.....	143
Fig. 6.9: Calculated $C_5$ mass-transfer rates at fracture-matrix surface in $N_2$ injection experiment.....	144
Fig. 6.10: Oil pressure distribution in $N_2$ injection experiment (A) .....	144
Fig. 6.11: Oil pressure distribution in $N_2$ injection experiment (B) .....	145
Fig. 6.12: Calculated local $N_2$ rates inside the matrix at $t = 8$ day for $N_2$ injection experiment (A) .....	145
Fig. 6.13: Calculated local $N_2$ rates inside the matrix at $t = 8$ day for $N_2$ injection experiment (B) .....	146
Fig. 6.14: Calculated local $N_2$ rates inside the matrix at $t = 28$ day for $N_2$ injection experiment (A) .....	146
Fig. 6.15: Calculated local $N_2$ rates inside the matrix at $t = 28$ day for $N_2$ injection experiment (B) .....	147

Fig. 6.16: Calculated local $C_1$ rates inside the matrix at $t = 8$ day for $N_2$ injection experiment (A) .....	147
Fig. 6.17: Calculated local $C_1$ rates inside the matrix at $t = 8$ day for $N_2$ injection experiment (B) .....	148
Fig. 6.18: Calculated local $C_1$ rates inside the matrix at $t = 28$ day for $N_2$ injection experiment (A) .....	148
Fig. 6.19: Calculated local $C_1$ rates inside the matrix at $t = 28$ day for $N_2$ injection experiment (B) .....	149
Fig. 6.20: Calculated local $C_5$ rates inside the matrix at $t = 8$ day for $N_2$ injection experiment (A) .....	149
Fig. 6.21: Calculated local $C_5$ rates inside the matrix at $t = 8$ day for $N_2$ injection experiment (B) .....	150
Fig. 6.22: Calculated local $C_5$ rates inside the matrix at $t = 28$ day for $N_2$ injection experiment (A) .....	150
Fig. 6.23: Calculated local $C_5$ rates inside the matrix at $t = 28$ day for $N_2$ injection experiment (B) .....	151
Fig. 6.24: Ternary diagram for methane-pentane-carbon dioxide at 913.74 psi and 38.5 °C (Le Romancer et. al. (1994)).....	152
Fig. 6.25: Calculated and experimental $C_1$ and $C_5$ recoveries in $CO_2$ injection experiment.....	153
Fig. 6.26: Differential pressure between matrix and fracture in $CO_2$ injection experiment.....	153

Fig. 6.27: Oil saturation at t = 7 day in CO <sub>2</sub> injection experiment.....	154
Fig. 6.28: Oil saturation at t = 23 day in CO <sub>2</sub> diffusion experiment.....	154
Fig. 6.29: Oil saturation at t = 53 day in CO <sub>2</sub> injection experiment.....	155
Fig. 6.30: Oil saturation at t = 67 day in CO <sub>2</sub> injection experiment.....	155
Fig. 6.31: Oil saturation at t = 88 day in CO <sub>2</sub> injection experiment.....	156
Fig. 6.32: Oil saturation at t = 95 day in CO <sub>2</sub> injection experiment.....	156
Fig. 6.33: Effect of CO <sub>2</sub> mole fraction in oil on oil density .....	157
Fig. 6.34: Effect of CO <sub>2</sub> mole fraction in gas on Gas density .....	157
Fig. 6.35: Calculated CO <sub>2</sub> mass-transfer rates at fracture-matrix surface in CO <sub>2</sub> injection experiment.....	158
Fig. 6.36: Calculated C <sub>1</sub> mass transfer rates at fracture-matrix surface in CO <sub>2</sub> injection experiment.....	158
Fig. 6.37: Calculated C <sub>5</sub> mass transfer rates at fracture-matrix surface in CO <sub>2</sub> injection experiment.....	159
Fig. 6.38: Calculated local CO <sub>2</sub> rates inside the matrix at t = 23 day for CO <sub>2</sub> injection experiment.....	159
Fig. 6.39: Calculated local CO <sub>2</sub> rates inside the matrix at t = 90 day for CO <sub>2</sub> injection experiment.....	160
Fig. 6.40: Calculated local C <sub>1</sub> rates inside the matrix at t = 23 day for CO <sub>2</sub> injection experiment.....	160
Fig. 6.41: Calculated local C <sub>1</sub> rates inside the matrix at t = 90 day for CO <sub>2</sub> injection experiment.....	161

Fig. 6.42: Calculated local $C_5$ rates inside the matrix at $t = 23$ day for $\text{CO}_2$ injection experiment.....	161
Fig. 6.43: Calculated local $C_5$ rates inside the matrix at $t = 90$ day for $\text{CO}_2$ injection experiment.....	162
Fig. 7.1: Layout of example 1.....	182
Fig. 7.2: Effect of grid size on $C_1$ molar recovery (Example 1).....	182
Fig. 7.3: Effect of grid size on $C_5$ molar recovery (Example 1).....	183
Fig. 7.4: Calculated $\text{CO}_2$ mass transfer rates at matrix-fracture surface for Case A, Case B, and Case C of Example 1.....	184
Fig. 7.5: Calculated $C_1$ mass transfer rates at matrix-fracture surface for Case A, Case B, and Case C of Example 1.....	185
Fig. 7.6: Calculated $C_5$ mass transfer rates at matrix-fracture surface for Case A, Case B, and Case C of Example 1.....	186
Fig. 7.7: Layout of example 2.....	187
Fig. 7.8: Effect of grid size on $C_1$ molar recovery (Example 2- Without scaling capillary pressure with IFT).....	188
Fig. 7.9: Effect of grid size on $C_5$ molar recovery (Example 2- Without scaling capillary pressure with IFT).....	188
Fig. 7.10: Effect of grid size on $C_1$ molar recovery (Example 2- With scaling capillary pressure with IFT).....	189
Fig. 7.11: Effect of grid size on $C_5$ molar recovery (Example 2- With scaling capillary pressure with IFT).....	189

Fig. 7.12: Effect of scaling capillary pressure with IFT on $C_1$ and $C_5$ molar recoveries (Example 2- Case A).....	190
Fig. 7.13: Effect of scaling capillary pressure with IFT on $C_1$ and $C_5$ molar recoveries (Example 2- Case B).....	190
Fig. 7.14: Effect of scaling capillary pressure with IFT on $C_1$ and $C_5$ molar recoveries (Example 2- Case C).....	191
Fig. 7.15: Calculated $CO_2$ mass transfer rates at matrix-fracture surface for Example 2- Case C.....	192
Fig. 7.16: Calculated $C_1$ mass transfer rates at matrix-fracture surface for Example 2- Case C.....	193
Fig. 7.17: Calculated $C_5$ mass transfer rates at matrix-fracture surface for Example 2- Case C.....	194
Fig. A.1: Volume Element for deriving the multiphase flow equations.....	213

## Chapter 1. Introduction

It is common to inject gas in naturally fractured reservoirs to maintain the reservoir pressure, and increase oil recovery primarily by gravity drainage and, to a lesser extent, by mass transfer between the flowing gas in the fracture and the porous matrix. In most cases, mass transfer is considered to contribute a small amount to the oil displacement. Mass transfer could be an important recovery mechanism in the case of a low permeability and/or small matrix block size. The mechanism is aided by the large area that is available for mass transfer in naturally fractured reservoirs. Although gravity drainage has been studied extensively, there has been limited research on mass-transfer mechanisms between the gas flowing in the fracture and fluids in the porous matrix.

The main objective of this dissertation is to develop a mathematical model which describes the mass transfer between a gas flowing in the fracture and resident fluid in a matrix block. The injected gas diffuses into the porous matrix through gas and liquid phases causing the vaporization of oil in the porous matrix which is transported by convection and diffusion to the gas flowing in the fracture.

Mass transfer between the fracture and the matrix is assumed to occur by diffusion mass transfer and fluid flow between the matrix and the fracture. The model accounts for diffusion, and convection mechanisms in both gas and oil phases in the porous matrix driven by capillary pressure gradients which are generated due to changes in phase behavior as the gas dissolves in the oil

phase. Compositions of equilibrium phases are computed using the Peng-Robinson EOS.

The mathematical model is validated by comparing calculations to sets of experimental data reported in the literature (reference), one involving nitrogen flow in the fracture and the second with carbon dioxide flow.

## Chapter 2. Literature review

Few laboratory publications have been devoted to describing the diffusion mechanism in naturally fractured reservoirs. No laboratory work was published on the diffusion effects in naturally fractured reservoirs before 1990. During that period (before 1990), simulation studies were conducted to investigate the of diffusion mechanism on oil recovery in naturally fractured reservoirs. The laboratory and simulation studies of diffusion as a recovery mechanism in naturally fractured reservoirs are discussed in what follows.

### 2.1. Laboratory studies

Morel et al. (1990) conducted laboratory studies of the effect of diffusion in 1-dimension on oil recovery in naturally fractured reservoirs. Figure 2.1 shows the layout of the experiments. The experiments were performed with cores of Paris Basin Chalk ( $0.105 \times 0.105 \times 1.1811$  ft<sup>3</sup>). The permeability and porosity of the samples were 2 md and 40%, respectively. Cores were saturated with a binary mixture of C<sub>1</sub>-C<sub>5</sub>. Methane or nitrogen was injected in the fracture. Fig. 2.2 shows the ternary diagram of methane-pentane-nitrogen at 10.1 Mpa and 38.5°C. They investigated the effects of the diffusing gas (N<sub>2</sub> or C<sub>1</sub>), gas flow rate in the fracture, and initial gas saturation in the core. The experiments were performed at 38.5°C. Table 2.1 shows the details of the experiments. They concluded the following:

- 1- Initial gas saturation has little effect on oil recovery.





Fig. 2.1: Diffusion experiment layout (Morel et al. (1990))

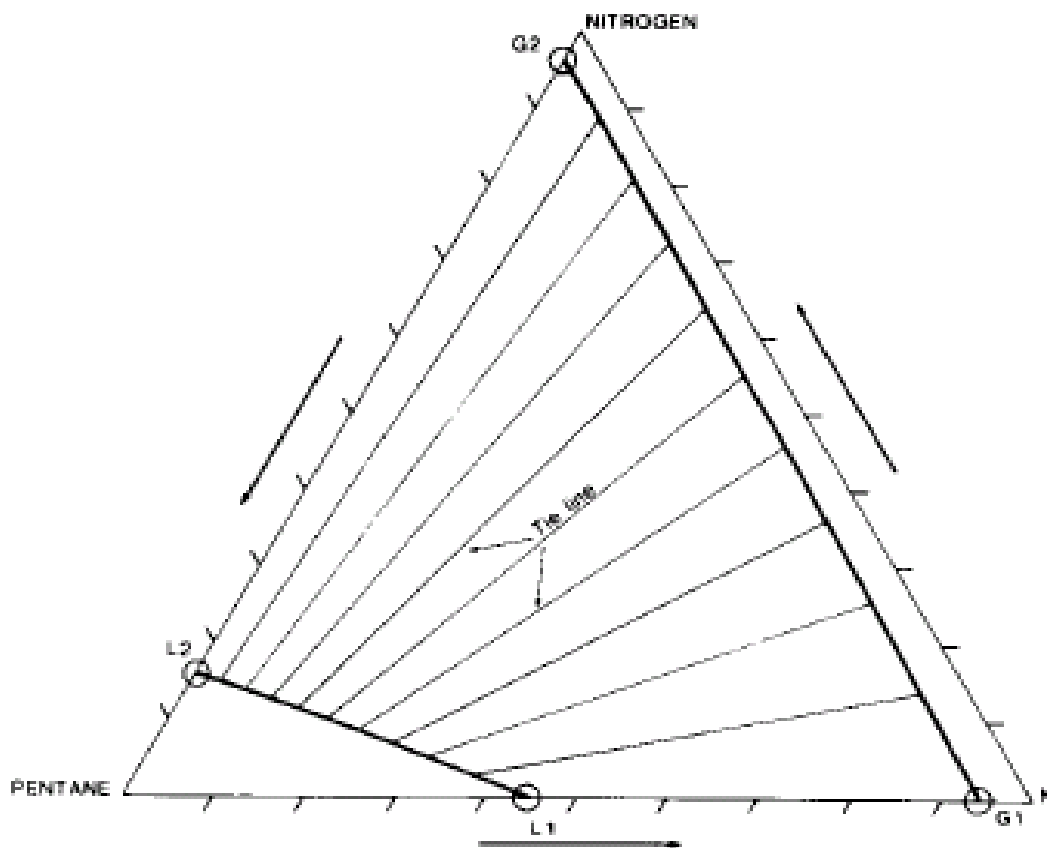


Fig. 2.2: Methane-pentane-nitrogen ternary phase diagram at 10.1 Mpa and 38.5°C (Morel et al. (1990))

**Table 2.1: Description of 1-dimension diffusion experiments by****Morel et al. (1990)**

Experiment No.	Composition of the mixture (mole %)	Initial gas saturation in core (%)	Pressure (MPa)	Total experiment time (days)	Gas injection flow rate in the fracture (cm <sup>3</sup> /hr)	Injected gas
M3	C <sub>1</sub> (44.1%), C <sub>5</sub> (55.9%)	0	10.1	24	4 then 8	Methane
M4	C <sub>1</sub> (52.4%), C <sub>5</sub> (47.6%)	25	10.1	16	4 then 8	Methane
M8	C <sub>1</sub> (45.8%), C <sub>5</sub> (54.2%)	7.2	9.8	15	4	Methane
M5	C <sub>1</sub> (52.4%), C <sub>5</sub> (47.6%)	29	10.1	16	4 then 8	Nitrogen
M6	C <sub>1</sub> (44.1%), C <sub>5</sub> (55.9%)	0	10.1	73	4	Nitrogen
M7	C <sub>1</sub> (50.7%), C <sub>5</sub> (49.3%)	0	11.7	13	8, 12 then 16	Nitrogen

2- Pentane recovery is linear with time, which indicates that the recovery process is not governed by a pure diffusion mechanism.

3- Pentane recovery by methane injection is 1.6 times faster than recovery by nitrogen injection at corresponding times. The pentane concentration in the gas phase in the core was 1.6 times higher for methane injection than for nitrogen injection.

4- In the nitrogen injection case, saturation profiles along the core revealed a strong capillary end effect resulting in accumulation of oil in the matrix near the fracture (Fig. 2.3).

5- When nitrogen is the diffusing gas, the flow rate has a small effect on pentane recovery; whereas flow rate greatly affects methane production.

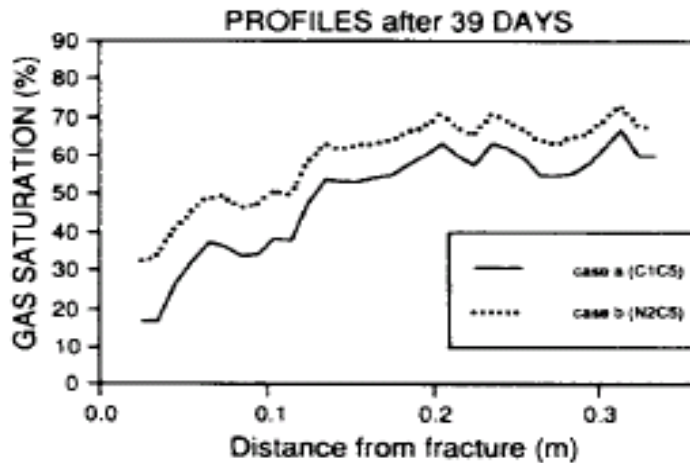


**Fig. 2.3: Gas saturation profile along the core for experiment No. M6 of**

**Table 2.1 (Morel et al. (1990))**

Chukwuma (1983) studied diffusion of  $\text{CO}_2$  into n-decane at  $100^\circ\text{F}$  and 206 psia. Fig. 2.4 shows the experimental setup. Glass rods of different diameters (2mm, 3mm, 4mm, etc) and Pyrex glass beads of 4mm diameter were used as packing in the study.  $\text{CO}_2$  diffuses into n-decane from the top. He recognized that the density of a  $\text{CO}_2$  and n-decane mixture had an unusual behavior increasing up to 70% mol  $\text{CO}_2$  and then decreasing at higher concentrations of  $\text{CO}_2$ . The density change causes free convection in the vertical direction with the denser fluid flowing down. Free convection enhances  $\text{CO}_2$  mass transfer. It took only 45 minutes to saturate n-decane by density induced vertical flow while for other gases, such as methane, it takes several hours. He concluded that the free convection causes the effective diffusivity to be much higher than a typical

molecular diffusion. For example, the asymptotic value of the effective diffusivity for carbon dioxide in n-decane is about  $0.2 \text{ cm}^2/\text{second}$  at 206psia and  $100^\circ\text{F}$  whereas the molecular diffusivity for ethane in n-decane at the same temperature and pressure is about  $5.0 \times 10^{-5} \text{ cm}^2/\text{second}$ .

Renner (1988) used an experimental setup similar to Chukwuma's (1983) experimental setup (Figure 2.4) to study  $\text{CO}_2$  and ethane diffusion into n-decane at  $100^\circ\text{F}$  temperature and pressures up to 846 psia. As  $\text{CO}_2$  diffuses into the oil (n-decane), the pressure tends to drop in the  $\text{CO}_2$  space. As this occurs, the pressure raised by compressing the  $\text{CO}_2$ . From the movement of the piston rod and the linear position transducer on the gas metering vessel, the volume of  $\text{CO}_2$  injected to maintain constant pressure over the rock face as a function of time may be readily determined. Because  $\text{CO}_2$  mass transfer into oil (n-decane) results in swelling of the oil, the gas/oil interface will move as a function of time. Horizontal and vertical Berea core (2-in diameter and 6-in long) setups were used in the experiments to investigate the effect of gravity-induced convection on the observed mass transfer. He observed that the effective diffusivity of  $\text{CO}_2$  in n-decane in vertical cores is more than in horizontal cores which appears to be because of combined diffusion and gravity-induced convection processes. On the other hand, diffusivity of ethane in n-decane is not affected by the orientation of the core.

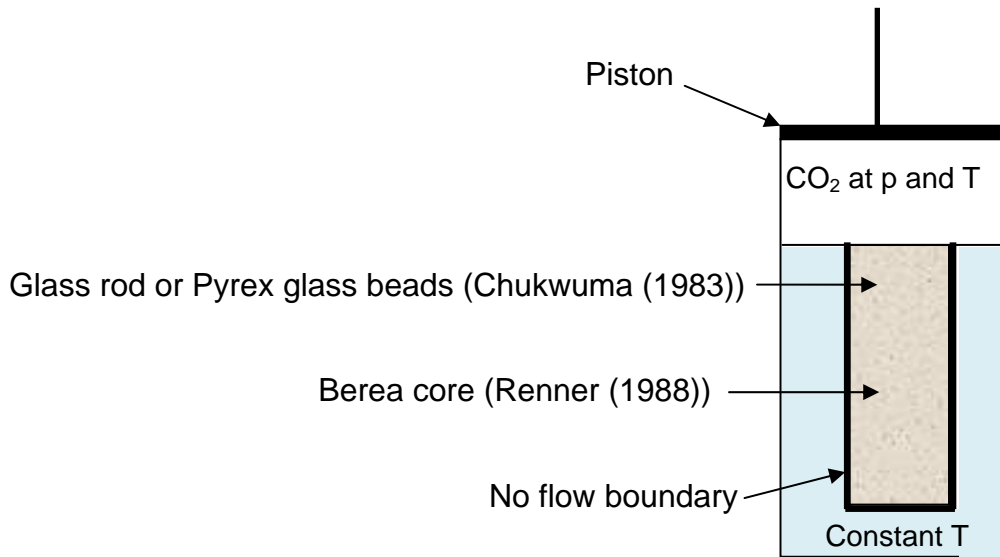


**Fig. 2.4: Schematic of diffusion experiment (Chukwuma (1983) and Renner (1988))**

Thiebot and Sakthikumar (1991) studied gravity drainage and mass transfer in cylindrical cores surrounded by fractures (Figure 2.5). They used a limestone and chalk cylindrical core with a length of 40 cm and permeabilities of 60 md and 2 md, respectively. First, the core was saturated with live oil, representative North Sea light oil with a bubble point pressure of 180 bar at a reservoir temperature of 132°C. Second, equilibrium gas was injected at the top of the core in the fracture and oil was produced from the bottom. Equilibrium gas is a gas in thermodynamic equilibrium with the live oil used in the experiment. Therefore, there is no mass transfer between the equilibrium gas and the live oil. Gravity is the recovery mechanism in this stage. The step was continued until oil production ceased (gravity drainage equilibrium). Third, methane or nitrogen was injected instead of the equilibrium gas. Mass transfer between nitrogen and methane as non-equilibrium gases and live oil in the core occurs in this stage. They

concluded that injection of non-equilibrium gas leads to significant additional oil recovery even after gravity drainage equilibrium.

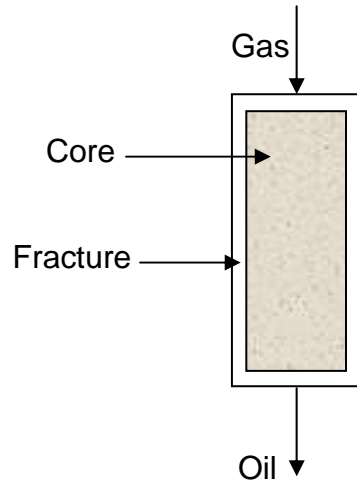


**Fig. 2.5: Experiment setup of Thiebot and Sakthikumar (1991), Darvish et al. (2006), and Karimaie (2007)**

Le Romancer et al. (1994a, 1994b) performed similar experiments as Morel et al. (1990) in 1-D conditions (Fig. 2.1) on chalk cores saturated with a methane-pentane mixture in the presence of different water saturations and with three diffusing gases: nitrogen, methane, and carbon dioxide. Table 2.2 shows the details of the experiments. Similar to Morel et al. (1990), it was observed that there is an accumulation of oil in the matrix near the fracture surface when nitrogen is injected. The gas saturation profiles were similar to Fig. 2.3. Fig. 2.6 shows the influence of the diffusing gas type on the pentane recovery. Based on Fig. 2.6., Le Romancer et al. (1994a) claimed that only nitrogen injection allows the obtaining of a constant and high pentane production rate. Therefore, it was

concluded that in a diffusion process it is essential to keep the highest oil saturation near the fracture. From this point of view, nitrogen is an interesting candidate. Their carbon dioxide diffusion experiment is simulated in this dissertation.

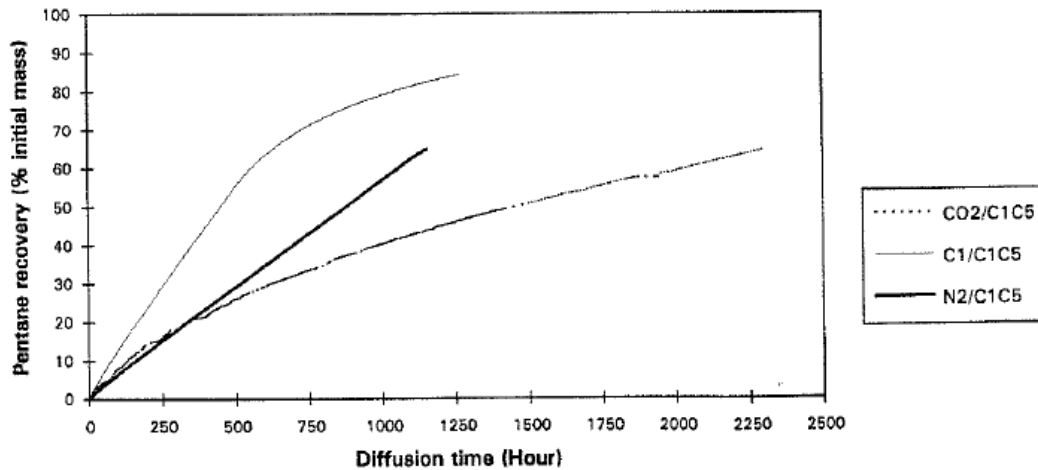


**Fig. 2.6: Effect of diffusing gas type on pentane recovery (Le Romancer et al. (1994a))**

**Table 2.2: Description of 1-dimension diffusion experiment by Le Romancer et al. (1994a, 1994b)**

Test	Injected gas	Water saturation (%)	Initial gas saturation (%)	Composition of the mixture (mole %)	Gas flow rate in the fracture (cm <sup>3</sup> /hr)	Pressure (MPa)	Total test time (days)
M3	C <sub>1</sub>	0	0	C <sub>1</sub> (44%), C <sub>5</sub> (56%)	4	10.1	23
M6	N <sub>2</sub>	0					73
M10	N <sub>2</sub>	30					60
M11	C <sub>1</sub>	30					39
M12	C <sub>1</sub>	13					52
M13	N <sub>2</sub>	13					49
M25	CO <sub>2</sub>	11		C <sub>1</sub> (28%), C <sub>5</sub> (72%)		6.3	95

Riazi et al. (1994) conducted a laboratory experiment to study the mechanism of diffusion at reservoir conditions (Fig. 2.7). In their experiment, diffusion of  $N_2$  into a mixture of oil and gas (in matrix) at 270 bar and 403K was studied. The oil components were  $N_2$ ,  $CO_2$ ,  $C_1$ ,  $C_2$ ,  $C_3$ ,  $iC_4$ ,  $nC_4$ ,  $iC_5$ ,  $nC_5$ ,  $C_6$ ,  $C_{7+}$ . Cylindrical core samples (8.3 cm height and 5.1 cm diameter) from the Ekofisk field in the North Sea were used in a vessel with limited free-volume which was purged with nitrogen immediately following depressurization from the initial bubble point at 382.8 bar to 275.9 bar. Porosity and permeability of a core sample were 0.31 and 0.29 md, respectively. A core sample was supported by the vessel so that all the surfaces were open to the free-volume. The diffusion process was monitored by analysis of the gas composition in the free volume with time. Their simulation of the experiment will be discussed in the next section. The results showed the importance of diffusion in recovery of oil components.

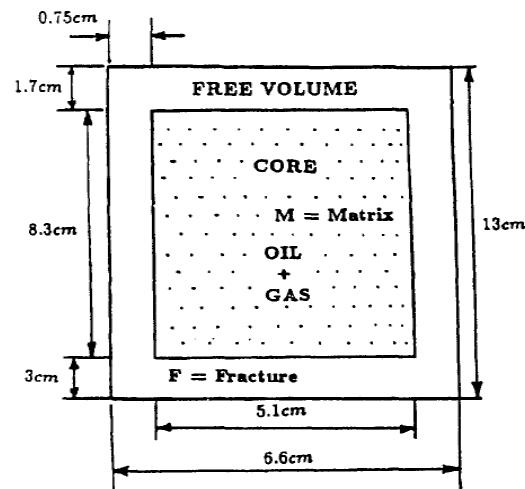


**Fig. 2.7: Schematic of high pressure experimental cell (Riazi et al. (1994))**



Le Gallo et al. (1997) used the same setup (Fig. 2.1) as Morel et al. (1990) to study diffusion in 1-dimension in Paris Basin Chalk. A description of the experiments is given in Table 2.3. Le Gallo et al. (1997) concluded that capillary phenomenon inside the matrix contributes to liquid flow towards the fracture and may be enhanced if interfacial tension is increased by injecting of a gas such as nitrogen.

**Table 2.3: Description of Le Gallo et al. (1997) 1-dimension diffusion experiment**

Test	Injected gas	Water saturation (%)	Initial gas saturation (%)	Composition of the mixture (mole %)	Gas flow rate in the fracture (cm <sup>3</sup> /hr)	Pressure (MPa)	Total test time (days)
M5	N <sub>2</sub>	0	29.5	C <sub>1</sub> (52.4%), C <sub>5</sub> (47.6%)	4-8	10.2	16
M29	C <sub>1</sub>	0	0	C <sub>5</sub> (100%)	4	10.2	65
M30	C <sub>1</sub>	0	0	C <sub>1</sub> (37%), C <sub>5</sub> (49%), C <sub>16</sub> (14%)	4	10	95

Darvish et al. (2006) conducted an experiment to study the effect of CO<sub>2</sub> injection into cylindrical cores (60 cm long and 4.6 cm diameter) from North Sea (Maastrichtian chalk) surrounded by fractures (Fig. 2.5) at reservoir conditions. Permeability and porosity of the core were 4 md and 44%. The oil components were N<sub>2</sub>, CO<sub>2</sub>, C<sub>1</sub>, C<sub>2</sub>, C<sub>3</sub>, C<sub>4</sub>, C<sub>5</sub>, C<sub>6</sub>, C<sub>7+</sub>. The volume between core and core holder (fracture) was filled by Wood's metal. After saturating the core with the oil mixture, a fracture volume surrounding the core was created by heating the solid

core and melting the wood's metal and draining the melted wood's metal from the space between the core and the core holder. The oil circulation was continued until fracture and core both were completely saturated with oil. Once the sealing material from the fracture was removed, the oil in the fracture was displaced by injecting CO<sub>2</sub> at high flow rate. Then CO<sub>2</sub> was injected at the top of the core and oil was produced from the bottom. The experiment was performed at 300 bars at 130°C.

The Eclipse compositional simulator was used to simulate the experiment. Mass transfer between gas in the fracture and oil in the matrix is not considered in Eclipse. Gas-gas and oil-oil diffusion are allowed in Eclipse only. Therefore, Darvish et al. (2006) had to initialize the fracture with oil and gas phases of rich CO<sub>2</sub> to initiate diffusion between oil in the matrix and oil in the surrounding fractures. The fracture was initialized with a mixture of 95 mole% CO<sub>2</sub> and 5 mole% of the heaviest component. The fluid inside the fracture has a two-phase condition in which liquid phase has a very high concentration of CO<sub>2</sub>. The presence of two-phase condition in the fracture with a high concentration of CO<sub>2</sub> in its liquid phase would start the liquid-liquid diffusion from the fracture to the matrix. A zero gas and oil diffusion coefficient was assigned for the heaviest component. The simulation results showed that the key mechanism to recover oil from a tight matrix block is diffusion and gravity drainage has no significant effect. They recommended that the existing compositional simulators should be updated

to take into account gas (in the fracture)-oil (in the matrix) mass transfer on oil recovery.

Karimaie (2007) investigated gas injection (secondary recovery) and gas injection after water injection (tertiary recovery) in oil-wet carbonate cores. The objective was to investigate an EOR process for oil-wet carbonate fractured rocks. The core samples were 20 cm long and 3.8 cm diameter. He used C<sub>7</sub>-C<sub>1</sub> as oil. Porosity and permeability values were in the ranges of 8-25% and 1.5 to 130md, respectively. His experimental setup and procedure was the same as for the Darvish et al. (2006) experiments (Fig. 2.5). Secondary gas injection experiments were done at 220 bars and 85°C. In secondary gas injection experiments, equilibrium gas was initially injected to displace oil by gravity. Equilibrium gas was in equilibrium with the oil in the core and therefore, there was no mass transfer between the equilibrium gas and the oil. Once oil production ceased, a second period of pure CO<sub>2</sub> or N<sub>2</sub> injection followed. In tertiary gas injection, first oil was displaced by water injection at 220 bars and 85°C. Then equilibrium gas injection started at 210 bars and 85°C, followed by a second period of equilibrium gas, N<sub>2</sub> or CO<sub>2</sub> injection at 220 bars and 85°C. He claimed that diffusion plays an important role in both secondary and tertiary oil recovery. He showed experimentally that tertiary oil recovery increased by increasing injection pressure from 210 bar to 220 bar at 85°C. However, the efficiency of the process strongly depends on the type of gas. Injecting CO<sub>2</sub> resulted in higher recovery than equilibrium gas or nitrogen injection in tertiary

recovery. He claimed this is due to the fact that, in CO<sub>2</sub> injection, several mechanisms such as gravity drainage, diffusion, swelling, and IFT reduction are contributing to oil recovery. Also in secondary recovery, when nitrogen is injected, ultimate recovery is lower than CO<sub>2</sub> injection. No detailed simulation was done.

## 2.2. Simulation studies

Coats (1989) included the effect of diffusion in dual-porosity models. Diffusion coefficients for liquid-liquid diffusion are about 100 times smaller than those for gas-gas diffusion. Liquid-gas diffusion coefficients are larger than liquid-liquid diffusion coefficients but still less than gas-gas diffusion coefficients. Therefore, Coats (1989) neglected gas-oil and oil-oil diffusion between fracture and matrix in his formulation and only gas-gas diffusion was considered as:

$$\text{Diffusion between matrix and fracture} = \phi S_{gg} D_g \left( (\rho_g y_i)_m - (\rho_g y_i)_f \right) \text{Eq. (2.1)}$$

where

$S_{gg}$  is the geometric mean of matrix and fracture gas saturation

$D_g$  is gas diffusion coefficient

$\rho_g, \rho_o$  are molar densities of gas and oil

$(y_i)_m, (y_i)_f$  are mole fraction of component  $i$  in gas phase in matrix and fracture

$\phi$  is matrix porosity

Coats (1989) solved the diffusion equation in 1-dimension (x-direction) to estimate diffusion transient time. The diffusion equation was derived for a linear horizontal core with length  $l$  initially saturated with fluid of unit concentration and then exposed to zero fluid concentration at  $x=0$  and  $x=l$ . The diffusion equation in 1-dimension is defined as follows:

$$\frac{\partial^2 C}{\partial x_D^2} = \frac{\partial C}{\partial t_D} \quad \text{Eq. (2.2)}$$

$$\text{Initial condition: } C(x_D, t_D=0)=1 \quad \text{Eq. (2.3)}$$

$$\text{Boundary conditions: } C(x_D=1, t_D)=0, \frac{\partial C}{\partial x_D}(x_D = 0, t_D) = 0 \quad \text{Eq. (2.4)}$$

Where

$$x_D = \frac{x}{(l/2)} \quad \text{Eq. (2.5)}$$

$$t_D = \frac{Dt}{\tau(l/2)^2} \quad \text{Eq. (2.6)}$$

$D$  is diffusion coefficient and  $\tau$  is tortuosity of the porous medium.

The average concentration is calculated as:

$$\hat{C} = \frac{\int_0^l C dx}{l} = 2 \sum_{n=1}^{\infty} \frac{1}{\lambda_n^2} e^{-\lambda_n t_D} \quad \text{Eq. (2.7)}$$

$$\text{where } \lambda_n = \frac{(2n-1)\pi}{2} \quad \text{Eq. (2.8)}$$

Using a first-term approximation in Eq. (2.7), the time necessary for  $\hat{C}$  to decay 90% from its initial value is:

$$t^* = 0.85\tau(l/2)^2/D \quad \text{Eq. (2.9)}$$

Coats (1989) assumed that for high pressure diffusion (e.g. 4500 psia), the gas-gas diffusion coefficient is in the order of 0.001 cm<sup>2</sup>/second. Therefore, for a 1-ft core and tortuosity of 3.5,  $t^*=8$  days from Eq. (2.9). For practical purposes for oil field situations this is instantaneous.

Da Silva and Belery (1989) simulated the effect of diffusion on oil recovery from highly fractured reservoirs with low matrix permeability in the North Sea and in Africa. The oil components were C<sub>1</sub>, C<sub>2</sub>-C<sub>6</sub>, and C<sub>7+</sub>. The injected gas was nitrogen. The simulation studies were done at 266°F and 4415 psia. The maximum matrix block height was 4 ft in their simulations. The diffusion equation for a matrix block was solved analytically for a step change in concentration at the matrix boundary. The analytical solution provided the concentration of each component as a function of time. Their analytical simulation results showed the significant effect of diffusion on the oil recovery, especially for small matrix block size of the order of several feet or less. They suggested taking into account the effect of diffusion on oil recovery in simulation of naturally fractured reservoirs.

Thomas et al. (1991) conducted a simulation study of nitrogen injection into the highly fractured Ekofisk field in the North Sea. The model temperature and pressure were 268°F and 4000psig. Bubble point pressure was 5545psia. They defined the diffusion time as the time required to increase concentration of N<sub>2</sub> in the core to 99% by diffusion. They showed that diffusion time for 1 and 10 ft blocks are 10 days and 5 years, respectively. The interfacial tension was increased by nitrogen diffusion.

Hua and Whitson (1991) simulated experiment No. M5 shown in Table 2.1. Their model combined an analytical solution for mass transfer in the fracture with a numerical model in the core. An analytical solution in the fracture was used to define a mass transfer coefficient between matrix and flowing gas in the fracture. Convection (driven by pressure gradient) between matrix and fracture is not considered in the model. They showed that diffusion is an important mechanism for transporting N<sub>2</sub> and C<sub>1</sub> in the porous media. C<sub>5</sub> is transported to the fracture face mainly by oil convection inside the core. They also recognized the importance of correction of capillary pressure for the variation of interfacial tension due to gas diffusion in oil recovery calculations. They used a ternary diagram (Figure 2.2) to explain why pentane recovery is not only by pure diffusion. They explained that as core fluid contacts nitrogen, the amount of pentane in the oil phase should increase (based on Fig. 2.2), which means that pentane will diffuse from the fracture into the core. This is impossible since the injected gas does not contain pentane from the fracture. The only way to keep

phases in equilibrium is to have pentane supplied from the lower part of the core. This is the reason behind oil convection from the matrix towards the fracture.

Fayers et al. (1992) simulated experiment No. M5 (nitrogen diffusion experiment) of the Morel et al. (1990) diffusion experiments (Table 2.1) to test their compositional simulator. The computational mesh had 20 grid blocks along the core and 3 grid blocks along the fracture, which allowed its inlet, mass transfer region, and outlet to be represented. The mass transfer coefficient between matrix and fracture was evaluated using a laminar flow theory similar to that described by Hua and Whitson (1991). They showed the importance of correcting capillary pressure with interfacial tension in the calculations. Also, they recognized that the shapes of the calculated saturation profiles are strongly dependent on the selection of a capillary pressure curve and on the accuracy of determining variations of interfacial tension.

Riazi et al. (1994) solved the diffusion equation (Eq. (2.2)) analytically to simulate their experiments (Fig. 2.7). They treated the fracture as a boundary condition for the matrix. Two boundary conditions were studied for the fracture-matrix interface. They were a stagnant condition and high flow in the fracture. Their simulation results showed good agreement with experimental data (composition of methane versus time) for both cases. They recognized that diffusion is a very important mechanism in oil recovery.



Saidi (1996) simulated performance of the Haft Kel field at Iran. Matrix block size varies from 8 to 14 ft in the Haft Kel field. Permeability changes between 0.05 to 0.8 md. He showed the importance of diffusion during history matching of the Haft Kel reservoir.

Lenormand et al. (1998) developed a mass transfer coefficient between matrix and fracture similar to the Hua and Whitson (1991) model. The model was used successfully to simulate the following experiments:

- 1- M5 nitrogen diffusion experiment in Table 2.1 (Morel et al. (1990)).
- 2- M12 methane diffusion experiment in Table 2.2 (Le Romancer et al. (1994a, 1994b)).
- 3- M29 and M30 methane diffusion experiments in Table 2.3 (Le Gallo et al. (1997)).

Hoteit and Firoozabadi (2006) simulated gas injection using finite element methods. The domain of the model is a 2-D vertical cross-section (xz) with 500m length and 100m height with different fracture spacing of 100mx10m, 10mx10m, and 10mx5m. Fig. 2.8 shows the configuration of the model. Matrix permeability was set 1md or 0.1md in the simulation studies. Matrix porosity was 20%. Fracture relative permeability was linear. Capillary pressures in matrix and fracture were assumed zero. Table 2.4 presents the details of their simulation study. One injection well and one production well were defined in the model. The injection well was located on top right corner and the production well was located

at the lower opposite corner. They took into account the effect of non-ideality to calculate the diffusion coefficients in a multi-component mixture. They concluded

**Table 2.4: Simulation examples of Hoteit and Firoozabadi (2006)**

Example No.	P(bar ) at top of the model	T(K)	Oil composition	Injected gas composition	Gas injection rate (PV/day)	Production
1	38	366	C <sub>3</sub>	C <sub>1</sub>	1.30E-04	BHP=38 bar
2	320	366	CO <sub>2</sub> &C <sub>3</sub> ,C <sub>1</sub> , C <sub>2</sub> ,C <sub>3</sub> ,C <sub>4</sub> ,C 5,C <sub>5</sub> ,C <sub>6</sub> , C <sub>7</sub> -9,C <sub>10</sub> +	C <sub>1</sub>	6.80E-05	BHP=320 bar
3	175	366	CO <sub>2</sub> ,N <sub>2</sub> - C <sub>1</sub> ,H <sub>2</sub> S-C <sub>2</sub> - C <sub>3</sub> ,C <sub>4</sub> -C <sub>6</sub> , C <sub>7</sub> -C <sub>9</sub> , C <sub>10</sub> - C <sub>14</sub> , C <sub>15</sub> - C <sub>18</sub> ,C <sub>19</sub> +	CO <sub>2</sub>	6.20E-05	BHP=175 bar
4	437	410	CO <sub>2</sub> ,N <sub>2</sub> -C <sub>1</sub> , C <sub>2</sub> ,C <sub>3</sub> ,C <sub>4</sub> -C <sub>5</sub> , C <sub>6</sub> -C <sub>7</sub> , C <sub>8</sub> - C <sub>11</sub> , C <sub>12</sub> -C <sub>19</sub> , C <sub>20</sub> -C <sub>29</sub> , C <sub>30</sub> +	CO <sub>2</sub> -N <sub>2</sub> - C <sub>1</sub> , C <sub>2</sub> , C <sub>3</sub> , C <sub>4</sub> - C <sub>5</sub> , C <sub>6</sub> -C <sub>7</sub>	5.76E-05	Constant rate= 7.2e-5 PV/day

BHP=Bottom Hole Pressure

that for a low permeability matrix (1 and 0.1 md) the effect of diffusion is much more than what current models predict. They treated the fracture as a boundary between adjacent matrices. In their simulation, the pressure, saturation, and

mole fraction in the fracture were calculated by interpolation between adjacent matrices. Their simulation results showed 25% increase in oil recovery by including diffusion with their method relative to the case without diffusion. The effect of diffusion was more pronounced for smaller fracture spacing.

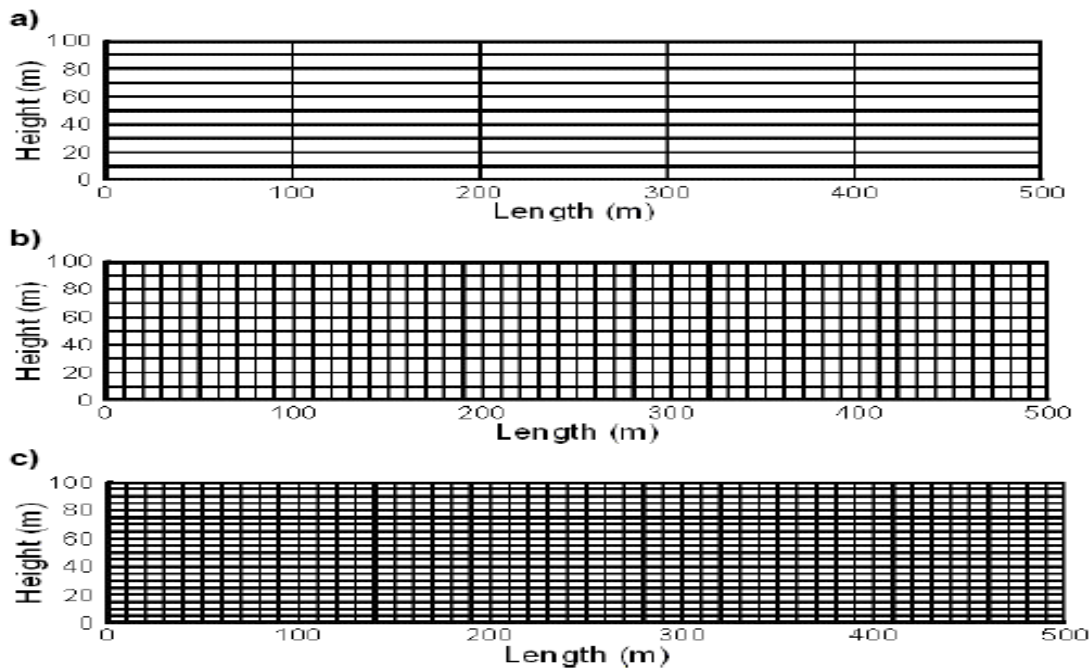


**Fig. 2.8: 2-D cross section with different fracture intensities: a) 100mx10m matrix blocks, b) 10mx10m matrix blocks, and c) 10mx5m matrix blocks**

**(Hoteit and Firoozabadi (2006))**

Alavian et al. (2009) simulated a secondary CO<sub>2</sub> injection experiment of Karimaie (2007). In the Karimaie (2007) experiments, equilibrium gas was in equilibrium with the oil in the core and therefore, there was no mass transfer between the equilibrium gas and the oil. The SENSOR compositional model (single porosity) was used to simulate the experiment. SENSOR does not have a

diffusion mechanism in the single porosity model. A cylindrical model (single porosity) with 10 grids in radial direction and 51 grids in vertical direction was used to simulate the experiment. The simulation results showed the following results:

- 1- Darcy displacement is the dominant recovery mechanism in the Karimaie (2007) secondary experiment during the equilibrium gas injection period because of a low conductivity in the surrounding fracture. The fracture space in the Karimaie (2007) experiments was created by melting wood's metal initially filled the space. Simulation results indicated that the fracture had low conductivity (20-30md) which means melting wood's metal was not a successful process.
- 2- It was concluded that near-miscible displacement was the dominant production mechanism during secondary CO<sub>2</sub> injection.
- 3- Gravity-capillary forces had a minor effect in Karimaie (2007) experiment.

Moortgat et al. (2009) simulated the Darvish et al. (2006) CO<sub>2</sub> experiment by finite element methods. Their simulation method is the same as Hoteit and Firoozabadi (2006) method. A Cartesian model with 19x1x40 grids in x, y, and z direction was used to simulate the experiment. It was found that diffusion was an important recovery mechanism. However, the impact of diffusion on oil recovery was not as significant as the Darvish et al. (2007) simulation results showed.

### 2.3. Literature summary

The literature review so far is notable for the following facts:

- 1- Diffusion could be an important recovery mechanism in naturally fractured reservoirs, especially for small matrix block size and low permeability (high capillary pressure) rocks where the gravity is not an efficient recovery mechanism.
- 2- Injected gas type and composition are important factors for evaluating the oil recovery by diffusion.
- 3- There are very few attempts to model mass transfer (diffusion and convection) between a flowing gas in the fracture and oil and gas in the matrix in a single porosity model. Hua and Whitson (1991) modeled diffusion mass transfer by a deriving mass transfer coefficient. Convection mass transfer is neglected in their model.

As stated in Chapter 1, the primary objective of this dissertation is to mathematically model mass transfer between a gas phase in the fracture and oil and gas phases in the matrix in a single porosity model. The proposed model is validated with experimental data from the literature.

### **Chapter 3. Mathematical model**

There are several commercial models available to conceptualize and model naturally fractured reservoirs. These models are classified as dual-porosity, dual-porosity/dual-permeability, and dual continuum, approaches. The dual continuum approach (or single-block model or single porosity model) was used to model gas injection in naturally fractured reservoirs in this dissertation. This model will be discussed in what follows next section.

Compositional simulators were developed to predict the phase and compositional behavior of reservoirs fluids under gas injection. In compositional simulation, it is assumed that water and hydrocarbon phases are insoluble. Therefore, separate mass conservation equations are written for the water and hydrocarbon components. Compositional simulators are written in moles instead of mass, since phase behavior equations are expressed in moles. For compositional multiphase flow, three forces must be properly accounted for: viscous, gravity, and capillarity. In addition, if gas is injected, diffusion mechanism must be included to quantify for mass-transfer between phases. Details of the model including mass-transfer mechanisms, governing equations, boundary conditions, initial conditions, and the numerical solution will be presented in this chapter.

### **3.1. Dual-continuum approach**

The approach used to model naturally fractured reservoirs on a local scale is to consider a fractured porous media as a single matrix block with an adjacent fracture. The fracture acts as a boundary condition for the matrix. This approach is a fine-scale representation of a naturally fractured reservoir since it allows one to study the fluid flow between the fracture and the matrix block. This approach is known as single porosity, dual-continuum, and single block model. Fig. 3.1 shows the layout of the model. The matrix is discretized, but the fracture is not, because the fracture acts as a boundary condition for the matrix. The single-block model has been used in many research studies. Yamamoto et al. (1971) used this model to study a single matrix block under several boundary conditions.

### **3.2. Mass transfer mechanisms**

There are three basic mechanisms to transport miscible and immiscible fluids in porous media: convection (or bulk flow), molecular diffusion, and mechanical dispersion. Mechanical dispersion is neglected in the model. A brief description of convection and molecular diffusion mechanisms follow.

#### **3.2.1. Convection (Bulk flow)**

Convection is the transport of the component as it is carried along within bulk fluid movement. The driving force for convection (bulk flow) is the potential gradient.

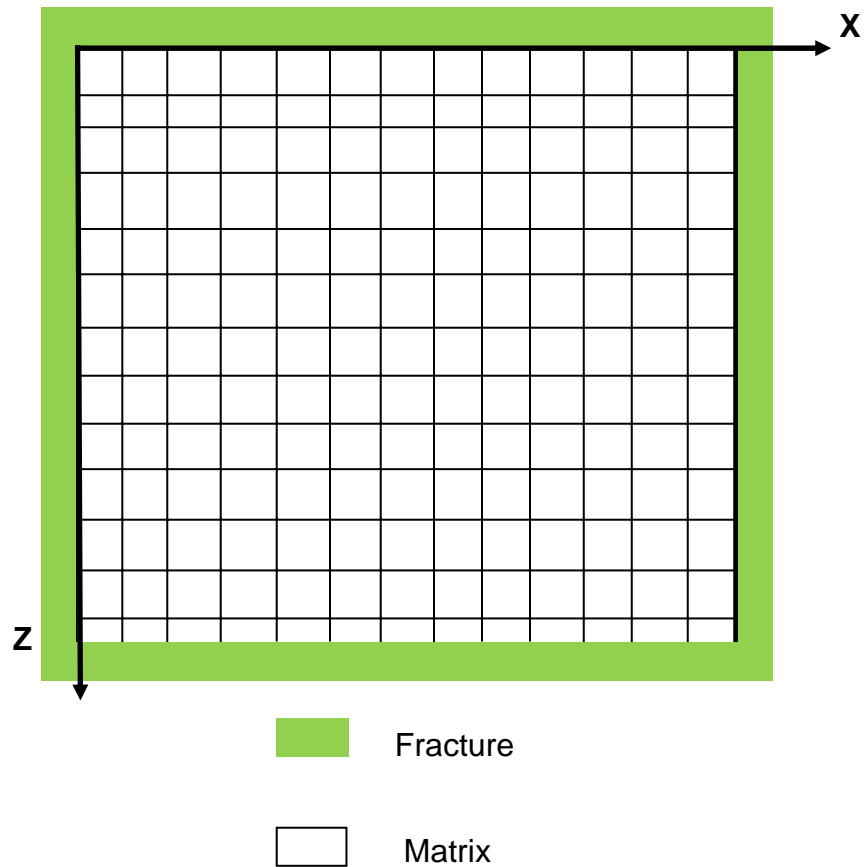


**Fig. 3.1: Model layout**

### 3.2.2. Molecular diffusion

Molecular diffusion is the mechanism of a component transport by random molecular motion. Molecular diffusion is the tendency to mix due to chemical potential gradient. Bird et al. (1960) showed that concentration gradient instead of chemical potential gradient can be used as the driving force for ideal or near ideal mixtures. Concentration gradient is used as the driving force of molecular diffusion in this dissertation.



### 3.3. Governing equations in the model

A compositional reservoir simulator consists of a set of partial differential equations with appropriate initial and boundary conditions.

The equations governing compositional multiphase flow in porous media arise from three sources (Lake et. al. (1984)):

- 1- Material balance equations govern transport of each component in oil and gas by the convection and diffusion mechanisms. Therefore,

Hydrocarbon components and CO<sub>2</sub>,

$$\begin{aligned} & \nabla \cdot \left( \rho_o x_c \frac{kk_{ro}}{\mu_o} (\bar{\nabla} p_o - \gamma_o \bar{\nabla} D) + \rho_g y_c \frac{kk_{rg}}{\mu_g} (\bar{\nabla} p_g - \gamma_g \bar{\nabla} D) \right) + \\ & \nabla \cdot \left( \phi S_o \rho_o (D_{c,o} \nabla x_c) + \phi S_g \rho_g (D_{c,g} \nabla y_c) \right) + q_{D, fm, c} + q_{C, fm, c} = \frac{\partial}{\partial t} \left[ \phi (\rho_o S_o x_c + \rho_g S_g y_c) \right] \end{aligned}$$

**Eq. (3.1)**

c=1, 2, ..., n<sub>c</sub>

The first bracket represents the convection mechanism in oil and gas phases. Diffusion mechanism is represented in the second bracket.  $q_{D, fm}$  and  $q_{C, fm}$  are diffusion and convection mass transfer between matrix and fracture at the matrix-fracture boundary.

One mass balance equation describes water movement by the convection mechanism only, because the hydrocarbon phases are assumed to be insoluble with the water phase.

Water phase,

$$\nabla \cdot \left[ \rho_w \frac{kk_{rw}}{\mu_w} (\nabla p_w - \gamma_w \nabla D) \right] = \frac{\partial}{\partial t} [\phi \rho_w S_w] \quad \text{Eq. (3.2)}$$

- 2- Phase equilibrium between hydrocarbon phases is expressed in the form of equality between the fugacity (from Peng-Robinson EOS) of each component in both oil and gas phases,

$$f_{o,c} = f_{g,c} \quad c=1, 2, \dots, n_c \quad \text{Eq. (3.3)}$$

- 3- Constraint equations that require the phase saturations to sum to unity and mole fraction in each phase to sum to unity. Besides, it is necessary to relate water, oil, and gas pressure, that is, capillary pressure relationships.

$$S_o + S_g + S_w = 1 \quad \text{Eq. (3.4)}$$

$$\sum_{c=1}^{n_c} x_c = 1, \quad \sum_{c=1}^{n_c} y_c = 1 \quad \text{Eq. (3.5)}$$

$$P_{cog} = p_g - p_o, \quad P_{cow} = p_o - p_w \quad \text{Eq. (3.6)}$$

If gas-oil capillary pressure ( $p_c^{ref}$ ) is reported at a reference interfacial tension ( $\sigma_{ref}$ ), in some cases it must be corrected by local interfacial tension ( $\sigma$ ) at each

grid as: 
$$p_{cog} = p_{cog}^{ref} \frac{\sigma}{\sigma_{ref}} \quad \text{Eq. (3.7)}$$

The equations governing compositional multiphase flow in porous media are given by equations (3.1) to (3.7). This equation system consists of set of  $(2n_c + 6)$  equations with the same number of unknowns. The  $(2n_c+6)$  unknowns are  $(p_o, p_g, p_w, S_o, S_g, S_w, x_1, x_2, \dots, x_{nc}, y_1, y_2, \dots, y_{nc})$ . Detailed derivation of the flow equations is presented in Appendix A.

### 3.4. Initial and boundary conditions

Initial conditions define the pressure, saturation, and composition distribution at time equal to zero. Boundary conditions specify the ways in which the reservoir interacts with its surrounding. The initial and boundary conditions will be presented next.

#### 3.4.1. Initial conditions

It is assumed that there is gravity equilibrium in the model at time equal to zero. Also, pressure and composition at a reference is known. Since there is gravity equilibrium at time equal to zero, convective flow vanishes. Therefore, from Darcy's law:

$$\rho_p \frac{kk_{rp}}{\mu_p} (\nabla p_p - \gamma_p \nabla D) = 0 \quad p=\text{gas, oil, and water} \quad \text{Eq. (3.8)}$$

For a horizontal plane  $\nabla D = 0$ , so Eq.(3.8) simplifies to:

$$\frac{\partial p_p}{\partial x} = 0 \quad p=\text{gas, oil, and water} \quad \text{Eq. (3.9)}$$

$$\frac{\partial p_p}{\partial y} = 0 \quad p=\text{gas, oil, and water} \quad \text{Eq. (3.10)}$$

Eq.(3.9) and Eq.(3.10) state that pressure, composition, and saturation are constant in a horizontal plane at time equal to zero.

For the vertical direction, Eq.(3.8) becomes:

$$\frac{\partial p_p}{\partial z} - \gamma_p = 0 \quad p=\text{gas, oil, and water} \quad \text{Eq. (3.11)}$$

Eq.(3.11) means that vertical pressure distribution is given by the column weight.

Integrating Eq.(3.11) results in:

$$p_p = p_{ref} + \overline{\gamma_p} (z - z_{ref}) \quad p=\text{gas, oil, and water} \quad \text{Eq. (3.12)}$$

where  $\overline{\gamma_p}$  is the average specific weight of phase p between z and  $z_{ref}$  height.

If pressure at a reference height is given, then pressure at any point in the model can be calculated from Eq.(3.12).

### 3.4.2. Matrix boundary conditions

There are two boundary condition types for the matrix: 1- sealed boundary and 2- matrix-fracture boundary (Fig. 3.1). These boundary conditions are taken care as follows:

### 3.4.2.1 Matrix sealed boundary conditions

The total mass flux for all components in all phases vanishes at these boundaries. That is,

Convection flux at the boundary:

$$\rho_p \frac{k k_{rp}}{\mu_p} (\nabla P_p - \gamma_p \nabla D) = 0 \quad p = \text{gas, oil, and water} \quad \text{Eq. (3.13)}$$

Diffusion flux at the boundary:

$$\phi S_p \rho_p (D_{c,p} \nabla x_c) = 0 \quad p = \text{gas and oil} \quad c = 1, 2, \dots, n_c \quad \text{Eq. (3.14)}$$

Eq.(3.13) and Eq.(3.14) are defined in the model by setting the transmissibilities equal to zero at the sealed boundaries.

### 3.4.2.2 Matrix-fracture boundary conditions

The continuity equation in the fracture includes mass transport by diffusion and convection mechanisms in a laminar flow regime. For example, steady state continuity equation for the top fracture in Fig. 3.1 can be expressed by the following partial differential equation:

$$-v \frac{\partial y_c}{\partial x} - D_{e,c} \frac{\partial^2 y_c}{\partial z^2} = 0 \quad c = 1, 2, \dots, n_c \quad \text{Eq. (3.15)}$$

where

$\bar{v}$  is the average gas velocity over the cross-sectional area normal to the bulk flow in the fracture, and

$D_{e,c}$  is the effective diffusion coefficient for component  $c$  between matrix and fracture

The boundary conditions are:

$$\begin{aligned} z = 0, \quad y_c &= y_{c,mf} \\ z = H, \quad \frac{\partial y_c}{\partial z} &= 0 \quad c=1, 2, \dots, n_c \\ x = 0, \quad y_c &= y_{c,f} \end{aligned} \quad \text{Eq. (3.16)}$$

where

$y_{c,mf}$  is composition of component  $c$  in the gas phase at matrix-fracture boundary,

$y_{c,f}$  is composition of component  $c$  at the entrance of the fracture, and

$H$  is the fracture thickness in the  $z$ -direction

Gas stream velocity and physical properties in the fracture are assumed constant in deriving Eq.(3.15). An analytical solution was derived for Eq.(3.15) to find composition ( $y_c$ ) distribution in the fracture. The details of the derivation are presented by Hua and Whitson (1991) and Lenormand et. al. (1998). The

diffusion mass transfer rate at matrix-fracture surface was found by differentiating  $y_c$  as follows:

$$q_{D, fm, c} = A \rho_g D_{e, c} \left( \frac{\partial y_c}{\partial z} \right)_{z=0} \quad c=1, 2, \dots, n_c \quad \text{Eq. (3.17)}$$

where  $\rho_g$  is gas stream density in the fracture

After simplifications, the final diffusion mass exchange rate between matrix and fracture is defined in the model as:

$$q_{D, fm, c} = k_c WH (y_{c, f} - y_{c, mf}) \quad c=1, 2, \dots, n_c \quad \text{Eq. (3.18)}$$

$$k_c = \alpha_s \rho_g \bar{v} \left( \exp \left( -\frac{D_{e, c}}{\bar{v}} \left( \frac{\pi}{2H} \right)^2 l \right) - 1 \right) \quad c=1, 2, \dots, n_c \quad \text{Eq. (3.19)}$$

where

$W$  is the fracture width in  $y$ -direction,

$\alpha_s$  is a factor for considering skin-effect at matrix-fracture boundary, and

$l$  is the fracture length in  $x$ -direction

If the matrix is saturated with oil (no initial gas saturation presents), then diffusion mass transfer occurs between flowing gas in the fracture and oil in the matrix. In this case,  $y_{c, mf}$  in Eq. (3.18) is defined as

$$y_{c, mf} = K_c x_{c, mf} \quad \text{Eq. (3.20)}$$

where

$K_c$  is the equilibrium ratio of component c

$x_{c,mf}$  is composition of component c in the oil phase at matrix-fracture boundary

Diffusion between the matrix and fracture is modeled by introducing a source/sink term (Eq. (3.18)) in the flow equations for the first matrix grid cell adjacent to the fracture. After a certain amount of each component has entered or left the first grid during a time step, flash calculations are performed to distribute the entered or remained amount of each component between oil and gas phases. Mass transfer between grids in the matrix occurs by diffusion and convection in both oil and gas phases (Eq. (3.1)).

Convection between a matrix grid cell and the adjacent fracture ( $q_{C, fm, c}$ ) is defined in the model based on Darcy's law as:

$$q_{C, fm, c} = \left( x_c \rho_o \frac{kk_{ro}}{\mu_o} \right)_{matrix} \left[ (\nabla p_o - \gamma_o \nabla D)_{matrix} - (\nabla p_g - \gamma_g \nabla D)_{fracture} \right] + \left( y_c \rho_g \frac{kk_{rg}}{\mu_g} \right)_{matrix} \left[ (\nabla p_g - \gamma_g \nabla D)_{matrix} - (\nabla p_g - \gamma_g \nabla D)_{fracture} \right] \quad c=1, 2, \dots, n_c$$

**Eq. (3.20)**



If the pressure in the oil and/or gas phase in the matrix grid cell is more than fracture gas pressure, all components in oil and/or gas will flow from the matrix to the fracture. On the other hand, if gas pressure in the fracture is more than gas pressure in the matrix grid cell, then the gas flows from the fracture to the matrix if difference between gas pressure in the fracture and oil pressure in the matrix grid cell exceeds threshold capillary pressure. If there is no gas saturation in the matrix grid ( $IFT=0$ ), then the threshold capillary pressure remains constant until a gas saturation forms in the matrix grid cell ( $IFT>0$ ) and the critical gas saturation is reached. After developing gas saturation in the matrix grid cell, threshold capillary pressure is scaled with interfacial tension. Oil does not flow from the fracture to the matrix, because there is no oil phase in the fracture.

### **3.5. Numerical solution**

The differential equations governing compositional multiphase flow in porous media are presented in the previous section. Some of these equations are nonlinear. The numerical technique replaces all derivatives by the finite-difference approximations resulting in a set of nonlinear algebraic equations. Then, the resultant equations are linearized and solved by the iterative Newton-Raphson method. Details of the Newton-Raphson method applied in this dissertation is presented in Appendix C.

In this section, the discretization of the differential equations governing compositional multiphase flow in porous media will be presented first. Then the numerical solution scheme will be discussed.

### 3.5.1. Discretization of the flow equations

Discretization of any partial differential equation consists of changing its continuum to a discrete domain in all its independent variables. In multiphase compositional flow simulation, the spatial and time domains are replaced by a network of discrete points. The approximate partial differential equations are then written for each of these discretized points. The system of algebraic equations is solved by a suitable technique, providing an approximate solution to the dependent variables at each node and at discrete points in time. Discretization of the flow equations (Eq.(3.1) and Eq.(3.2)) is presented in Appendix B in details.

The discretized form of the flow equations is written as follows:

for hydrocarbon components and CO<sub>2</sub>:

$$\begin{aligned} & \Delta \left[ T_o x_c (\Delta p_o - \Delta(\gamma_o D)) \right]_{i,j,k}^{n+1} + \Delta \left[ T_g y_c (\Delta p_g - \Delta(\gamma_g D)) \right]_{i,j,k}^{n+1} + \\ & \Delta \left[ T_{o,c}^M \Delta x_c \right]_{i,j,k}^{n+1} + \Delta \left[ T_{g,c}^M \Delta y_c \right]_{i,j,k}^{n+1} + (q_{D,fm,c} + q_{C,fm,c})^{n+1} = \quad \mathbf{c=1, 2, \dots, n_c} \\ & \frac{V_{r,i,j,k}}{\Delta t} \Delta_t \left[ \phi x_c \rho_o S_o + \phi y_c \rho_g S_g \right]_{i,j,k} \end{aligned}$$

**Eq. (3.21)**

and for water:

$$\Delta \left[ T_w (\Delta p_w - \gamma_w \Delta D) \right]_{i,j,k}^{n+1} = \frac{V_{r,i,j,k}}{\Delta t} \Delta_t \left[ \phi \rho_w S_w \right]_{i,j,k} \quad \text{Eq. (3.22)}$$

Eq. (3.21) and Eq. (3.22) are simplified by using the following relations:

$$F = \rho_o S_o + \rho_g S_g \quad \text{Eq.(3.23)}$$

$$W = \rho_w S_w \quad \text{Eq.(3.24)}$$

$$Fz_c = x_c \rho_o S_o + y_c \rho_g S_g \quad c = 1 \text{ to } n_c \quad \text{Eq. (3.25)}$$

Substituting Eq. (3.23), Eq. (3.24), and Eq. (3.25) into Eq. (3.21) and Eq. (3.22)

result in:

for hydrocarbon components and CO<sub>2</sub>:

$$\begin{aligned} R_c = & \Delta \left[ T_o x_c (\Delta p_o - \Delta(\gamma_o D)) \right]_{i,j,k}^{n+1} + \Delta \left[ T_g y_c (\Delta p_g - \Delta(\gamma_g D)) \right]_{i,j,k}^{n+1} + \\ & \Delta \left[ T_{o,c}^M \Delta x_c \right]_{i,j,k}^{n+1} + \Delta \left[ T_{g,c}^M \Delta y_c \right]_{i,j,k}^{n+1} + \quad c=1, 2, \dots, n_c \\ & \left( q_{D,fm,c} + q_{C,fm,c} \right)^{n+1} - \frac{V_{r,i,j,k}}{\Delta t} \Delta_t \left[ \phi Fz_c \right]_{i,j,k} \end{aligned}$$

**Eq. (3.26)**

$$R_w = \Delta \left[ T_w (\Delta p_w - \gamma_w \Delta D) \right]_{i,j,k}^{n+1} - \frac{V_{r,i,j,k}}{\Delta t} \Delta_t \left[ \phi W \right]_{i,j,k} \quad \text{Eq. (3.27)}$$

Summing Eq.(3.26) for all hydrocarbon components and CO<sub>2</sub> results in an overall hydrocarbon and CO<sub>2</sub> equation as:

$$\begin{aligned}
R_H = & \Delta \left[ T_o (\Delta p_o - \Delta(\gamma_o D)) \right]_{i,j,k}^{n+1} + \Delta \left[ T_g (\Delta p_g - \Delta(\gamma_g D)) \right]_{i,j,k}^{n+1} + \\
& \sum_{c=1}^{n_c} \Delta \left[ T_{o,c}^M \Delta x_c \right]_{i,j,k}^{n+1} + \sum_{c=1}^{n_c} \Delta \left[ T_{g,c}^M \Delta y_c \right]_{i,j,k}^{n+1} + \quad \mathbf{c=1, 2, \dots, n_c} \\
& \sum_{c=1}^{n_c} \left( q_{D, fm, c} + q_{C, fm, c} \right)^{n+1} - \frac{V_{r,i,j,k}}{\Delta t} \Delta_t [\phi F]_{i,j,k}
\end{aligned}$$

**Eq. (3.28)**

the equilibrium thermodynamic equation:

$$R_{gc} = f_{o,c}^{n+1} - f_{g,c}^{n+1} = 0 \quad \mathbf{c=1,2,\dots,n_c} \quad \mathbf{Eq.(3.29)}$$

constraints and capillary pressure relations also have to be discretized as:

$$\left( \sum_1^{n_c} x_c \right)^{n+1} = 1 \quad \mathbf{Eq. (3.30)}$$

$$\left( \sum_1^{n_c} y_c \right)^{n+1} = 1 \quad \mathbf{Eq. (3.31)}$$

$$R_s = 1 - S_o^{n+1} - S_g^{n+1} - S_w^{n+1} \quad \mathbf{Eq. (3.32)}$$

$$P_{cog}^{n+1} = p_g^{n+1} - p_o^{n+1} \quad \mathbf{Eq. (3.33)}$$

$$P_{cow}^{n+1} = p_o^{n+1} - p_w^{n+1} \quad \mathbf{Eq. (3.34)}$$

In summary, the system of algebraic nonlinear equations given by Eq.(3.26) to Eq.(3.34) consists of a set of  $2n_c+6$  equations with the same number of

unknowns for every grid and every time step  $n+1$ . The  $2n_c+6$  unknowns are  $(p_o, p_g, p_w, S_o, S_g, S_w, x_1, x_2, \dots, x_{n_c}, y_1, y_2, \dots, y_{n_c})$ . There are  $2n_c+6$  equations:  $n_c$  equations of Eq. (3.26), one water equation (Eq. (3.27)),  $n_c$  equations of Eq. (3.29), two mole fraction constraints of Eq. (3.30) and Eq. (3.31), saturation constraint of Eq. (3.32), and two capillary pressure relations of Eq. (3.33) and Eq. (3.34).

### 3.5.1. Numerical solution scheme

The Young and Stephenson (1983) numerical method was used as the numerical technique. Young and Stephenson (1983) defined  $p$ ,  $W$ ,  $F$ ,  $Z_c$ ,  $V$ , and  $y_c$  as primary variables and  $x_c$ ,  $S_o$ ,  $S_g$ , and  $S_w$  as secondary variables. This method is known as IMPESC (Implicit Pressure Explicit Saturation Composition) method.

In this method, the Newton-Raphson scheme is used to solve  $2n_c+2$  primary unknowns ( $p$ ,  $W$ ,  $F$ ,  $Z_c$ ,  $V$ , and  $y_c$ ,  $c=1, 2, \dots, n_c-1$ ) for each grid block containing two hydrocarbon phases, and  $n_c+2$  primary unknowns ( $p$ ,  $W$ ,  $F$ , and  $Z_c$   $c=1, 2, \dots, n_c-1$ ) for each grid block containing a single hydrocarbon phase. Transmissibilities and diffusion terms in the flow equations are evaluated explicitly.

The Newton-Raphson scheme consists of linearized forms of five sets of  $2n_c+2$  equations as follows:

(1)  $n_c$  phase equilibrium relationships of Eq. (3.29) for each grid block containing two hydrocarbon phases.

Since component fugacities are functions of pressure and compositions, then:

$$R_{gc} = R_{gc}(p, x_c, y_c) \quad c=1,2,\dots,n_c \quad \text{Eq. (3.35)}$$

$$\text{Since: } x_c = \frac{Z_c - Vy_c}{1-V} \quad c=1, 2,\dots,n_c \quad \text{Eq. (3.36)}$$

$$y_{n_c} = 1 - \sum_1^{n_c-1} y_c \quad \text{Eq. (3.37)}$$

$$Z_{n_c} = 1 - \sum_1^{n_c-1} Z_c \quad \text{Eq. (3.38)}$$

Then Eq. (3.35) may also be expressed as:

$$R_{fc} = R_{fc}(p, Z_c, V, y_c, c=1,2,\dots,n_c-1) \quad \text{Eq. (3.39)}$$

Fugacity must be differentiated with respect to all of the variables listed in Eq.(3.39). But, differentiating the fugacity with respect to  $Z_c$ ,  $V$ , and  $y_c$  yields terms with  $L$  in the denominator. To prevent the Jacobian from becoming ill-conditioned when a grid block contains only small amount of a liquid hydrocarbon phase, the fugacity constraints are scaled by  $L$  after being linearized. The scaled fugacity constraint for component  $c$  is:

$$R_{gc} = LR_{gc} = L(f_{oc} - f_{gc}) \quad c = 1, 2, \dots, n_c \quad \text{Eq. (3.40)}$$

(2)  $n_c - 1$  hydrocarbon component material balance of Eq. (3.26) are functions of  $p$ ,  $Z_c$ , and  $F$  as:

$$R_c = R_c(p, Z_c, F, c = 1, 2, \dots, n_c - 1) \quad \text{Eq. (3.41)}$$

(3) one overall hydrocarbon material balance of Eq. (3.28) is a function of  $p$  and  $F$  as:

$$R_H = R_H(p, F) \quad \text{Eq. (3.42)}$$

(4) one water material balance of Eq. (3.27)

Since water equation is a function of  $p$  and  $W$ , therefore:

$$R_w = R_w(p, W) \quad \text{Eq. (3.43)}$$

(5) one saturation constraint of Eq. (3.29)

Eq. (3.29) in terms of  $W$ ,  $F$ , and  $V$  gives:

$$R_s = 1 - S_o - S_g - S_w = 1 - F \left( \frac{1 - V}{\rho_o} + \frac{V}{\rho_g} \right) - \frac{W}{\rho_w} \quad \text{Eq. (3.44)}$$

Since the hydrocarbon molar densities are functions of pressure and composition, Eq.(3.44) may also be written as:

$$R_s = R_s(p, W, F, Z_c, V, y_c, c = 1, 2, \dots, n_c - 1) \quad \text{Eq. (3.45)}$$

Equations 3.40, 3.41, 3.42, 3.43, and 3.45 are linearized by differentiating with respect to the primary unknowns ( $p$ ,  $W$ ,  $F$ ,  $Z_c$ ,  $V$ , and  $y_c$ ,  $c=1, 2, \dots, n_c-1$ ). Writing the linearized equations in matrix form:

$$\left[ \begin{array}{cccccc} \frac{\partial R_{fc}}{\partial y} = G_y & \frac{\partial R_{fc}}{\partial v} = G_v & \frac{\partial R_{fc}}{\partial Z} = G_z & & & \frac{\partial R_{fc}}{\partial p} = G_p \\ & & \frac{\partial R_c}{\partial Z} = B_z & \frac{\partial R_c}{\partial F} = B_c & & \frac{\partial R_c}{\partial p} = T_c \\ & & & \frac{\partial R_H}{\partial F} = B_F & & \frac{\partial R_H}{\partial p} = T_f \\ & & & & \frac{\partial R_w}{\partial W} = B_w & \frac{\partial R_w}{\partial p} = T_w \\ \frac{\partial R_s}{\partial y} = C_y & \frac{\partial R_s}{\partial v} = C_v & \frac{\partial R_s}{\partial Z} = C & \frac{\partial R_s}{\partial F} = C_f & \frac{\partial R_s}{\partial W} = C_w & \frac{\partial R_s}{\partial p} = C_p \end{array} \right] \begin{bmatrix} \delta y \\ \delta V \\ \delta Z \\ \delta F \\ \delta W \\ \delta p \end{bmatrix} = - \begin{bmatrix} R_{fc} \\ R_c \\ R_H \\ R_w \\ R_s \end{bmatrix} \quad \text{Eq. (3.46)}$$

$c=1, 2, \dots, n_c$

where  $\delta y, \delta V, \delta Z, \delta F, \delta W$ , and  $\delta p$  represent change in  $y, V, Z, F, W$ , and  $p$  during an iteration.

For example, for a 3-component system the matrix has the following form:



$$\begin{bmatrix} G_{y11} & G_{y12} & G_{V1} & G_{Z11} & G_{Z12} & & & & & & G_{P1} \\ G_{y21} & G_{y22} & G_{V2} & G_{Z21} & G_{Z22} & & & & & & G_{P2} \\ G_{y31} & G_{y32} & G_{V3} & G_{Z31} & G_{Z32} & & & & & & G_{P3} \\ & & & B_Z & & B_1 & & & & & T_1 \\ & & & & B_Z & B_2 & & & & & T_2 \\ & & & & & B_F & & & & & T_f \\ & & & & & & B_W & T_W & & & \\ C_{y1} & C_{y2} & C_V & C_1 & C_2 & C_f & C_W & C_P & & & \end{bmatrix} \begin{bmatrix} \delta y_1 \\ \delta y_2 \\ \delta V \\ \delta Z_1 \\ \delta Z_2 \\ \delta F \\ \delta W \\ \delta p \end{bmatrix} = - \begin{bmatrix} R_{f1} \\ R_{f2} \\ R_{f3} \\ R_{c1} \\ R_{c2} \\ R_H \\ R_W \\ R_s \end{bmatrix} \quad \text{Eq. (3.47)}$$

The elements of Jacobian in Eq.(3.47) are presented next:

### G elements

The Jacobian in Eq.(3.46) consists of four G submatrices resulting from differentiating fugacity constraints with respect to the variables in Eq. (3.40).

The four G sub matrices in Eq.(3.46) have the following structures:

$$G_y = \begin{bmatrix} G_{y11} & G_{y12} & G_{y13} & \cdot & \cdot & \cdot & G_{y1n_c-1} \\ G_{y21} & G_{y22} & G_{y23} & \cdot & \cdot & \cdot & G_{y2n_c-1} \\ G_{y31} & G_{y32} & G_{y33} & \cdot & \cdot & \cdot & G_{y3n_c-1} \\ \cdot & \cdot & \cdot & \cdot & \cdot & \cdot & \cdot \\ \cdot & \cdot & \cdot & \cdot & \cdot & \cdot & \cdot \\ \cdot & \cdot & \cdot & \cdot & \cdot & \cdot & \cdot \\ G_{yn_c1} & G_{yn_c2} & G_{yn_c3} & \cdot & \cdot & \cdot & G_{yn_cn_c-1} \end{bmatrix} \quad \text{Eq. (3.48)}$$

$$G_V = \begin{bmatrix} G_{V1} \\ G_{V2} \\ G_{V3} \\ \cdot \\ \cdot \\ \cdot \\ G_{Vn_c} \end{bmatrix} \quad \text{Eq. (3.49)}$$

$$G_Z = \begin{bmatrix} G_{Z11} & G_{Z12} & G_{Z13} & \cdot & \cdot & \cdot & G_{Z1n_c-1} \\ G_{Z21} & G_{Z22} & G_{Z23} & \cdot & \cdot & \cdot & G_{Z2n_c-1} \\ G_{Z31} & G_{Z32} & G_{Z33} & \cdot & \cdot & \cdot & G_{Z3n_c-1} \\ \cdot & \cdot & \cdot & \cdot & \cdot & \cdot & \cdot \\ \cdot & \cdot & \cdot & \cdot & \cdot & \cdot & \cdot \\ \cdot & \cdot & \cdot & \cdot & \cdot & \cdot & \cdot \\ G_{Zn_c1} & G_{Zn_c2} & G_{Zn_c3} & \cdot & \cdot & \cdot & G_{Zn_cn_c-1} \end{bmatrix} \quad \text{Eq. (3.50)}$$

$$G_P = \begin{bmatrix} G_{P1} \\ G_{P2} \\ G_{P3} \\ \cdot \\ \cdot \\ \cdot \\ G_{Pn_c} \end{bmatrix} \quad \text{Eq. (3.51)}$$

$$x_c = \frac{Z_c - Vy_c}{1 - V} \quad c=1,2,\dots,n_c-1 \quad \text{Eq. (3.52)}$$

Differentiating Eq. (3.40) with respect to  $Z_c$ ,  $V$ , and  $y_c$  yields:

$$\frac{\partial x_c}{\partial Z_c} = \frac{1}{1 - V} \quad c=1,2,\dots,n_c-1 \quad \text{Eq. (3.53)}$$

$$\frac{\partial x_c}{\partial V} = \frac{-y_c(1-V) - (-1)(Z_c - Vy_c)}{(1-V)^2} = \frac{-y_c(1-V) + (1-V)x_c}{(1-V)^2} = \frac{x_c - y_c}{1-V} \quad \text{Eq. (3.54)}$$

$$\frac{\partial x_c}{\partial y_c} = \frac{-V}{1-V} \quad c=1,2,\dots,n_c-1 \quad \text{Eq. (3.55)}$$

$$G_{yij} = (1-V) \frac{\partial}{\partial y_j} (f_{o,c} - f_{g,c}) = (1-V) \left( \frac{\partial f_{o,c}}{\partial x_j} \frac{\partial x_j}{\partial y_j} - \frac{\partial f_{g,c}}{\partial y_j} \right) = -V \frac{\partial f_{o,c}}{\partial x_j} - (1-V) \frac{\partial f_{g,c}}{\partial y_j}$$

$$c,j=1,2,\dots,n_c-1 \quad \text{Eq. (3.56)}$$

$$G_{Zij} = (1-V) \frac{\partial}{\partial Z_j} (f_{o,c} - f_{g,c}) = (1-V) \left( \frac{\partial f_{o,c}}{\partial x_j} \frac{\partial x_j}{\partial Z_j} \right) = \frac{\partial f_{o,c}}{\partial x_j} \quad c,j=1,2,\dots,n_c-1 \quad \text{Eq. (3.57)}$$

$$G_{Vc} = (1-V) \frac{\partial}{\partial V} (f_{o,c} - f_{g,c}) = (1-V) \sum_{j=1}^{n_c-1} \frac{\partial f_{o,c}}{\partial x_j} \frac{\partial x_j}{\partial V} = \sum_{j=1}^{n_c-1} \frac{\partial f_{o,c}}{\partial x_j} (x_j - y_j)$$

$$c,j=1,2,\dots,n_c-1 \quad \text{Eq. (3.58)}$$

$$G_{Pc} = (1-V) \frac{\partial}{\partial p} (f_{o,c} - f_{g,c}) = (1-V) \left( \frac{\partial f_{o,c}}{\partial p} - \frac{\partial f_{g,c}}{\partial p} \right) \quad c=1,2,\dots,n_c-1 \quad \text{Eq. (3.59)}$$

## C elements

There are six C submatrices in the Jacobian of Eq.(3.46) which arise from differentiating the saturation constraint equation (Eq.(3.44)) with respect to  $(p, W, F, Z_c, V, y_c, c=1,2,\dots,n_c-1)$ . The  $C_y$  and  $C$  submatrices have the following structure:

$$C_y = [C_{y1} \quad C_{y2} \quad C_{y3} \quad \cdot \quad \cdot \quad \cdot \quad C_{y_{n_c-1}}] \quad \text{Eq. (3.60)}$$

$$C = [C_1 \quad C_2 \quad C_3 \quad \cdot \quad \cdot \quad \cdot \quad C_{n_c-1}] \quad \text{Eq. (3.61)}$$

Eq. (3.44) can be written in terms of compressibility factors  $\left(\rho = \frac{P}{ZRT}\right)$  as:

$$R_s = 1 - S_o - S_g - S_w = 1 - F \left( \frac{1-V}{\rho_o} + \frac{V}{\rho_g} \right) - \frac{W}{\rho_w} = 1 - F [(1-V)Z_o + VZ_g] \left( \frac{RT}{P} \right) - \frac{W}{\rho_w}$$

**Eq. (3.62)**

$$C_{y_c} = \frac{\partial}{\partial y_c} (1 - S_o - S_g - S_w) = -F \left( \frac{RT}{P} \right) \left[ (1-V) \frac{\partial Z_o}{\partial x_c} \frac{\partial x_c}{\partial y_c} + V \frac{\partial Z_g}{\partial y_c} \right] = FV \left( \frac{RT}{P} \right) \left[ \frac{\partial Z_o}{\partial x_c} - \frac{\partial Z_g}{\partial y_c} \right]$$

$c=1,2,\dots,n_c-1$  **Eq. (3.63)**

$$C_c = \frac{\partial}{\partial Z_c} (1 - S_o - S_g - S_w) = -F \left( \frac{RT}{P} \right) \left[ (1-V) \frac{\partial Z_o}{\partial x_c} \frac{\partial x_c}{\partial Z_c} \right] = -F \left( \frac{RT}{P} \right) \frac{\partial Z_o}{\partial x_c}$$

$c=1,2,\dots,n_c-1$

**Eq. (3.64)**

$$C_v = \frac{\partial}{\partial V} (1 - S_o - S_g - S_w) = F \left( \frac{RT}{P} \right) \left[ Z_o - Z_g - (1-V) \sum_{c=1}^{n_c-1} \frac{\partial Z_o}{\partial x_c} \frac{\partial x_c}{\partial V} \right] = F \left( \frac{RT}{P} \right) \left[ Z_o - Z_g - \sum_{c=1}^{n_c-1} \frac{\partial Z_o}{\partial x_c} (x_c - y_c) \right]$$

**Eq. (3.65)**

$$C_p = \frac{\partial}{\partial p} (1 - S_o - S_g - S_w) = F \left( \frac{RT}{P} \right) \left[ (1-V) \left( \frac{Z_o}{p} - \frac{\partial Z_o}{\partial p} \right) + V \left( \frac{Z_g}{p} - \frac{\partial Z_g}{\partial p} \right) \right] - W \frac{\partial}{\partial p} \left( \frac{1}{\rho_w} \right)$$

**Eq. (3.66)**

$$C_w = \frac{\partial}{\partial W} (1 - S_o - S_g - S_w) = -\frac{1}{\rho_w} \quad \text{Eq. (3.67)}$$

$$C_f = \frac{\partial}{\partial F} (1 - S_o - S_g - S_w) = -\left( \frac{1-V}{\rho_o} + \frac{V}{\rho_g} \right) \quad \text{Eq. (3.68)}$$

## B elements

$B_Z$  is a diagonal matrix and  $B_C$  is a column matrix as follows:

$$B_Z = \begin{bmatrix} B_{Z1} & 0 & 0 & \dots & 0 \\ 0 & B_{Z2} & 0 & \dots & 0 \\ 0 & 0 & B_{Z3} & \dots & 0 \\ \cdot & \cdot & \cdot & \dots & \cdot \\ \cdot & \cdot & \cdot & \dots & \cdot \\ \cdot & \cdot & \cdot & \dots & \cdot \\ \cdot & \cdot & \cdot & \dots & \cdot \\ 0 & 0 & 0 & \dots & B_{Zn_c-1} \end{bmatrix} \quad \text{Eq. (3.69)}$$

$$B = \begin{bmatrix} B_1 \\ B_2 \\ B_3 \\ \cdot \\ \cdot \\ \cdot \\ B_{n_c-1} \end{bmatrix} \quad \text{Eq. (3.70)}$$

and,

$$B_z = \frac{\partial R_c}{\partial Z_c} = \frac{V_r \phi}{\Delta t} F \quad c=1,2,\dots,n_c-1 \quad \text{Eq. (3.71)}$$

$$B_c = \frac{\partial R_c}{\partial F} = \frac{V_r \phi}{\Delta t} Z_c \quad c=1,2,\dots,n_c-1 \quad \text{Eq. (3.72)}$$

$$B_f = \frac{\partial R_H}{\partial F} = \frac{\partial R_H}{\partial W} = \frac{V_r \phi}{\Delta t} \quad \text{Eq. (3.73)}$$

### T elements

T submatrices are derivative of component and CO<sub>2</sub> material balance (Eq.(3.41)), overall hydrocarbon material balance(Eq.(3.42)), and water material balance (Eq.(3.43)) with respect to pressure. T<sub>c</sub> has the following structures:

$$T_c = \begin{bmatrix} T_1 \\ T_2 \\ T_3 \\ \cdot \\ \cdot \\ \cdot \\ T_{n_c-1} \end{bmatrix} \quad \text{Eq. (3.74)}$$

Element of T<sub>c</sub>, T<sub>f</sub>, and T<sub>w</sub> are defined as follows:

$$T_c = \frac{\partial R_c}{\partial p} = \Delta [T_o x_c]_{i,j,k}^n + \Delta [T_g y_c]_{i,j,k}^n - \frac{V_{r,i,j,k} F Z_c \phi_0 c_\phi}{\Delta t} \quad c=1,2,\dots,n_c-1 \quad \text{Eq. (3.75)}$$

$$T_f = \frac{\partial R_H}{\partial p} = \Delta [T_o]_{i,j,k}^n + \Delta [T_g]_{i,j,k}^n - \frac{V_{r,i,j,k} F \phi_0 c_\phi}{\Delta t} \quad \text{Eq. (3.76)}$$

$$T_w = \frac{\partial R_w}{\partial p} = \Delta [T_w]_{i,j,k}^n - \frac{V_{r,i,j,k} W \phi_0 c_\phi}{\Delta t} \quad \text{Eq. (3.77)}$$

$$\phi = \phi_0 \left[ 1 + c_\phi (p_o - p_{ref}) \right] \quad \text{Eq. (3.78)}$$

Transmissibilities are calculated by upstream weighting. Last terms in the right hand side of Eq.(3.75), Eq.(3.77) are not included in the calculations for off-diagonal elements of  $T_c$ ,  $T_f$ , and  $T_w$ .

The IMPESC (Implicit Pressure Explicit Saturation Composition) method has the following steps:

**Step 1:** Solving for pressure (P) implicitly

The sparsity of the Jacobian in Eq. (3.46) is used to reduce the Jacobian matrix to an upper triangular matrix using forward elimination. Once the upper triangular matrix is obtained, the  $\delta p^{l+1}$  is solved from the reduced system. Then the pressure is updated as:

$$p^{l+1} = p^l + \delta p^{l+1} \quad \text{Eq. (3.79)}$$

where  $l$  is the iteration level.

**Step 2:** Solving explicitly for W and F

Then  $\delta W^{l+1}$  and  $\delta F^{l+1}$  are calculated by back substitution in the reduced form of Eq.(3.46). Porosity and water molar density are updated with the pressure

calculated from step 1 before solving for  $\delta W$  and  $\delta F$ .  $W$  and  $F$  are updated by adding  $\delta W$  and  $\delta F$  as:

$$W^{l+1} = W^l + \delta W^{l+1} \quad \text{Eq. (3.80)}$$

$$F^{l+1} = F^l + \delta F^{l+1} \quad \text{Eq. (3.81)}$$

**Step 3:** Solving explicitly for overall mole fraction ( $Z_c$ )

Change in overall mole fraction  $\delta Z_c^{l+1}$  is calculated by back substitution from the reduced form of Eq.(3.46). Young and Stephenson (1983) suggested using updated total molar density ( $F$ ) in the back substitution process for calculating  $\delta Z_c^{l+1}$ . Then  $Z_c$  is calculated as:

$$Z_c^{l+1} = Z_c^l + \delta Z_c^{l+1} \quad \text{Eq. (3.82)}$$

**Step 4:** Calculating  $V$  and  $y_c$

1- If  $0 < V < 1$ , continue back substitution for  $\delta V^{l+1}$  and  $\delta y_c^{l+1}$  and update  $V$  and

$y_c$  as:

$$V^{l+1} = V^l + \delta V^{l+1} \quad \text{Eq. (3.83)}$$

$$y_c^{l+1} = y_c^l + \delta y_c^{l+1} \quad \text{Eq. (3.84)}$$

Calculate  $x_c$  from the following equation:

$$x_c^{l+1} = \frac{Z_c^{l+1} - V^{l+1} y_c^{l+1}}{1 - V^{l+1}} \quad \text{Eq. (3.85)}$$



2- If  $V=0$  or  $V=1$  (single phase grid cell)

Perform flash calculation by using new pressure (P) and overall mole fraction ( $Z_c$ ) calculated from step 1 and step 3 respectively to update  $x_c$ ,  $y_c$ , and V.

**Step 5:** Calculating  $S_w$ ,  $S_o$  and  $S_g$

Phase saturations are calculated from the following relationships:

$$S_w^{l+1} = \frac{W^{l+1}}{\rho_w^{l+1}} \quad \text{Eq. (3.86)}$$

$$S_o^{l+1} = \frac{L^{l+1} F^{l+1}}{\rho_o^{l+1}} = \frac{(1 - V^{l+1}) F^{l+1}}{\rho_o^{l+1}} \quad \text{Eq. (3.87)}$$

$$S_g^{l+1} = \frac{V^{l+1} F^{l+1}}{\rho_g^{l+1}} \quad \text{Eq. (3.88)}$$

Fig. 3.2 shows the flow chart of the numerical technique.

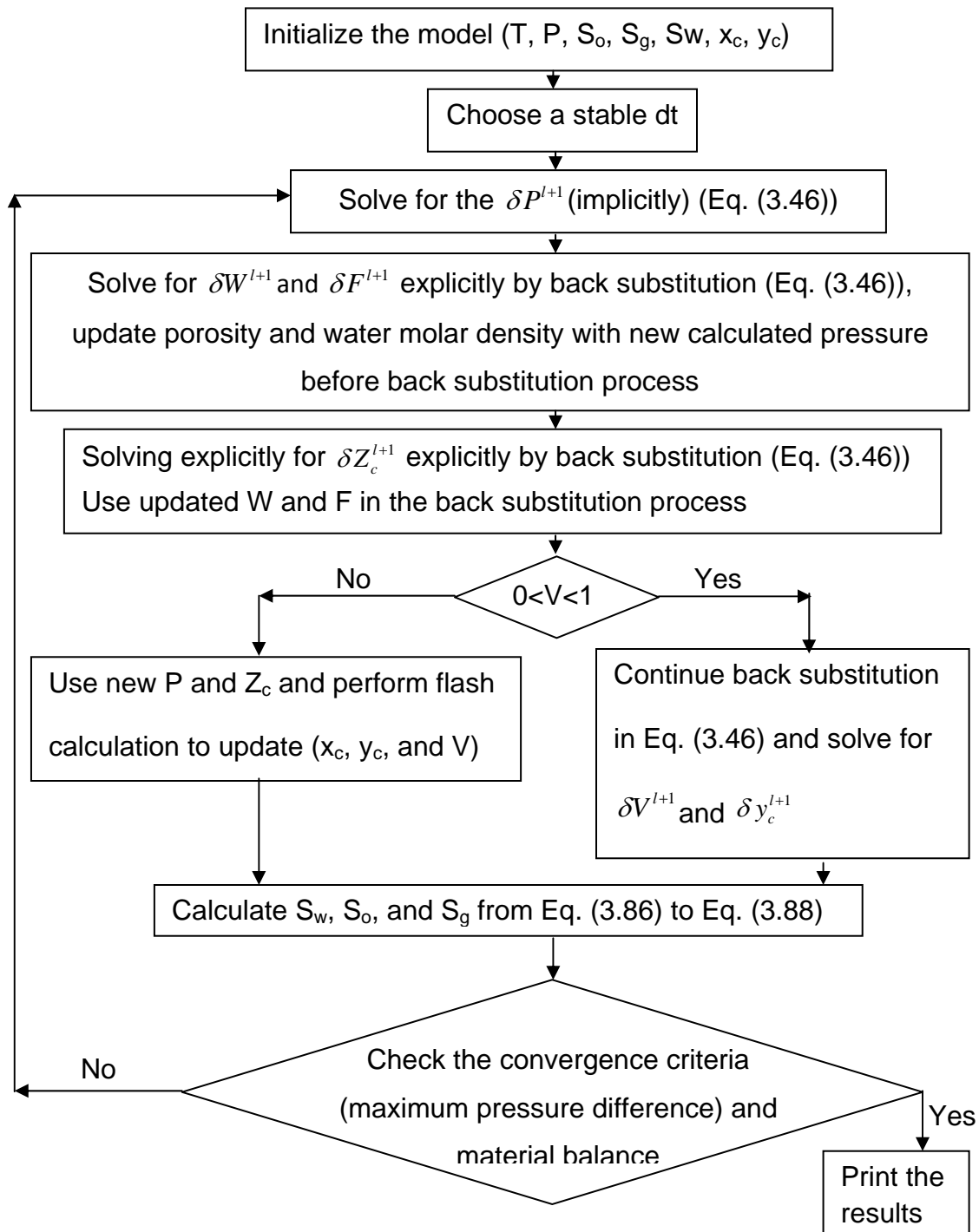


**Fig. 3.2: flow chart of Implicit Pressure Explicit Saturation Composition (IMPESC) numerical technique**

## Chapter 4. Rock properties, phase behavior , and fluid properties

This chapter briefly defines and describes the rock properties, phase behavior, and fluid properties related to this work. First, rock properties will be addressed followed by a discussion of fluid properties.

### 4.1. Rock properties

#### 4.1.1. Porosity

Porosity is a measure of storage capacity of a rock. It is defined as the ratio of connected pore volume to bulk volume of the rock as:

$$\phi = \frac{V_p}{V_r} \quad \text{Eq. (4.1)}$$

If porosity is assumed as a function of pressure, total rock compressibility can be defined as:

$$c_r = c_b + c_\phi \quad \text{Eq. (4.2)}$$

where  $c_b$  is bulk compressibility and  $c_\phi$  is pore compressibility. Assuming negligible bulk compressibility, Eq.(4.2) simplifies to:

$$c_r = c_\phi = \frac{1}{\phi} \frac{\partial \phi}{\partial p} \quad \text{Eq. (4.3)}$$

Porosity changes with pressure can be calculated by integrating Eq.(4.3):

$$\phi = \phi_0 \exp \left[ c_\phi (p_o - p_{ref}) \right] \quad \text{Eq. (4.4)}$$

#### 4.1.2. Absolute permeability

Absolute permeability of a rock is the measure of the ease that fluid can flow through it. Based on Darcy's law, absolute permeability can be expressed as:

$$k = \frac{q\mu l}{A\Delta p} \quad \text{Eq. (4.5)}$$

where  $q, \mu, L, A,$  and  $\Delta p$  are the flow rate, flowing fluid viscosity, length of porous media, cross section of porous media, and pressure gradient across porous medium.

#### 4.1.2. Relative permeability

Relative permeability is the ratio of the effective permeability of a fluid at a fixed saturation to the absolute permeability of the porous media when more than one phase is flowing in the porous media. When oil, gas, and water are flowing simultaneously in the porous media, three-phase relative permeability must be calculated. Three-phase relative permeability calculations are based on the following assumptions:

- 1- Water and gas relative permeabilities are functions of their saturation

$$\left( k_{rw}(S_w), k_{rg}(S_g) \right)$$

2- Oil relative permeability is a function of both water and gas saturation

$$(k_{ro}(S_o))$$

Coats (1980) proposed a model to include the effect of interfacial tension on relative permeability as:

For gas-oil system:

$$k_{rg} = k_{rgcw} \left\{ f(\sigma) \bar{S}_g^{n_g} + [1 - f(\sigma)] \bar{S}_g \right\} \quad \text{Eq. (4.6)}$$

$$k_{rog} = k_{rocw} \left[ f(\sigma) \bar{S}_g^{n_{og}} + (1 - f(\sigma)) \bar{S}_g \right] \quad \text{Eq. (4.7)}$$

$$\bar{S}_g = \frac{S_g - S_{gr}^*}{1 - S_{wir} - S_{gr}^*} \quad \text{Eq. (4.8)}$$

$$\bar{S}_o = \frac{1 - S_g - S_{wir} - S_{org}^*}{1 - S_{wir} - S_{org}^*} \quad \text{Eq. (4.9)}$$

$$f(\sigma) = \left( \frac{\sigma}{\sigma_0} \right)^{1/n_1} \quad \text{Eq. (4.10)}$$

As interfacial tension decreases,  $S_{gr}^*$  and  $S_{org}^*$  approach zero as:

$$S_{gr}^* = f(\sigma) S_{gr} \quad \text{Eq. (4.11)}$$

$$S_{org}^* = f(\sigma) S_{org} \quad \text{Eq. (4.12)}$$

where

$\sigma$  is interfacial tension

$\sigma_0$  is initial interfacial tension corresponding to the prescribed capillary pressure curve

$n_1$  is an exponent in the range of 4 to 10

$n_{og}$  and  $n_g$  are exponents on relative permeability curves

$k_{rgcw}$  is relative permeability to gas at connate water

$k_{rocw}$  is relative permeability to oil at connate water

$S_{wir}$  is irreducible water saturation

$S_{org}$  is residual oil saturation to gas

$S_{gr}$  is residual gas saturation

For large  $n_1$ , as  $\sigma$  decreases below  $\sigma_0$ , the value of  $f(\sigma)$  will remain near 1.0 until  $\sigma/\sigma_0$  is very small. This means that  $k_{rg}$  and  $k_{rog}$  will vary little with interfacial tension until close proximity to the critical point is attained.

For the three-phase (oil, gas, and water) case:

$$k_{rw} = k_{rwo} \left( \frac{S_w - S_{wir}}{1 - S_{wir} - S_{orw}} \right)^{n_w} \quad \text{Eq. (4.13)}$$

$$k_{row} = k_{rocw} \left( \frac{1 - S_w - S_{orw}}{1 - S_{wir} - S_{orw}} \right)^{n_{ow}} \quad \text{Eq. (4.14)}$$

$$k_{ro} = k_{rocw} \left[ \left( \frac{k_{row}}{k_{rocw}} + k_{rw} \right) \left( \frac{k_{rog}}{k_{rocw}} + k_{rg} \right) - (k_{rw} + k_{rg}) \right] \quad \text{Eq. (4.15)}$$

In summary, gas, water, and oil relative permeabilities for the three-phase case are calculated from Eq.(4.6), Eq.(4.13), and Eq.(4.15). If effect of interfacial tension on relative permeability is not required in the calculations, then  $f(\sigma)$  must be set equal to one.

#### 4.1.3. Capillary pressure

Capillary pressure is the pressure difference across an interface between two immiscible fluids. Capillary pressure is defined as the non-wetting phase pressure minus wetting phase pressure as:

$$P_c = P_{nw} - P_w \quad \text{Eq. (4.16)}$$

For a gas-oil system:

$$P_{cog} = P_g - P_o \quad \text{Eq. (4.17)}$$

For a water-oil system (water-wet system):

$$P_{cow} = P_w - P_o \quad \text{Eq. (4.18)}$$

The effect of IFT on capillary pressure is calculated as follows:

$$P_c = P_c^0 \left( \frac{\sigma}{\sigma^0} \right) \quad \text{Eq. (4.19)}$$

where

$P_c$  modified capillary pressure

$P_c^0$  reference capillary pressure at reference interfacial tension

$\sigma$  interfacial tension

$\sigma^0$  reference interfacial tension

#### 4.1.4. Tortuosity

Tortuosity is a characteristic of a porous medium and defined as the ratio of the true length of the flow path of a fluid particle and the straight-line distance between the starting and finishing point of that particle's motion. Tortuosity depends on porosity of the porous medium. If the porosity is high, tortuosity is low and vice versa. Because of the tortuosity in a porous medium, effective diffusion coefficients are lower than their values without a porous medium. This effect is shown by the following relation:

$$D_{effective} = \frac{D}{\tau} \quad \text{Eq. (4.20)}$$

where

D is a diffusion coefficient for a component

$\tau$  is tortuosity of the porous medium

$D_{effective}$  is the effective diffusion coefficient corrected for porous medium which should be used in calculations.

Tortuosity is related to porosity through the formation resistivity factor (F) with the following form:



$$\tau = F\phi \quad \text{Eq. (4.21)}$$

Where

$$F = \phi^{-m} \quad \text{Eq. (4.22)}$$

where  $m$  is cementation factor which depends on the nature of porous media and usually varies from 1.5 to 2.5. Amyx et al. (1960) and Langness et al. (1972) presented a good review of the relationship between tortuosity and porosity. They also gave the following relation based on experimental results:

$$\tau = (F\phi)^{2/1.67} \quad \text{Eq. (4.23)}$$

Substituting Eq.(4.22) into Eq.(4.23) gives one relation between tortuosity and porosity as:

$$\tau = \phi^{1.2-1.2m} \quad \text{Eq. (4.24)}$$

In this work, Eq.(4.24) is used for estimation of the effective diffusion coefficient for oil and gas components in the porous medium. The tortuosity is often treated as an adjustable parameter. The tortuosity is used to modify the molecular diffusion coefficients, adapting it for use in porous media.

## 4.2. Phase behavior and fluid properties

A compositional phase-behavior model is used to predict all the PVT data by using the composition, pressure, and temperature of the reservoir fluid. The

phase-behavior model must be tuned against the available measured PVT data prior to being used in reservoir simulation. In general any equation of state can be used to describe the fluid phase behavior. Following is a description of equations of state, flash calculations, fluid density, and volume shift, followed by a discussion of how different fluid properties are computed including viscosity, molecular diffusion, and interfacial tension.

#### **4.2.1. Equations of State (EOS)**

EOS is used to describe the fluid phase behavior. There are several families of EOS. The Van Der Waals family enjoys a simple cubic form, and generally has two constants. Basic parameters for these equations are the critical properties and the normal boiling point or vapor pressure. Five cubic EOS are mostly used in the literature: a) Redlich-Kwong(RK) (Redlich et al. (1949)), b) Zudkevitch-Joffe-Redlich-Kwong (ZJRK) (Zudkevitch et al. (1970)), c) Soave-Redlich-Kwong (SRK) (Soave (1972)), d) Peng-Robinson (PR) (Peng and Robinson (1976), Robinson et al. (1985)), and e)Schmidt-Wenzel (SW) (Schmidt-Wenzel (1980)). However, non-cubic EOS with very many constants could more precisely represent the PVT data of pure components. As an example, the modified Benedict-Webb-Rubin equation with 11 constants is admittedly more accurate than the cubic EOS (such as the PR EOS) for the PVT description of pure substances, but it may be less accurate than the two-constant cubic equations for vapor-liquid equilibria (VLE) computation of complex reservoir fluid systems, because of mixing rule complexities.

Cubic equations with more than two constants also may not improve the volumetric behavior prediction of complex reservoir fluids. In fact, most cubic equations have about the same accuracy for phase-behavior prediction of complex hydrocarbon systems; the simpler equations often do better.

The Peng-Robinson EOS is used in this dissertation. Following is a detailed discussion of the Peng-Robinson (PR) EOS. The equation has the following form:

$$p = \frac{RT}{v_m - b_m} - \frac{a_m}{v_m(v_m + b_m) + b_m(v_m - b_m)} \quad \text{Eq. (4.25)}$$

where  $p$  is the pressure,  $T$  is the temperature,  $R$  is the universal gas constant,  $v_m$  is the molar volume.

EOS parameters are defined as follows:

$$a_i = 0.45724 \frac{R^2 T_{c,i}^2}{P_{c,i}} \quad i = 1, 2, \dots, n_c \quad \text{Eq. (4.26)}$$

$$b_i = 0.0778 \frac{RT_{c,i}}{P_{c,i}} \quad i = 1, 2, \dots, n_c \quad \text{Eq. (4.27)}$$

$$\alpha_i = \left[ 1 + (0.37464 + 1.54226\omega_i - 0.26992\omega_i^2)(1 - \sqrt{T_{r,i}}) \right]^2 \quad \text{Eq. (4.28)}$$

$$a_{i,j} = (1 - k_{i,j}) \sqrt{(a_i \alpha_i)(a_j \alpha_j)} \quad \text{Eq. (4.29)}$$

where  $k_{i,j}$  represents the binary interaction coefficient between component i and j.

$$a_m = \sum_{i=1}^{n_c} \sum_{j=1}^{n_c} x_{i,m} x_{j,m} a_{i,j} \quad \text{Eq. (4.30)}$$

$$b_m = \sum_{i=1}^{n_c} x_{i,m} b_i \quad \text{Eq. (4.31)}$$

$$A_m = \frac{a_m P}{R^2 T^2} \quad \text{Eq. (4.32)}$$

$$B_m = \frac{b_m P}{RT} \quad \text{Eq. (4.33)}$$

Fluid compressibility factor ( $Z_m$ ) of phase m is defined as:

$$Z_m = \frac{Pv_m}{RT} \quad \text{Eq. (4.34)}$$

The equation of state in terms of compressibility factor ( $Z_m$ ) for phase m is as follows:

$$Z_m^3 - (1 - B_m)Z_m^2 + (A_m - 3B_m^2 - 2B_m)Z_m - (A_mB_m - B_m^2 - B_m^3) = 0 \quad \text{Eq. (4.35)}$$

In general, Eq.(4.35) is applied separately to oil and gas phases, and if there are three real roots for the phase compressibility factor ( $Z_m$ ), the largest real and

positive root is taken when considering the vapor phase and the smallest real and positive root when considering the oil phase.

The partial fugacity of component  $i$  in phase  $m$  can be expressed as:

$$\ln \left( \frac{f_{m,i}}{px_{i,m}} \right) = -\ln(Z_m - B_m) + \frac{b_i}{b_m}(Z_m - 1) + \frac{A_m}{2\sqrt{2}B_m} \ln \left( \frac{Z_m + (\sqrt{2} + 1)B_m}{Z_m - (\sqrt{2} - 1)B_m} \right) \left( \frac{b_i}{b_m} - \frac{2}{a_m} \sum_{k=1}^{n_c} x_{k,m} a_{i,k} \right)$$

**Eq. (4.36)**

#### 4.2.2. Flash calculation

A flash calculation basically consists of determining the composition of each equilibrium phase, gas ( $y_1, y_2, \dots, y_{nc}$ ) and oil ( $x_1, x_2, \dots, x_{nc}$ ), and the number of moles in gas,  $V$ , and in oil,  $L$ , given the mole fraction of components in the feed ( $z_1, z_2, \dots, z_{nc}$ ), the pressure, and temperature. For one mole of mixture at pressure  $p$  and temperature  $T$ , the governing equations in the flash calculation are:

$$(1) \text{ Total material balance: } L + V = 1 \quad \text{Eq. (4.37)}$$

Where  $L$  is the molar fraction of oil phase and  $V$  is the molar fraction of gas phase.

$$(2) \text{ Material balance for each component:}$$

$$x_c L + y_c V = z_c \quad c=1, 2, \dots, nc \quad \text{Eq. (4.38)}$$

(3) Mole fraction constraints:  $\sum_{c=1}^{nc} z_c = 1, \sum_{c=1}^{nc} x_c = 1, \sum_{c=1}^{nc} y_c = 1$  **Eq. (4.39)**

(4) Equality of fugacity of each component in oil and gas phases

$$f_{o,c} = f_{g,c} \quad c=1, 2, \dots, n_c \quad \text{Eq. (4.40)}$$

Eq.(4.40) can also be expressed by the equilibrium ratio,  $K_c$ , as:

$$\phi_{o,c} p x_c = \phi_{g,c} p y_c \quad c=1, 2, \dots, n_c \quad \text{Eq. (4.41)}$$

and,  $K_c = \frac{y_c}{x_c} = \frac{\phi_{o,c}}{\phi_{g,c}} \quad c=1, 2, \dots, n_c$  **Eq. (4.42)**

Eq.(4.38) to Eq.(4.40) provide the required  $2n_c+2$  equations to determine  $2n_c+2$  unknowns, namely  $(y_1, y_2, \dots, y_{n_c}), (x_1, x_2, \dots, x_{n_c}), L$ , and  $V$ . The successive substitution technique is used for the flash calculation. It is an iterative method where only the fraction of oil or vapor ( $L$  or  $V$ ) is searched. Combining Eq.(4.38) and Eq.(4.42) results in:

$$x_c L + K_c x_c V = z_c \quad c=1, 2, \dots, n_c \quad \text{Eq. (4.43)}$$

Combining Eq.(4.37) and Eq.(4.43) and solving for  $x_c$  results in:

$$x_c = \frac{z_c}{(K_c - 1)V + 1} \quad c=1, 2, \dots, n_c \quad \text{Eq. (4.44)}$$

Substituting  $x_c$  from Eq.(4.44) into Eq.(4.38) and solving for  $y_c$ :

$$y_c = \frac{K_c z_c}{(K_c - 1)V + 1} \quad c=1, 2, \dots, n_c \quad \text{Eq. (4.45)}$$

Combining Eq.(4.39), Eq.(4.44), and Eq.(4.45) to obtain the expression known as the Rachford-Rice equation:

$$F(V) = \sum_{c=1}^{n_c} (y_c - x_c) = \sum_{c=1}^{n_c} \frac{z_c (K_c - 1)}{(K_c - 1)V + 1} = 0 \quad \text{Eq. (4.46)}$$

The derivative of Eq. (4.46) with respect to V:

$$\frac{\partial F}{\partial V} = - \sum_{c=1}^{n_c} \frac{z_c (K_c - 1)^2}{[(K_c - 1)V + 1]^2} \quad \text{Eq. (4.47)}$$

The method of successive substitution involves the following steps:

- 1- Estimate the initial values of  $K_c$  at the fixed pressure and temperature.

Wilson's correlation can be used for this purpose:

$$K_c = \frac{1}{P_{rc}} \exp\left[5.37(1 + \omega_c)(1 - T_{rc}^{-1})\right] \quad c=1, 2, \dots, n_c \quad \text{Eq. (4.48)}$$

- 2- Calculate F(0) and F(1) from Eq. (4.46)

If  $F(0) > 0$  and  $F(1) < 0$ , then the system is two-phase: Compute  $V^0$  from Eq.(4.46) using Newton-Raphson method as:

$$V^{l+1} = V^l - \frac{F(V)}{\partial F / \partial V} \quad \text{Eq. (4.49)}$$

Otherwise if  $F(0) \leq 0$  or  $F(1) \geq 0$ , then the system may be single phase.

Start with  $V^l = 0.5$  and proceed with the calculation.

3- Calculate  $y_c$  and  $x_c$  from Eq.(4.44) and Eq.(4.45).

4- Use  $y_c$  to calculate vapor compressibility ( $Z_V$ ) and  $x_c$  to compute liquid compressibility ( $Z_L$ ) by solving Eq.(4.35). Calculate oil and gas fugacities from Eq.(4.36). Update  $K_c$  from the following equation:

$$K_c^{l+1} = \frac{\phi_{o,c}}{\phi_{g,c}} = \frac{f_{o,c} / x_c P}{f_{g,c} / y_c P} = \frac{f_{o,c}}{f_{g,c}} \cdot \frac{y_c}{x_c} = F_c \frac{y_c}{x_c} = F_c K_c^l \quad c=1, 2, \dots, n_c \quad \text{Eq. (4.50)}$$

where  $l$  is the iteration level, and,  $F_c = \frac{f_{o,c}}{f_{g,c}} \quad c=1, 2, \dots, n_c \quad \text{Eq. (4.51)}$

Check the convergence criterion:

$$\max |F_c - 1| \leq \varepsilon \quad \text{Eq. (4.52)}$$

If converged then stop; if not, then go to step 5.

5- Compute  $F(0)$  and  $F(1)$  from Eq. (4.46) using updated  $K_i^{l+1}$



If  $F(0) < 0$ , single phase oil, set  $V = 0$ ,  $x_c = z_c$ .

If  $F(1) > 0$ , single phase vapor, set  $V = 1$ ,  $y_c = z_c$ .

If  $F(0) > 0$  and  $F(1) < 0$ , solve for  $V$  from Eq.(4.46) using the Newton-Raphson method, go to step 3.

The number of iterations depends on the proximity to the critical point. The successive substitution method allows detection of the single-phase region without computing the saturation pressure.

#### 4.2.3. Density

The densities of liquid and gas phases can be calculated by using the compressibility factor ( $Z$ ) from the flash calculation results (Section 4.2.2) as:

$$\rho_p = \frac{p}{Z_p RT} \quad p=\text{oil or gas} \quad \text{Eq. (4.53)}$$

where  $p$  is the pressure,  $T$  is the temperature,  $R$  is the universal gas constant, and  $Z_p$  is compressibility factor of phase  $p$  from Eq.(4.35).

#### 4.2.4. Volume translation (or Volume shift)

The major deficiency of the EOS is liquid density prediction. In PR and SRK EOS, no parameter is adjusted for density. As a result, these two equations have a density-deficiency prediction. The main idea behind developing new EOS was the failure of the SRK EOS in predicting liquid density. Equations of state are a

generalized form of a gas equation of state, and therefore they predict gas properties better than liquid properties. Jhaveri and Youngren (1988) reported 3-5% error in predicting gas compressibility factor ( $Z_g$ ) and the error in the liquid density predictions ranged from 6-12%. Firoozabadi (1988, 1999) reported that the SRK EOS underestimates liquid density whereas the PR EOS overestimates liquid density up to an acentric factor of about 0.35 and then underestimates liquid density of n-alkanes heavier than nC<sub>8</sub>. The SRK EOS is best suited for density prediction of pure hydrocarbons with  $\omega \approx 0$ , while the PR EOS performs best for n-heptane and other hydrocarbons with  $\omega \approx 0.35$ . Firoozabadi (1988, 1999) reported that the SW EOS predicts liquid density better than other EOS and the PR EOS predicts liquid density better than the SRK EOS. Peneloux et al. (1982) developed a procedure for improving the volumetric predictions of the SRK EOS by introducing a volume correction parameter  $c_i$  into the equation. The third parameter ( $c_i$ ) does not change the vapor-liquid equilibrium conditions determined by the unmodified SRK equation, but modifies the liquid and gas volumes by affecting the following translation along the volume axis:

$$V_{corr}^L = V^L - \sum_{i=1}^{nc} (x_i c_i) \quad \text{Eq. (4.54)}$$

$$V_{corr}^v = V^v - \sum_{i=1}^{nc} (y_i c_i) \quad \text{Eq. (4.55)}$$

$$c_i = 4.43797878 (0.00261 + 0.0928 \omega_i) T_{c,i} / p_{c,i} \quad \text{Eq. (4.56)}$$

where (the units are required for Eq. (4.54) to Eq. (4.56))

$$V^L = \frac{Z^L RT}{P} \text{ is liquid molar volume, } ft^3 / mole$$

$$V^v = \frac{Z^v RT}{P} \text{ is gas molar volume, } ft^3 / mole$$

$$V_{corr}^L \text{ is corrected liquid molar volume, } ft^3 / mole$$

$$V_{corr}^v \text{ is corrected gas molar volume, } ft^3 / mole$$

$x_i$  is mole fraction of component  $i$  in the liquid phase

$y_i$  is mole fraction of component  $i$  in the gas phase

$c_i$  is correction factor for component  $i$ ,  $ft^3 / mole$

$T_{ci}$  is critical temperature of component  $i$ , ( $^{\circ}R$ )

$p_{ci}$  is critical pressure of component  $i$ , psia

Jhaveri and Youngren (1988) applied the Peneloux et al. (1982) method to improve volumetric predictions of the PR EOS. They defined  $c_i$  parameter in Eq. (4.54) and Eq. (4.55) as follows:

$$c_i = S_i b_i \tag{Eq. (4.57)}$$

where

$S_i$  is a dimensionless parameter and is called the shift parameter

$b_i$  is from Eq. (4.27)

Table 4.1 gives the shift parameters for well-defined lighter hydrocarbons as presented by Jhaveri and Youngren (1988). Jhaveri and Youngren (1988) proposed a correlation for calculating  $S_i$  for hydrocarbons heavier than hexane as:

$$S_i = 1 - \frac{d}{MW_i^e} \quad \text{Eq. (4.58)}$$

where

$MW_i$  is molecular weight of component  $i$ , and

$d$  and  $e$  are positive correlation coefficients from Table 4.2

Deo et al. (1989) studied shift parameters for the SW and PR EOS and proposed  $0.06 \text{ ft}^3 / \text{lb} - \text{mole}$  for  $\text{CO}_2$  as volume translation ( $c_i$ ) for the PR EOS.

**Table 4.1: Shift parameter for hydrocarbons (Jhaveri and Youngren (1988))**

Component	$S_i$
Methane	-0.154
Ethane	-0.1002
Propane	-0.08501
Iso-butane	-0.07935
Normal butane	-0.6413
Iso-pentan	-0.0435
Normal pentane	-0.04183
Normal Hexane	-0.01478

**Table 4.2: Shift parameter correlation coefficients for hydrocarbons heavier than hexane (Jhaveri and Youngren (1988))**

Component type	d	e
n-alkanes	2.258	0.1823
n-alkylcyclohexanes	3.004	0.2324
n-alkylbenzenes	2.516	0.2008

#### 4.2.5. Viscosity

Viscosity is calculated by the Lorenz et al. (1964) correlation. The correlation expresses the viscosity (in cp) as a function of reduced density as:

$$\mu = \mu^0 + \frac{(0.1023 + 0.023364\rho_r + 0.058533\rho_r^2 - 0.040758\rho_r^3 + 0.0093324\rho_r^4) - 0.0001}{\lambda} \quad \text{Eq. (4.59)}$$

$\rho_r, \lambda,$  and  $\mu^0$  are given by:

$$\rho_r = \frac{\rho}{\rho_{pc}} \quad \text{Eq. (4.60)}$$

where (the units are required for Eq. (4.54) to Eq. (4.56))

$\rho_r$  is reduced density

$\rho$  is density, lb-mole/ft<sup>3</sup>

$\rho_{pc}$  is pseudo critical density, lb-mole/ft<sup>3</sup>

The pseudo critical density is calculated as follows:

$$\rho_{pc} = \sum_1^{nc} x_c \rho_{C,c} \quad \text{Eq. (4.61)}$$

where  $\rho_{C,c}$  is critical density of component c

$$\lambda = \frac{\left[ \sum_1^{nc} x_c T_{C,c} \right]^{\frac{1}{6}}}{\left[ \sum_1^{nc} x_c MW_c \right]^{\frac{1}{2}} \left[ \sum_1^{nc} x_c P_{C,c} \right]^{\frac{2}{3}}} \quad \text{Eq. (4.62)}$$

where  $T_{c,c}$ ,  $p_{c,c}$ , and  $MW_c$  are critical temperature (K), critical pressure (atm), and molecular weight of component c , respectively. Units must be set as mentioned to calculate viscosity correctly.

$$\mu^0 = \frac{\sum_1^{nc} (x_c \mu_c^0 MW_c^{0.5})}{\sum_1^{nc} (x_c MW_c^{0.5})} \quad \text{Eq. (4.63)}$$

$$\begin{aligned} \mu_c^0 \zeta_c &= 34 \times 10^{-5} T_{r,c}^{0.94} \quad (T_{r,c} < 1.5) \\ \mu_c^0 \zeta_c &= 17.78 \times 10^{-5} (4.58 T_{r,c} - 1.67)^{\frac{5}{8}} \quad (T_{r,c} > 1.5) \end{aligned} \quad \text{Eq. (4.64)}$$

$$\zeta_c = \frac{T_{C,c}^{1/6}}{MW_c^{1/2} P_{C,c}^{2/3}} \quad \text{Eq. (4.65)}$$

$$T_{r,c} = \frac{T}{T_{C,c}} \text{ is the reduced temperature of component c} \quad \text{Eq. (4.66)}$$

#### 4.2.6. Molecular diffusion

Molecular diffusion coefficients are calculated by the method of Da Silva and Belery (1989). This method is based on the published work of Sigmund (1976).

From kinetics theory, the diffusion coefficients for binary systems are related to pressure, temperature, and composition through the Hirschfelder et al. equation (Bird et al, 1960), which gives the low pressure limit of the density-diffusivity product (Sigmund (1976)):

$$\rho_m^0 D_{ij}^0 = \frac{2.2648 \times 10^{-5}}{\sigma_{ij}^2 \Omega_{ij}} \left( \frac{1}{MW_i} + \frac{1}{MW_j} \right)^{0.5} T^{0.5} \quad i, j = 1, 2, \dots, n_c \quad \text{Eq. (4.67)}$$

$\Omega_{ij}$  and  $\sigma_{ij}$  are collision diameter and collision integral of the Lennard-Jones potential in Eq. (4.67). They are related to the component critical properties ( $T_{C,i}$ ,  $P_{C,i}$ ,  $V_{C,i}$ , and  $Z_{C,i}$ ) of component  $i$  through the following set of equations:

$$\sigma_i = 0.18666 V_{C,i}^{1/3} Z_{C,i}^{-6/5} \quad i=1, 2, \dots, n_c \quad \text{Eq. (4.68)}$$

$$\sigma_{ij} = 0.5 (\sigma_i + \sigma_j) \quad i, j = 1, 2, \dots, n_c \quad \text{Eq. (4.69)}$$

$$\varepsilon_i = 65.3 T_{C,i} Z_{C,i}^{18/5} \quad i=1, 2, \dots, n_c \quad \text{Eq. (4.70)}$$

$$\varepsilon_{ij} = (\varepsilon_i \varepsilon_j)^{0.5} \quad i, j = 1, 2, \dots, n_c \quad \text{Eq. (4.71)}$$

$$T_{ij} = \frac{T}{\varepsilon_{ij}} \quad i, j = 1, 2, \dots, n_c \quad \text{Eq. (4.72)}$$

$$\Omega_{ij} = \frac{1.06036}{T_{ij}^{0.1561}} + 0.193 \exp(-0.47635 T_{ij}) + 1.03587 \exp(-1.52996 T_{ij}) + 1.76474 \exp(-3.89411 T_{ij}) \quad \text{Eq. (4.73)}$$

The density-diffusivity product as given by Eq.(4.81) does not remain valid for the high pressures encountered in hydrocarbon reservoirs. A polynomial correction expressed as a function of the reduced molar density has to be used as in the following equation:



$$D_{ij} = \frac{\rho_m^0 D_{ij}^0}{\rho_m} \times \begin{cases} (0.99589 + 0.096016\rho_{mr} - 0.22035\rho_{mr}^2 + 0.032874\rho_{mr}^3) & \text{if } \rho_{mr} \leq 3 \\ (0.18839 \exp(3 - \rho_{mr})) & \text{if } \rho_{mr} > 3 \end{cases} \quad \text{Eq. (4.74)}$$

where

$\rho_m$  is the mixture molar density

$$\rho_{mr} = \frac{\rho_m}{\rho_{mc}} \text{ is reduced density of the mixture} \quad \text{Eq. (4.75)}$$

$$\text{and } \rho_{mc} = \frac{\sum_1^{nc} z_i V_{C,i}^{2/3}}{\sum_1^{nc} z_i V_{C,i}^{5/3}} \text{ is critical density of the mixture} \quad \text{Eq. (4.76)}$$

$z_i$  is the mixture composition

Finally, effective diffusion coefficients for each component of the mixture are estimated on the basis of the Wilke formula (Sigmund (1976)):

$$D_{e,i} = \frac{1 - z_i}{\sum_{\substack{j=1 \\ j \neq i}}^{nc} \frac{z_j}{D_{ij}}} \quad i=1,2,\dots,n_c \quad \text{Eq. (4.77)}$$

#### 4.2.7. Interfacial tension (IFT)

The standard method of interfacial tension prediction in most reservoir simulators is the Parachor method. In this method, interfacial tension is estimated from the Macleod-Sugden (Reid et. al. (1977)) correlation as follows:

$$\sigma = (P_o \rho_o - P_g \rho_g)^4 \quad \text{Eq. (4.78)}$$

$$P_o = \sum_{i=1}^{n_c} x_i P_i \quad \text{Eq. (4.79)}$$

$$P_g = \sum_{i=1}^{n_c} y_i P_i \quad \text{Eq. (4.80)}$$

where

$\rho_o$  and  $\rho_g$  are densities of liquid and vapor phases

$x_i$  and  $y_i$  are mole fractions of component  $i$  in liquid and vapor phases

$n_c$  is number of components in liquid and vapor phases

$P_i$  is the Parachor of component  $i$

## Chapter 5. Preliminary testing of the model

This chapter presents the results of testing the model. The first section compares the model phase-behavior calculation results, including flash calculations and bubble point calculations, with published data. Simulation results of 1-D and 2-D problems versus results from the CMG model are presented in the second section.

### 5.1. Phase behavior

Phase behavior of the model is tested by performing flash calculations and bubble-point calculations of sample mixtures.

A mixture of  $C_1$ - $nC_4$ - $C_{10}$  was flashed at a pressure of 1000 psi and a temperature of 160 °F. Tables 5.1 and 5.2 present overall composition, critical properties, and binary interaction coefficients of the mixture. Flash calculations were performed using the Peng-Robinson EOS. Comparison of properties of oil and gas phases between flash calculation results from this work and the flash calculation results of McCain (1990) are shown in Table 5.3. Table 5.4 shows compositions of oil and gas phases calculated from this work, and the experimental data of Sage et al. (1950). The results from this work are in good agreement with the flash calculation results of McCain (1990) and the experimental data of Sage et al. (1950). Compositions of oil and gas at the critical point ( $p=1653$  psi,  $T=539^\circ\text{F}$ ) are presented in Table 5.5. Compositions of

oil and gas phases are very close and in good agreement with each other. Table 5.6 compares the bubble-point pressure calculations of the mixture at different temperatures between the results of Hashem (1998) and this work. The agreement is quite good.

**Table 5.1: Overall composition and critical properties of C<sub>1</sub>-nC<sub>4</sub>-C<sub>10</sub> mixture for flash calculations at p=1000 psi and T=160°F (McCain (1990))**

Component	Overall composition z , mole fraction	P <sub>c</sub> , psi	T <sub>c</sub> , °R	MW, lb/mole	ω
C <sub>1</sub>	0.5301	666.4	343.0	16.043	0.0104
nC <sub>4</sub>	0.1055	550.6	765.3	58.12	0.1995
C <sub>10</sub>	0.3644	305.2	1111.7	142.285	0.4898

**Table 5.2: Binary interaction coefficients of C<sub>1</sub>-nC<sub>4</sub>-C<sub>10</sub> mixture****(McCain (1990))**

	C <sub>1</sub>	nC <sub>4</sub>	C <sub>10</sub>
C <sub>1</sub>	0	0.02	0.04
nC <sub>4</sub>	0.02	0	0
C <sub>10</sub>	0.04	0	0

**Table 5.3: Comparison of oil and gas phases properties**

Flash calculations from this work and flash calculations of McCain (1990) at

**p=1000 psi and T=160°F**

Property	This work	McCain (1990)
v, mole	0.4024	0.4015
$Z_L$	0.3928	0.3922
$\rho_o, lb/ft^3$	38.02	38
Oil MW, lb/mole	99.15	99.12
$Z_V$	0.9054	0.9051
$\rho_g, lb/ft^3$	2.97	2.96
Gas MW, lb/mole	17.83	17.84

**Table 5.4: Comparison of oil and gas phases composition**

Flash calculations from this work and the experimental data of

**Sage et al. (1950) at p=1000 psi and T=160°F**

Component	x mole fraction (This work)	x mole fraction (Experimental data, Sage et al. (1950))	y mole fraction (This work)	y mole fraction (Experimental data, Sage et al. (1950))
C <sub>1</sub>	0.2398	0.242	0.9612	0.963
nC <sub>4</sub>	0.1518	0.152	0.0367	0.036
C <sub>10</sub>	0.6084	0.606	0.0021	0.0021

**Table 5.5: Compositions of oil and gas phases at critical point (p=1653 psi, T=539°F) from this work**

Component	x, mole fraction	y, mole fraction
C <sub>1</sub>	0.5303	0.5306
nC <sub>4</sub>	0.1052	0.1054
C <sub>10</sub>	0.3645	0.364



**Table 5.6: Comparison of bubble-point pressure calculations between this work and Hashem (1998)**

Temperature, °F	Bubble point pressure, psi (This work)	Bubble point pressure, psi (Hashem (1998))
100	2421	2420
160	2683	2682
260	2819	2818
360	2672	2673
460	2261	2260
540	1653	1652

## 5.2. Testing the model with 1-dimension and 2-dimension flow problems versus CMG

The model performance was tested against the GEM compositional model of CMG for 1-dimension (x-dimension) and 2-dimension (xz-dimensions) cases. Single porosity models were built which consist of 5 nodes in the x-direction for the 1-dimension case and 5x3 nodes in the x-z direction for the 2-dimension case. Fig. 5.1 shows the physical layouts for the 1-dimension and 2-dimension cases. All boundaries in Fig. 5.1 are assumed to be bounded by impermeable rocks and isolated from the outside environment. No fracture was introduced in the models. The effect of diffusion in the models was insignificant.

All calculations were done at reservoir conditions. The initial reservoir pressure is set to 4002.63 psi for the 1-dimension case and the top layer of the 2-dimension case, which is above the bubble-point pressure of the resident fluid (3142.1 psi), and a temperature of 160 °F. Total oil production rate from wells located at node (5,1,1) are 100 RB/day and 400 RB/day for the 1-dimension and the 2-dimension cases, respectively.

The reservoir rock and fluid properties are presented in Table 5.7. Capillary pressure was assumed to be zero. Relative permeabilities were calculated from Eq. (4.6) to Eq. (4.15) of Section 4.1.2 by assuming  $f(\sigma) = 1$ . Table 5.8 shows overall composition and critical properties of the mixture (C<sub>1</sub>-nC<sub>4</sub>-C<sub>10</sub>) used in the simulation studies. The composition of the mixture was uniform throughout the

porous media. Binary interaction coefficients are listed in Table 5.9. The Peng-Robinson EOS is used for phase behavior calculations.

Tables 5.10 to 5.20 show simulation results for pressure, oil saturation, and gas saturation at each node from CMG output and output from this work for both the 1-dimension and 2-dimension cases. As seen from Tables 5.10, 5.11, 5.16, and 5.17, the pressure decreased as production continued in the 1-dimension and the 2-dimension cases until it finally dropped below the bubble-point pressure. Tables 5.14, 5.15, 5.20, and 5.21 show that, the first gas saturation appeared at 14 days and 11 days for the 1-dimension and 2-dimension cases, respectively. The agreement in pressure, oil saturation, and gas saturation from this work and the CMG output is very good. For example, the pressure agreement between this work and CMG is in the order of 1psi and 3psi at 16 days for the 1-dimension and the 2-dimension cases, respectively. Oil and gas saturations from this work and CMG are in agreement within 0.2% at 16 days for the 1-dimension and 2-dimension cases, respectively.

### **5.3. Summary**

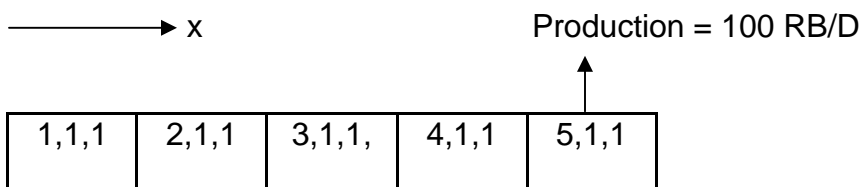
Summary of testing the model is as follows:

- 1- Model phase behavior was tested against published data. The agreement between calculation results from this work phase behavior and the published data was very good.

2- The model flow behavior in 1-D and 2-D was tested against GEM model of CMG. The calculated results from this work and CMG were in an excellent agreement.

**Fig. 5.1: Grid numbering in 1-dimension and 2-dimension flow problems**

Grid numbering in the 1-D problem



Grid numbering in the 2-D problem

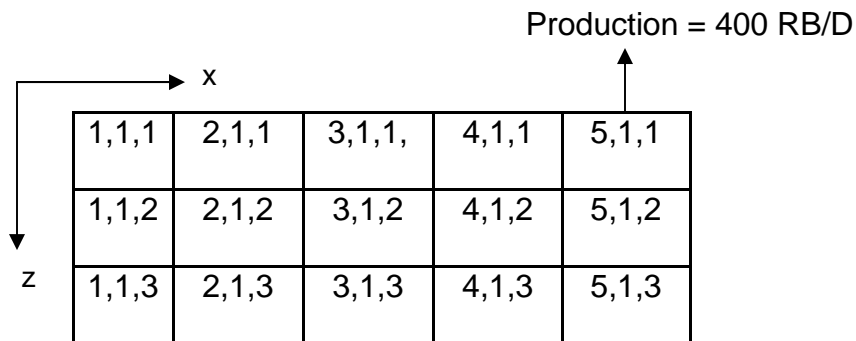


**Table 5.7: Reservoir properties (Hashem (1998))**

Grid size, ft	dx=200, dy=100, dz=20
Porosity	0.2
Rock compressibility, 1/psi	$4 \times 10^{-6}$
Water compressibility, 1/psi	$3 \times 10^{-6}$
Permeability, k, md	100
Water saturation	0.2
Irreducible water saturation, $S_{wir}$	0.2
Residual oil saturation to gas, $S_{org}$	0.25
Residual oil saturation to water, $S_{orw}$	0.2
Residual gas saturation, $S_{gr}$	0.0
Water relative permeability at residual oil saturation, $k_{rwro}$	0.15
Oil relative permeability to connate water, $k_{rocw}$	0.8
Gas relative permeability at connate water saturation, $k_{rgcw}$	0.6
Exponent on relative permeability curves	
$n_w$	1.5
$n_{ow}$	2.0
$n_g$	2.0
$n_{og}$	1.5
Capillary pressure	0
Initial reservoir pressure, psi	4002.63
Reservoir temperature, F	160
Total production rate, RB/D	100
Oil composition, $C_1/nC_4/nC_{10}$ , mole fraction	0.5301, 0.1055, 0.3644

**Table 5.8: Overall composition and critical properties of C<sub>1</sub>-nC<sub>4</sub>-C<sub>10</sub> mixture from WinProp (CMG)**

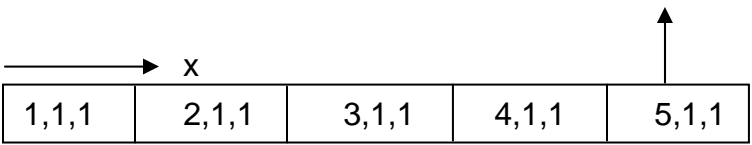
Component	Overall composition z , mole fraction	P <sub>c</sub> , psi	T <sub>c</sub> , °K	MW, lb/mole	ω
C <sub>1</sub>	0.5301	667.2	190.6	16.043	0.008
nC <sub>4</sub>	0.1055	551.1	425.2	58.124	0.193
C <sub>10</sub>	0.3644	367.5	622.1	134	0.443774

**Table 5.9: Binary interaction coefficients of C<sub>1</sub>-nC<sub>4</sub>-C<sub>10</sub> mixture from WinProp (CMG)**

	C <sub>1</sub>	nC <sub>4</sub>	C <sub>10</sub>
C <sub>1</sub>	0	0.014749	0.044372
nC <sub>4</sub>	0.014749	0	0.008452
C <sub>10</sub>	0.044372	0.008452	0

**Table 5.10: Pressure output for 1-D flow problem (CMG)**

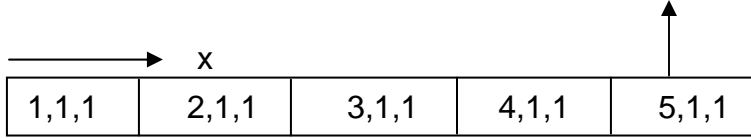
Production = 100 RB/D



		1,1,1	2,1,1	3,1,1	4,1,1	5,1,1
t = 1 day	P(psi)	3951	3948	3941	3930	3916
t = 2 day	P(psi)	3888	3884	3877	3866	3851
t = 3 day	P(psi)	3824	3820	3813	3802	3787
t = 4 day	P(psi)	3761	3757	3750	3739	3725
t = 5 day	P(psi)	3699	3695	3688	3677	3662
t = 6 day	P(psi)	3637	3634	3626	3616	3601
t = 7 day	P(psi)	3576	3573	3566	3555	3541
t = 8 day	P(psi)	3516	3512	3505	3495	3481
t = 9 day	P(psi)	3456	3453	3446	3435	3421
t = 10 day	P(psi)	3397	3394	3387	3376	3362
t = 11 day	P(psi)	3339	3335	3328	3318	3304
t = 12 day	P(psi)	3281	3278	3271	3260	3247
t = 13 day	P(psi)	3224	3221	3214	3203	3190
t = 14 day	P(psi)	3168	3165	3159	3150	3139
t = 15 day	P(psi)	3138	3137	3135	3129	3117
t = 16 day	P(psi)	3133	3130	3124	3115	3102

**Table 5.11: Pressure output for 1-D flow problem (This work)**

Production = 100 RB/D



		1,1,1	2,1,1	3,1,1	4,1,1	5,1,1
t = 1 day	P(psi)	3950	3947	3941	3932	3918
t = 2 day	P(psi)	3888	3884	3877	3866	3852
t = 3 day	P(psi)	3824	3820	3813	3802	3788
t = 4 day	P(psi)	3761	3757	3750	3739	3725
t = 5 day	P(psi)	3699	3695	3688	3677	3663
t = 6 day	P(psi)	3637	3633	3626	3615	3601
t = 7 day	P(psi)	3576	3572	3565	3555	3540
t = 8 day	P(psi)	3515	3512	3505	3494	3480
t = 9 day	P(psi)	3455	3452	3445	3435	3421
t = 10 day	P(psi)	3396	3393	3386	3376	3362
t = 11 day	P(psi)	3338	3334	3328	3317	3304
t = 12 day	P(psi)	3280	3277	3270	3260	3246
t = 13 day	P(psi)	3223	3219	3213	3203	3189
t = 14 day	P(psi)	3167	3164	3158	3149	3138
t = 15 day	P(psi)	3137	3135	3134	3128	3115
t = 16 day	P(psi)	3132	3129	3123	3114	3101



**Table 5.12: Oil saturation output for 1-D flow problem (CMG)**

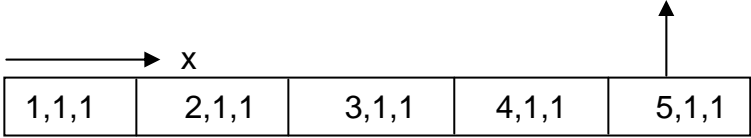
Production = 100 RB/D

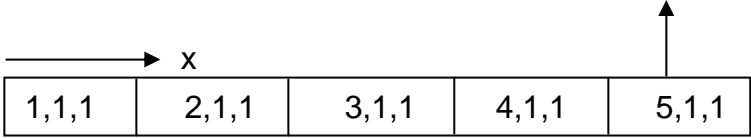


		1,1,1	2,1,1	3,1,1	4,1,1	5,1,1
t = 1 day	So	0.800	0.800	0.800	0.800	0.800
t = 2 day	So	0.800	0.800	0.800	0.800	0.800
t = 3 day	So	0.800	0.800	0.800	0.800	0.800
t = 4 day	So	0.800	0.800	0.800	0.800	0.800
t = 5 day	So	0.800	0.800	0.800	0.800	0.800
t = 6 day	So	0.800	0.800	0.800	0.800	0.800
t = 7 day	So	0.800	0.800	0.800	0.800	0.800
t = 8 day	So	0.800	0.800	0.800	0.800	0.800
t = 9 day	So	0.800	0.800	0.800	0.800	0.800
t = 10 day	So	0.800	0.800	0.800	0.800	0.800
t = 11 day	So	0.800	0.800	0.800	0.800	0.800
t = 12 day	So	0.800	0.800	0.800	0.800	0.800
t = 13 day	So	0.800	0.800	0.800	0.800	0.800
t = 14 day	So	0.800	0.800	0.800	0.800	0.798
t = 15 day	So	0.798	0.798	0.797	0.796	0.793
t = 16 day	So	0.797	0.796	0.795	0.792	0.789

**Table 5.13: Oil saturation output for 1-D flow problem (This work)**

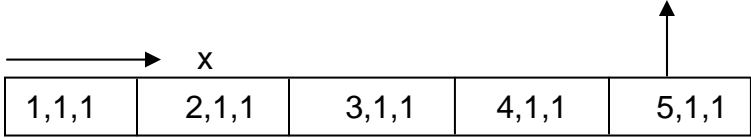
Production = 100 RB/D



						
		1,1,1	2,1,1	3,1,1	4,1,1	5,1,1
t = 1 day	So	0.800	0.800	0.800	0.800	0.800
t = 2 day	So	0.800	0.800	0.800	0.800	0.800
t = 3 day	So	0.800	0.800	0.800	0.800	0.800
t = 4 day	So	0.800	0.800	0.800	0.800	0.800
t = 5 day	So	0.800	0.800	0.800	0.800	0.800
t = 6 day	So	0.800	0.800	0.800	0.800	0.800
t = 7 day	So	0.800	0.800	0.800	0.800	0.800
t = 8 day	So	0.800	0.800	0.800	0.800	0.800
t = 9 day	So	0.800	0.800	0.800	0.800	0.800
t = 10 day	So	0.800	0.800	0.800	0.800	0.800
t = 11 day	So	0.800	0.800	0.800	0.800	0.800
t = 12 day	So	0.800	0.800	0.800	0.800	0.800
t = 13 day	So	0.800	0.800	0.800	0.800	0.800
t = 14 day	So	0.800	0.800	0.800	0.800	0.796
t = 15 day	So	0.796	0.796	0.795	0.794	0.791
t = 16 day	So	0.795	0.794	0.793	0.79	0.787

**Table 5.14: Gas saturation output for 1-D flow problem (CMG)**

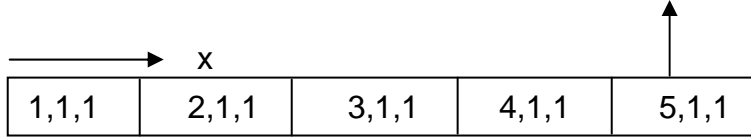
Production = 100 RB/D



		1,1,1	2,1,1	3,1,1	4,1,1	5,1,1
t = 1 day	Sg	0.000	0.000	0.000	0.000	0.000
t = 2 day	Sg	0.000	0.000	0.000	0.000	0.000
t = 3 day	Sg	0.000	0.000	0.000	0.000	0.000
t = 4 day	Sg	0.000	0.000	0.000	0.000	0.000
t = 5 day	Sg	0.000	0.000	0.000	0.000	0.000
t = 6 day	Sg	0.000	0.000	0.000	0.000	0.000
t = 7 day	Sg	0.000	0.000	0.000	0.000	0.000
t = 8 day	Sg	0.000	0.000	0.000	0.000	0.000
t = 9 day	Sg	0.000	0.000	0.000	0.000	0.000
t = 10 day	Sg	0.000	0.000	0.000	0.000	0.000
t = 11 day	Sg	0.000	0.000	0.000	0.000	0.000
t = 12 day	Sg	0.000	0.000	0.000	0.000	0.000
t = 13 day	Sg	0.000	0.000	0.000	0.000	0.000
t = 14 day	Sg	0.000	0.000	0.000	0.000	0.002
t = 15 day	Sg	0.002	0.002	0.003	0.004	0.007
t = 16 day	Sg	0.003	0.003	0.005	0.008	0.011

**Table 5.15: Gas saturation output for 1-D flow problem (This work)**

Production = 100 RB/D



		1,1,1	2,1,1	3,1,1	4,1,1	5,1,1
t = 1 day	Sg	0.000	0.000	0.000	0.000	0.000
t = 2 day	Sg	0.000	0.000	0.000	0.000	0.000
t = 3 day	Sg	0.000	0.000	0.000	0.000	0.000
t = 4 day	Sg	0.000	0.000	0.000	0.000	0.000
t = 5 day	Sg	0.000	0.000	0.000	0.000	0.000
t = 6 day	Sg	0.000	0.000	0.000	0.000	0.000
t = 7 day	Sg	0.000	0.000	0.000	0.000	0.000
t = 8 day	Sg	0.000	0.000	0.000	0.000	0.000
t = 9 day	Sg	0.000	0.000	0.000	0.000	0.000
t = 10 day	Sg	0.000	0.000	0.000	0.000	0.000
t = 11 day	Sg	0.000	0.000	0.000	0.000	0.000
t = 12 day	Sg	0.000	0.000	0.000	0.000	0.000
t = 13 day	Sg	0.000	0.000	0.000	0.000	0.000
t = 14 day	Sg	0.000	0.000	0.000	0.000	0.004
t = 15 day	Sg	0.004	0.004	0.005	0.006	0.009
t = 16 day	Sg	0.005	0.005	0.007	0.01	0.013

Table 5.16: Pressure output for 2-D flow problem (CMG)

Production = 400 RB/D

	1,1,1	2,1,1	3,1,1	4,1,1	5,1,1
	1,1,2	2,1,2	3,1,2	4,1,2	5,1,2
	1,1,3	2,1,3	3,1,3	4,1,3	5,1,3

t = 0 day	P(psi)	4003	4003	4003	4003	4003
		4008	4008	4008	4008	4008
		4013	4013	4013	4013	4013
t = 1 day	P(psi)	3936	3931	3921	3907	3887
		3941	3936	3926	3912	3892
		3946	3941	3932	3917	3897
t = 2 day	P(psi)	3851	3846	3836	3821	3802
		3856	3851	3841	3826	3807
		3861	3856	3846	3832	3812
t = 3 day	P(psi)	3766	3761	3752	3737	3718
		3772	3767	3757	3742	3723
		3777	3772	3762	3748	3728
t = 4 day	P(psi)	3683	3678	3669	3654	3636
		3689	3684	3674	3660	3641
		3694	3689	3679	3665	3645
t = 5 day	P(psi)	3601	3597	3587	3573	3554
		3607	3602	3592	3578	3559
		3612	3607	3598	3583	3564
t = 6 day	P(psi)	3521	3516	3507	3492	3474
		3526	3521	3512	3498	3479
		3531	3526	3517	3503	3484
t = 7 day	P(psi)	3441	3436	3427	3413	3395
		3446	3442	3432	3418	3400
		3452	3447	3438	3424	3405
t = 8 day	P(psi)	3363	3358	3349	3335	3317
		3368	3363	3354	3340	3322
		3373	3369	3359	3345	3327

**Table 5.16: Pressure output for 2-D flow problem (CMG), Cont.**

Production = 400 RB/D

	1,1,1	2,1,1	3,1,1	4,1,1	5,1,1
	1,1,2	2,1,2	3,1,2	4,1,2	5,1,2
	1,1,3	2,1,3	3,1,3	4,1,3	5,1,3

t = 9 day	P(psi)	3286	3281	3272	3258	3240
		3291	3286	3277	3263	3245
		3296	3291	3282	3268	3250
t = 10 day	P(psi)	3209	3205	3196	3182	3164
		3215	3210	3201	3187	3169
		3220	3215	3206	3193	3174
t = 11 day	P(psi)	3146	3143	3138	3132	3118
		3151	3149	3144	3137	3123
		3156	3154	3149	3142	3127
t = 12 day	P(psi)	3131	3128	3122	3111	3094
		3136	3133	3127	3116	3099
		3141	3139	3132	3121	3104
t = 13 day	P(psi)	3119	3115	3106	3094	3076
		3124	3120	3112	3099	3081
		3129	3125	3117	3104	3086
t = 14 day	P(psi)	3104	3100	3091	3078	3060
		3110	3105	3096	3083	3065
		3115	3110	3102	3088	3069
t = 15 day	P(psi)	3090	3085	3076	3062	3044
		3095	3090	3081	3068	3049
		3100	3096	3087	3073	3054
t = 16 day	P(psi)	3075	3071	3061	3047	3029
		3080	3076	3067	3053	3034
		3085	3081	3072	3058	3038



**Table 5.17: Pressure output for 2-D flow problem (This work), Cont.**

Production = 400 RB/D

	1,1,1	2,1,1	3,1,1	4,1,1	5,1,1
	1,1,2	2,1,2	3,1,2	4,1,2	5,1,2
	1,1,3	2,1,3	3,1,3	4,1,3	5,1,3

t = 9 day	P(psi)	3282	3278	3268	3254	3236
		3288	3283	3273	3259	3241
		3293	3288	3278	3265	3247
t = 10 day	P(psi)	3207	3202	3192	3179	3162
		3212	3207	3198	3185	3168
		3217	3213	3203	3190	3173
t = 11 day	P(psi)	3142	3140	3135	3128	3113
		3147	3145	3141	3133	3119
		3153	3150	3146	3138	3123
t = 12 day	P(psi)	3130	3126	3120	3108	3091
		3135	3132	3125	3113	3096
		3140	3137	3130	3118	3102
t = 13 day	P(psi)	3116	3112	3104	3091	3073
		3121	3117	3109	3097	3079
		3126	3122	3114	3102	3084
t = 14 day	P(psi)	3102	3097	3089	3075	3057
		3107	3103	3094	3081	3062
		3112	3108	3099	3086	3068
t = 15 day	P(psi)	3087	3083	3074	3060	3041
		3092	3088	3079	3065	3046
		3097	3093	3084	3070	3052
t = 16 day	P(psi)	3072	3068	3059	3045	3026
		3077	3073	3064	3050	3031
		3083	3078	3069	3055	3036



**Table 5.18: Oil saturation output for 2-D flow problem (CMG)**

Production = 400 RB/D

	1,1,1	2,1,1	3,1,1	4,1,1	5,1,1
	1,1,2	2,1,2	3,1,2	4,1,2	5,1,2
	1,1,3	2,1,3	3,1,3	4,1,3	5,1,3

t = 0 day	So	0.800	0.800	0.800	0.800	0.800
		0.800	0.800	0.800	0.800	0.800
		0.800	0.800	0.800	0.800	0.800
t = 1 day	So	0.800	0.800	0.800	0.800	0.800
		0.800	0.800	0.800	0.800	0.800
		0.800	0.800	0.800	0.800	0.800
t = 2 day	So	0.800	0.800	0.800	0.800	0.800
		0.800	0.800	0.800	0.800	0.800
		0.800	0.800	0.800	0.800	0.800
t = 3 day	So	0.800	0.800	0.800	0.800	0.800
		0.800	0.800	0.800	0.800	0.800
		0.800	0.800	0.800	0.800	0.800
t = 4 day	So	0.800	0.800	0.800	0.800	0.800
		0.800	0.800	0.800	0.800	0.800
		0.800	0.800	0.800	0.800	0.800
t = 5 day	So	0.800	0.800	0.800	0.800	0.800
		0.800	0.800	0.800	0.800	0.800
		0.800	0.800	0.800	0.800	0.800
t = 6 day	So	0.800	0.800	0.800	0.800	0.800
		0.800	0.800	0.800	0.800	0.800
		0.800	0.800	0.800	0.800	0.800
t = 7 day	So	0.800	0.800	0.800	0.800	0.800
		0.800	0.800	0.800	0.800	0.800
		0.800	0.800	0.800	0.800	0.800
t = 8 day	So	0.800	0.800	0.800	0.800	0.800
		0.800	0.800	0.800	0.800	0.800
		0.800	0.800	0.800	0.800	0.800

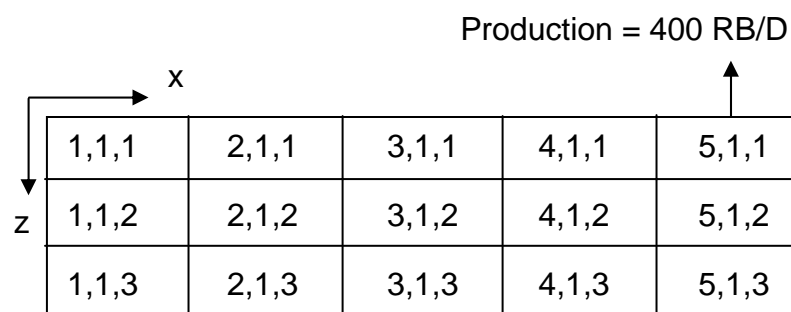
**Table 5.18: Oil saturation output for 2-D flow problem (CMG), Cont.**

Production = 400 RB/D

	x					
						↑
		1,1,1	2,1,1	3,1,1	4,1,1	5,1,1
		1,1,2	2,1,2	3,1,2	4,1,2	5,1,2
		1,1,3	2,1,3	3,1,3	4,1,3	5,1,3
z	↓					

t = 9 day	So	0.800	0.800	0.800	0.800	0.800
		0.800	0.800	0.800	0.800	0.800
		0.800	0.800	0.800	0.800	0.800
t = 10 day	So	0.800	0.800	0.800	0.800	0.800
		0.800	0.800	0.800	0.800	0.800
		0.800	0.800	0.800	0.800	0.800
t = 11 day	So	0.800	0.800	0.798	0.796	0.793
		0.800	0.800	0.800	0.797	0.794
		0.800	0.800	0.800	0.800	0.795
t = 12 day	So	0.796	0.795	0.794	0.791	0.787
		0.797	0.797	0.795	0.792	0.788
		0.798	0.798	0.796	0.794	0.790
t = 13 day	So	0.793	0.792	0.790	0.787	0.782
		0.794	0.793	0.791	0.788	0.784
		0.795	0.795	0.793	0.790	0.785
t = 14 day	So	0.789	0.788	0.786	0.783	0.777
		0.791	0.790	0.788	0.785	0.780
		0.792	0.791	0.789	0.786	0.782
t = 15 day	So	0.786	0.785	0.782	0.778	0.773
		0.787	0.786	0.784	0.781	0.776
		0.789	0.788	0.786	0.783	0.779
t = 16 day	So	0.782	0.780	0.778	0.774	0.767
		0.784	0.783	0.781	0.778	0.773
		0.786	0.785	0.783	0.780	0.777

Table 5.19: Oil saturation output for 2-D flow problem (This work)



t = 0 day	So	0.800	0.800	0.800	0.800	0.800
		0.800	0.800	0.800	0.800	0.800
		0.800	0.800	0.800	0.800	0.800
t = 1 day	So	0.800	0.800	0.800	0.800	0.800
		0.800	0.800	0.800	0.800	0.800
		0.800	0.800	0.800	0.800	0.800
t = 2 day	So	0.800	0.800	0.800	0.800	0.800
		0.800	0.800	0.800	0.800	0.800
		0.800	0.800	0.800	0.800	0.800
t = 3 day	So	0.800	0.800	0.800	0.800	0.800
		0.800	0.800	0.800	0.800	0.800
		0.800	0.800	0.800	0.800	0.800
t = 4 day	So	0.800	0.800	0.800	0.800	0.800
		0.800	0.800	0.800	0.800	0.800
		0.800	0.800	0.800	0.800	0.800
t = 5 day	So	0.800	0.800	0.800	0.800	0.800
		0.800	0.800	0.800	0.800	0.800
		0.800	0.800	0.800	0.800	0.800
t = 6 day	So	0.800	0.800	0.800	0.800	0.800
		0.800	0.800	0.800	0.800	0.800
		0.800	0.800	0.800	0.800	0.800
t = 7 day	So	0.800	0.800	0.800	0.800	0.800
		0.800	0.800	0.800	0.800	0.800
		0.800	0.800	0.800	0.800	0.800
t = 8 day	So	0.800	0.800	0.800	0.800	0.800
		0.800	0.800	0.800	0.800	0.800
		0.800	0.800	0.800	0.800	0.800

**Table 5.19: Oil saturation output for 2-D flow problem (This work), Cont.**

Production = 400 RB/D

		1,1,1	2,1,1	3,1,1	4,1,1	5,1,1
		1,1,2	2,1,2	3,1,2	4,1,2	5,1,2
		1,1,3	2,1,3	3,1,3	4,1,3	5,1,3
t = 9 day	So	0.800	0.800	0.800	0.800	0.800
		0.800	0.800	0.800	0.800	0.800
		0.800	0.800	0.800	0.800	0.800
t = 10 day	So	0.800	0.800	0.800	0.800	0.800
		0.800	0.800	0.800	0.800	0.800
		0.800	0.800	0.800	0.800	0.800
t = 11 day	So	0.798	0.798	0.796	0.794	0.791
		0.799	0.799	0.798	0.796	0.792
		0.799	0.799	0.799	0.797	0.793
t = 12 day	So	0.795	0.794	0.793	0.790	0.786
		0.796	0.795	0.794	0.791	0.787
		0.797	0.797	0.795	0.792	0.788
t = 13 day	So	0.792	0.791	0.789	0.786	0.781
		0.793	0.792	0.790	0.787	0.783
		0.794	0.793	0.791	0.789	0.784
t = 14 day	So	0.788	0.787	0.785	0.781	0.776
		0.790	0.789	0.787	0.783	0.779
		0.791	0.790	0.788	0.785	0.781
t = 15 day	So	0.785	0.783	0.781	0.777	0.772
		0.786	0.785	0.783	0.780	0.775
		0.788	0.787	0.785	0.782	0.778
t = 16 day	So	0.781	0.779	0.777	0.773	0.767
		0.783	0.782	0.780	0.776	0.772
		0.784	0.783	0.781	0.779	0.775

**Table 5.20: Gas saturation output for 2-D flow problem (CMG)**

Production = 400 RB/D

Time (day)	Variable	1,1	2,1	3,1	4,1	5,1
t = 0 day	Sg	0.000	0.000	0.000	0.000	0.000
		0.000	0.000	0.000	0.000	0.000
		0.000	0.000	0.000	0.000	0.000
t = 1 day	Sg	0.000	0.000	0.000	0.000	0.000
		0.000	0.000	0.000	0.000	0.000
		0.000	0.000	0.000	0.000	0.000
t = 2 day	Sg	0.000	0.000	0.000	0.000	0.000
		0.000	0.000	0.000	0.000	0.000
		0.000	0.000	0.000	0.000	0.000
t = 3 day	Sg	0.000	0.000	0.000	0.000	0.000
		0.000	0.000	0.000	0.000	0.000
		0.000	0.000	0.000	0.000	0.000
t = 4 day	Sg	0.000	0.000	0.000	0.000	0.000
		0.000	0.000	0.000	0.000	0.000
		0.000	0.000	0.000	0.000	0.000
t = 5 day	Sg	0.000	0.000	0.000	0.000	0.000
		0.000	0.000	0.000	0.000	0.000
		0.000	0.000	0.000	0.000	0.000
t = 6 day	Sg	0.000	0.000	0.000	0.000	0.000
		0.000	0.000	0.000	0.000	0.000
		0.000	0.000	0.000	0.000	0.000
t = 7 day	Sg	0.000	0.000	0.000	0.000	0.000
		0.000	0.000	0.000	0.000	0.000
		0.000	0.000	0.000	0.000	0.000
t = 8 day	Sg	0.000	0.000	0.000	0.000	0.000
		0.000	0.000	0.000	0.000	0.000
		0.000	0.000	0.000	0.000	0.000

**Table 5.20: Gas saturation output for 2-D flow problem (CMG), Cont.**

Production = 400 RB/D

		1,1,1	2,1,1	3,1,1	4,1,1	5,1,1
		1,1,2	2,1,2	3,1,2	4,1,2	5,1,2
		1,1,3	2,1,3	3,1,3	4,1,3	5,1,3
t = 9 day	Sg	0.000	0.000	0.000	0.000	0.000
		0.000	0.000	0.000	0.000	0.000
		0.000	0.000	0.000	0.000	0.000
t = 10 day	Sg	0.000	0.000	0.000	0.000	0.000
		0.000	0.000	0.000	0.000	0.000
		0.000	0.000	0.000	0.000	0.000
t = 11 day	Sg	0.000	0.000	0.002	0.004	0.007
		0.000	0.000	0.000	0.003	0.006
		0.000	0.000	0.000	0.000	0.005
t = 12 day	Sg	0.004	0.005	0.006	0.009	0.013
		0.003	0.003	0.005	0.008	0.012
		0.002	0.002	0.004	0.006	0.010
t = 13 day	Sg	0.007	0.008	0.010	0.013	0.018
		0.006	0.007	0.009	0.012	0.016
		0.005	0.005	0.007	0.010	0.015
t = 14 day	Sg	0.011	0.012	0.014	0.017	0.023
		0.009	0.010	0.012	0.015	0.020
		0.008	0.009	0.011	0.014	0.018
t = 15 day	Sg	0.014	0.015	0.018	0.022	0.027
		0.013	0.014	0.016	0.019	0.024
		0.011	0.012	0.014	0.017	0.021
t = 16 day	Sg	0.018	0.020	0.022	0.026	0.033
		0.016	0.017	0.019	0.022	0.027
		0.014	0.015	0.017	0.020	0.023

**Table 5.21: Gas saturation output for 2-D flow problem (This work)**

Production = 400 RB/D

		1,1,1	2,1,1	3,1,1	4,1,1	5,1,1
		1,1,2	2,1,2	3,1,2	4,1,2	5,1,2
		1,1,3	2,1,3	3,1,3	4,1,3	5,1,3
t = 0 day	Sg	0.000	0.000	0.000	0.000	0.000
t = 1 day	Sg	0.000	0.000	0.000	0.000	0.000
		0.000	0.000	0.000	0.000	0.000
t = 2 day	Sg	0.000	0.000	0.000	0.000	0.000
		0.000	0.000	0.000	0.000	0.000
t = 3 day	Sg	0.000	0.000	0.000	0.000	0.000
		0.000	0.000	0.000	0.000	0.000
t = 4 day	Sg	0.000	0.000	0.000	0.000	0.000
		0.000	0.000	0.000	0.000	0.000
t = 5 day	Sg	0.000	0.000	0.000	0.000	0.000
		0.000	0.000	0.000	0.000	0.000
t = 6 day	Sg	0.000	0.000	0.000	0.000	0.000
		0.000	0.000	0.000	0.000	0.000
t = 7 day	Sg	0.000	0.000	0.000	0.000	0.000
		0.000	0.000	0.000	0.000	0.000
t = 8 day	Sg	0.000	0.000	0.000	0.000	0.000
		0.000	0.000	0.000	0.000	0.000

**Table 5.21: Gas saturation output for 2-D flow problem (This work), Cont.**

Production = 400 RB/D

		1,1,1	2,1,1	3,1,1	4,1,1	5,1,1
		1,1,2	2,1,2	3,1,2	4,1,2	5,1,2
		1,1,3	2,1,3	3,1,3	4,1,3	5,1,3
t = 9 day	Sg	0.000	0.000	0.000	0.000	0.000
		0.000	0.000	0.000	0.000	0.000
		0.000	0.000	0.000	0.000	0.000
t = 10 day	Sg	0.000	0.000	0.000	0.000	0.000
		0.000	0.000	0.000	0.000	0.000
		0.000	0.000	0.000	0.000	0.000
t = 11 day	Sg	0.002	0.003	0.004	0.006	0.010
		0.001	0.001	0.002	0.005	0.008
		0.001	0.001	0.001	0.003	0.007
t = 12 day	Sg	0.005	0.006	0.008	0.010	0.015
		0.004	0.005	0.006	0.009	0.013
		0.003	0.003	0.005	0.008	0.012
t = 13 day	Sg	0.008	0.009	0.011	0.015	0.019
		0.007	0.008	0.010	0.013	0.017
		0.006	0.007	0.009	0.012	0.016
t = 14 day	Sg	0.012	0.013	0.015	0.019	0.024
		0.010	0.011	0.014	0.017	0.021
		0.009	0.010	0.012	0.015	0.019
t = 15 day	Sg	0.016	0.017	0.019	0.023	0.028
		0.014	0.015	0.017	0.020	0.025
		0.013	0.014	0.015	0.018	0.022
t = 16 day	Sg	0.019	0.021	0.023	0.027	0.033
		0.017	0.018	0.021	0.024	0.028
		0.016	0.017	0.019	0.022	0.025



## Chapter 6. Validation of the proposed model

### 6.1. Introduction

The proposed model was validated by simulation of two injection experiments reported in the literature (Morel et. al. (1990) and Le Romancer et. al. (1994)). The experiments were done in one-dimensional systems designed to model mass transfer between a gas ( $N_2$  or  $CO_2$ ) flowing in a fracture and a resident fluid ( $C_1$ - $C_5$ ) in a horizontal matrix block.

The injected gas (nitrogen or carbon dioxide) diffuses into the fluid ( $C_1$ - $C_5$ ) in the porous matrix through gas and liquid phases causing the vaporization of oil in the porous matrix which is transported by convection and diffusion to the gas flowing in the fracture. The diffusion process changes the fluid composition inside the core, which leads to the variations of phase properties such as densities and viscosities. The nitrogen and carbon dioxide injection experiments are experiments No. M5 in Table 2.1 and No. M25 in Table 2.2, respectively.

Recovery of each component ( $C_1$ - $C_5$ ) and saturation along the matrix were measured in both experiments. Also, differential pressure between the fracture and end of the matrix was reported for carbon dioxide injection experiment. First, the same technique of measuring gas saturation along the core in both nitrogen and carbon dioxide injection experiments will be described in detail followed by

presenting a description, simulation results, and summary for the nitrogen and carbon dioxide injection experiments.

## 6.2. Measurement of local gas saturation along the core

Gas saturation along the core was measured by a same technique for both nitrogen and carbon dioxide injection experiments (Morel et. al. (1990) and Le Romancer et. al. (1994)). The description of the procedure of measuring gas saturation in the experiments is followed from Morel et. al. (1990).

“A gamma-ray attenuation technique was used to measure local gas saturation along the core. The technique is based on the Beer-Lambert Law for a given wave-length radiation as:

$$I = I_0 e^{-\mu y} \quad \text{Eq. (6.1)}$$

Where  $\mu$  and  $y$  are linear absorption coefficient and thickness of material respectively. The intensity  $I_0(I)$ , is proportional to the number of counts  $n_0(n)$ , hence Eq. (6.1) can be written as:

$$n = n_0 e^{-\mu y} \quad \text{Eq. (6.2)}$$

In the diffusion experiments, a porous material is saturated with two fluids: gas and oil, with  $\mu_g$  and  $\mu_l$  as respective linear absorption coefficients. The transmitted count is given by:

$$n = n_0 e^{-[\mu_g s_g + \mu_l (1-s_g)] \phi y} \quad \text{Eq. (6.3)}$$

Where  $\phi$  is porosity.

The respective counts  $n_g$  and  $n_l$  transmitted through the porous medium, fully saturated by gas and liquid, enable the calculation of the gas saturation,  $S_g$ , as a linear function of the logarithm of the number of counts as:

$$S_g = \frac{\log(n/n_l)}{\log(n_g/n_l)} \quad \text{Eq. (6.4)}$$

In practice, measurement conditions ensuring a linear relationship between  $S_g$  and  $\log(n)$  must be found for. The local gas saturation can be then calculated from the value of count  $n$  at any position in the porous medium, provided that the two calibration counts  $n_l$  and  $n_g$  have been measured under the same pressure and temperature conditions.

The absorption coefficient of any fluid mixture strongly depends on its composition and density. The first step of every experiment is to measure the absorption profile of the porous medium under vacuum. Then it is successively saturated with nitrogen (if necessary), methane, and pentane at the pressure and temperature of the experiment, and absorption profiles are measured.

The nitrogen diffusion experiment involves a ternary fluid system, i.e. oil and gas phases whose compositions, densities and absorption coefficients are continuously changing inside the sample. Since the local compositions were not measured, the local calibration counts  $n_g$  and  $n_l$  required for the calculation of local saturations could not be determined. For this reason, the saturations were

calculated for two extreme situations, (a) the gas and liquid phases are binary mixtures of methane and pentane, (b) the gas and liquid phases are binary mixtures of nitrogen and pentane. Situation (a) corresponds to the initial state of the experiment, when no nitrogen has entered the porous medium. It underestimates the gas saturation when nitrogen penetrates the porous medium. In fact, the solubility of nitrogen in liquid pentane is less than that of methane, which makes the liquid phase all the denser and absorbent, as nitrogen content increases. Situation (b) corresponds to the end of the experiment, when methane has been totally replaced by nitrogen in the fluid system. At any time during the experiment, the true situation is intermediate between (a) and (b). As nitrogen concentration is higher near the fracture, the situation is more similar to situation (b), and the dead-end face situation is more similar to situation (a), because little nitrogen is found there, at least at the beginning of the experiment.”

### **6.3. Nitrogen injection experiment**

First, description of the nitrogen injection experiment (Morel et. al. (1990)) will be presented followed by simulation results of the experiment and a brief summary.

#### **6.3.1. Description of the nitrogen injection experiment**

The nitrogen injection experiment was performed in a 1-dimension horizontal core by Morel et. al. (1990). Fig. 6.1 shows the layout of the experiment. All sides

of the core were sealed except one side, where a nitrogen gas stream flowed across that face. Paris Basin Chalk samples were used as cores.

Nitrogen was injected in the fracture at 1479 psi and 38.5°C. Initially the pressure (1479 psi), temperature (38.5°C), and composition ( $C_1$  (52.4 mole%)- $C_5$  (47.6 mole%)) were uniform along the core. At the beginning of the experiment, the porous matrix contains a mixture of  $C_1$  and  $C_5$  distributed between gas and liquid phases in equilibrium (Table 6.5). A uniform 25% initial gas saturation exists within the matrix. The injected gas  $N_2$  diffuses into the gas phase and dissolves in the liquid phase at the boundary between the fracture and the matrix. The injected gas may also flow into or out from the matrix through the gas phase if the pressure in the fracture is greater than or less than the gas phase pressure at the fracture-matrix boundary.

Since there is no  $C_1$  in the gas injected into the fracture,  $C_1$  is recovered from the matrix by countercurrent diffusion through the gas phase and flow from the matrix to the fracture if the gas phase pressure in the matrix is larger than the gas pressure in the fracture.  $C_5$  diffuses to the fracture through the gas phase. However,  $C_5$  remains primarily in the liquid phase where it is removed from the matrix by evaporation into the flowing gas stream at the fracture-matrix boundary. The oil phase flows countercurrent to the direction of the injected gas.  $C_1$  in the liquid phase is also evaporated into the fracture at the fracture-matrix boundary.

Compositions and volumes of produced oil and gas were measured. Gas saturation along the core was measured at certain times in the experiments.

### 6.3.2. Simulation of 1-D nitrogen injection experiment

Table 6.1 shows the model inputs for simulation of the experiment. Relative permeabilities and capillary pressure are presented in Table 6.2. Critical properties and volume shift parameter ( $S_i$ ) of the components are listed in Table 6.3. Binary interaction coefficients are assumed zero. Pen-Robinson EOS was used for phase-behavior calculations. Fig. 6.2 shows the ternary diagram of methane-pentane-nitrogen at 1479 psi and 38.5°C. Tables 6.4 and 6.5 show compositions and densities of oil and gas phases for tie-lines 1 and 2 of Fig. 6.2 from Morel et. al. (1990) and this work. The phase behavior calculations agreement between Morel et. al. (1990) and this work is very good.

Pressure at fracture-core boundary was set to 1479 psi constant for the entire simulation. The core was simulated with 20 grids in the x direction. Gas-oil capillary pressure was reported at a reference interfacial tension ( $\sigma_0 = 2.9 \text{ dynes/cm}$ ) and was corrected by interfacial tension.

Nitrogen injection experiment was performed for 16 days. Simulation of the nitrogen injection experiment for 30 days was carried out for two cases: A-no convection at matrix-fracture boundary (same as Hua and Whitson (1991) model or  $q_{C,fm,c}=0$ ) and B-with convection at matrix-fracture boundary. Recoveries of methane and pentane from experimental measurements and simulation are

compared in Fig. 6.3. Fig. 6.4 to 6.6 show gas saturation profiles at 4, 8, and 16 day of the experiment and simulation. The agreements between simulation results and measured data are very good. Saturation profiles from simulation are closer to lower limit of saturation measurements (case a) at the beginning of the core. Towards end of the core, the agreement is good between saturation profiles from simulation and higher limit of saturation measurements (case b). Matrix-fracture boundary conditions (A and B cases) do not have a significant effect on the recovery curves and saturation profiles along the core.

Mass transfer rates for nitrogen, methane, and pentane by diffusion and convection between fracture and matrix were computed in the model and are plotted in Fig. 6.7 to Fig. 6.9. Mass transfer from the fracture-core boundary to the core is positive and from the core to the fracture-core boundary is defined negative. Nitrogen flow rate in the fracture changed from  $4\text{cm}^3/\text{s}$  to  $8\text{cm}^3/\text{s}$  at 14.4 day of the experiment. Therefore, the diffusion mass transfer coefficient at matrix-fracture boundary doubled because it depends linearly on gas stream flow velocity in the fracture (Chapter 3, Eq. (3.19)). The increase in the nitrogen gas velocity in the fracture causes increase in pentane diffusion mass transfer (Fig. 6.9) at 14.4 day. Fig. 6.7 to Fig. 6.9 show that nitrogen, methane, and pentane are transported between matrix and fracture primarily by diffusion. Vaporization of methane and pentane at the matrix-fracture surface is the dominant recovery mechanism. After 15 days, nitrogen flows from the fracture through the matrix but is still significantly less than transport by diffusion. This is

because gas pressure in the matrix drops below fracture pressure (1479psi). Fig. 6.10 and 6.11 show oil pressure profiles in the core for the two cases of no convection (A) and with convection (B) at matrix-fracture boundary. Fig. 6.10 shows that oil phase pressure drops significantly from 1479psi (at  $t=0$  day) to 1320psi (at  $t=30$  day) when no convection (A) is allowed at the matrix-fracture boundary. On the other hand, Fig. 6.11 shows that nitrogen convection from fracture to inside the matrix causes core pressure to stabilize around 1473psi at 30 days.

The magnitudes of diffusion and convection mechanisms in transporting each component inside the core are plotted in Fig. 6.12 to Fig. 6.23. In these figures, a positive sign means mass transports from the fracture-core boundary to the core and a negative sign means mass transports from the matrix to the fracture-core boundary. Nitrogen mass transfer from the fracture to the core creates a countercurrent flow in the core. While oil flows from the core towards the fracture-core boundary where it evaporates into the flowing nitrogen gas in the fracture, gas moves from the fracture-core boundary towards the end of the core.

Fig. 6.12 to Fig. 6.15 show that nitrogen is transported from the fracture-core boundary towards end of the core by oil and gas molecular diffusion and gas convection (positive rates). Countercurrent flow of oil from end of the core towards the fracture-core boundary causes transport of nitrogen to the fracture boundary by convection (negative rates). Fig. 6.12 and 6.13 show that nitrogen is



transported mainly by molecular diffusion in the gas phase inside the core at early time of the simulation regardless of no convection (A) or with convection (B) matrix-fracture boundary conditions. Fig. 6.14 shows that if convection between matrix and fracture is not considered in the model (A), then gas molecular diffusion still remains the main mechanism in transporting nitrogen inside the core at 28 days. However, if convection between matrix and fracture is considered (B), then gas convection becomes the most significant transport mechanism at 28 days (Fig. 6.15).

Fig. 6.16 to Fig. 6.19 compare the magnitudes of oil and gas convection and diffusion mechanisms in transporting methane inside the core. Methane is transported from end of the core to the fracture-core boundary by diffusion through oil and gas phases and by convection in the oil phase (negative rates). Gas flows from the fracture-core boundary towards end of the core transporting methane counter current to the direction of diffusion of methane (positive rates). Fig. 6.16 and Fig. 6.17 show that methane is transferred mainly by molecular diffusion inside the core at early time of the experiment ( $t = 8$  days) for both cases of no convection (A) and with convection (B) at matrix-fracture boundary conditions. Because oil and gas convection are transporting methane in opposite directions, and the net diminishing each other effect. If convection between fracture and matrix is neglected (A), gas molecular diffusion remains the dominant transporting mechanism (Fig. 6.18). However, Fig. 6.19 shows that if convection between matrix and fracture is considered in the model (B), gas

convection becomes the most important mechanism in transporting methane from fracture-core boundary to inside the core at late time of simulation.

Fig. 6.20 to Fig. 6.23 confirm that oil convection is the dominant mechanism of mass transfer of pentane inside the core from end of the core towards fracture-core boundary (negative rates) regardless of considering (A) or not considering (B) convection between matrix and fracture. It is the most important mechanism in transporting pentane inside the core for the entire simulation time.

The transport mechanism for each component inside the core depends on fracture-matrix boundary condition (A and B).

### **6.3.2. Summary**

The following conclusions are based on simulation of nitrogen injection experiment:

- Recovery of each component ( $C_1$  and  $C_5$ ) and saturation profiles along the core were matched successfully.
- Matrix-fracture boundary conditions (A and B) had a similar effect on each component ( $C_1$  and  $C_5$ ) recovery and saturation profiles along the core.
- Diffusion between matrix and fracture was the main transport mechanism of components.

- Nitrogen diffusion created a countercurrent flow inside the core. Oil flows from end of the core towards the fracture-core boundary and gas moves in the opposite direction.
- Nitrogen and methane were transported mainly by gas molecular diffusion inside the core at early time of the simulation.
- Gas molecular diffusion remained the main mechanism in transporting nitrogen and methane inside the core for case A matrix-fracture boundary condition at late time of simulation.
- For case B fracture-matrix boundary condition, gas convection became the most significant transport mechanism of nitrogen and methane inside the core at late time of simulation.
- Oil convection was the dominant mechanism in transporting pentane inside the core.

## **6.4. Carbon dioxide injection experiment**

A description of the carbon dioxide injection experiment by Le Romancer et. al. (1994) will be presented followed by simulation results of the experiment and a brief summary.

### **6.4.1. Description of the carbon dioxide injection experiment**

The carbon dioxide injection experiment was performed in a 1-dimension horizontal core by Le Romancer et. al. (1994). The layout of the experiment is the same as nitrogen injection experiment (Fig. 6.1). Similar to the nitrogen injection

experiment, all sides of the core were sealed except one side, where a carbon dioxide gas stream flowed across that face. Paris Basin Chalk samples were used as matrices.

Carbon dioxide was injected in the fracture at a pressure of 913.74 psi and temperature of 38.5°C. In this set of experiment, the porous matrix was initially saturated with a liquid phase containing C<sub>1</sub> (28 mole%) and C<sub>5</sub> (72 mole%). No initial gas saturation was present in the core. There was an immobile water phase at a saturation of 11%. Initial pressure (913.74 psi), temperature (38.5°C), composition (C<sub>1</sub>-C<sub>5</sub>), and gas saturation (0%) were constant throughout the core. CO<sub>2</sub> dissolves in the liquid phase causing the liquid phase to swell and consequently the liquid phase pressure to increase. The liquid phase flows countercurrently to the fracture-matrix boundary where C<sub>1</sub> and C<sub>5</sub> are evaporated into the flowing stream. Depletion of C<sub>1</sub> and C<sub>5</sub> coupled with diffusion of CO<sub>2</sub> into the liquid phase causes phase behavior to change and an equilibrium gas saturation evolves in portions of the matrix adjacent to the fracture. Subsequently, C<sub>1</sub> may be recovered by diffusion or flow to the fracture matrix boundary while C<sub>5</sub> is recovered by diffusion in the gas phase and evaporation of the liquid phase at the fracture-matrix boundary. Carbon dioxide mass transfer from the fracture to the core causes a countercurrent flow in the core. Oil flows from the core toward the fracture-core and gas moves in the opposite direction.

Compositions and volumes of produced oil and gas were measured in the experiment. Gas saturation along the core was measured at certain times in the experiments. Also differential pressure between the fracture and end of the core was measured in this experiment.

#### **6.4.2. Simulation of 1-D carbon dioxide injection experiment**

Capillary pressure and relative permeabilities were the same as for the nitrogen injection experiment (Table 6.2). Table 6.3 presents critical properties of carbon dioxide. Volume shift parameter ( $S_i$ ) was assumed zero for the phase behavior calculations. The model inputs are shown in Table 6.6. Fig. 6.24 shows ternary diagram of methane-pentane-carbon dioxide at pressure of 913.74 psi and temperature of 38.5°C. Peng-Robinson EOS was used for phase behavior calculations. Binary interaction coefficients were adjusted to match phase behavior of the methane-pentane-carbon dioxide system (Fig. 6.24) reported by Le Romancer et. al. (1994). The adjusted binary interaction coefficients are listed in Table 6.7. Results of phase behavior calculations for tie-lines of Fig. 6.24 are presented in Tables 6.8 to 6.18. Phase behavior calculations are performed for several compositions along each tie-line. The agreement is excellent between this work phase behavior calculations and tie-lines of methane-pentane-carbon dioxide ternary diagram (Fig. 6.24).

The core was simulated with 10 grids in the x-direction. Pressure at the fracture-core boundary was held constant at 913.74 psi for the entire simulation.

Correction of capillary pressure with interfacial tension was not considered in the model.

Calculated recoveries of methane and pentane are compared with experimental data in Fig. 6.25. Fig. 6.26 shows the differential pressure between the fracture-core boundary and end of the core from simulation and experimental measurement. The agreements between the results calculated from the model and the experimental data are very good. Convection between matrix and fracture played a very important role in simulation of this experiment especially in matching the reported saturation profiles and the differential pressure between fracture-core surface and end of the core. Pressure in the core dropped significantly in absence of convection between the matrix and the fracture. It was not possible to simulate the experiment successfully without including convection between fracture and matrix.

Fig. 6.27 to 6.32 compares oil saturation profiles along the core at 7, 23, 53, 67, 88, and 95 days of the experiment and the simulation. The agreement at 7 and 23 day is good. Diffusion of  $\text{CO}_2$  and depletion of  $\text{C}_1$  and  $\text{C}_5$  causes the phase behavior to change which creates an equilibrium gas saturation in parts of the matrix adjacent to the fracture. However, since the 11% water saturation in the core is immobile, the oil saturation cannot exceed 89%. Measured oil saturation exceeds 100% at 7 and 23 day (Fig. 6.27 and 6.28), indicating errors in the measurements. Fig. 6.29 to 6.32 show that gas propagates faster in the

simulation than in the experiment at 53, 67, 88, and 95 days. Oil saturation from simulation is lower than experimental data at 53, 67, 88, and 95 days. Simulation result demonstrates that gas reaches end of the core at 88 day, but experimental data doesn't agree with the calculations.

Material balance calculations were performed at 95 day to investigate the disagreement between experimental data and simulation results of oil saturation. The procedure has the following steps:

**Step 1:** Calculating initial moles of C<sub>1</sub> and C<sub>5</sub> in the core

Since there is no initial gas saturation in the core, the initial mole of C<sub>1</sub> and C<sub>5</sub> present in the oil phase only, therefore:

Initial C<sub>1</sub> mole =

$$(\text{Oil density, mole/m}^3)(\text{Oil saturation, } S_o)(\text{Pore volume, m}^3) (\text{mole fraction of C}_1)$$

**Eq. (6.5)**

Initial C<sub>5</sub> mole =

$$(\text{Oil density, mole/m}^3)(\text{Oil saturation, } S_o)(\text{Pore volume, m}^3) (\text{mole fraction of C}_5)$$

**Eq. (6.6)**

Details of the calculations are showed in Table 6.19.

**Step 2:** Calculating the remaining moles of C<sub>1</sub> and C<sub>5</sub> in the core at 95 day by using the recovery of C<sub>1</sub> and C<sub>5</sub> at 95 day

Mole of C<sub>1</sub> and C<sub>5</sub> remain in the core at 95 day are calculated as follows:

Mole C<sub>1</sub> remain in the core = (Initial C<sub>1</sub> mole)(1- C<sub>1</sub> Recovery at 95 day) **Eq. (6.7)**

Mole C<sub>5</sub> remain in the core = (Initial C<sub>5</sub> mole)(1- C<sub>5</sub> Recovery at 95 day) **Eq. (6.8)**

Table 6.20 shows the calculation results.

**Step 3:** Calculating mole of CO<sub>2</sub> in the core at 95 day by material balance and performing a flash calculation to determine oil and gas saturations

Total mole of C<sub>1</sub>, C<sub>5</sub>, and CO<sub>2</sub> in gas and oil phases must be calculated at 95 days. Oil and gas densities and also oil and gas saturations are required to calculate total mole of C<sub>1</sub>, C<sub>5</sub>, and CO<sub>2</sub> as follows:

Total mole C<sub>1</sub>, C<sub>5</sub>, and CO<sub>2</sub> in the core at 95 day =

$$\begin{aligned} & (\text{Oil density, mole/m}^3)(\text{Oil saturation, } S_o)(\text{Pore volume, m}^3) + \\ & (\text{Gas density, mole/m}^3)(\text{Gas saturation, } S_g)(\text{Pore volume, m}^3) \quad \mathbf{Eq. (6.9)} \end{aligned}$$

Since we know the mole of C<sub>1</sub> and C<sub>5</sub> at 95 day from step 2, CO<sub>2</sub> mole can be calculated by subtracting C<sub>1</sub> and C<sub>5</sub> mole from the total mole.

A procedure is developed to assign density and saturation of oil and gas in Eq. (6.9). Fig. 6.33 and 6.34 show how oil and gas densities change with mole fraction of CO<sub>2</sub> in oil and gas phase. As one may see, oil density increases from 10.5 to 12.2 mole/m<sup>3</sup> when mole fraction of CO<sub>2</sub> in oil phase increases from 19% to 67%. As CO<sub>2</sub> mole fraction in gas phase increases from 52% to 91%, gas



density rises from 3.15 to 4.05mole/m<sup>3</sup>. Two cases are assumed for oil and gas densities in Eq. (6.9):

Case 1: High density-Oil and gas densities are assumed to have their highest value from Fig. 6.33 and 6.34 as 12.21 and 4.05mole/m<sup>3</sup> respectively.

Case 2: Low density-The lowest value from Fig. 6.33 and 6.34 are assigned to oil and gas densities as 10.54 and 3.15mole/m<sup>3</sup> respectively.

The average oil and gas saturation at 95 days from the experiment measurements are 65% and 24% respectively. These values are used in Eq. (6.9).

The detailed of the calculations are shown in Table 6.21 and 6.22. Material balance calculations showed that average gas saturation in the core should be 52 to 59% at 95 days of the experiment. The measured average gas saturation in the experiment at 95 days is 24%. So, there is almost 30% error in saturation measurement. The average gas saturation from simulation is 51%, which is in agreement with the material balance.

Fig. 6.35 to 6.37 show mass exchange rates for carbon dioxide, methane, and pentane at matrix-fracture boundary by diffusion and gas convection mechanisms. Negative rate means flow from the fracture-core boundary to the fracture (recovery or production). Positive rate is flow from the fracture to the fracture-core boundary. Diffusion of CO<sub>2</sub> causes the oil and /or gas phase

pressures to increase. If oil and/or gas pressure exceeds the fracture pressure, then the oil and/or gas phases will flow from fracture-core boundary to the fracture. Before around 40 days of simulation, the oil phase flows from the fracture-core boundary to the fracture, because oil saturation was high in the matrix next to the fracture. After around 40 days of simulation, the oil saturation decreased significantly in the portions of matrix adjacent to the fracture due to CO<sub>2</sub> diffusion and recovery of C<sub>1</sub> and C<sub>5</sub>. As a result, the oil phase permeability decreases and flow from the matrix to the fracture-core boundary stops. Under these conditions, the gas phase flows from the fracture-core boundary to the fracture.

Fig. 6.35 shows that carbon dioxide is transported at the fracture-core boundary mainly by diffusion until about 40 days of the experiment. After 40 days, carbon dioxide leaves the core by convection in the gas phase while entering the core by diffusion at the fracture-core boundary. The magnitude of gas convection mechanism increases with time relative to diffusion mechanism in transporting carbon dioxide at fracture-core boundary. For example, at 90 days, the magnitudes of gas convection and diffusion mechanisms are about 7.5E-5 mole/day and less than 1.0E-5 mole/day respectively.

In Fig. 6.36, methane is recovered at fracture-core boundary mainly by diffusion until almost 40 days of the experiment. After 40 days, gas convection starts to transport methane from the fracture-core boundary to the fracture. Mass

transfer by diffusion and gas convection at the fracture-core boundary becomes equally important in methane recovery after 70 days of the experiment.

Fig. 6.37 shows that diffusion or vaporization at fracture-core surface is the main recovery mechanism of pentane until around 40 days. After 40 days, gas convection from the fracture-core boundary to the fracture begins to contribute in pentane recovery. Although, recovery of pentane with gas convection increases with time, pentane transport by diffusion remains a more important mechanism.

Fig. 6.38 to 6.43 compare the magnitudes of diffusion and convection mechanisms in transporting carbon dioxide, methane, and pentane inside the core. A positive sign means that mass transfers from the fracture-core boundary to the core and a negative sign means that mass transfers from the matrix to the fracture-matrix boundary. Carbon dioxide mass transfer from the fracture to the core causes a countercurrent flow in the core. Oil flows from the end of the core towards the fracture-core boundary and gas moves in the opposite direction.

Fig. 6.38 shows that carbon dioxide is transported from the fracture-core surface towards end of the core by oil and gas molecular diffusion and gas convection at 23 days of the experiment (positive rates). Gas convection and diffusion transport carbon dioxide only in the parts of the matrix where gas saturation developed. Oil convection (negative rates) transports carbon dioxide countercurrent to the direction of oil and gas molecular diffusion and gas convection. Molecular diffusion plays an important role in transporting carbon

dioxide inside the core at 23 days. However, Fig. 6.39 shows that oil and gas convection become the most important mechanisms in transporting carbon dioxide inside the core towards end of the experiment (90 days). The magnitude of oil convection is more than magnitude of gas convection in transporting carbon dioxide (Fig. 6.39).

Fig. 6.40 demonstrates that methane is transported from the core towards the fracture-core surface by oil and gas diffusion and oil convection (negative rates). At the same time, gas convection (positive rates) transports methane countercurrent to the direction of oil and gas diffusion and oil convection. Diffusion and convection are able to transport methane only in the portions of the matrix adjacent to the fracture where gas saturation exists. Oil and gas molecular diffusion have the most important roles in transporting methane inside the core at 23 days. Fig. 6.41 shows that methane is almost recovered completely towards end of the experiment at 90 days.

Fig. 6.42 shows that pentane is transported from end of the core towards the fracture-core surface by diffusion through oil and gas phase and oil convection (negative rates). Gas convection transports pentane countercurrent to the direction of oil and gas diffusion and oil convection (positive rates). Again, gas diffusion and convection are active in transporting pentane in parts of matrix where a gas phase has formed. Oil molecular diffusion and convection play the most important role in transporting pentane inside the core. Fig. 6.43 shows that

oil convection becomes the dominant mechanism in transporting pentane inside the core towards end of the experiment at 90 days.

### 6.4.3. Summary

Simulation of carbon dioxide injection experiment can be summarized as follows:

- The binary interaction coefficients were adjusted to match the reported phase behavior of methane-pentane-carbon dioxide by Le Romancer et. al. (1994).
- The recoveries of each component ( $C_1$  and  $C_5$ ) and differential pressure between matrix and fracture matched experimental data of Le Romancer et. al. (1994).
- Convection between matrix and fracture played a very important role in simulation of this experiment especially in matching differential pressure between matrix and fracture.
- Material balance confirmed that there is an experimental error in the measurement of gas saturation.
- Diffusion and vaporization were the main transport mechanism at matrix-fracture boundary until 40 days of the simulation. After 40 days, gas convection became an important mechanism in transporting components between matrix and fracture.

- Carbon dioxide and methane were transported mostly by oil and gas diffusion inside the core at early time of simulation. Oil and gas convection became the most important mechanism in transporting carbon dioxide and methane inside the core towards end of simulation.
- Oil convection and diffusion were the most important mechanisms in transporting pentane inside the core. Oil convection became the dominant mechanism in transporting pentane inside the core towards end of simulation.
- Mass transfer of carbon dioxide from the fracture to the core created a countercurrent flow in the core. While oil flowed from the end of the core towards the fracture-core boundary, gas moved in the opposite direction.

**Table 6.1: Model inputs for simulation of the nitrogen injection experiment**

Rock material	Paris Basin Chalk
Core length (m)	0.357
Core cross section (m <sup>2</sup> )	0.032 x 0.032
Core porosity	0.4
Core permeability (mD)	2
Water saturation (%)	0
Residual oil saturation (%)	0.2
Pressure (psi)	1479
Temperature (°C)	38.5
Initial gas saturation (%)	0.25
Mole fraction C <sub>1</sub>	0.524
Mole fraction C <sub>5</sub>	0.476
N <sub>2</sub> flow rate in the fracture (cm <sup>3</sup> /s)	4 until 14.4 day then 16
N <sub>2</sub> mass transfer coefficient between matrix and fracture (k <sub>c</sub> , Eq. (3.19))	0.1425
C <sub>1</sub> mass transfer coefficient between matrix and fracture (k <sub>c</sub> , Eq. (3.19))	0.3664
C <sub>5</sub> mass transfer coefficient between matrix and fracture (k <sub>c</sub> , Eq. (3.19))	0.6292

**Table 6.2: Relative permeabilities and capillary pressure (Hua et. al. (1991))**

S <sub>g</sub>	K <sub>ro</sub>	K <sub>rg</sub>	P <sub>cog</sub> , psi
0	1	0	2.22865
0.1	0.9	0.0002	2.3548
0.2	0.586	0.004	2.48095
0.3	0.316	0.02	2.6071
0.4	0.153	0.045	2.71223
0.5	0.063	0.1	2.83838
0.55	0.037	0.15	2.93306
0.6	0.02	0.21	3.0276
0.65	0.0096	0.3	3.15375
0.7	0.0039	0.5	3.2789
0.8	0	0.9	3.99475

**Table 6.3: Critical properties of N<sub>2</sub>, C<sub>1</sub>, C<sub>5</sub>, and CO<sub>2</sub>**

Component	T <sub>c</sub> (K)	P <sub>c</sub> (Mpa)	MW	$\omega$	Parachor	S <sub>i</sub>
N <sub>2</sub>	126.2	3.39	28.013	0.039	41	-0.12839
C <sub>1</sub>	190.4	4.6	16.043	0.0092	77	-0.15386
C <sub>5</sub>	469.7	3.37	72.151	0.251	225	-0.03446
CO <sub>2</sub>	304.2	7.34	44.01	0.225	78	0

**Table 6.4: Compositions and densities of oil and gas phases for tie-lines 1 and 2 of methane-pentane-nitrogen ternary diagram at 1479 psi and 38.5°C from Morel et. al. (1990)**

Binary mixture	C <sub>5</sub> gas composition mole%	Gas density kg/m <sup>3</sup>	C <sub>5</sub> oil composition mole %	Oil density kg/m <sup>3</sup>
C <sub>1</sub> (52.4)- C <sub>5</sub> (47.6)	5.7	95.2	55.3	494
N <sub>2</sub> (52.4)- C <sub>5</sub> (47.6)	3.5	119	83.8	605

**Table 6.5: Compositions and densities of oil and gas phases for tie-lines 1 and 2 of methane-pentane-nitrogen ternary diagram at 1479 psi and 38.5°C from this work**

Binary mixture	C <sub>5</sub> gas composition mole%	Gas density kg/m <sup>3</sup>	C <sub>5</sub> oil composition mole %	Oil density kg/m <sup>3</sup>
C <sub>1</sub> (52.4)- C <sub>5</sub> (47.6)	5.6	95.2	55	490
N <sub>2</sub> (52.4)- C <sub>5</sub> (47.6)	3.3	118	84	600

**Table 6.6: Model inputs for simulation of the CO<sub>2</sub> injection experiment**

Water saturation (%)	11
Pressure (psi)	913.74
Temperature, C	38.5
Initial gas saturation (%)	0
Mole fraction C <sub>5</sub>	0.72
CO <sub>2</sub> flow rate in the fracture (cm <sup>3</sup> /s)	4
CO <sub>2</sub> mass transfer coefficient between matrix and fracture (k <sub>c</sub> , Eq. (3.19))	0.1296
C <sub>1</sub> mass transfer coefficient between matrix and fracture (k <sub>c</sub> , Eq. (3.19))	0.291
C <sub>5</sub> mass transfer coefficient between matrix and fracture (k <sub>c</sub> , Eq. (3.19))	0.0648



**Table 6.7: Binary interaction coefficients for methane-pentane-carbon Dioxide mixture**

	C <sub>1</sub>	C <sub>5</sub>	CO <sub>2</sub>
C <sub>1</sub>	0.0000	0.1800	0.1485
C <sub>5</sub>	0.1800	0.0000	0.0000
CO <sub>2</sub>	0.1485	0.0000	0.0000

**Table 6.8: Phase behavior calculations for C<sub>1</sub>-C<sub>5</sub> tie-line of Fig. 6.24**

	Z (Overall composition) mole%	x (mole%)		y (mole%)		v (mole fraction)	
		Fig. 6.24	This work	Fig. 6.24	This work	Fig. 6.24	This work
CO <sub>2</sub>	0.00	0	0	0.00	0.00	0.0000	7.0E-4
C <sub>1</sub>	30.00	30	30	4.70	4.76		
C <sub>5</sub>	70.00	70	70	95.30	95.24		
CO <sub>2</sub>	0.00	0	0	0.00	0.00	0.1544	0.1539
C <sub>1</sub>	40.00	30	30	4.70	4.76		
C <sub>5</sub>	60.00	70	70	95.30	95.24		
CO <sub>2</sub>	0.00	0	0	0.00	0.00	0.3089	0.3070
C <sub>1</sub>	50.00	30	30	4.70	4.76		
C <sub>5</sub>	50.00	70	70	95.30	95.24		
CO <sub>2</sub>	0.00	0	0	0.00	0.00	0.4634	0.4602
C <sub>1</sub>	60.00	30	30	4.70	4.76		
C <sub>5</sub>	40.00	70	70	95.30	95.24		
CO <sub>2</sub>	0.00	0	0	0.00	0.00	0.6097	0.6134
C <sub>1</sub>	70.00	30	30	4.70	4.76		
C <sub>5</sub>	30.00	70	70	95.30	95.24		
CO <sub>2</sub>	0.00	0	0	0.00	0.00	0.7642	0.7665
C <sub>1</sub>	80.00	30	30	4.70	4.76		
C <sub>5</sub>	20.00	70	70	95.30	95.24		
CO <sub>2</sub>	0.00	0	0	0.00	0.00	0.9186	0.9197
C <sub>1</sub>	90.00	30	30	4.70	4.76		
C <sub>5</sub>	10.00	70	70	95.30	95.24		
CO <sub>2</sub>	0.00	0	0	0.00	0.00	1.0000	0.9999
C <sub>1</sub>	4.76	30	30	4.70	4.76		
C <sub>5</sub>	95.24	70	70	95.30	95.24		

**Table 6.9: Phase behavior calculations for CO<sub>2</sub>-C<sub>5</sub> tie-line of Fig. 6.24**

	Z (Overall composition) mole%	x (mole%)		y (mole%)		v (mole fraction)	
		Fig. 6.24	This work	Fig. 6.24	This work	Fig. 6.24	This work
CO <sub>2</sub>	76.60	76.6	76.6	95.6	95.58	0.0000	9.0E-5
C <sub>1</sub>	0.00	0.0	0.0	0.0	0.0		
C <sub>5</sub>	23.40	23.4	23.4	4.4	4.42		
CO <sub>2</sub>	85.00	76.6	76.6	95.6	95.58	0.4430	0.4425
C <sub>1</sub>	0.00	0.0	0.0	0.0	0.0		
C <sub>5</sub>	15.00	23.4	23.4	4.4	4.42		
CO <sub>2</sub>	90.00	76.6	76.6	95.6	95.58	0.7030	0.7059
C <sub>1</sub>	10.00	0.0	0.0	0.0	0.0		
C <sub>5</sub>	0.00	23.4	23.4	4.4	4.42		
CO <sub>2</sub>	95.58	76.6	76.6	95.6	95.6	1.0000	0.9997
C <sub>1</sub>	0.00	0.0	0.0	0.0	0.0		
C <sub>5</sub>	4.42	23.4	23.4	4.4	4.4		

**Table 6.10: Phase behavior calculations for tie-line 1 of Fig. 6.24**

	Z (Overall composition) mole%	x (mole%)		y (mole%)		v (mole fraction)	
		Fig. 6.24	This work	Fig. 6.24	This work	Fig. 6.24	This work
CO <sub>2</sub>	8.0	8.00	8.00	15.00	15.19	0.0000	6.3E-4
C <sub>1</sub>	25.5	25.50	25.47	80.00	80.07		
C <sub>5</sub>	66.5	66.50	66.54	5.00	4.74		
CO <sub>2</sub>	10.0	8.00	8.06	15.00	15.32	0.2615	0.2673
C <sub>1</sub>	40.0	25.50	25.43	80.00	79.95		
C <sub>5</sub>	50.0	66.50	66.51	5.00	4.74		
CO <sub>2</sub>	15.0	8.00	8.23	15.00	15.63	0.9170	0.9147
C <sub>1</sub>	75.0	25.50	25.34	80.00	79.63		
C <sub>5</sub>	10.0	66.50	66.43	5.00	4.74		
CO <sub>2</sub>	15.0	8.00	7.94	15.00	15.03	1.0000	0.9958
C <sub>1</sub>	80.0	25.50	25.51	80.00	80.23		
C <sub>5</sub>	5.0	66.50	66.58	5.00	4.74		

**Table 6.11: Phase behavior calculations for tie-line 2 of Fig. 6.24**

	Z (Overall composition) mole%	x (mole%)		y (mole%)		v (mole fraction)	
		Fig. 6.24	This work	Fig. 6.24	This work	Fig. 6.24	This work
CO <sub>2</sub>	16.0	16.00	15.98	30.00	29.66	0.0000	1.2E-3
C <sub>1</sub>	21.1	21.10	21.25	65.30	65.63		
C <sub>5</sub>	62.9	62.90	62.77	4.70	4.71		
CO <sub>2</sub>	20.0	16.00	15.84	30.00	29.40	0.3060	0.3070
C <sub>1</sub>	35.0	21.10	21.32	65.30	65.89		
C <sub>5</sub>	45.0	62.90	62.84	4.70	4.71		
CO <sub>2</sub>	25.0	16.00	16.07	30.00	29.80	0.6480	0.6500
C <sub>1</sub>	50.0	21.10	21.20	65.30	65.48		
C <sub>5</sub>	25.0	62.90	62.73	4.70	4.71		
CO <sub>2</sub>	30.0	16.00	16.21	30.00	30.00	1.0000	1.0000
C <sub>1</sub>	65.3	21.10	21.19	65.30	65.3		
C <sub>5</sub>	4.7	62.90	62.60	4.70	4.70		

**Table 6.12: Phase behavior calculations for tie-line 3 of Fig. 6.24**

	Z (Overall composition) mole%	x (mole%)		y (mole%)		v (mole fraction)	
		Fig. 6.24	This work	Fig. 6.24	This work	Fig. 6.24	This work
CO <sub>2</sub>	24.0	24.00	23.91	43.00	43.02	0.0000	4.6E-3
C <sub>1</sub>	17.5	17.50	17.34	52.30	52.3		
C <sub>5</sub>	58.5	58.50	58.75	4.70	4.69		
CO <sub>2</sub>	30.0	24.00	23.42	43.0	42.22	0.3480	0.3499
C <sub>1</sub>	30.0	17.50	17.57	52.30	53.09		
C <sub>5</sub>	40.0	58.50	59.01	4.70	4.69		
CO <sub>2</sub>	35.0	24.00	23.28	43.00	41.99	0.6236	0.6266
C <sub>1</sub>	40.0	17.50	17.64	52.30	53.32		
C <sub>5</sub>	25.0	58.50	59.08	4.70	4.69		
CO <sub>2</sub>	43.0	24.00	23.91	43.00	43.00	1.0000	0.9998
C <sub>1</sub>	52.3	17.50	17.34	52.30	52.31		
C <sub>5</sub>	4.7	58.50	58.75	4.70	4.69		

**Table 6.13: Phase behavior calculations for tie-line 4 of Fig. 6.24**

	Z (Overall composition) mole%	x (mole%)		y (mole%)		v (mole fraction)	
		Fig. 6.24	This work	Fig. 6.24	This work	Fig. 6.24	This work
CO <sub>2</sub>	30.5	30.50	30.39	53.00	53.02	0.0000	4.7E-3
C <sub>1</sub>	14.5	14.50	14.37	42.30	42.32		
C <sub>5</sub>	55.0	55.00	55.24	4.70	4.66		
CO <sub>2</sub>	35.0	30.50	30.42	53.00	53.06	0.2000	0.2000
C <sub>1</sub>	20.0	14.50	14.36	42.30	42.27		
C <sub>5</sub>	45.0	55.00	55.22	4.70	4.66		
CO <sub>2</sub>	40.0	30.50	30.93	53.00	53.8	0.3960	0.3960
C <sub>1</sub>	25.0	14.50	14.14	42.30	41.54		
C <sub>5</sub>	35.0	55.00	54.93	4.70	4.66		
CO <sub>2</sub>	53.0	30.50	30.4	53.00	53.02	1.0000	0.9993
C <sub>1</sub>	42.3	14.50	14.37	42.30	42.32		
C <sub>5</sub>	4.7	55.00	55.23	4.70	4.66		

**Table 6.14: Phase behavior calculations for tie-line 5 of Fig. 6.24**

	Z (Overall composition) mole%	x (mole%)		y (mole%)		v (mole fraction)	
		Fig. 6.24	This work	Fig. 6.24	This work	Fig. 6.24	This work
CO <sub>2</sub>	37.5	37.50	37.39	62.70	62.75	0.0000	4.2E-3
C <sub>1</sub>	11.5	11.50	11.41	32.60	32.61		
C <sub>5</sub>	51.0	51.00	51.20	4.70	4.64		
CO <sub>2</sub>	46.0	37.50	37.45	62.70	62.81	0.3330	0.3498
C <sub>1</sub>	19.0	11.50	11.40	32.60	32.55		
C <sub>5</sub>	35.0	51.00	51.15	4.70	4.64		
CO <sub>2</sub>	60.0	37.50	37.53	62.70	62.93	0.880	0.8846
C <sub>1</sub>	30.0	11.50	11.36	32.60	32.43		
C <sub>5</sub>	10.0	51.00	51.11	4.70	4.64		
CO <sub>2</sub>	62.7	37.50	37.38	62.70	62.86	1.0000	0.9987
C <sub>1</sub>	32.6	11.50	11.42	32.60	32.50		
C <sub>5</sub>	4.7	51.00	51.20	4.70	4.64		

**Table 6.15: Phase behavior calculations for tie-line 6 of Fig. 6.24**

	Z (Overall composition) mole%	x (mole%)		y (mole%)		v (mole fraction)	
		Fig. 6.24	This work	Fig. 6.24	This work	Fig. 6.24	This work
CO <sub>2</sub>	52.0	52.00	51.76	79.00	78.93	0.0000	8.8E-3
C <sub>1</sub>	6.3	6.30	6.21	16.50	16.49		
C <sub>5</sub>	41.7	41.70	42.03	4.50	4.58		
CO <sub>2</sub>	61.0	52.00	52.57	79.00	79.67	0.3060	0.3109
C <sub>1</sub>	9.0	6.30	5.96	16.50	15.74		
C <sub>5</sub>	30.0	41.70	41.47	4.50	4.58		
CO <sub>2</sub>	75.0	52.00	51.77	79.00	78.93	0.8468	0.8553
C <sub>1</sub>	15.0	6.30	6.21	16.50	16.49		
C <sub>5</sub>	10.0	41.70	42.02	4.50	4.58		
CO <sub>2</sub>	79.0	52.00	52.73	79.00	79.00	1.0000	1.0000
C <sub>1</sub>	16.5	6.30	6.28	16.50	16.50		
C <sub>5</sub>	4.5	41.70	40.99	4.50	4.50		

**Table 6.16: Phase behavior calculations for tie-line 7 of Fig. 6.24**

	Z (Overall composition) mole%	x (mole%)		y (mole%)		v (mole fraction)	
		Fig. 6.24	This work	Fig. 6.24	This work	Fig. 6.24	This work
CO <sub>2</sub>	60.0	60.00	59.98	85.50	85.84	0.0000	8.3E-4
C <sub>1</sub>	3.8	3.80	3.80	10.00	9.61		
C <sub>5</sub>	36.2	36.20	36.23	4.50	4.55		
CO <sub>2</sub>	65.0	60.00	59.86	85.50	85.74	0.2000	0.1985
C <sub>1</sub>	5.0	3.80	3.83	10.00	9.71		
C <sub>5</sub>	30.0	36.20	36.30	4.50	4.55		
CO <sub>2</sub>	80.0	60.00	59.16	85.50	85.20	0.7910	0.8000
C <sub>1</sub>	9.0	3.80	4.03	10.00	10.24		
C <sub>5</sub>	11.0	36.20	36.82	4.50	4.55		
CO <sub>2</sub>	85.5	60.00	60.25	85.50	85.50	1.0000	1.0000
C <sub>1</sub>	10.0	3.80	3.97	10.00	10.00		
C <sub>5</sub>	4.5	36.20	35.79	4.50	4.50		

**Table 6.17: Phase behavior calculations for tie-line 8 of Fig. 6.24**

	Z (Overall composition) mole%	x (mole%)		y (mole%)		v (mole fraction)	
		Fig. 6.24	This work	Fig. 6.24	This work	Fig. 6.24	This work
CO <sub>2</sub>	67.6	67.60	67.33	91.00	90.73	0.0000	1.2E-2
C <sub>1</sub>	2.0	2.00	1.97	4.50	4.76		
C <sub>5</sub>	30.4	30.40	30.70	4.50	4.51		
CO <sub>2</sub>	75.0	67.60	67.09	91.00	90.58	0.3261	0.3367
C <sub>1</sub>	3.0	2.00	2.03	4.50	4.91		
C <sub>5</sub>	22.0	30.40	30.88	4.50	4.51		
CO <sub>2</sub>	85.0	67.60	67.50	91.00	90.81	0.7500	0.7508
C <sub>1</sub>	4.0	2.00	1.94	4.50	4.68		
C <sub>5</sub>	11.0	30.40	30.57	4.50	4.51		
CO <sub>2</sub>	91.0	67.60	67.88	91.00	91.00	1.0000	1.0000
C <sub>1</sub>	4.5	2.00	1.87	4.50	4.50		
C <sub>5</sub>	4.5	30.40	30.25	4.50	4.50		

**Table 6.18: Phase behavior calculations for tie-line 9 of Fig. 6.24**

	Z (Overall composition) mole%	x (mole%)		y (mole%)		v (mole fraction)	
		Fig. 6.24	This work	Fig. 6.24	This work	Fig. 6.24	This work
CO <sub>2</sub>	72.0	72.00	71.79	93.00	93.21	0.0000	9.7E-3
C <sub>1</sub>	1.0	1.00	1.00	2.50	2.32		
C <sub>5</sub>	27.0	27.00	27.22	4.50	4.47		
CO <sub>2</sub>	80.0	72.00	71.79	93.00	93.21	0.3750	0.3834
C <sub>1</sub>	1.5	1.00	0.99	2.50	2.32		
C <sub>5</sub>	18.5	27.00	27.22	4.50	4.47		
CO <sub>2</sub>	90.0	72.00	71.06	93.00	92.82	0.8625	0.8704
C <sub>1</sub>	2.5	1.00	1.14	2.50	2.70		
C <sub>5</sub>	7.5	27.00	27.8	4.50	4.48		
CO <sub>2</sub>	93.0	72.00	71.44	93.00	93.02	1.0000	0.9989
C <sub>1</sub>	2.5	1.00	1.06	2.50	2.50		
C <sub>5</sub>	4.5	27.00	27.49	4.50	4.47		

**Table 6.19: Calculating initial total mole of methane and pentane in the core in CO<sub>2</sub> injection experiment**

Core thickness (m)	3.19E-02
Core width (m)	3.19E-02
Core length (m)	3.57E-01
Porosity	4.00E-01
Pore volume (m <sup>3</sup> )	1.46E-04
C <sub>1</sub> initial mole fraction	0.28
C <sub>5</sub> initial mole fraction	0.72
MW C <sub>1</sub>	16.04
MW C <sub>5</sub>	72.15
MW CO <sub>2</sub>	44.01
MW oil	56.44
Oil density (kg/m <sup>3</sup> )	566.87
Oil density (mole/m <sup>3</sup> )	10.04
Oil saturation (S <sub>o</sub> )	0.89
Oil initial total mole	1.30E-03
C <sub>1</sub> initial total mole	3.65E-04
C <sub>5</sub> initial total mole	9.37E-04

**Table 6.20 : Calculating total mole of methane and pentane in the core at 95 days in CO<sub>2</sub> injection experiment**

Recovery C <sub>1</sub> (%)	93
Recovery C <sub>5</sub> (%)	65
C <sub>1</sub> total mole remained in the core	9.11E-05
C <sub>5</sub> total mole remained in the core	3.28E-04

**Table 6.21: Calculating average oil and gas saturation at 95 day in CO<sub>2</sub> injection experiment when highest value of density used for oil and gas**

Oil density (mole/m <sup>3</sup> )	12.21
Gas density (mole/m <sup>3</sup> )	4.05
Total mole in the core	0.001298
Mole of CO <sub>2</sub> in the core	0.000878
C <sub>1</sub> mole fraction	0.070
C <sub>5</sub> mole fraction	0.253
CO <sub>2</sub> mole fraction	0.677
Average S <sub>o</sub> (%)	30
Average S <sub>g</sub> (%)	59

**Table 6.22: Calculating average oil and gas saturation at 95 day in CO<sub>2</sub> injection experiment when lowest value of density used for oil and gas**

Oil density (mole/m <sup>3</sup> )	10.54
Gas density (mole/m <sup>3</sup> )	3.15
Total mole in the core	0.001108
Mole of CO <sub>2</sub> in the core	0.000689
C <sub>1</sub> mole fraction	0.082
C <sub>5</sub> mole fraction	0.296
CO <sub>2</sub> mole fraction	0.622
Average S <sub>o</sub> (%)	37
Average S <sub>g</sub> (%)	52

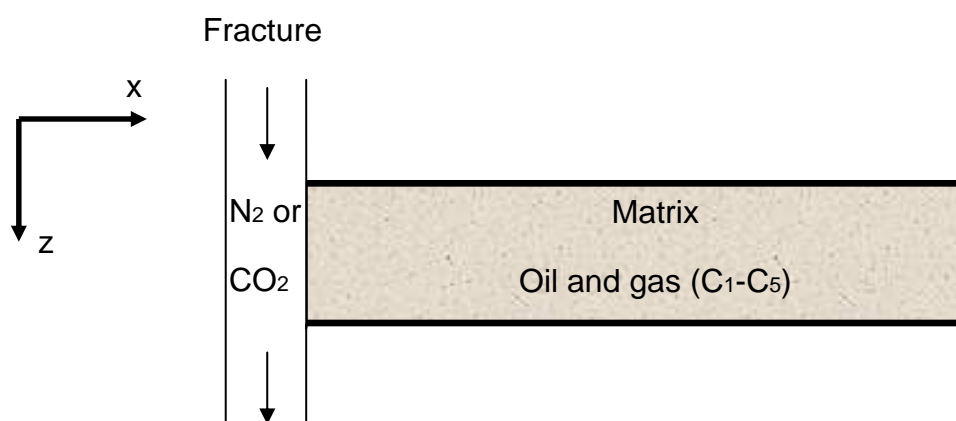


**Fig. 6.1: Diffusion experiment layout (Morel et al. (1990))**



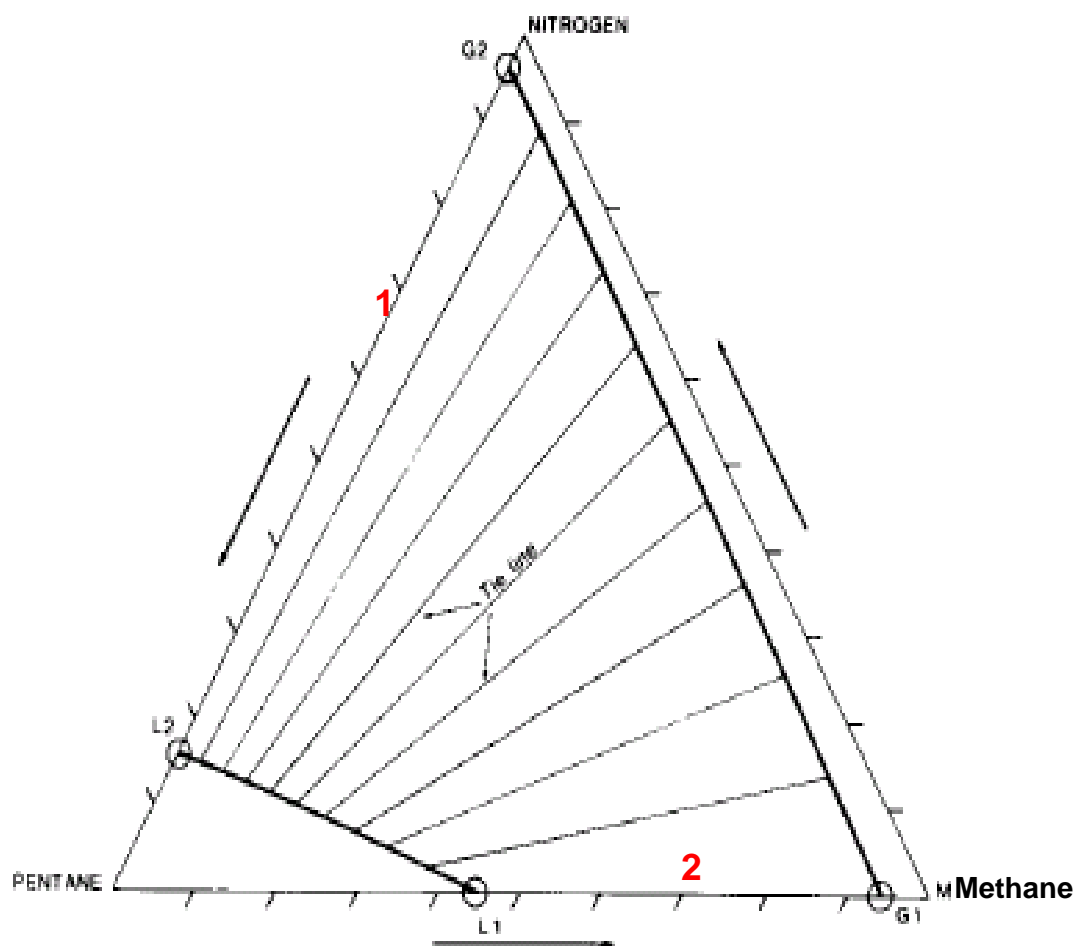


**Fig. 6.2: Ternary diagram for methane-pentane-nitrogen at 1479 psi and 38.5°C (Morel et al. (1990))**

Fig. 6.3: Calculated and experimental  $C_1$  and  $C_5$  recoveries in  $N_2$  injection experiment

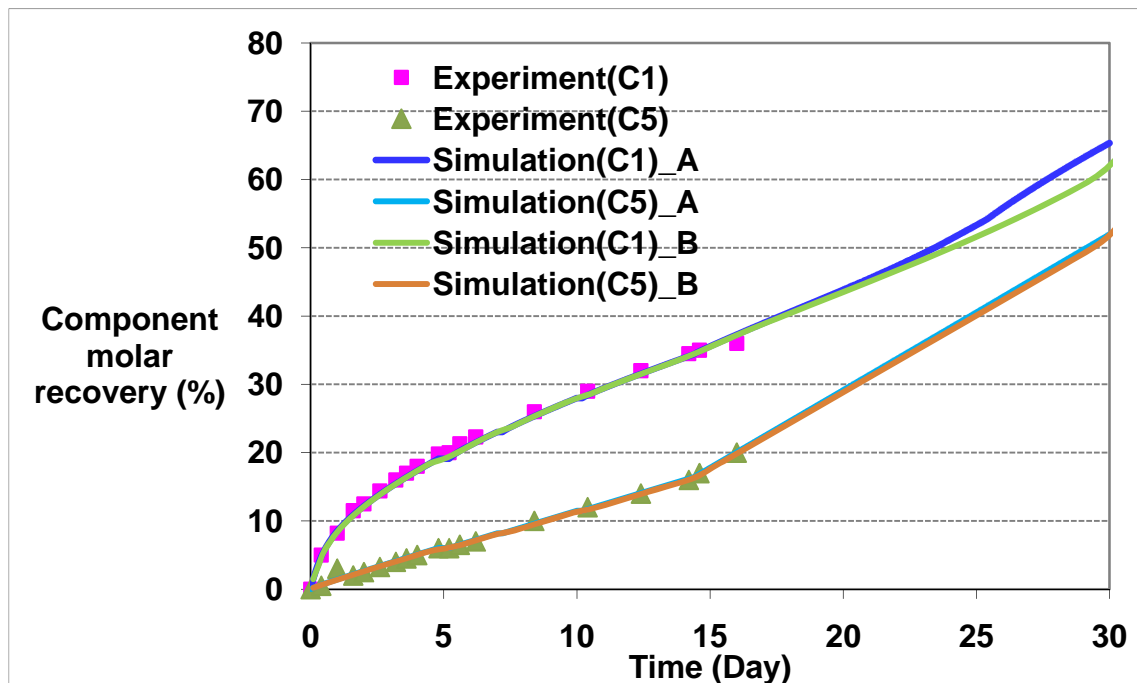


Fig. 6.4: Gas saturation at  $t = 4$  day in  $N_2$  injection experiment

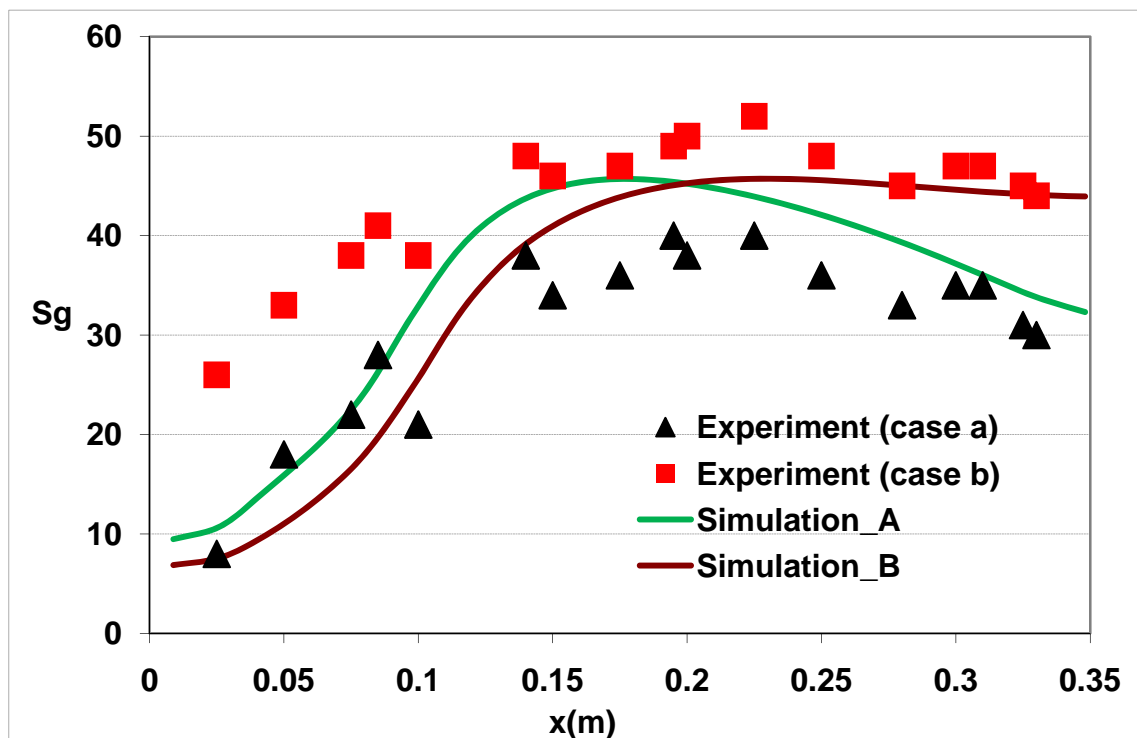


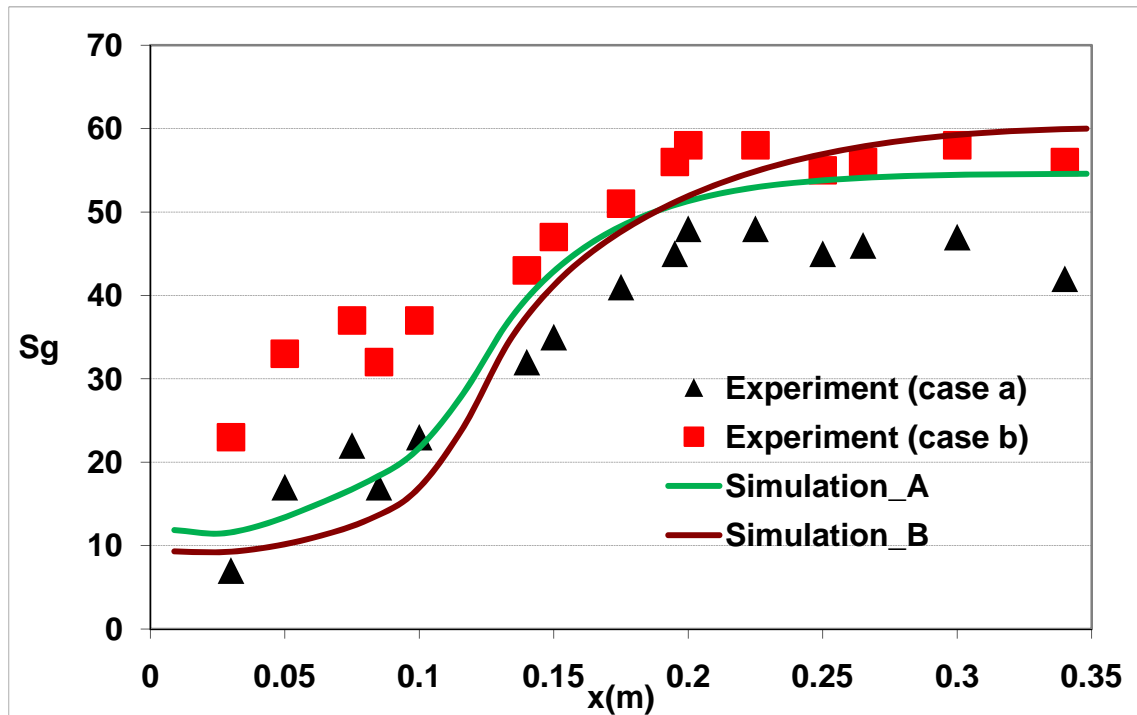
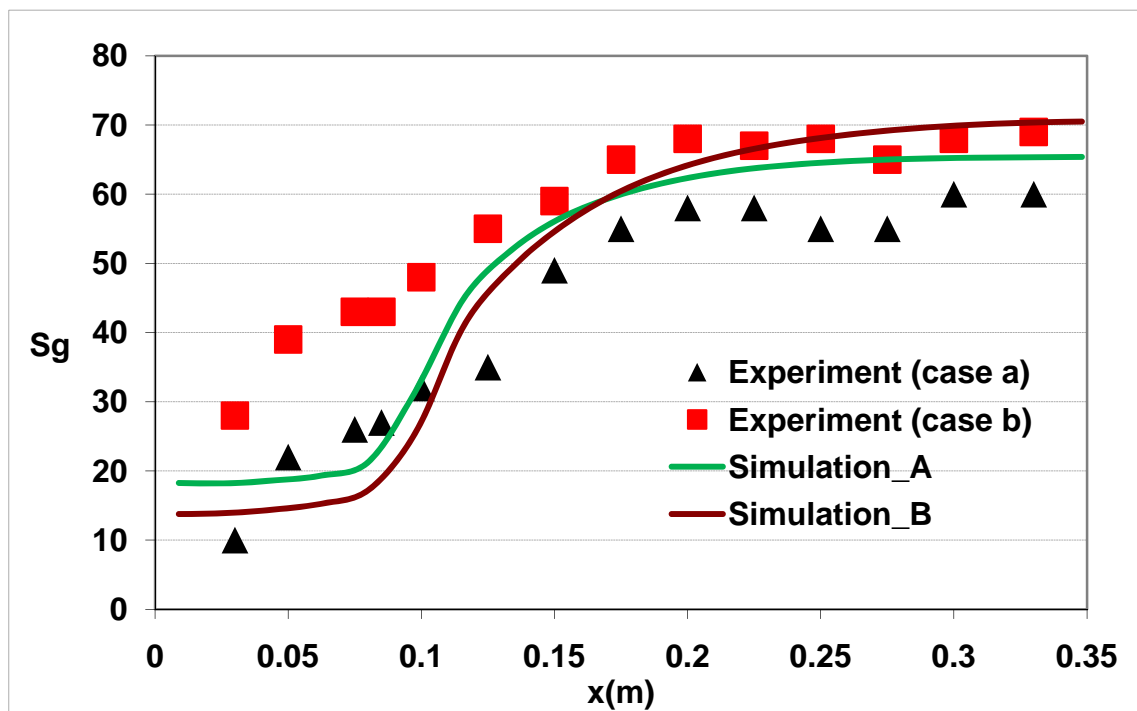
Fig. 6.5: Gas saturation at  $t = 8$  day in  $N_2$  diffusion experimentFig. 6.6: Gas saturation at  $t = 16$  day in  $N_2$  diffusion experiment

Fig. 6.7: Calculated  $N_2$  mass-transfer rates at fracture-matrix surface in  $N_2$  injection experiment

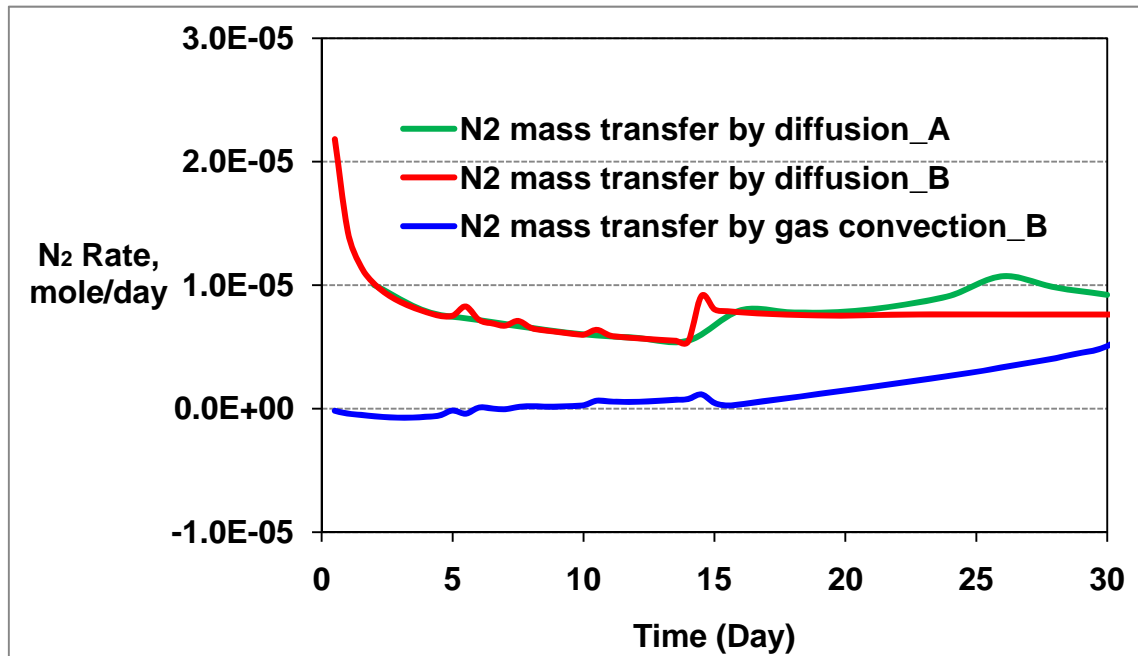


Fig. 6.8: Calculated  $C_1$  mass-transfer rates at fracture-matrix surface in  $N_2$  injection experiment

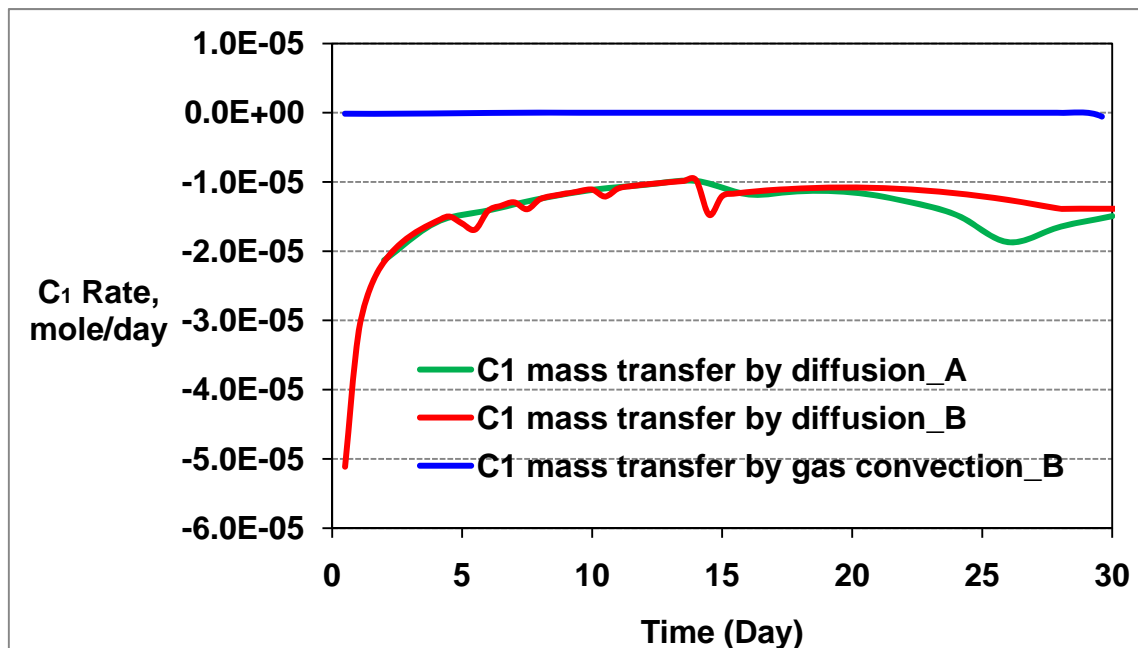


Fig. 6.9: Calculated  $C_5$  mass-transfer rates at fracture-matrix surface in  $N_2$  injection experiment

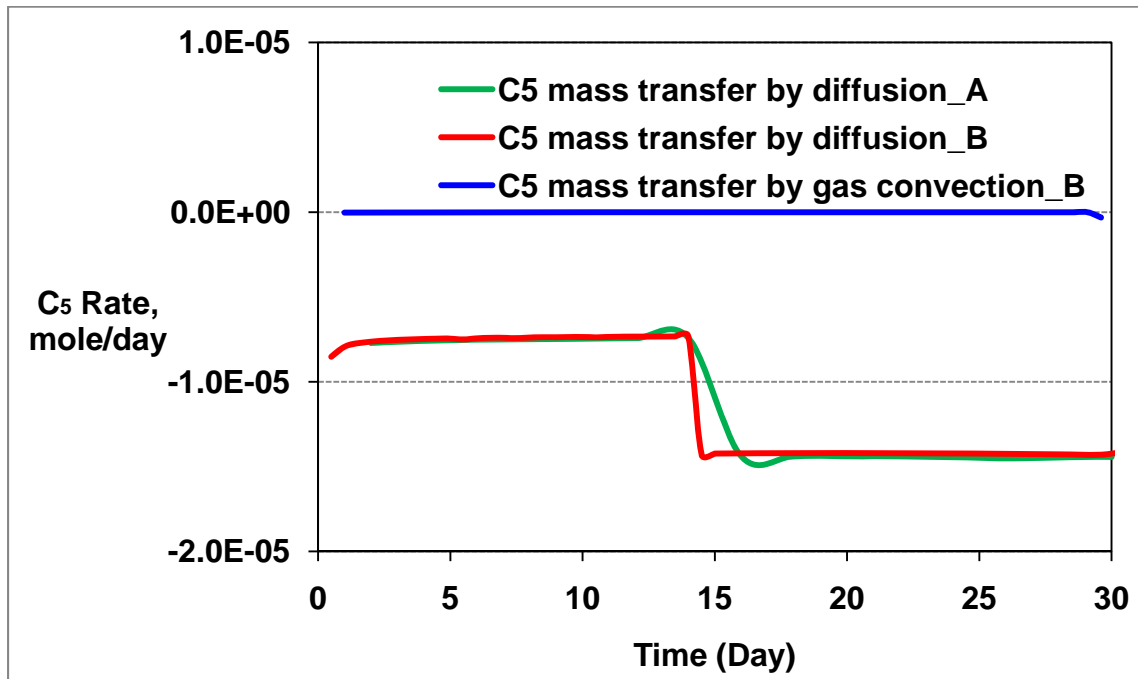


Fig. 6.10: Oil pressure distribution in  $N_2$  injection experiment (A)

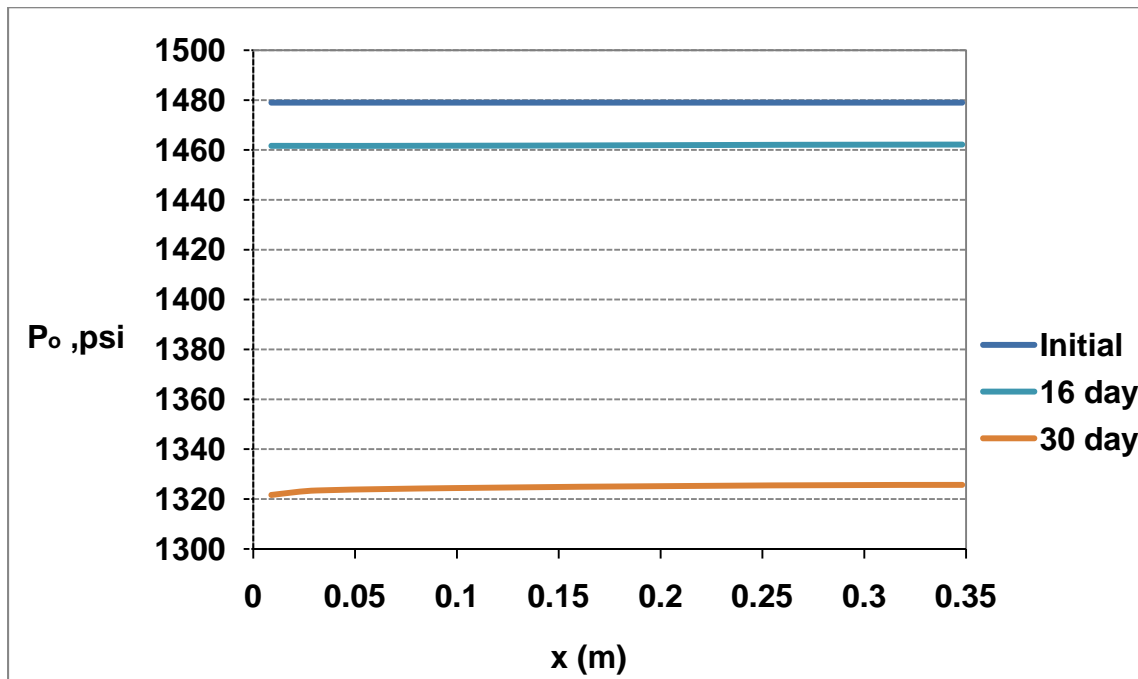


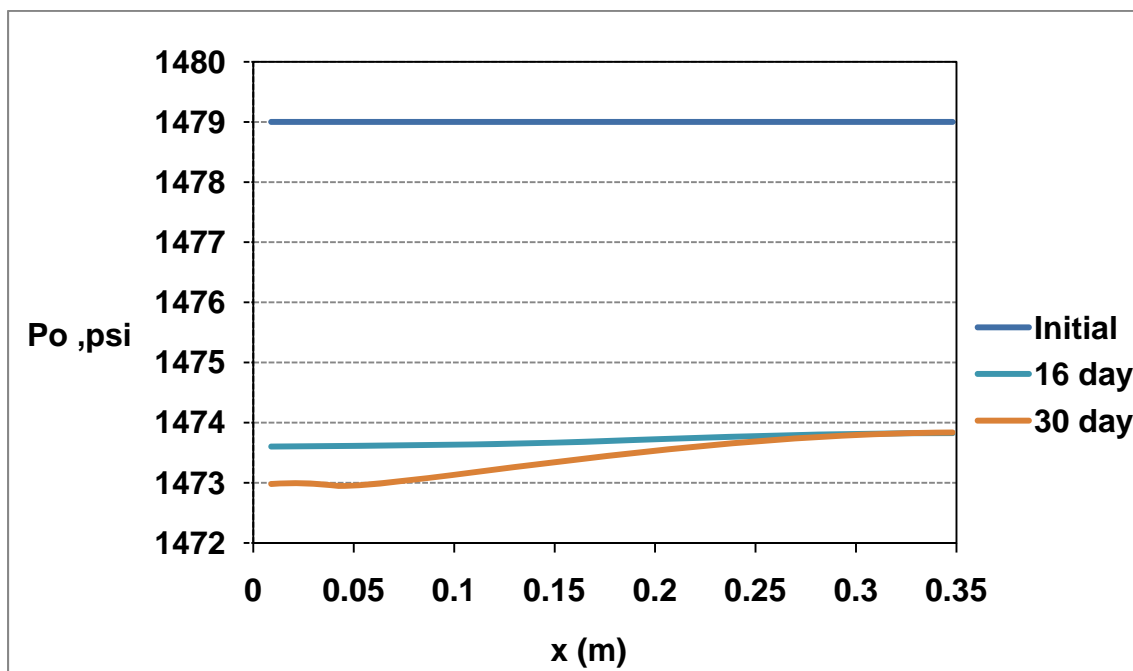
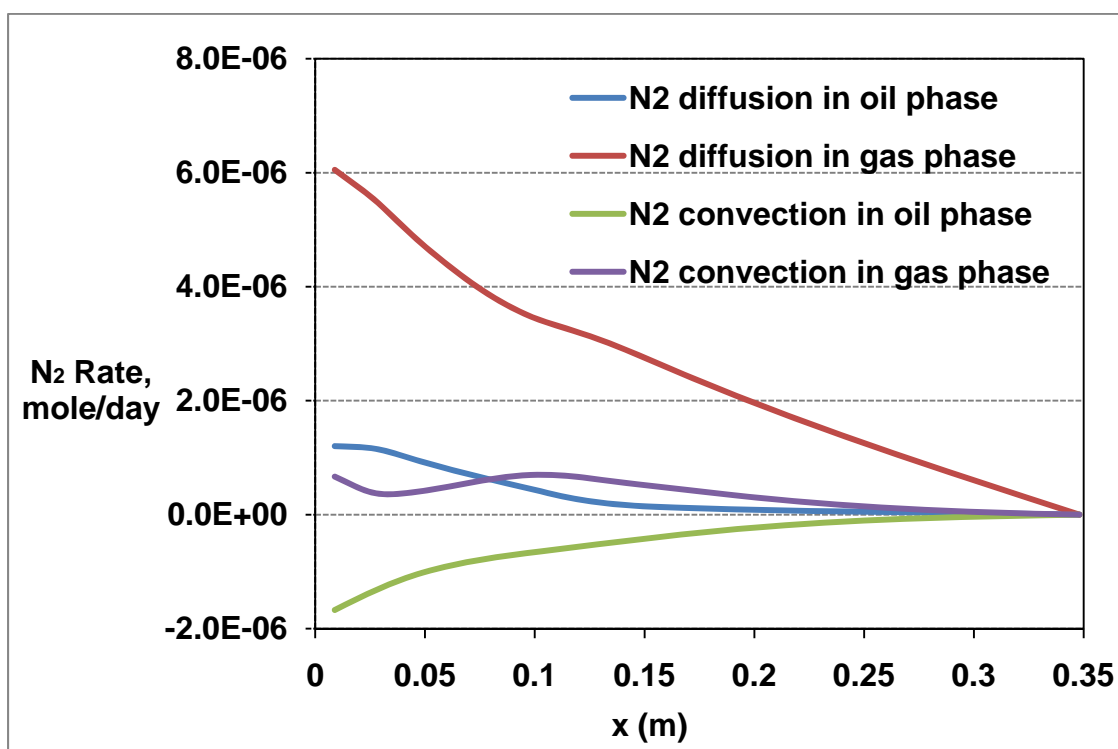
Fig. 6.11: Oil pressure distribution in N<sub>2</sub> injection experiment (B)Fig. 6.12: Calculated local N<sub>2</sub> rates inside the matrix at t = 8 day for N<sub>2</sub> injection experiment (A)

Fig. 6.13: Calculated local  $N_2$  rates inside the matrix at  $t = 8$  day for  $N_2$  injection experiment (B)

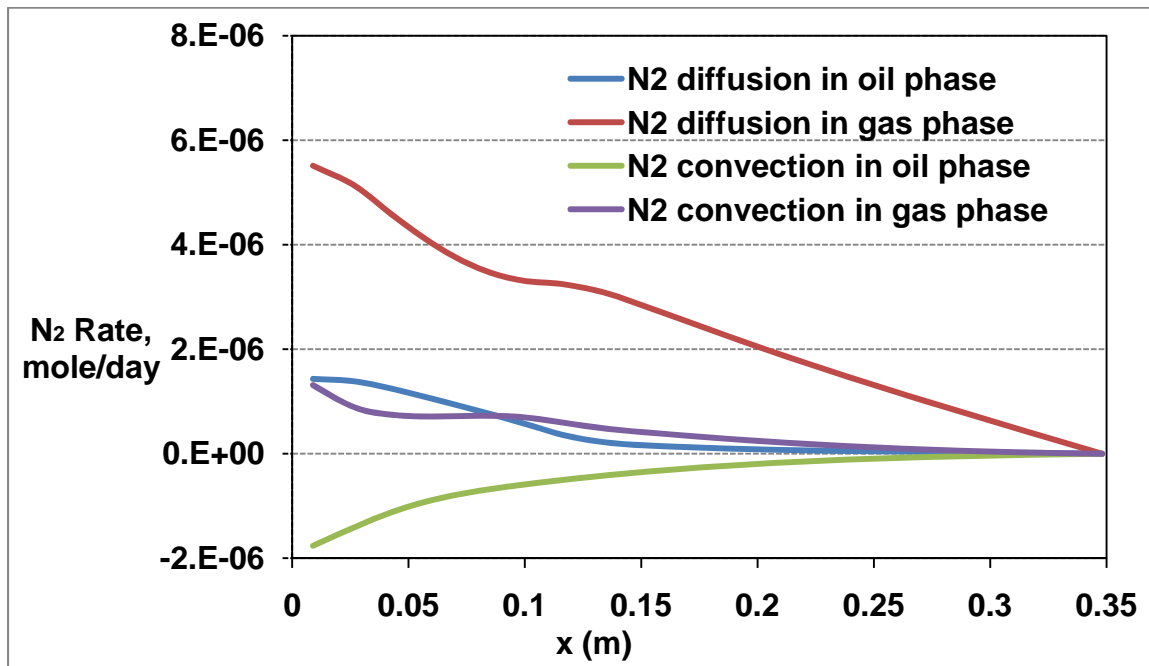


Fig. 6.14: Calculated local  $N_2$  rates inside the matrix at  $t = 28$  day for  $N_2$  injection experiment (A)

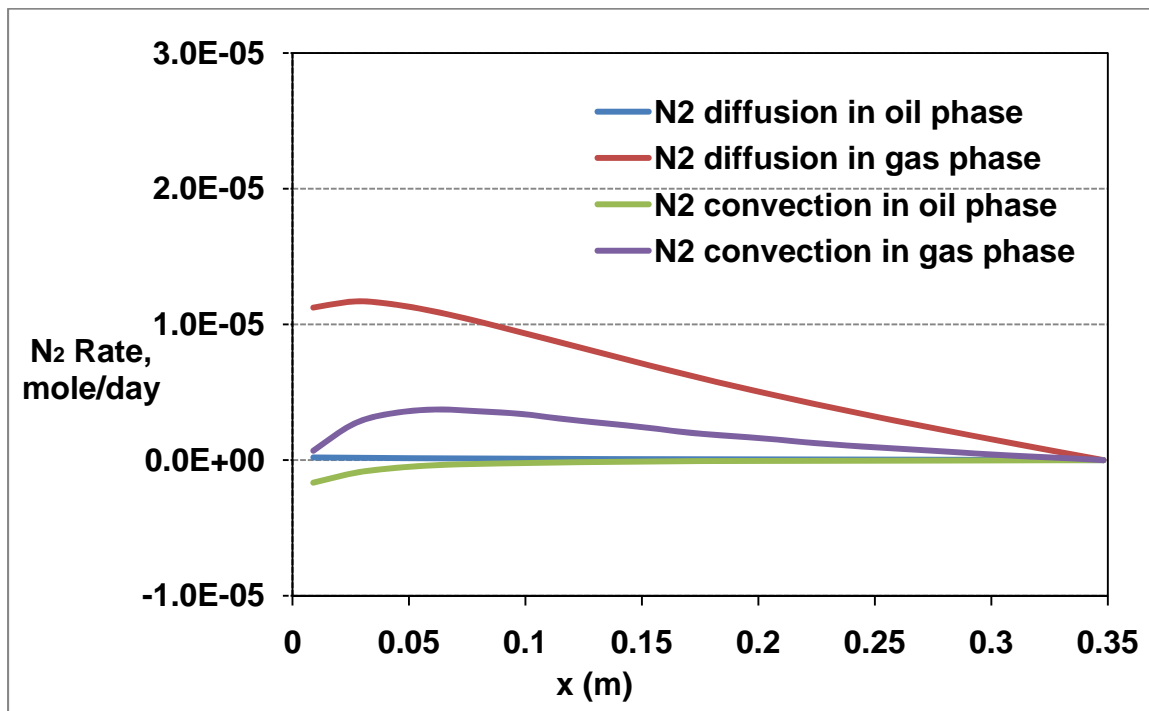


Fig. 6.15: Calculated local  $N_2$  rates inside the matrix at  $t = 28$  day for  $N_2$  injection experiment (B)

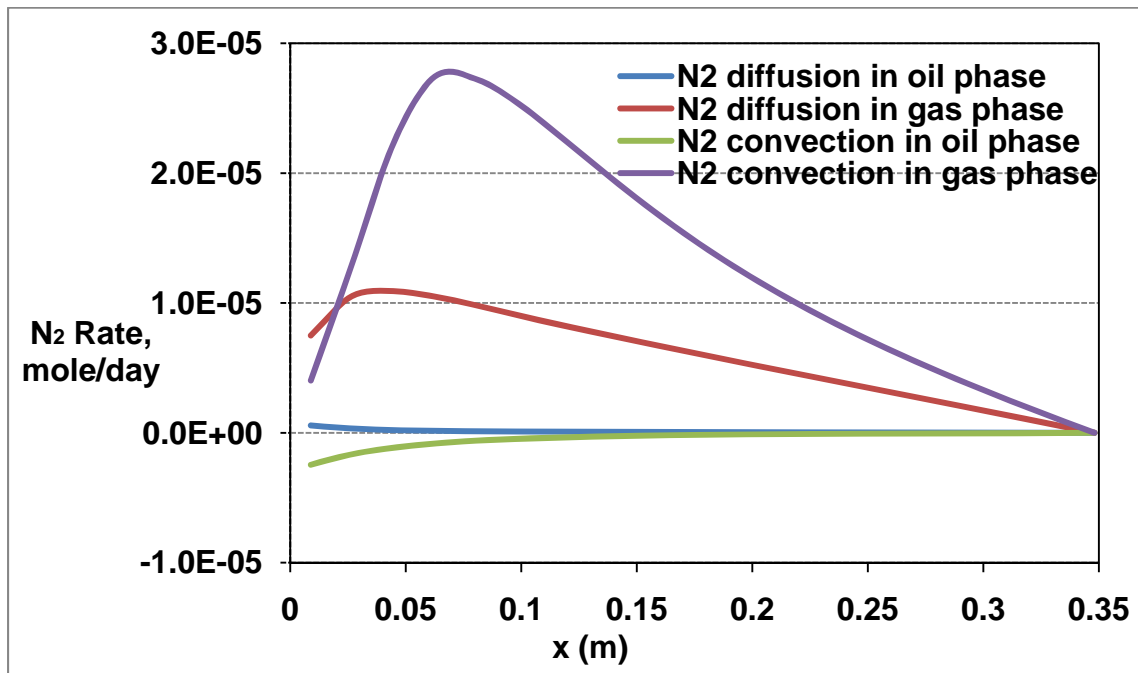


Fig. 6.16: Calculated local  $C_1$  rates inside the matrix at  $t = 8$  day for  $N_2$  injection experiment (A)

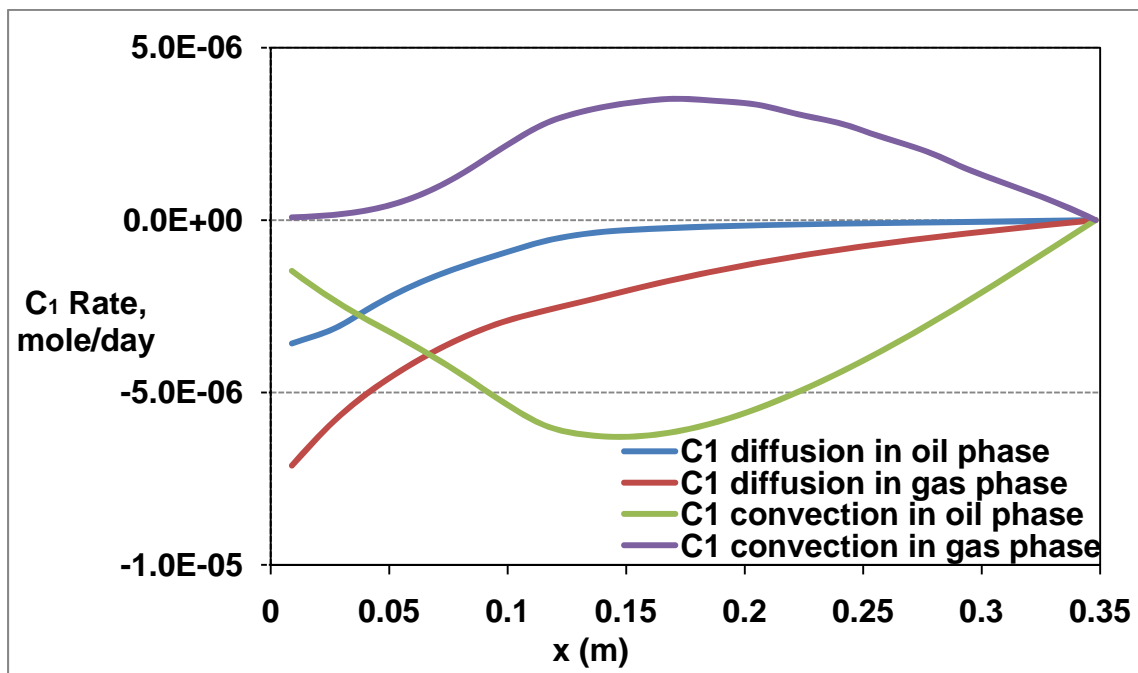




Fig. 6.17: Calculated local  $C_1$  rates inside the matrix at  $t = 8$  day for  $N_2$  injection experiment (B)

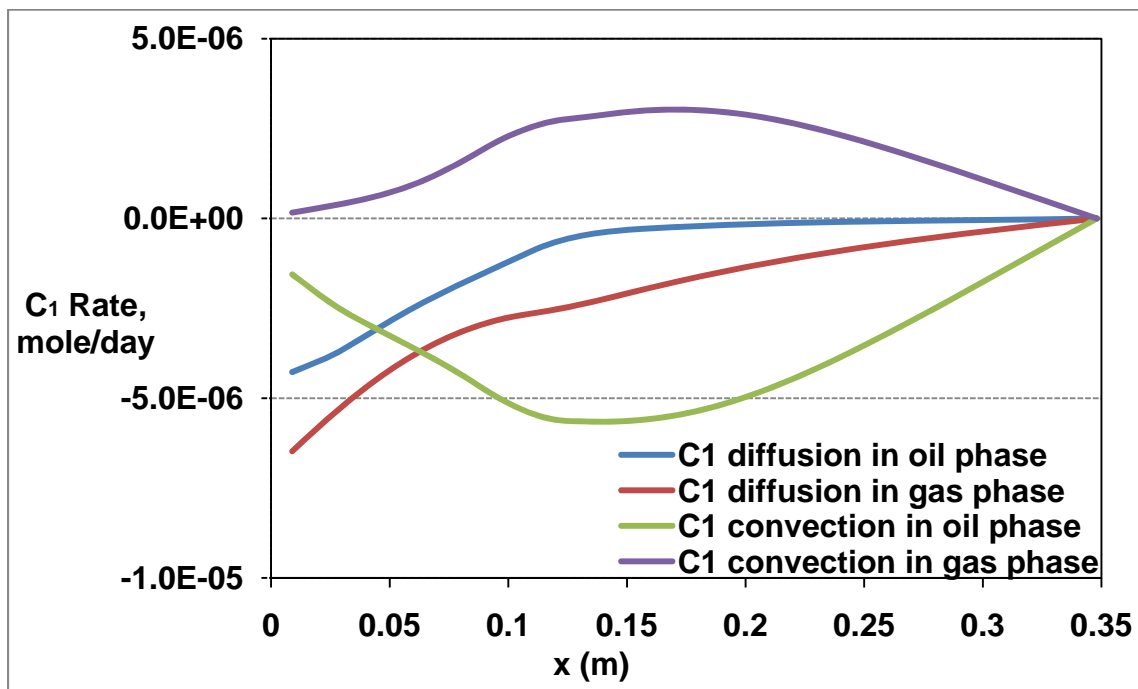


Fig. 6.18: Calculated local  $C_1$  rates inside the matrix at  $t = 28$  day for  $N_2$  injection experiment (A)

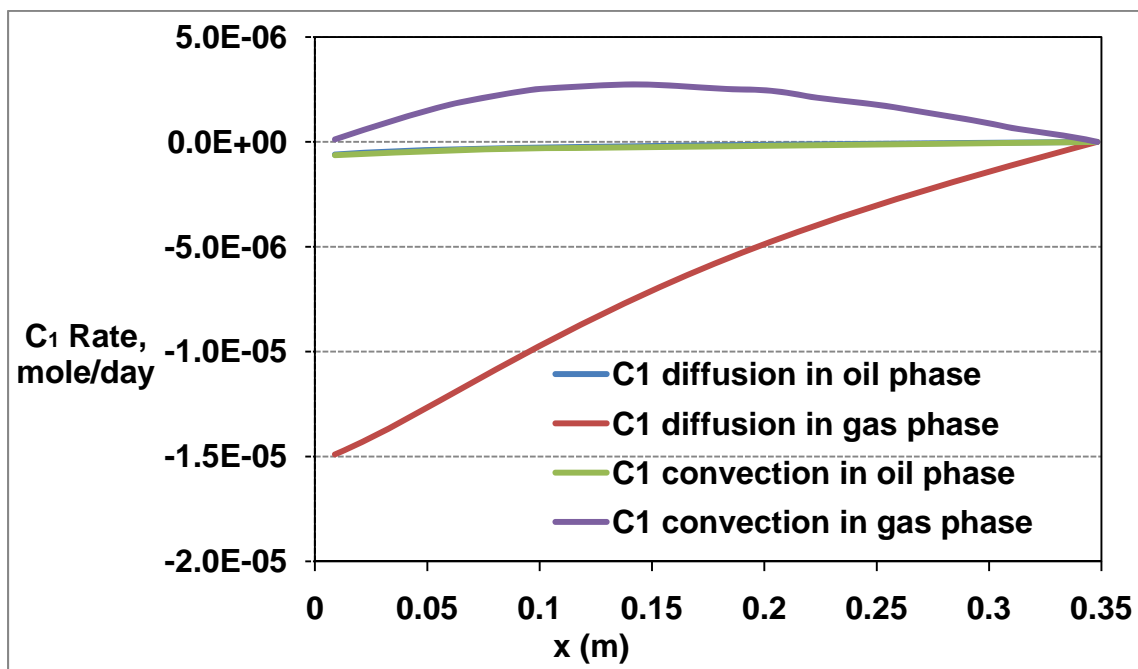


Fig. 6.19: Calculated local  $C_1$  rates inside the matrix at  $t = 28$  day for  $N_2$  injection experiment (B)

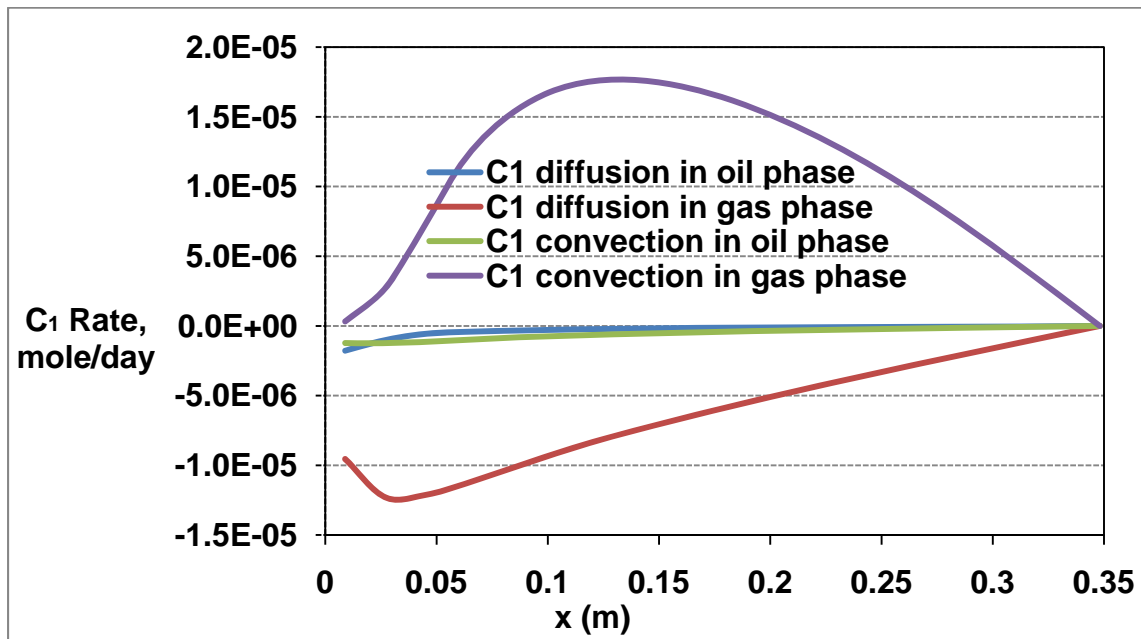


Fig. 6.20: Calculated local  $C_5$  rates inside the matrix at  $t = 8$  day for  $N_2$  injection experiment (A)

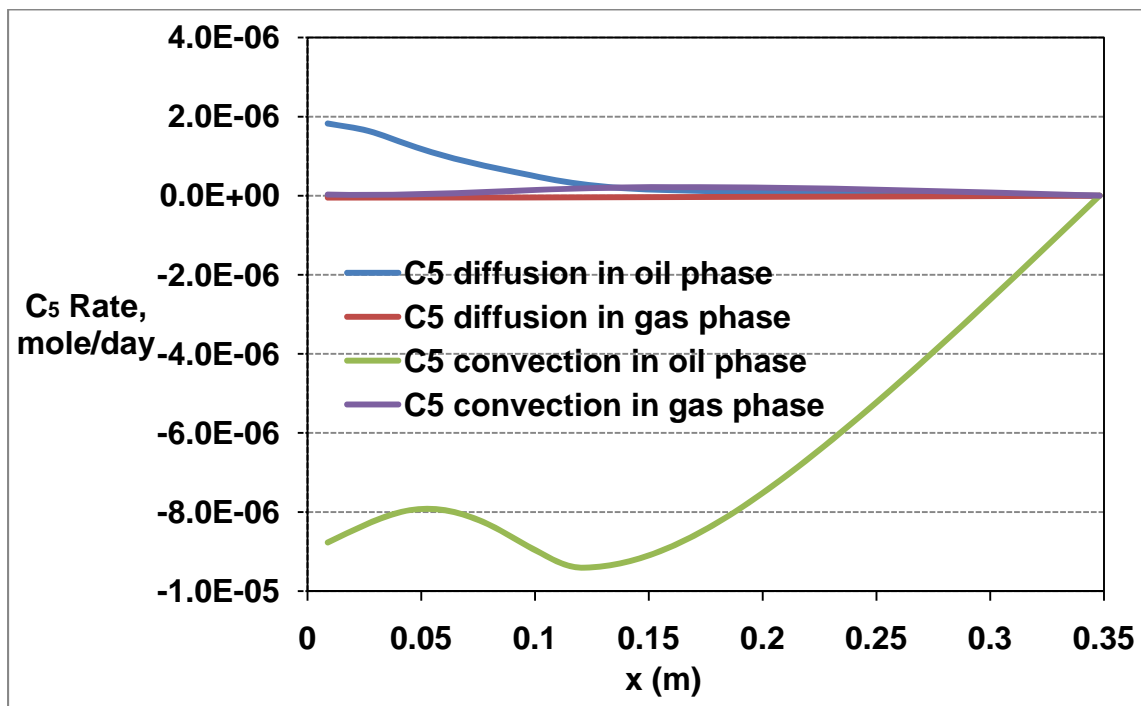


Fig. 6.21: Calculated local  $C_5$  rates inside the matrix at  $t = 8$  day for  $N_2$  injection experiment (B)

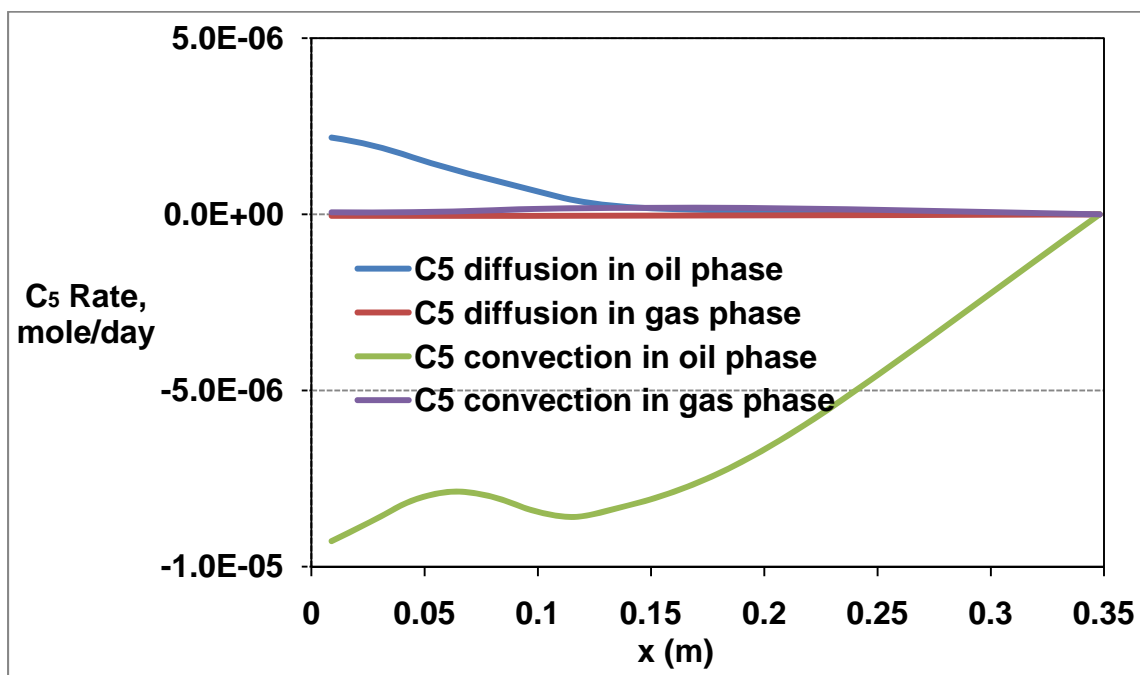


Fig. 6.22: Calculated local  $C_5$  rates inside the matrix at  $t = 28$  day for  $N_2$  injection experiment (A)

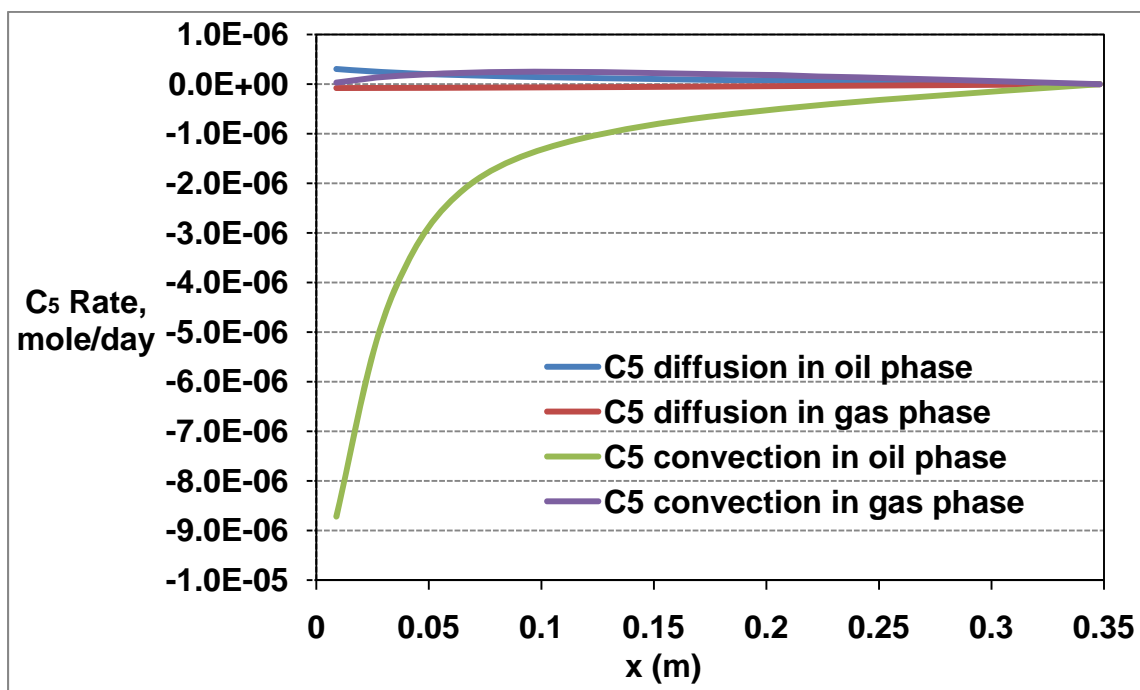
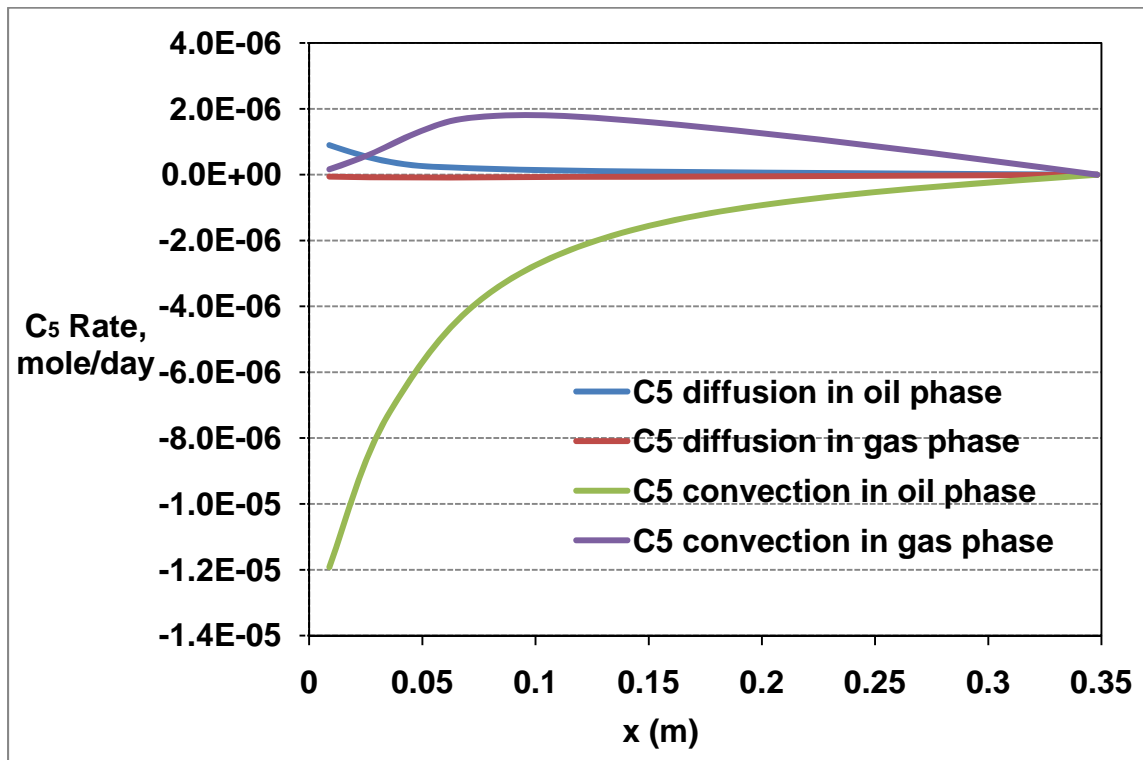
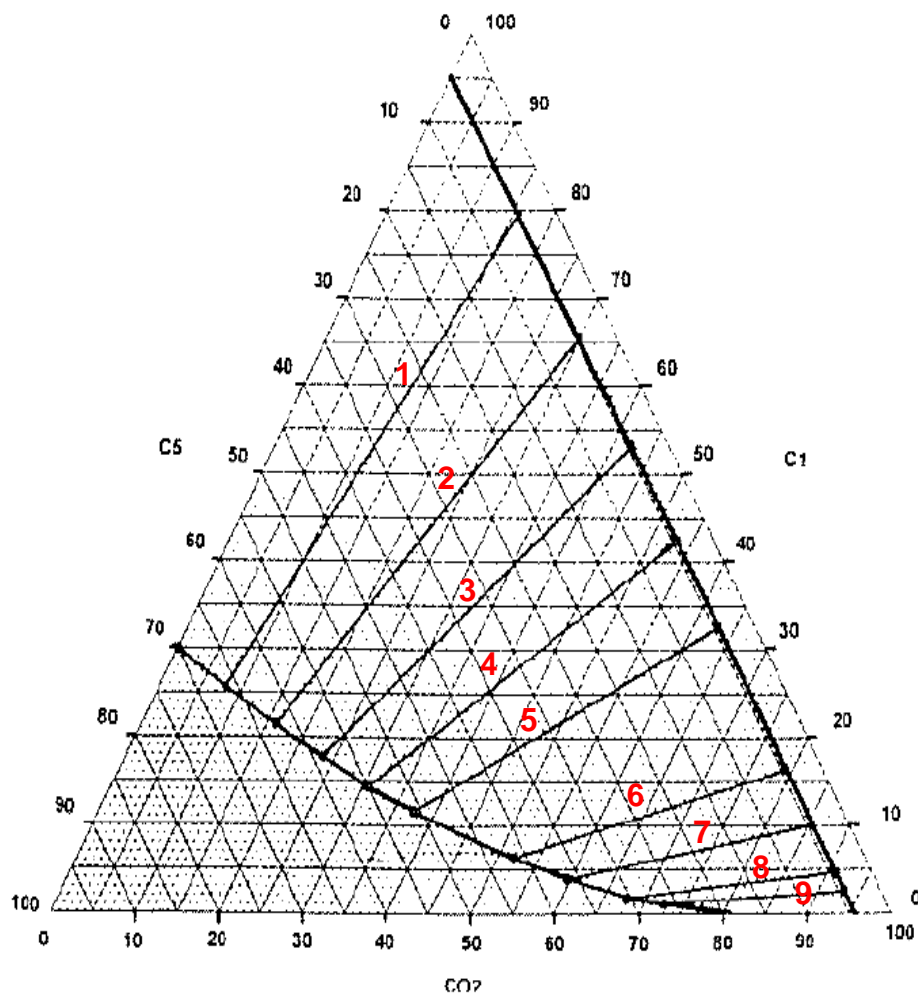


Fig. 6.23: Calculated local  $C_5$  rates inside the matrix at  $t = 28$  day for  $N_2$  injection experiment (B)





**Fig. 6.24: Ternary diagram for methane-pentane-carbon dioxide at 913.74 psi and 38.5 °C (Le Romancer et. al. (1994))**

Fig. 6.25: Calculated and experimental  $C_1$  and  $C_5$  recoveries in  $CO_2$  injection experiment

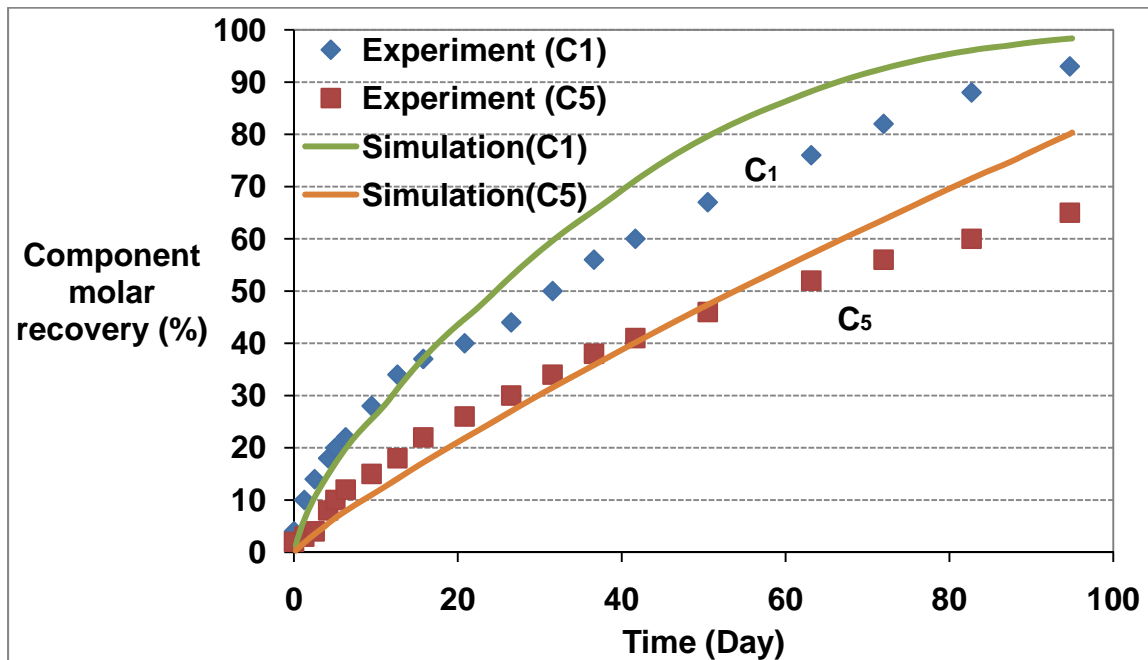


Fig. 6.26: Differential pressure between matrix and fracture in  $CO_2$  injection experiment

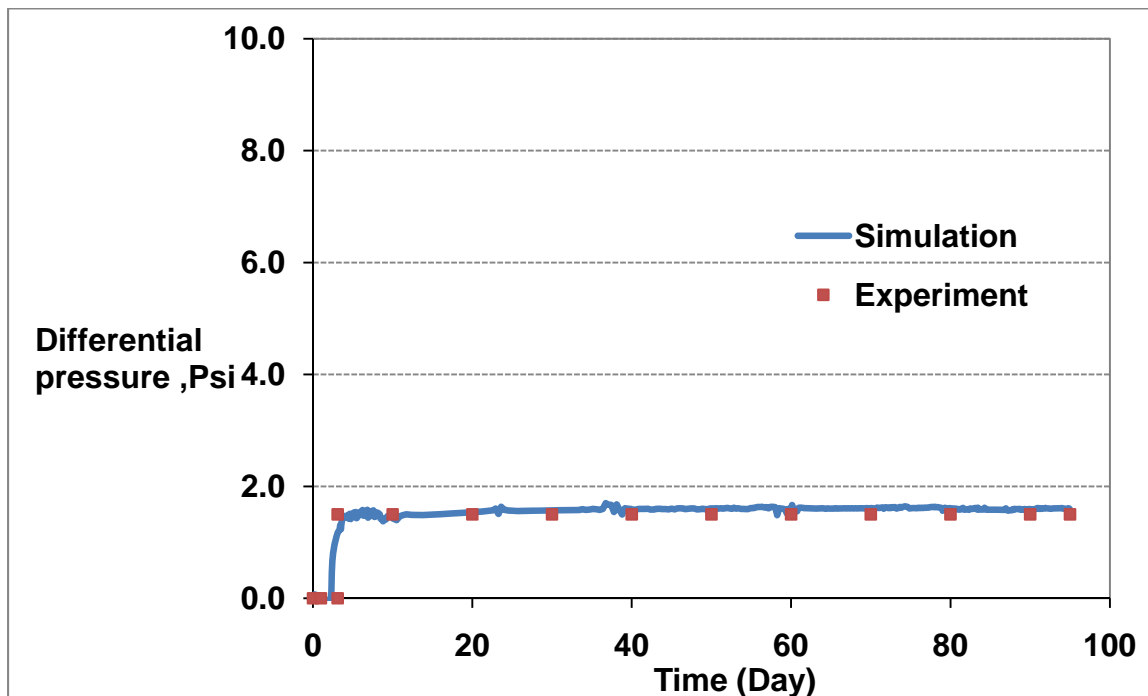


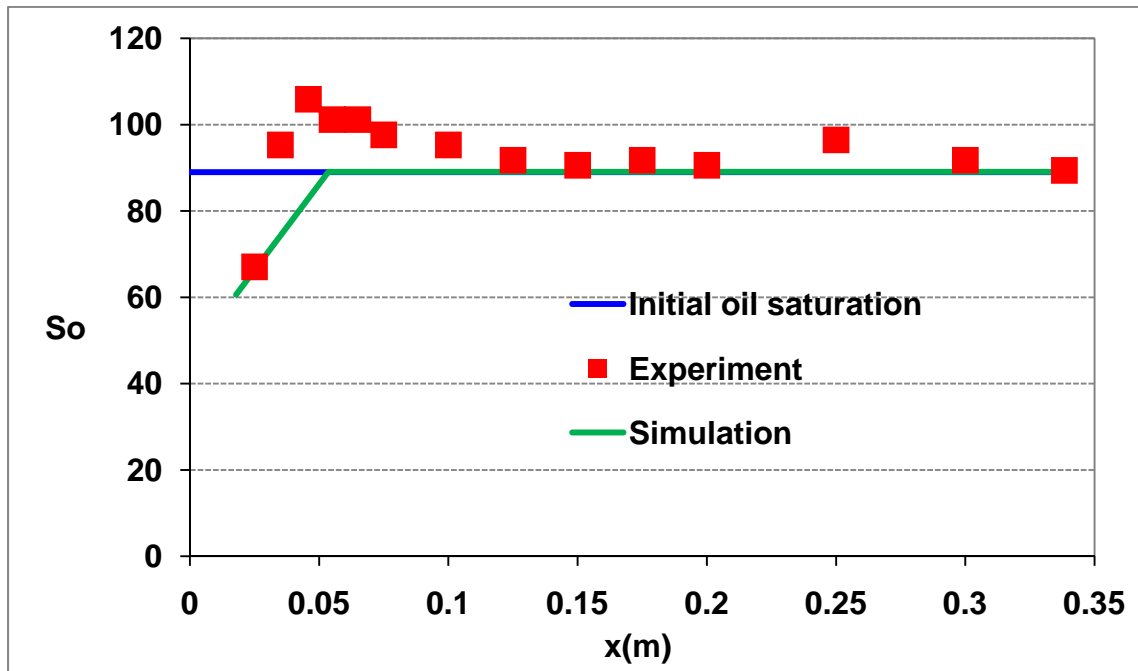
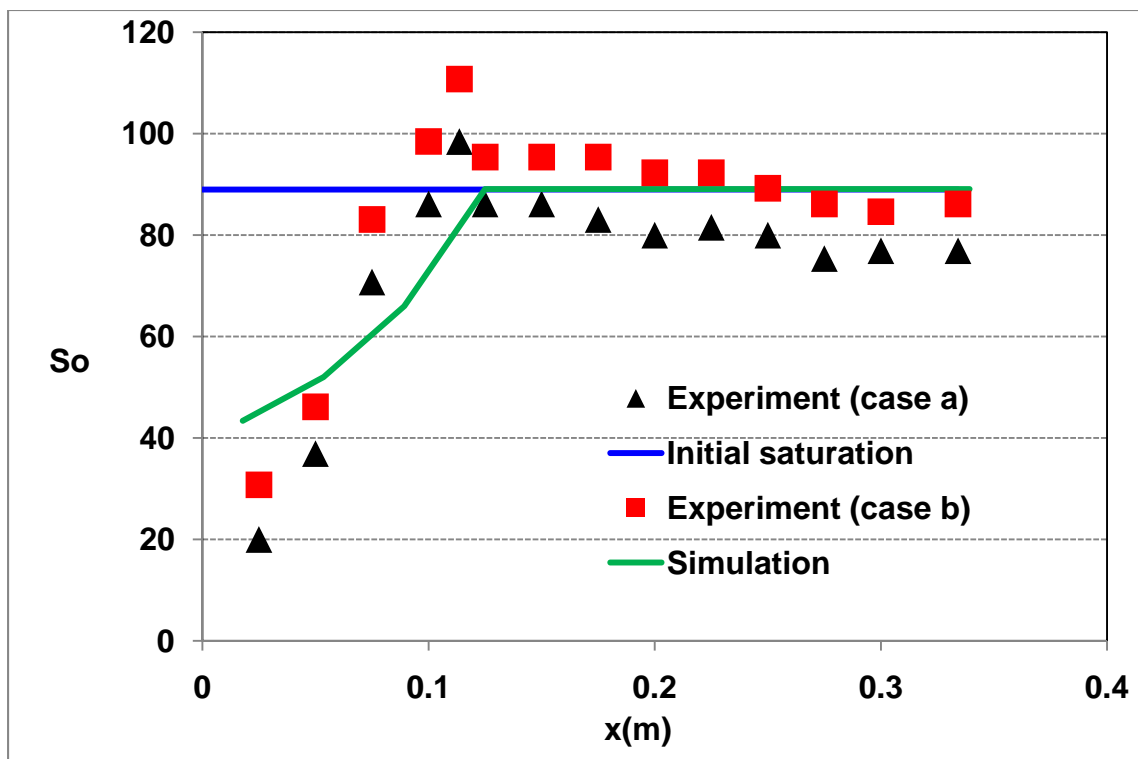
Fig. 6.27: Oil saturation at  $t = 7$  day in  $\text{CO}_2$  injection experimentFig. 6.28: Oil saturation at  $t = 23$  day in  $\text{CO}_2$  diffusion experiment

Fig. 6.29: Oil saturation at  $t = 53$  day in  $\text{CO}_2$  injection experiment

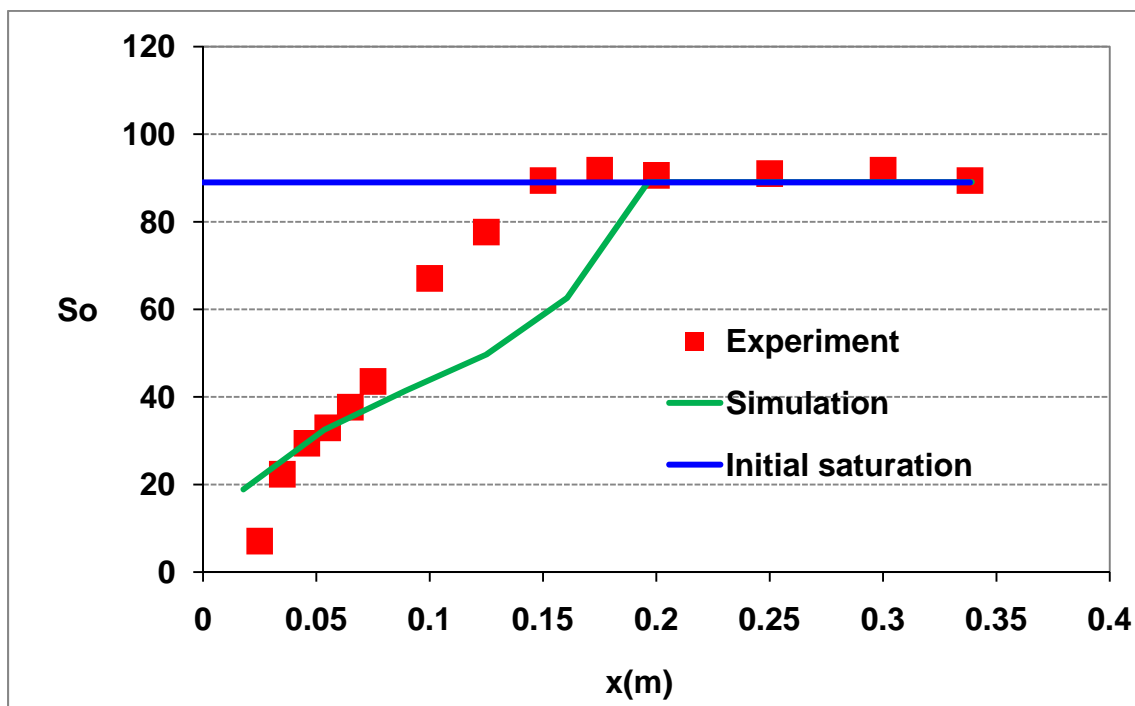


Fig. 6.30: Oil saturation at  $t = 67$  day in  $\text{CO}_2$  injection experiment

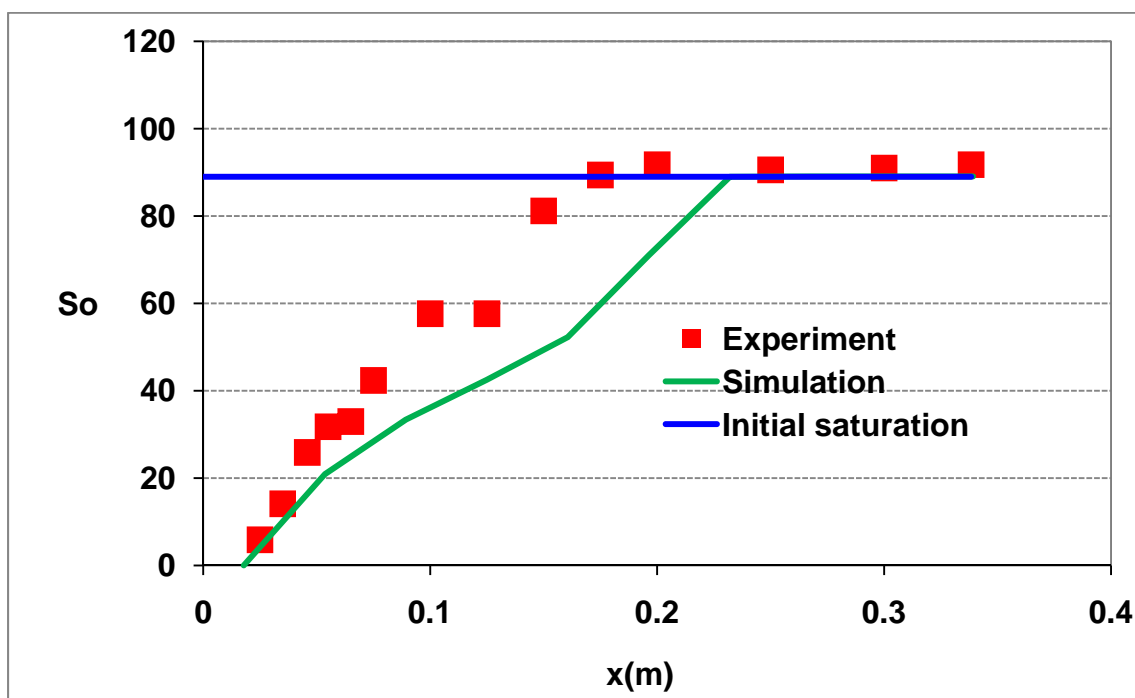




Fig. 6.31: Oil saturation at  $t = 88$  day in  $\text{CO}_2$  injection experiment

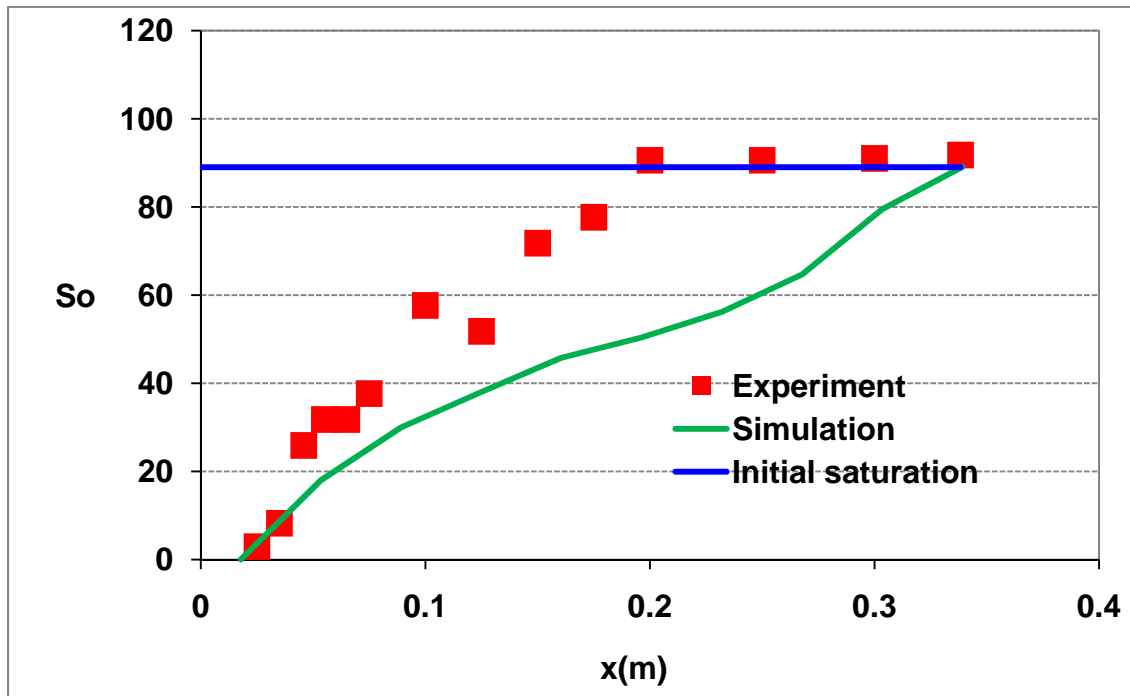
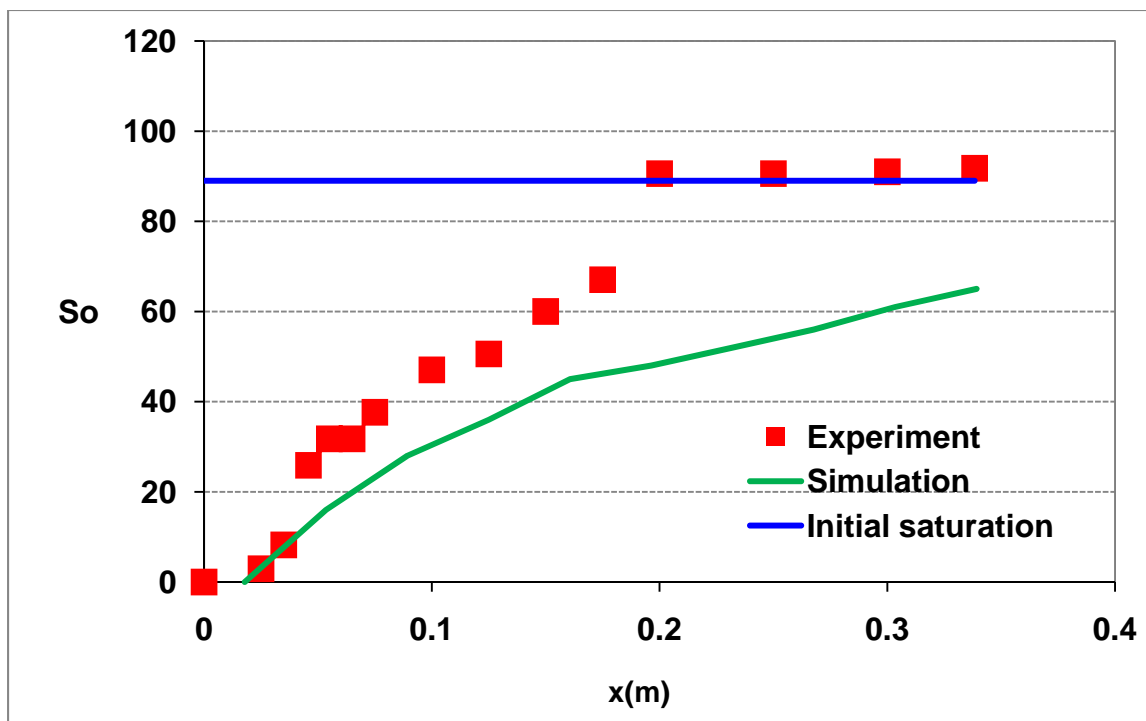


Fig. 6.32: Oil saturation at  $t = 95$  day in  $\text{CO}_2$  injection experiment



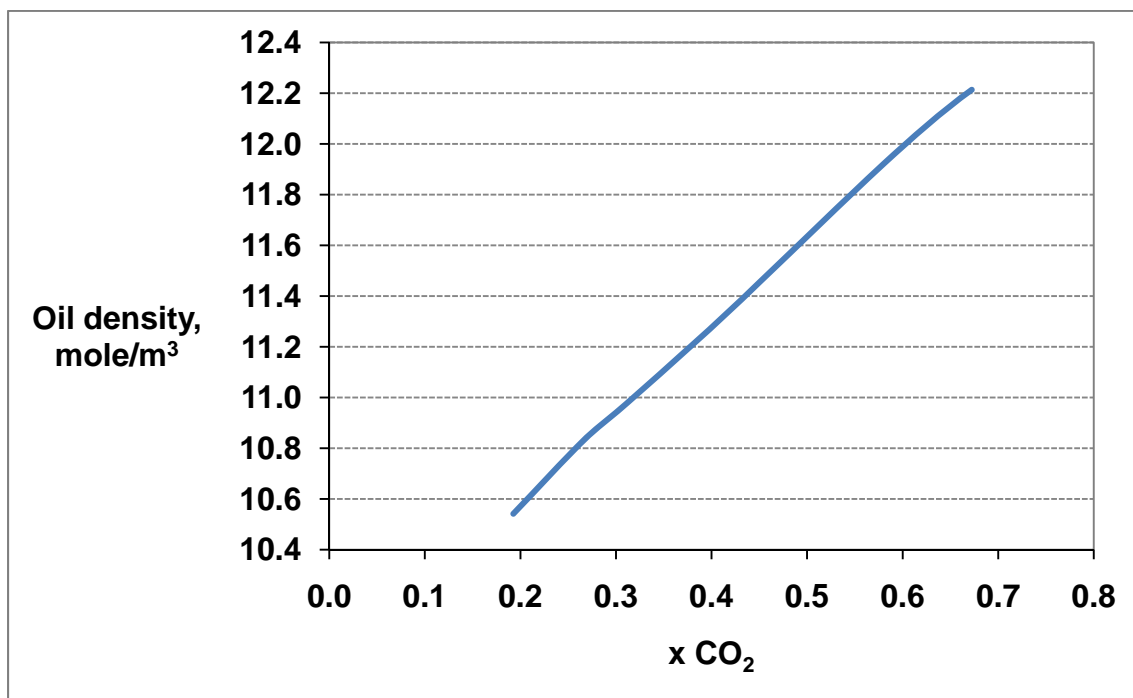
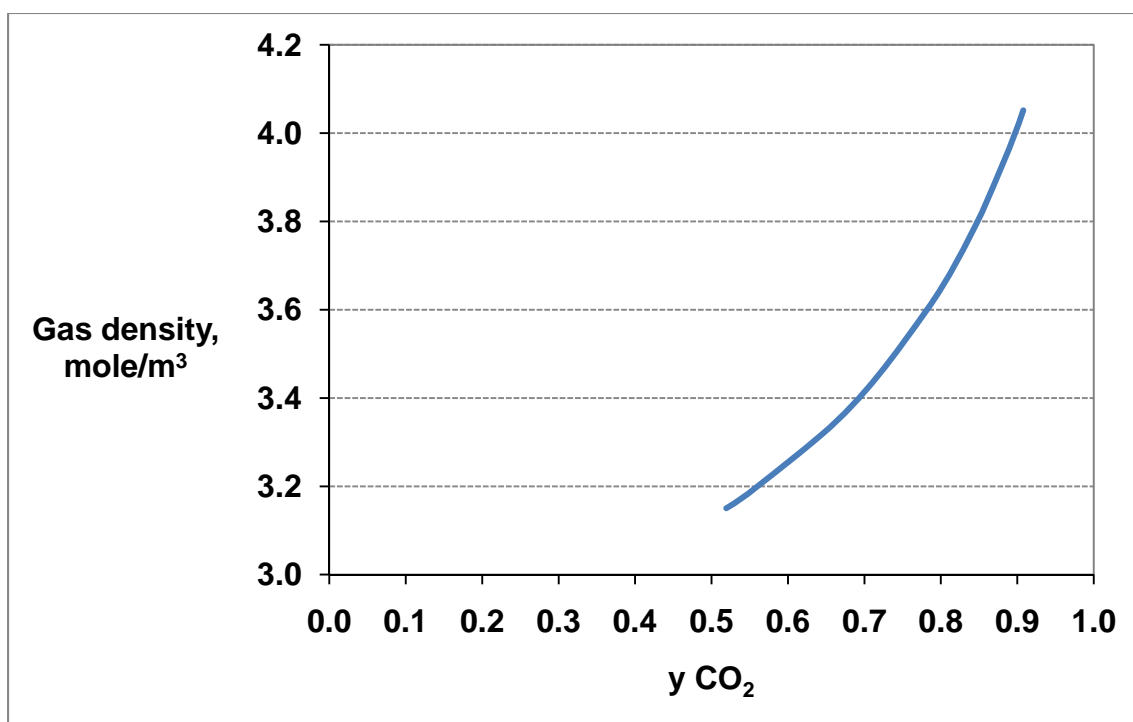
**Fig. 6.33: Effect of CO<sub>2</sub> mole fraction in oil on oil density****Fig. 6.34: Effect of CO<sub>2</sub> mole fraction in gas on Gas density**

Fig. 6.35: Calculated CO<sub>2</sub> mass-transfer rates at fracture-matrix surface in CO<sub>2</sub> injection experiment

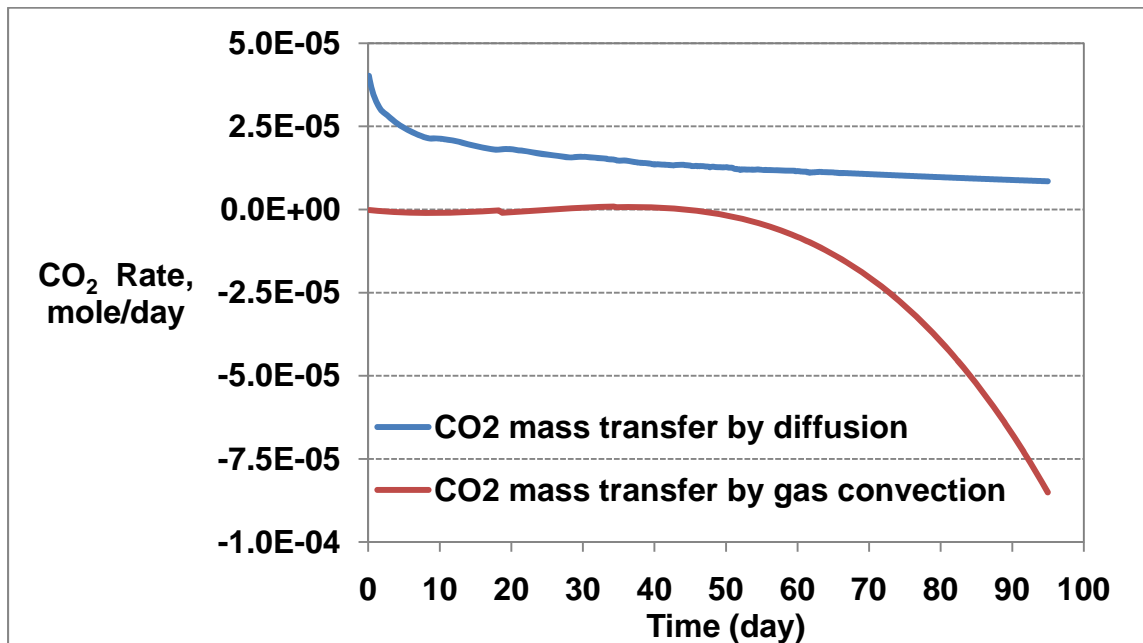


Fig. 6.36: Calculated C<sub>1</sub> mass transfer rates at fracture-matrix surface in CO<sub>2</sub> injection experiment

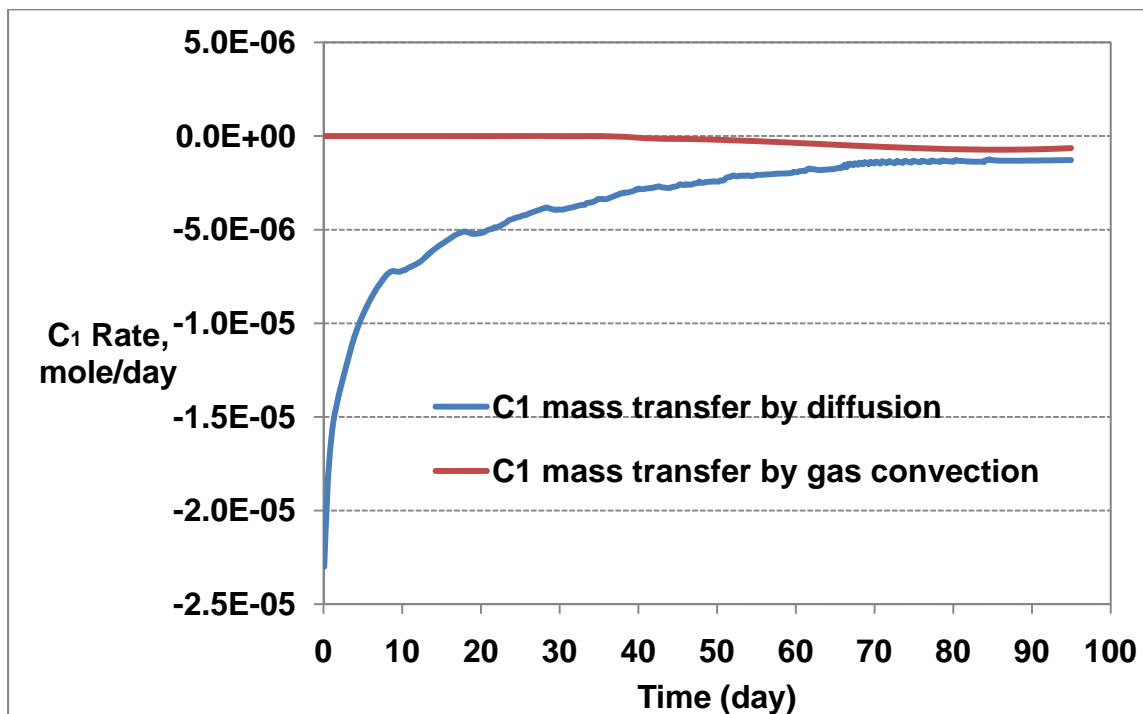


Fig. 6.37: Calculated C<sub>5</sub> mass transfer rates at fracture-matrix surface in CO<sub>2</sub> injection experiment

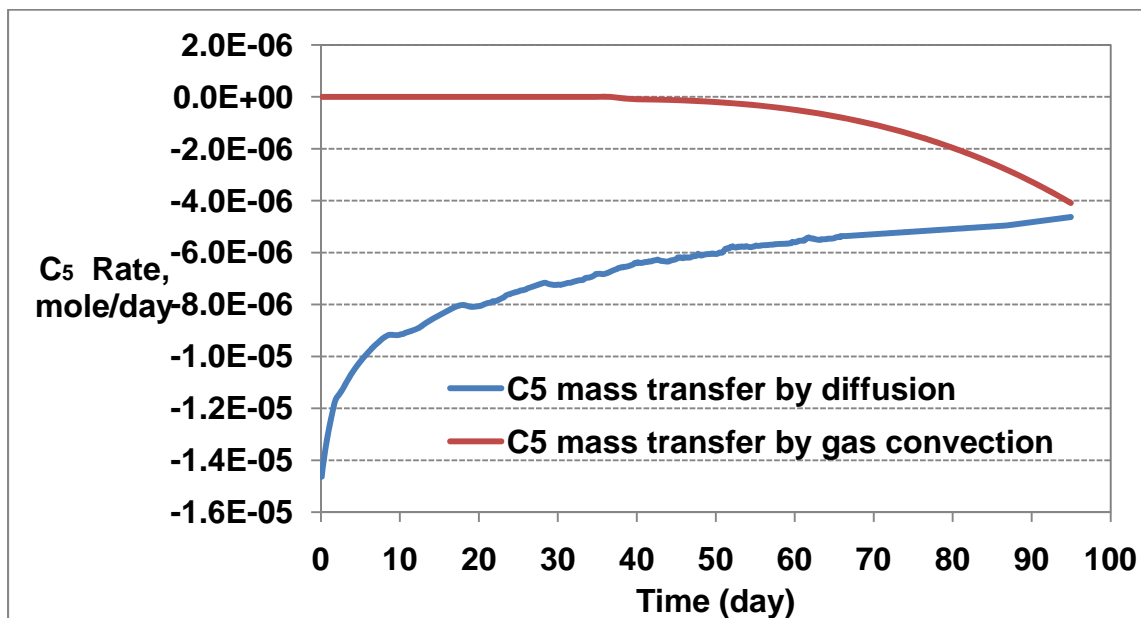


Fig. 6.38: Calculated local CO<sub>2</sub> rates inside the matrix at t = 23 day for CO<sub>2</sub> injection experiment

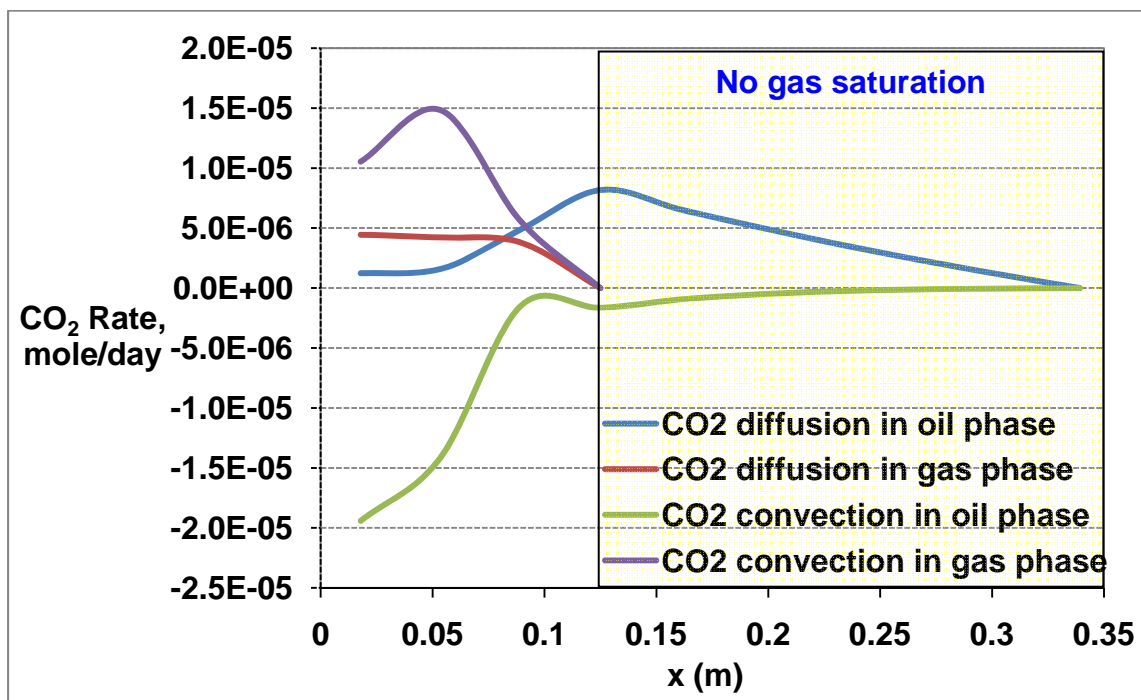


Fig. 6.39: Calculated local CO<sub>2</sub> rates inside the matrix at t = 90 day for CO<sub>2</sub> injection experiment

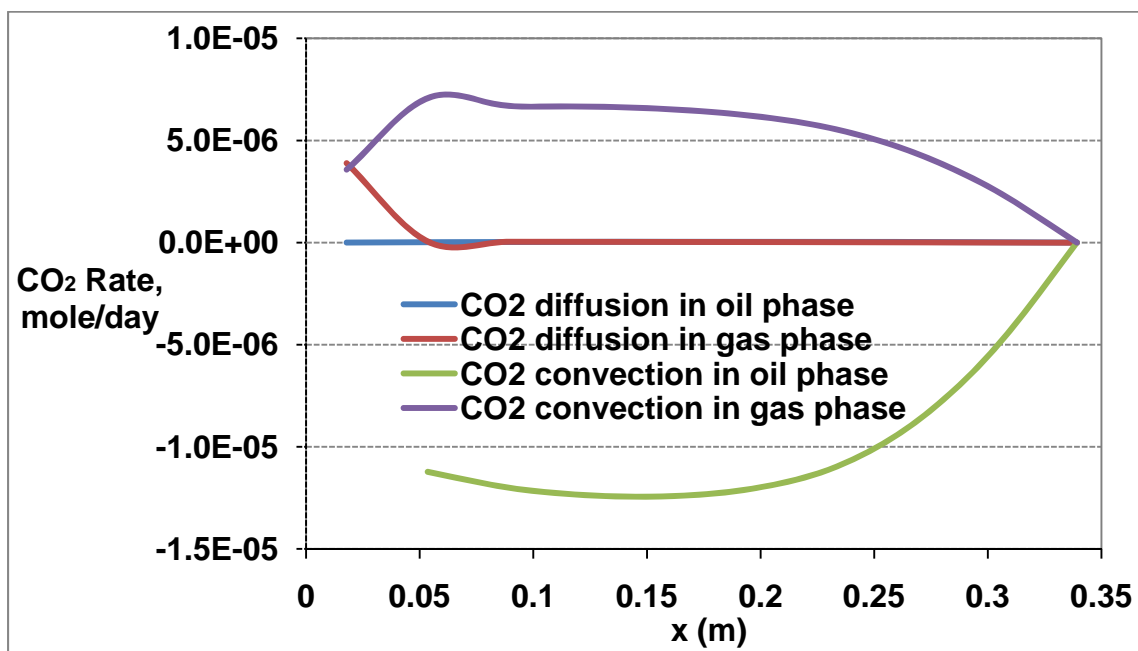


Fig. 6.40: Calculated local C<sub>1</sub> rates inside the matrix at t = 23 day for CO<sub>2</sub> injection experiment

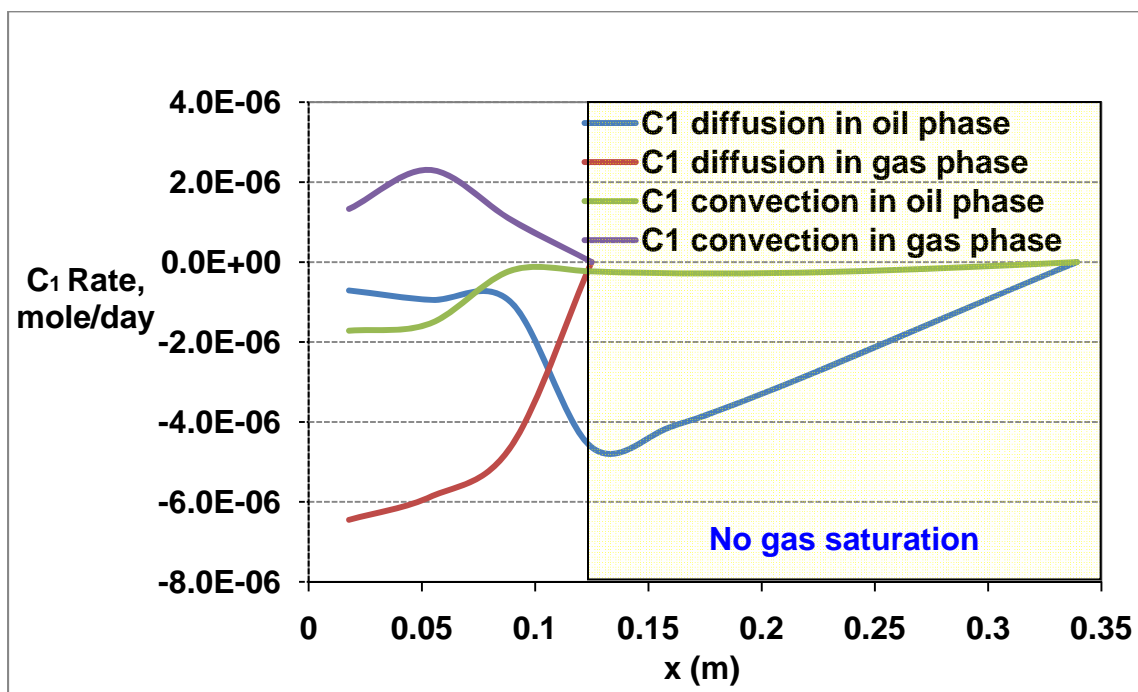


Fig. 6.41: Calculated local  $C_1$  rates inside the matrix at  $t = 90$  day for  $CO_2$  injection experiment

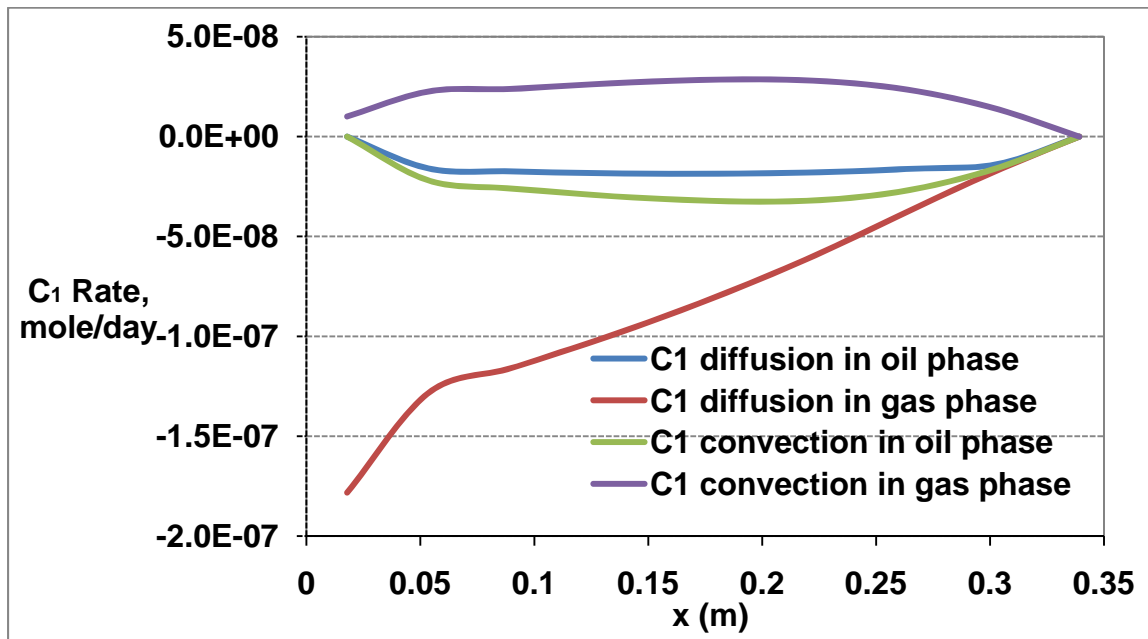


Fig. 6.42: Calculated local  $C_5$  rates inside the matrix at  $t = 23$  day for  $CO_2$  injection experiment

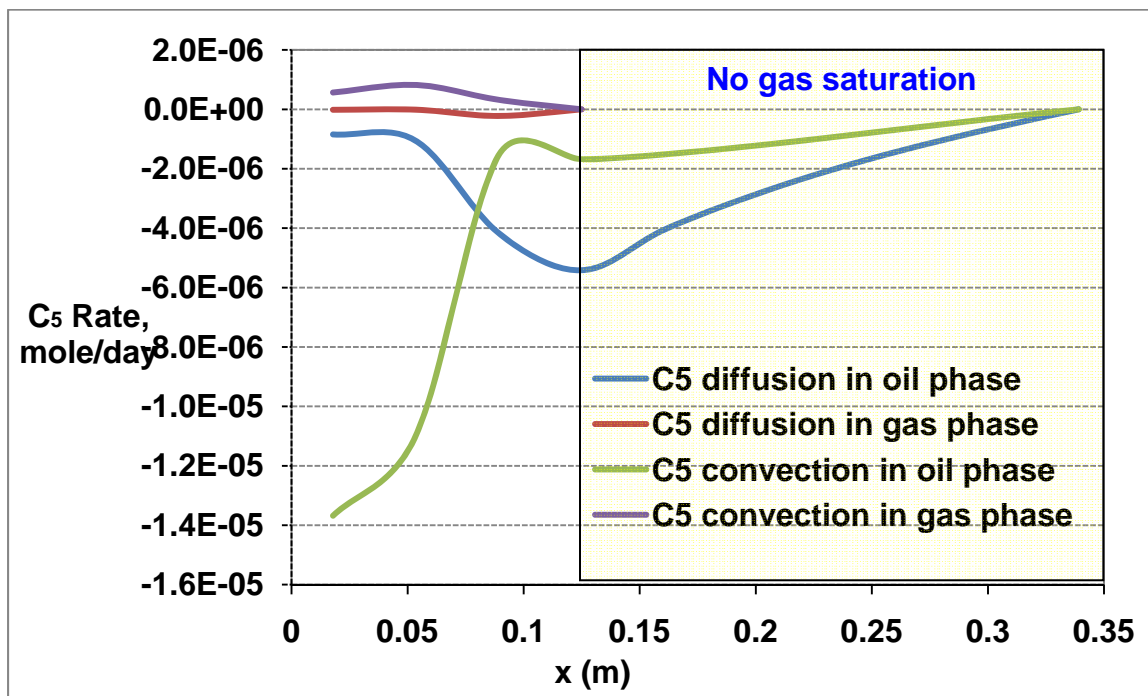
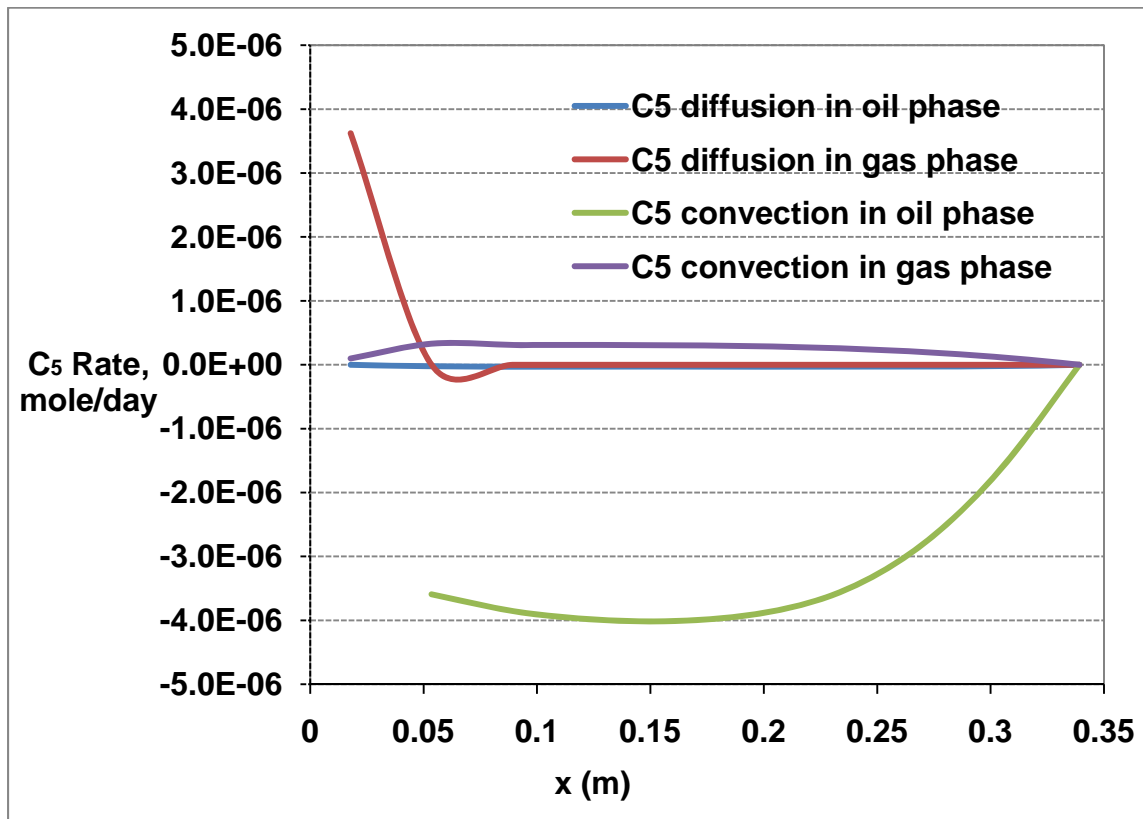


Fig. 6.43: Calculated local C<sub>5</sub> rates inside the matrix at t = 90 day for CO<sub>2</sub> injection experiment



## **Chapter 7. Simulation of CO<sub>2</sub> injection in a fracture in**

### **2-dimension**

#### **7.1. Introduction**

Simulation studies in 2-D (xz) were conducted to investigate the effect of gravity on recovery from a matrix block under CO<sub>2</sub> injection into a fracture. The dissolution of CO<sub>2</sub> in the oil reduces the interfacial tension between the oil and the equilibrium vapor phase, increases the density of the liquid phase and reduces the viscosity of the liquid phase. When the interfacial tension is reduced, the threshold pressure required for CO<sub>2</sub> to enter the matrix is reduced proportionally so that gravity drainage can occur after contact with CO<sub>2</sub>. Gravity drainage was accelerated due to the increase in the density of liquid phase resulting from the dissolution of CO<sub>2</sub> as well as the decrease in the liquid phase viscosity. All of these factors enhance the mechanism of gravity drainage from a matrix.

#### **7.2. Simulation results**

Simulation results of CO<sub>2</sub> injection in 2-dimension (xz) are presented in this section. Two matrix blocks with different heights were simulated to study the following:

- 1- Effect of gravity, scaling capillary pressure with interfacial tension, and grid size on recovery from a matrix block, and



- 2- Investigate recovery mechanisms between matrix and fracture.

The details of the simulation studies will be presented next.

### **7.2.1. Example 1: Simulation of CO<sub>2</sub> injection in a short matrix block**

CO<sub>2</sub> injection in a short 2-dimension (xz) matrix block with 3.28ftx0.5ftx3.28ft (xyz) dimensions was simulated. Fig. 7.1 shows the layout of the example. The matrix block is surrounded by fractures. CO<sub>2</sub> was injected into the fractures at a pressure of 913.74 psi and 38.5 °C. The porous matrix was initially saturated with a liquid phase containing C<sub>1</sub> (28 mole%) and C<sub>5</sub> (72 mole%). No initial gas saturation was present in the porous matrix. There was 11% immobile water saturation in the matrix. Mass transfer coefficients between matrix and fracture were obtained from matching CO<sub>2</sub> injection experiment (Section 6.2.3). The model inputs are listed in Table 7.1. Capillary pressure, relative permeabilities, phase behavior parameters, and Peng-Robinson EOS were used same as CO<sub>2</sub> injection experiment (Section 6.2.3).

The matrix block was simulated for four different cases to study the effect of gravity, grid size, and scaling capillary pressure with interfacial tension on recovery as follows:

- 1- Case A: 3x3 grids (xz) with and without scaling capillary pressure with interfacial tension
- 2- Case B: 6x5 grids (xz) with and without scaling capillary pressure with interfacial tension

### 3- Case C: 8x7 grids (xz) with and without scaling capillary pressure with interfacial tension

The model was run for the left part of the symmetry line (Fig. 7.1) for cases B, and C, because the left and right parts of the symmetry line are the same.

Fig. 7.2 and 7.3 show the methane and pentane molar recoveries for the cases. The grid size had an effect on methane and pentane recoveries. The recoveries increased by decreasing the grid size. This is probably due to higher concentration and pressure gradients within the matrix block for smaller grid size.

In the model, mass transfer between matrix and fracture occurs through diffusion, oil convection, and gas convection (See section 3.4.2.2). Fig. 7.4 to 7.6 compare the mass-transfer rates by diffusion and oil convection between matrix and fracture for carbon dioxide, methane, and pentane for case A, case B, and case C. Mass transfer between matrix and fracture was dominated by diffusion for carbon dioxide, methane, and pentane. Case C with smaller grid size had higher mass transfer rates by diffusion between matrix and fracture than case A and case B for carbon dioxide, methane, and pentane. The matrix block started to drain (oil convection) from the bottom of the block around 700, 600, and 500 days of simulation for case A, case B, and case C, respectively. The matrix block with smaller grid size (case C) started to drain sooner. Tables 7.2, 7.3, and 7.4 show calculated oil pressure inside the matrix at 715, 600, and 600 day for case A, case B, and case C, respectively. Drainage occurs because the oil pressure at

the bottom of the matrix for all cases is higher than gas pressure in the fracture (913.74 psi). Therefore, oil phase flows from bottom of the matrix to the fracture where it evaporates. Gas convection had an insignificant role in mass transfer between matrix and fracture.

Scaling capillary pressure with interfacial tension did not affect the simulation results.

### **7.2.2. Example 2: Simulation of CO<sub>2</sub> injection in a tall matrix block**

CO<sub>2</sub> injection in a 2-D matrix block with 3.28ftx0.5ftx10ft (xyz) dimensions was simulated. Fig. 7.2 demonstrates the layout of example 2 where a matrix block is surrounded by fractures. Similar to example 1, CO<sub>2</sub> was injected into the fractures at a pressure of 913.74 psi and 38.5 °C. The porous matrix was filled with a liquid phase containing C<sub>1</sub> (28 mole%) and C<sub>5</sub> (72 mole%). Initial gas saturation was zero in the porous matrix. There was immobile water at 11% saturation in the matrix. Mass transfer coefficients between matrix and fracture for carbon dioxide, methane, and pentane were similar to CO<sub>2</sub> injection experiment of Section 6.2.3. Table 7.5 shows the model inputs. Rock and fluid properties (Capillary pressure, relative permeabilities, phase behavior parameters, and Peng-Robinson EOS) were same as CO<sub>2</sub> injection experiment of Section 6.2.3.

The matrix block was simulated for three different cases to investigate the effects of gravity, grid size, scaling capillary pressure with interfacial tension, and

matrix permeability on recovery from the matrix block. The three cases are as follows:

- 1- Case A: 6x10 grids (xz) with and without scaling capillary pressure with interfacial tension
- 2- Case B: 8x7 grids (xz) with and without scaling capillary pressure with interfacial tension
- 3- Case C: 10x10 grids (xz) with and without scaling capillary pressure with interfacial tension

Fig. 7.8 to 7.11 show the effect of grid size on methane and pentane molar recoveries. Capillary pressure was not scaled with interfacial tension in Fig. 7.8 and 7.9. Fig. 7.10 and 7.11 show molar recoveries of methane and pentane when the capillary pressure was scaled with interfacial tension. Methane and pentane recoveries increased by increasing the number of grids in the x-direction. Since the block height is 10ft, gravity drainage played an important role in recovering methane and pentane. Table 7.6 shows calculated oil pressure inside the matrix for case B (without scaling capillary pressure with interfacial tension) at 160 days of simulation. Oil pressure at the bottom of the matrix block (914.31 psi) is more than gas pressure in the fracture (913.74 psi). Therefore, the block produced oil mostly from the bottom due to the gravity. As a result, more grids in the x-direction enhanced the oil production by gravity from the matrix block bottom.

Fig. 7.12, 7.13, and 7.14 illustrate the effect of scaling capillary pressure with interfacial tension on the methane and pentane recoveries in cases A, B, and C. Scaling capillary pressure with interfacial tension increased the methane and pentane recoveries.

Mass transfer rates by diffusion, oil convection, and gas convection between matrix and fracture were following similar trend in cases A, B, and C. Therefore, mass transfer rates between matrix and fracture in case C is discussed. Fig. 7.15, 7.16, and 7.17 show carbon dioxide, methane, and pentane mass transfer rates between matrix and fracture by diffusion, oil convection, and gas convection in case C. Fig. 7.15 and 7.16 show that carbon dioxide and methane were transported between matrix and fracture mainly by diffusion. Also, they were transported by gas convection towards end of simulation. Fig. 7.17 shows that oil convection and diffusion were the most important mechanisms in transporting pentane between matrix and fracture. Pentane mainly transported by oil convection after scaling capillary pressure with interfacial tension. Fig. 7.15 to 7.17 show that scaling capillary pressure with interfacial tension enhanced diffusion, gas convection, and oil convection between the matrix and the fracture.

The calculated interfacial tension,  $\text{CO}_2$  mole fraction in the oil composition, oil density, oil pressure, gas saturation, and oil viscosity inside the matrix block were compared for case C (with and without scaling capillary pressure with interfacial

tension) to investigate the effect of scaling capillary pressure with interfacial tension on flow behavior inside the matrix block.

Diffusion of CO<sub>2</sub> into the oil phase reduces the interfacial tension between oil and the equilibrium gas phase. As a result, capillary pressure decreases as the content of CO<sub>2</sub> in the oil phase increases. Reduction in capillary pressure causes the flowing gas CO<sub>2</sub> in the fracture to enter the porous matrix easier. When first gas saturation appeared, the IFT was 6.6 dynes/cm. Table 7.7 compares the calculated local IFT inside the matrix for case C with and without scaling capillary pressure with interfacial tension at 200 days. The IFT was reduced from 6.6 dynes/cm to almost 3.2 to 4.2 dynes/cm at 200 days because of CO<sub>2</sub> mass transfer from the fracture to the matrix. As one may see, when capillary pressure was scaled with interfacial tension, the IFT and capillary pressure reduced more and therefore enhanced CO<sub>2</sub> flow from the fracture to the matrix. Table 7.8 confirms that the CO<sub>2</sub> mole fraction in the oil phase in the matrix is higher when capillary pressure was scaled with interfacial tension.

Diffusion of CO<sub>2</sub> into the oil phase increases the oil density and enhances the gravity drainage. Table 7.9 shows that oil density increased from its initial value of 586.8 kg/m<sup>3</sup>. The oil density increased by increasing CO<sub>2</sub> mole fraction in the oil phase. Scaling capillary pressure with IFT enhanced CO<sub>2</sub> flow from the fracture to the matrix and gravity drainage.

CO<sub>2</sub> diffusion into the oil phase causes the oil phase to swell and the pressure in the oil phase to increase. Table 7.10 compares calculated oil pressure inside the matrix for case C with and without scaling capillary pressure with interfacial tension at 200 days. Gas pressure in the fracture is 913.74 psi. When capillary pressure was not scaled with interfacial tension, oil drained mainly from the bottom of the matrix block where the oil pressure inside the matrix (914.21 psi) is more than gas pressure in the fracture (913.74 psi). When capillary pressure was scaled with interfacial tension, oil flowed from the matrix bottom (915.02 psi) and sides to the fracture (913.74 psi). This confirms that scaling capillary pressure with interfacial tension has the following effect:

- 1- Increased CO<sub>2</sub> flow from the fracture to the matrix, and
- 2- Enhanced the matrix block oil drainage.

Mass transfer of CO<sub>2</sub> from the fracture to the matrix drives the system phase behavior to form a gas phase in high CO<sub>2</sub> content area of the matrix adjacent to the fracture. Table 7.11 illustrates calculated gas saturation inside the matrix for case C with and without scaling capillary pressure with interfacial tension at 200 days. Again, scaling capillary pressure with interfacial tension increased CO<sub>2</sub> mass transfer from the fracture to the matrix. This caused forming higher gas saturation in the matrix compare to the gas saturation for the case of without scaling capillary pressure with IFT.

Oil phase viscosity usually decreases by increasing mole fraction of CO<sub>2</sub> in the oil phase. The oil phase viscosity at the beginning of simulation with composition of 28 mole% C<sub>1</sub> and 72 mole% C<sub>5</sub> at pressure of 913.74 psi and temperature of 38.5° C was 0.1261 cp. Table 7.12 shows oil phase viscosity for case C at 200 days with and without scaling capillary pressure with interfacial tension. The oil viscosity dropped by almost 30% from its original value to 0.1 cp and 0.09 cp in the matrix top.

### 7.3. Summary

Results of simulation studies of CO<sub>2</sub> injection in 2-dimension is summarized as follows:

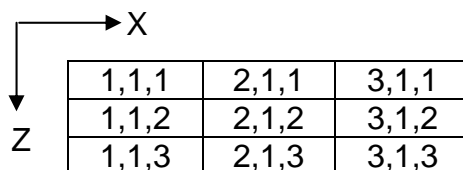
- Diffusion played an important role in transporting carbon dioxide, methane, and pentane between matrix and fracture in the 2D examples.
- In Example 1, the matrix block started to drain (oil convection) around 500 days of simulation.
- Scaling capillary pressure with interfacial tension did not affect the simulation results of Example 1.
- Recoveries of methane and pentane recoveries in Examples 1 and 2 increased by decreasing the grid size.
- Gravity drainage played an important role in recovering methane and pentane by oil production in Example 2.



- In Example 2, scaling capillary pressure with interfacial tension increased the methane and pentane recoveries.
- In Example 2, diffusion and oil convection mass transfer between matrix and fracture were enhanced by scaling capillary pressure with interfacial tension.
- In Example 2, oil convection became the dominant mechanism in transporting pentane after scaling capillary pressure with interfacial tension.
- Interfacial tension decreased by dissolution of CO<sub>2</sub> in the oil phase.
- Oil density, oil pressure, and gas saturation increased by diffusion of CO<sub>2</sub> into the oil phase.
- Oil viscosity did not change by increasing mole fraction of CO<sub>2</sub> in the oil phase.
- Scaling capillary pressure with IFT increased flow of CO<sub>2</sub> from the fracture to the matrix compare to the same case without scaling capillary pressure with IFT.

**Table 7.1: Model inputs in simulation of 2D CO<sub>2</sub> injection (Example 1)**

Lx(ft), Lz(ft)	3.28
Ly(ft)	0.5
Matrix Porosity	0.4
Matrix permeability (md)	2
Fracture pressure (psi)	913.74
<b>Initial conditions</b>	
So, matrix	0.89
Sg, matrix	0
Sw, matrix	0.11
Sg, fracture	1
Overall composition, C <sub>1</sub>	0.28
Overall composition, C <sub>5</sub>	0.72
Temperature (°F)	101.3

**Table 7.2: Calculated local oil pressure inside the matrix at t=715 day for Example 1-Case A**


	1,1,1	2,1,1	3,1,1
	1,1,2	2,1,2	3,1,2
	1,1,3	2,1,3	3,1,3

p (psi)	913.18	913.18	913.18
	913.48	913.48	913.48
	913.78	913.78	913.78









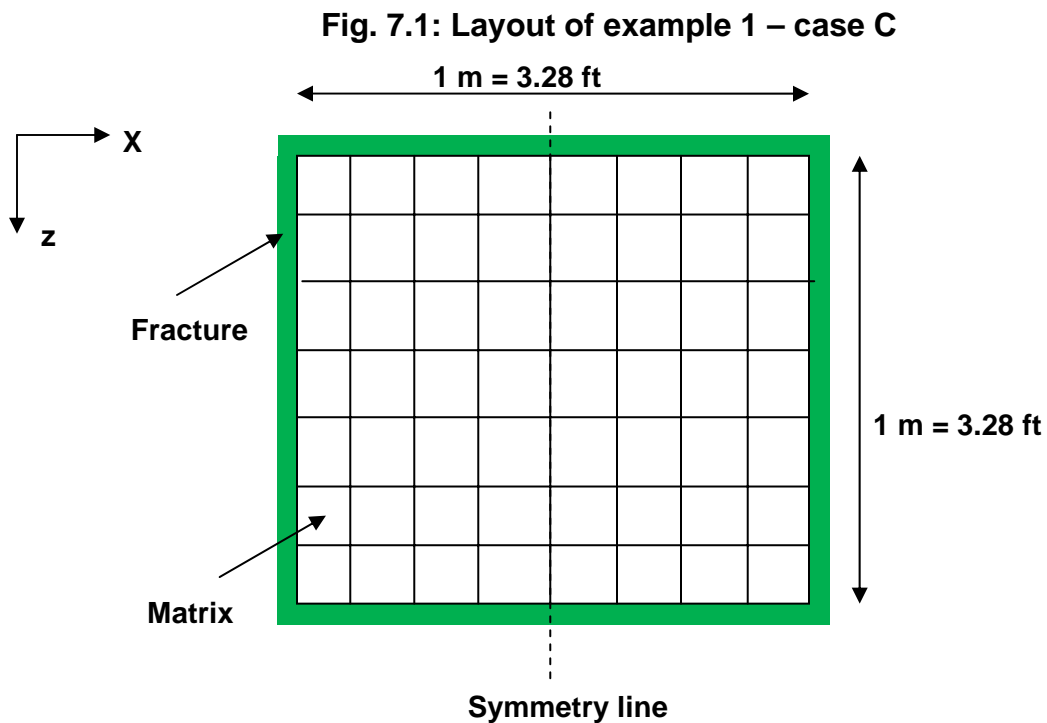




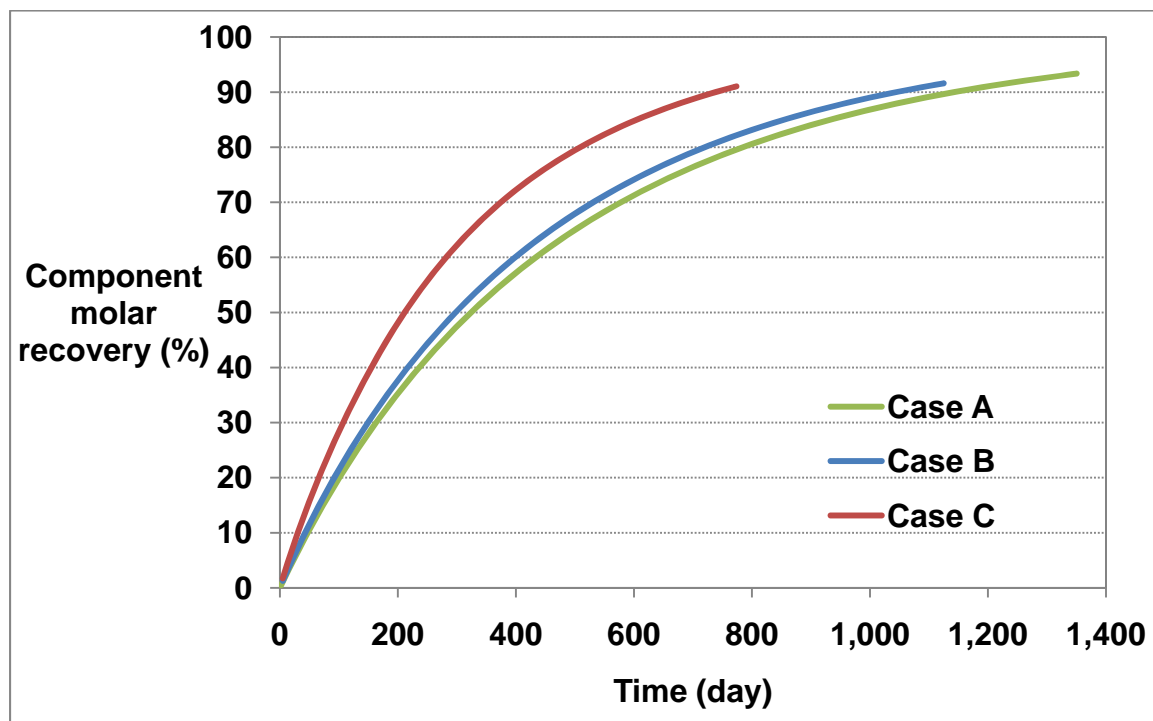








**Fig. 7.2: Effect of grid size on  $C_1$  molar recovery (Example 1)**



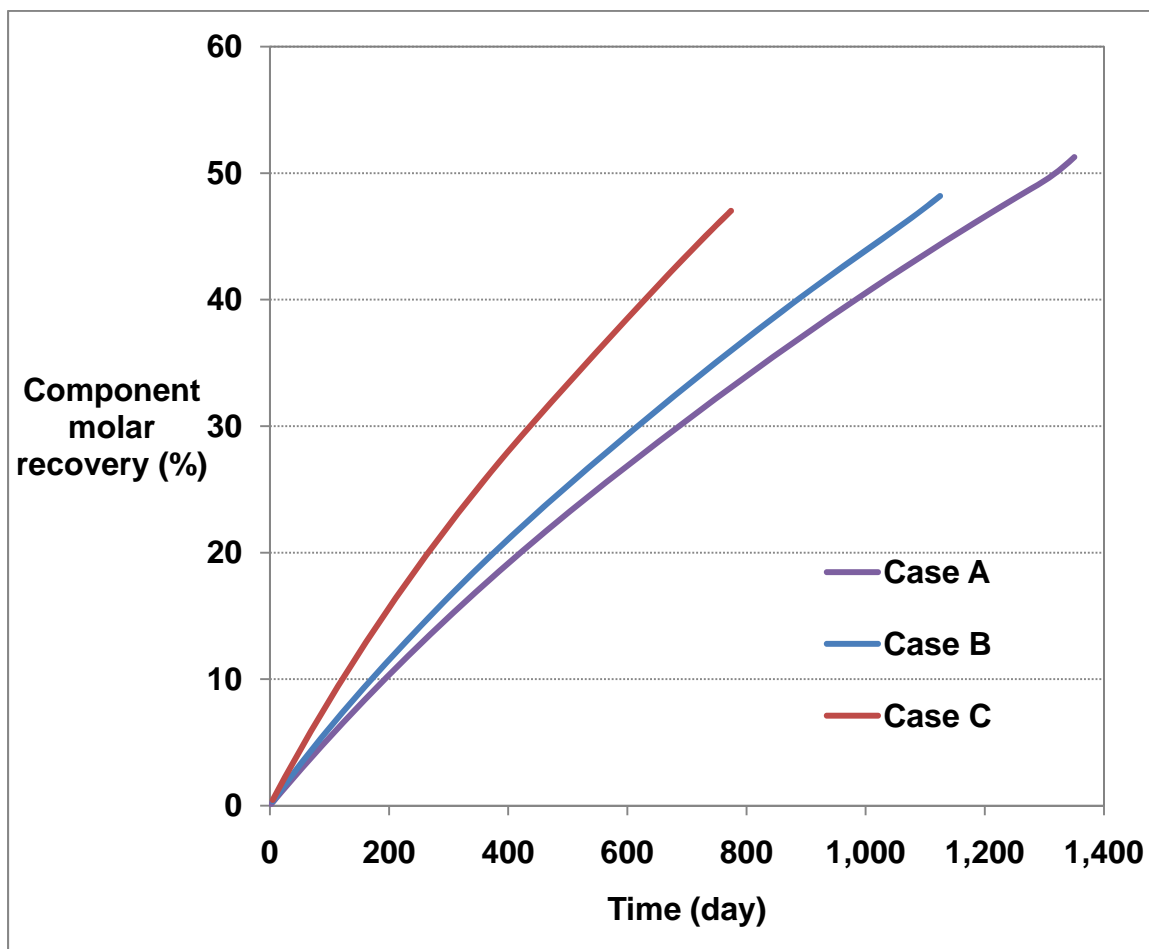
**Fig. 7.3: Effect of grid size on  $C_5$  molar recovery (Example 1)**

Fig. 7.4: Calculated CO<sub>2</sub> mass transfer rates at matrix-fracture surface for Case A, Case B, and Case C of Example 1

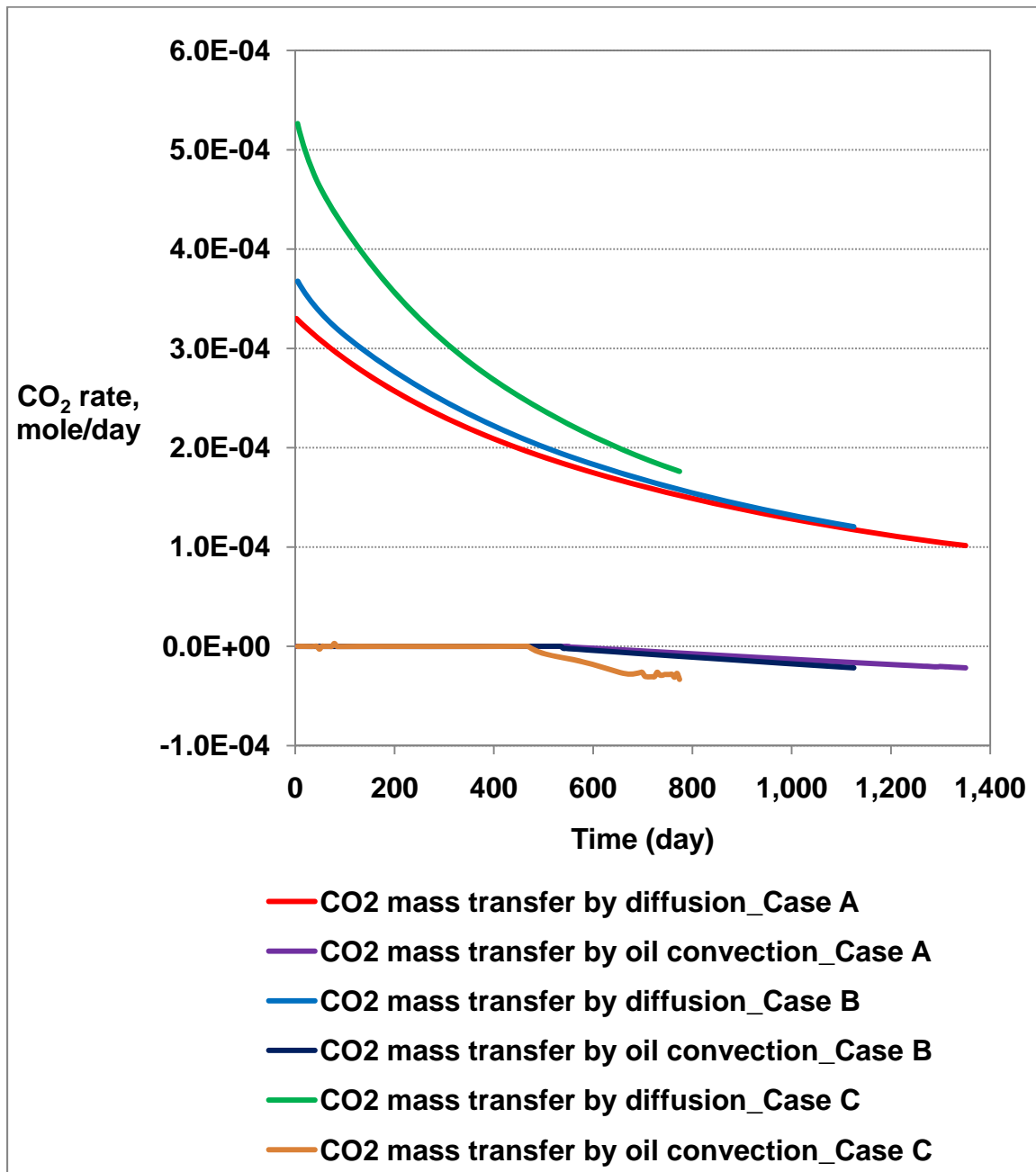


Fig. 7.5: Calculated  $C_1$  mass transfer rates at matrix-fracture surface for Case A, Case B, and Case C of Example 1

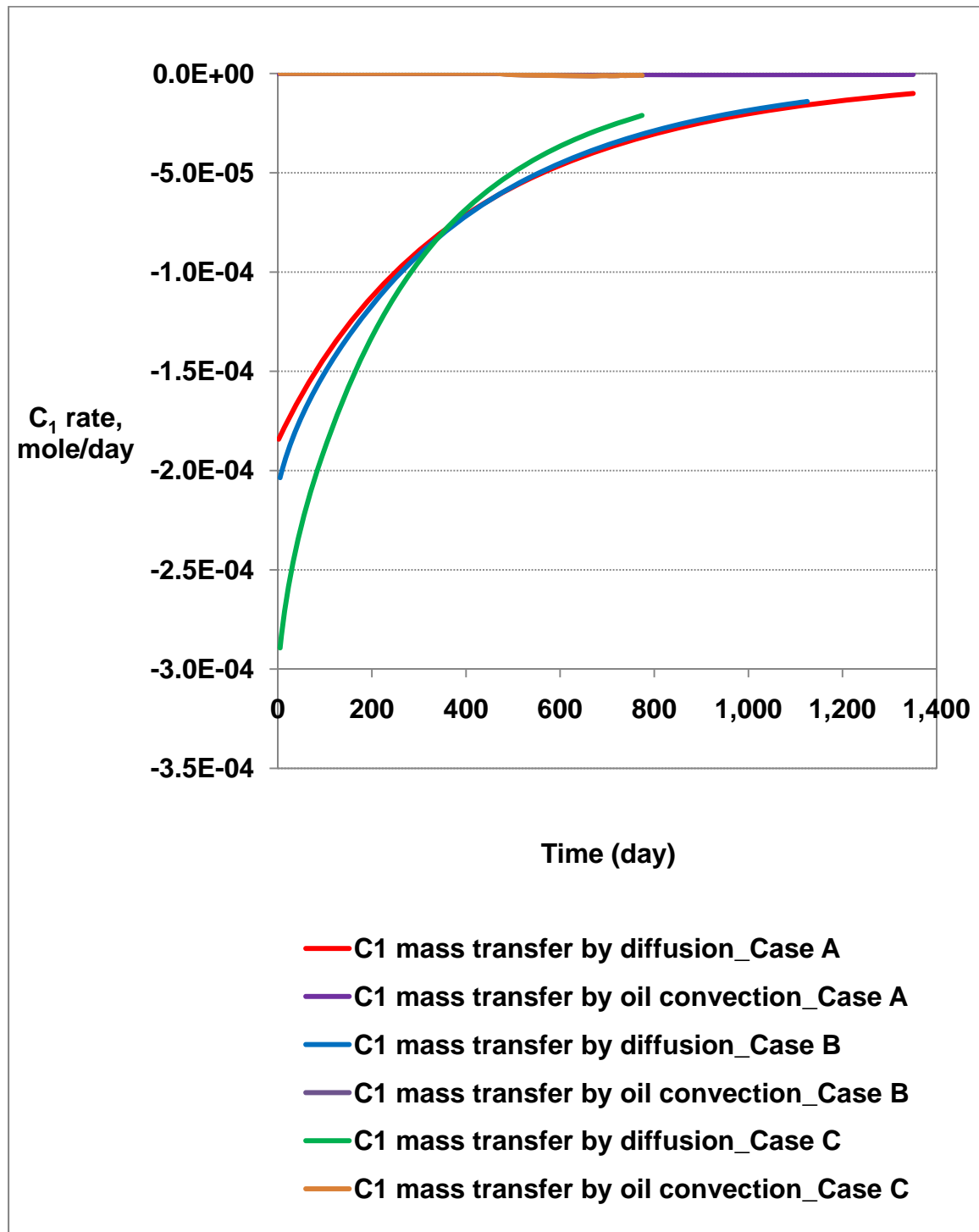
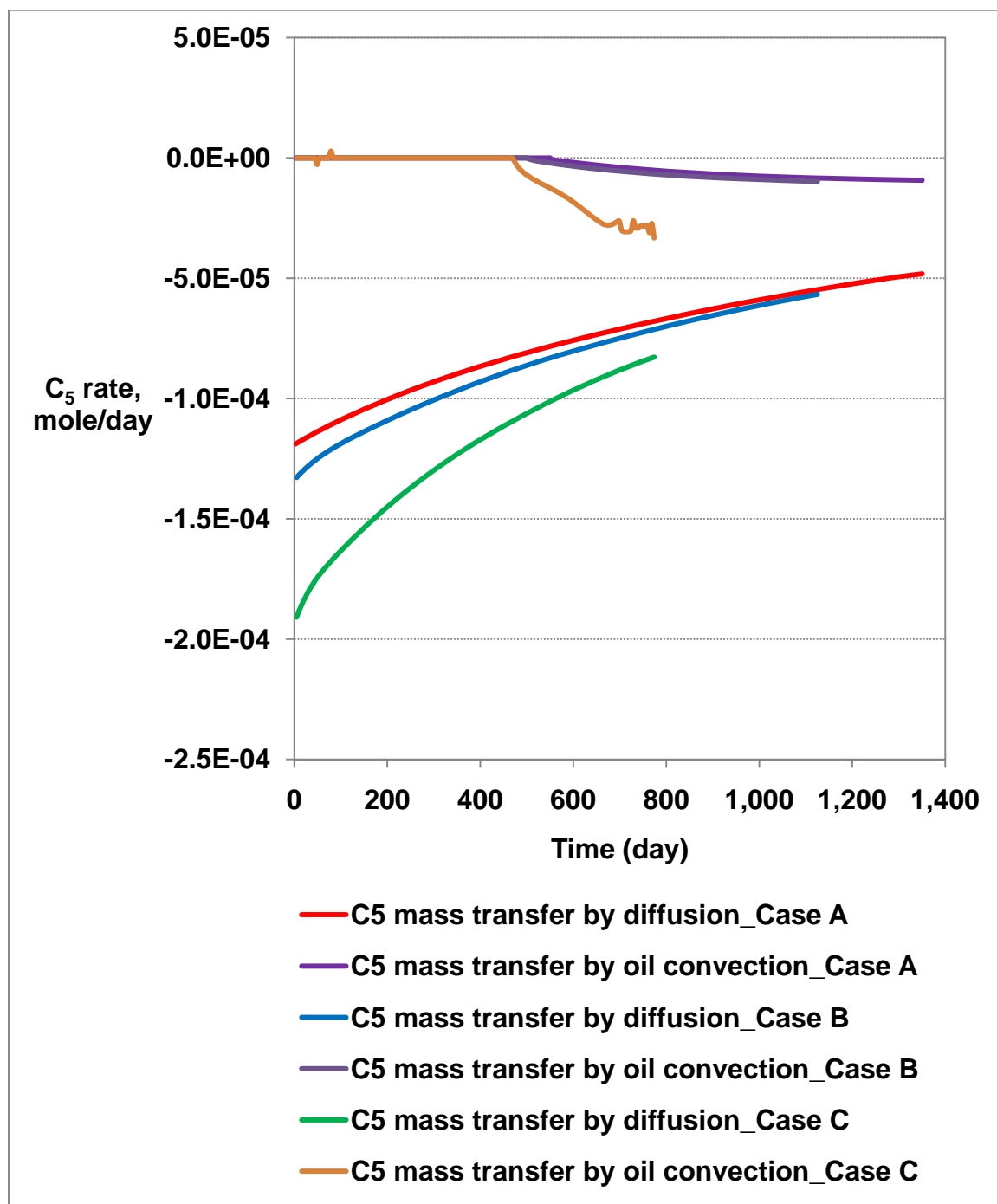
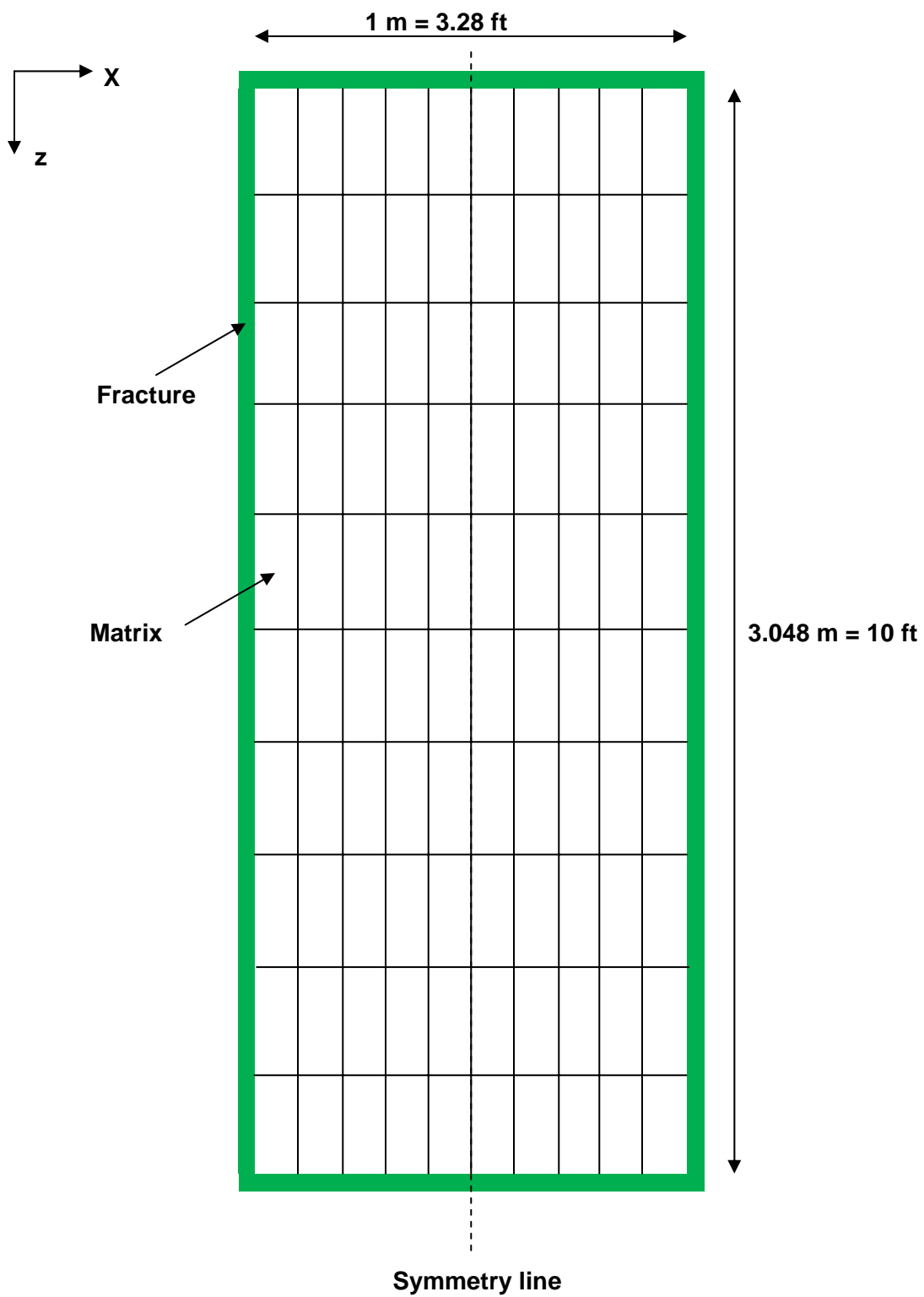


Fig. 7.6: Calculated C<sub>5</sub> mass transfer rates at matrix-fracture surface for Case A, Case B, and Case C of Example 1



**Fig. 7.7: Layout of example 2 – case C**



**Fig. 7.8: Effect of grid size on  $C_1$  molar recovery (Example 2- Without scaling capillary pressure with IFT)**

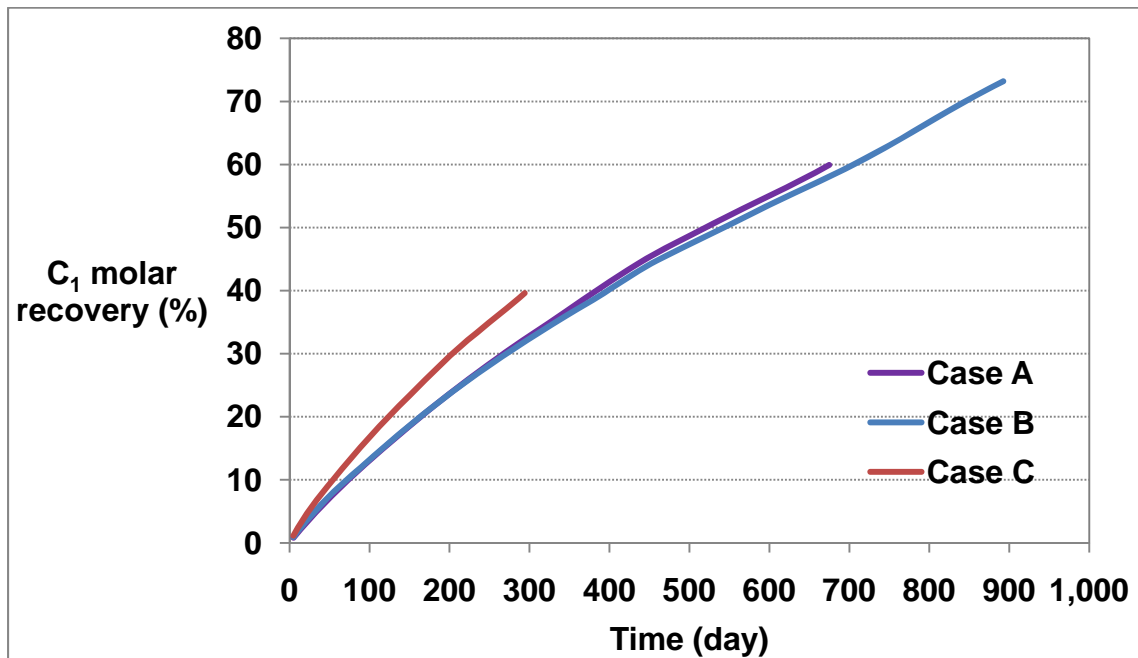


**Fig. 7.9: Effect of grid size on  $C_5$  molar recovery (Example 2- Without scaling capillary pressure with IFT)**

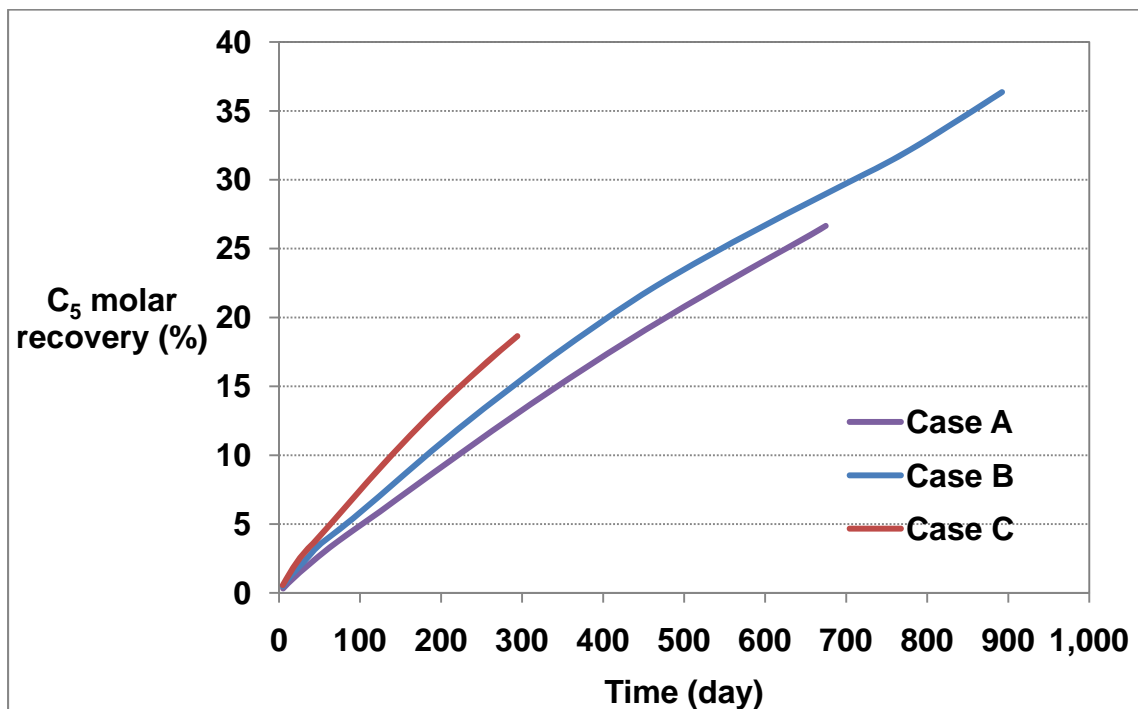


Fig. 7.10: Effect of grid size on  $C_1$  molar recovery (Example 2- With scaling capillary pressure with IFT)

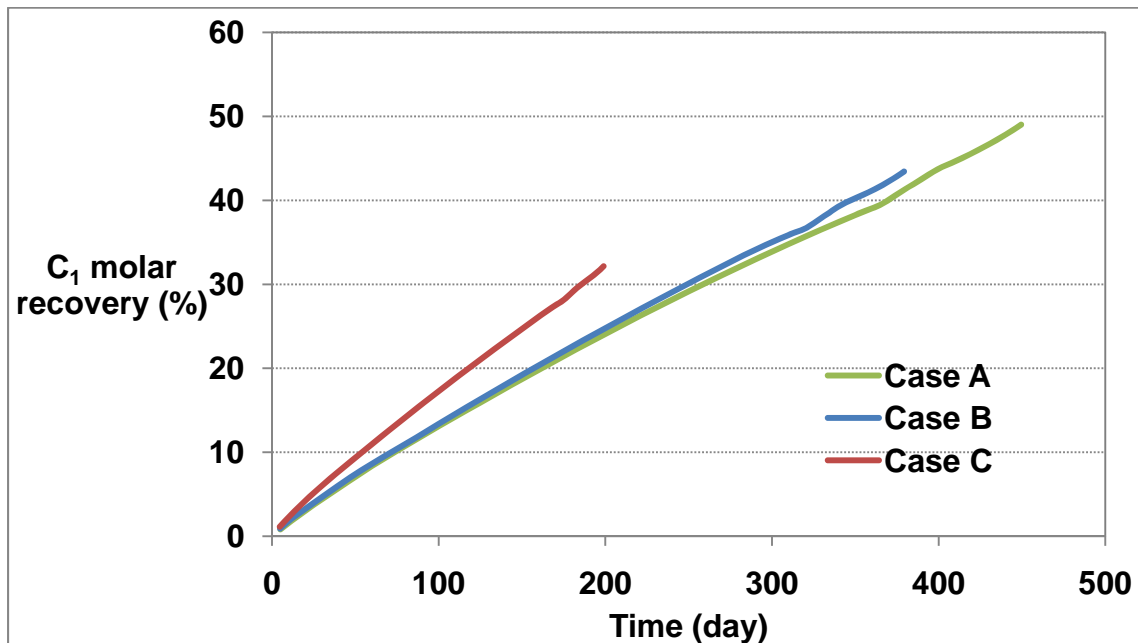


Fig. 7.11: Effect of grid size on  $C_5$  molar recovery (Example 2- With scaling capillary pressure with IFT)

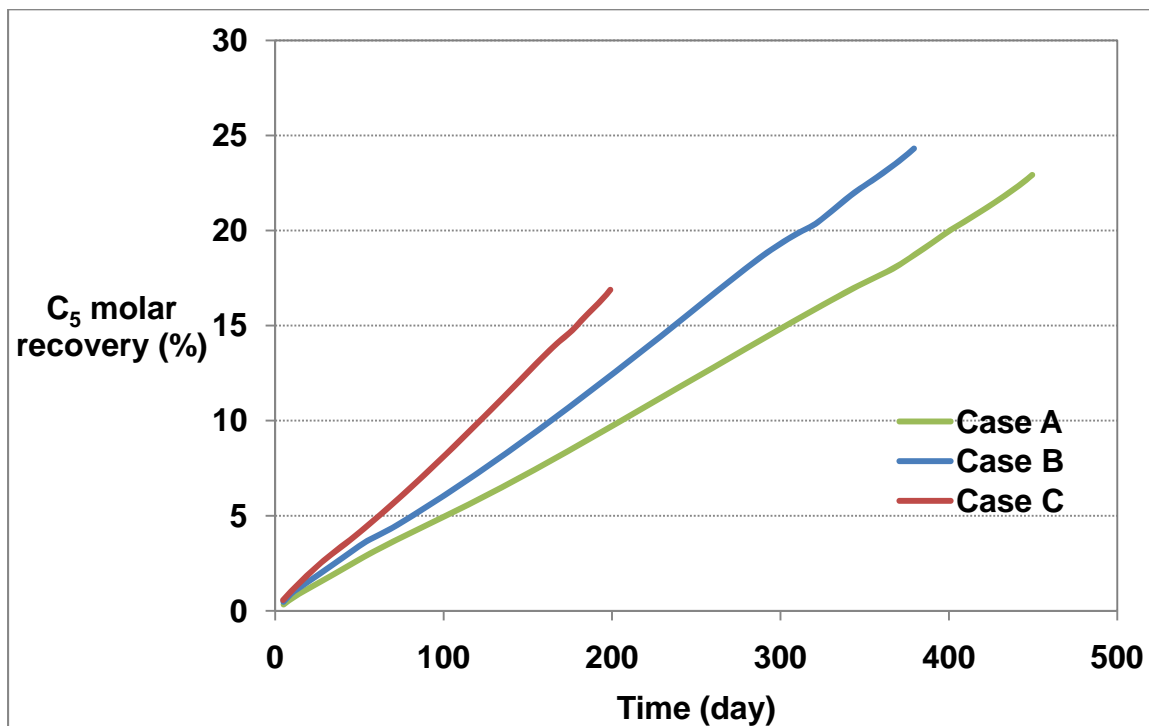


Fig. 7.12: Effect of scaling capillary pressure with IFT on  $C_1$  and  $C_5$  molar recoveries (Example 2- Case A)

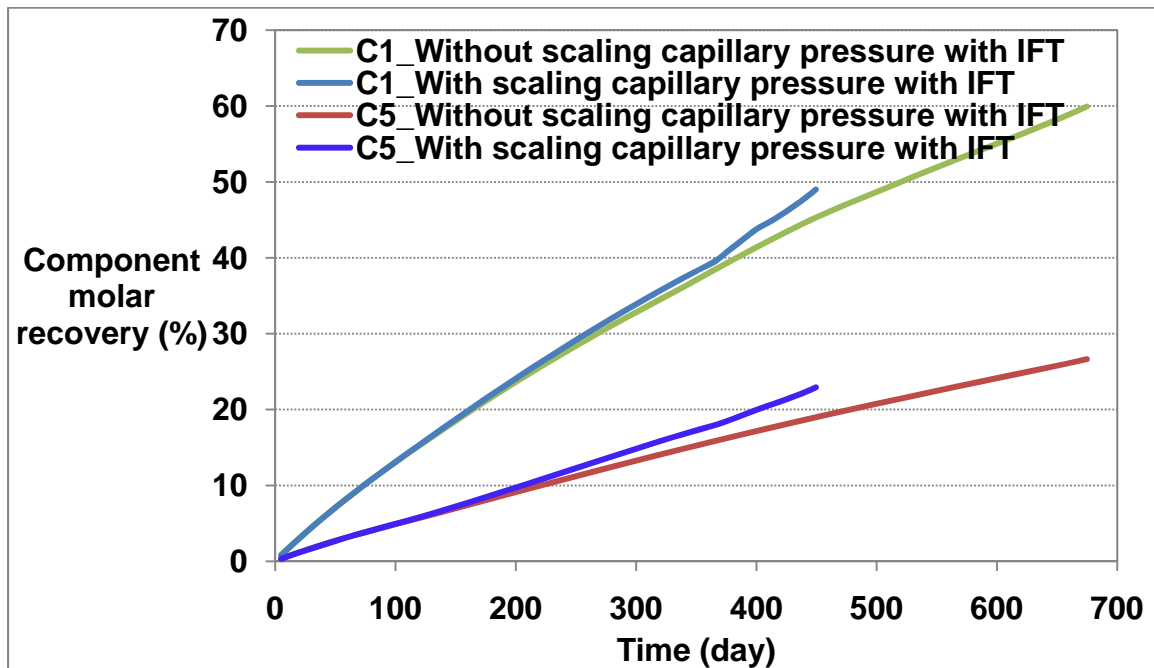


Fig. 7.13: Effect of scaling capillary pressure with IFT on  $C_1$  and  $C_5$  molar recoveries (Example 2- Case B)

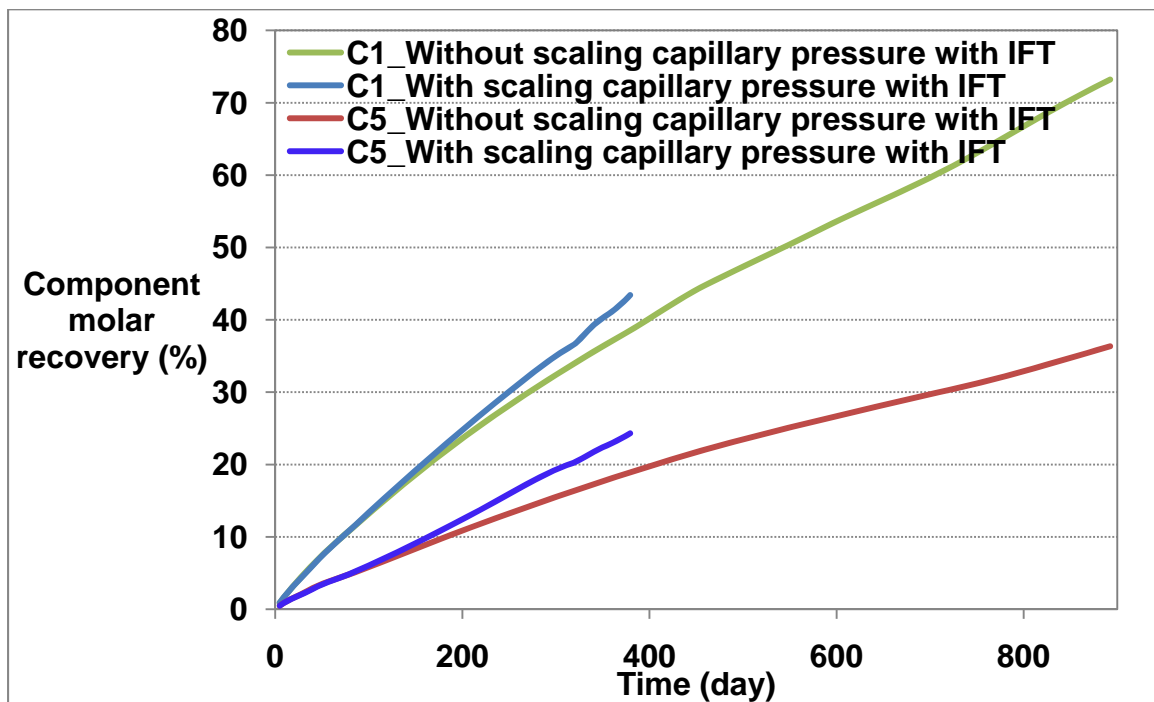


Fig. 7.14: Effect of scaling capillary pressure with IFT on C<sub>1</sub> and C<sub>5</sub> molar recoveries (Example 2- Case C)

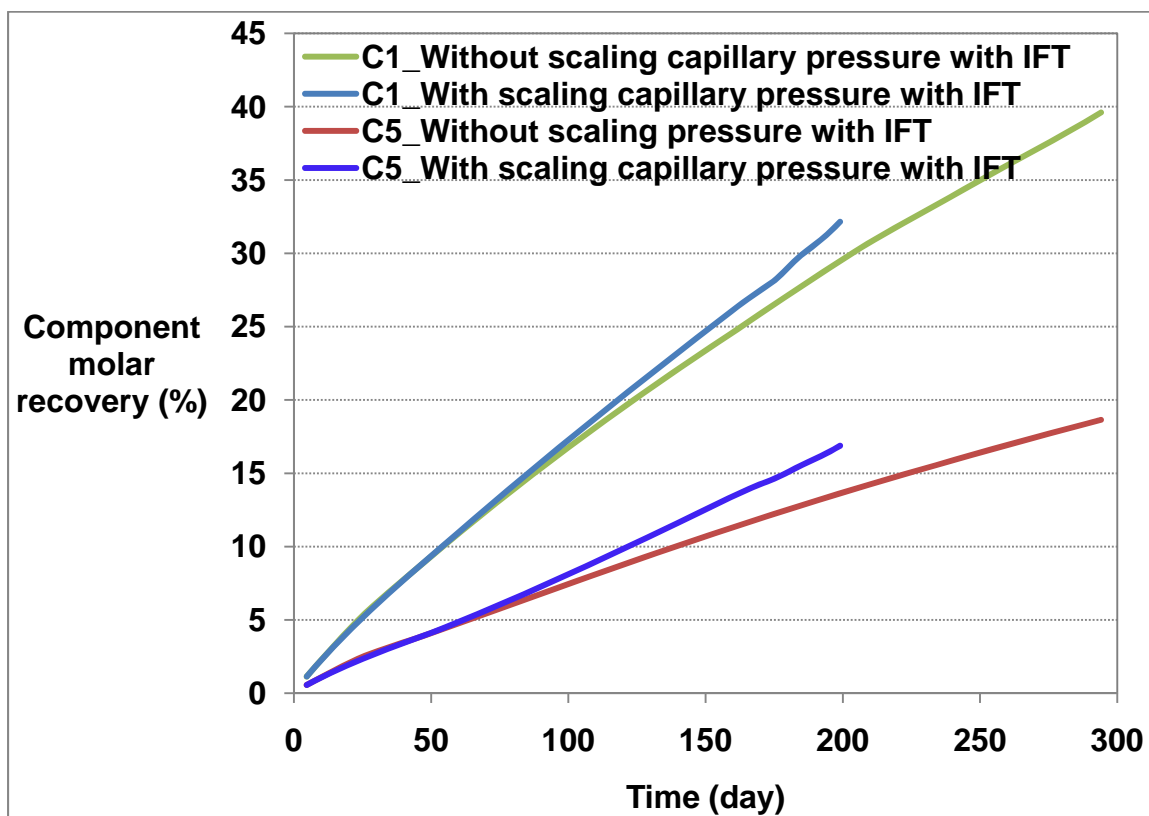


Fig. 7.15: Calculated CO<sub>2</sub> mass transfer rates at matrix-fracture surface for Example 2- Case C

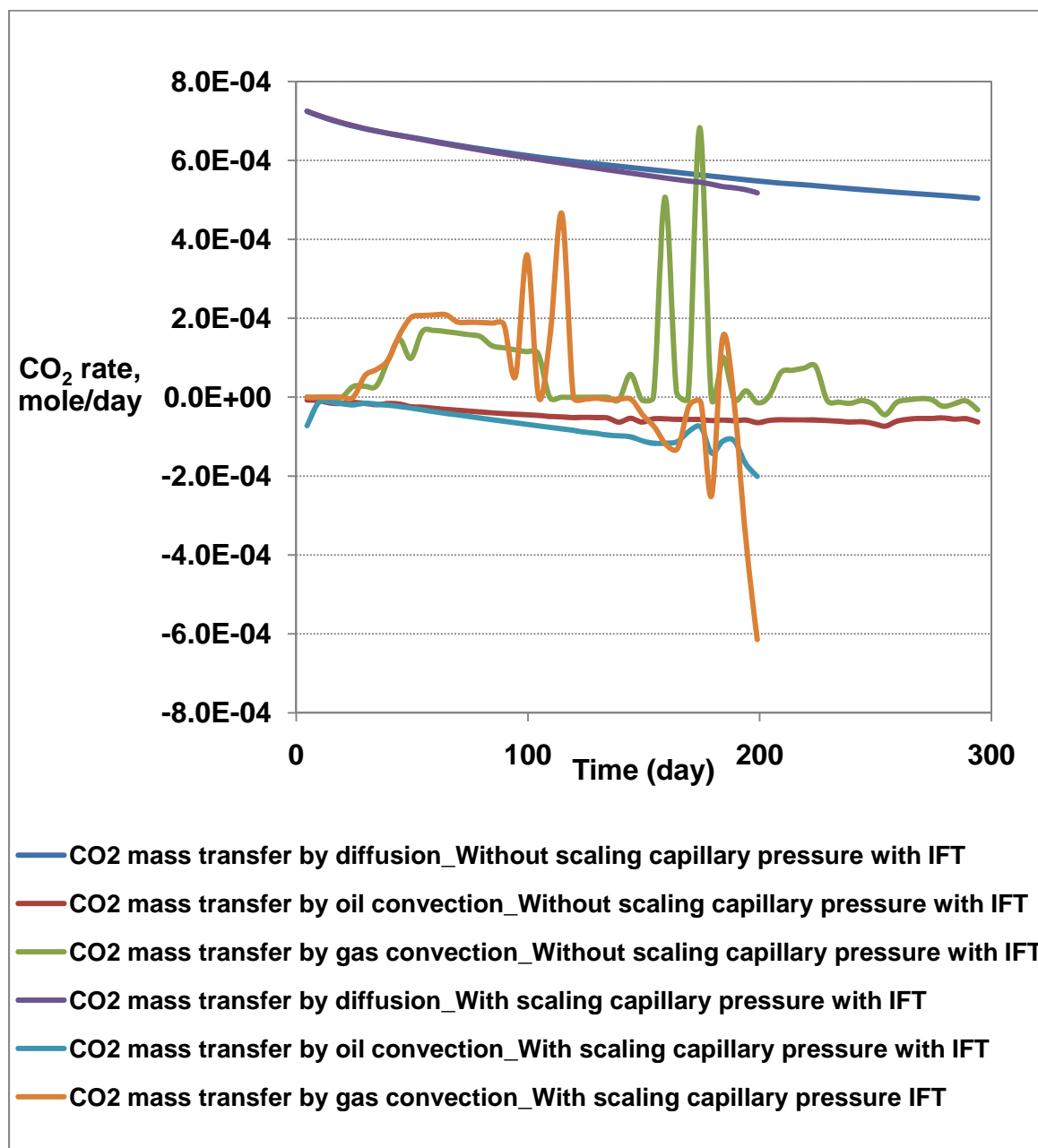


Fig. 7.16: Calculated  $C_1$  mass transfer rates at matrix-fracture surface for Example 2- Case C

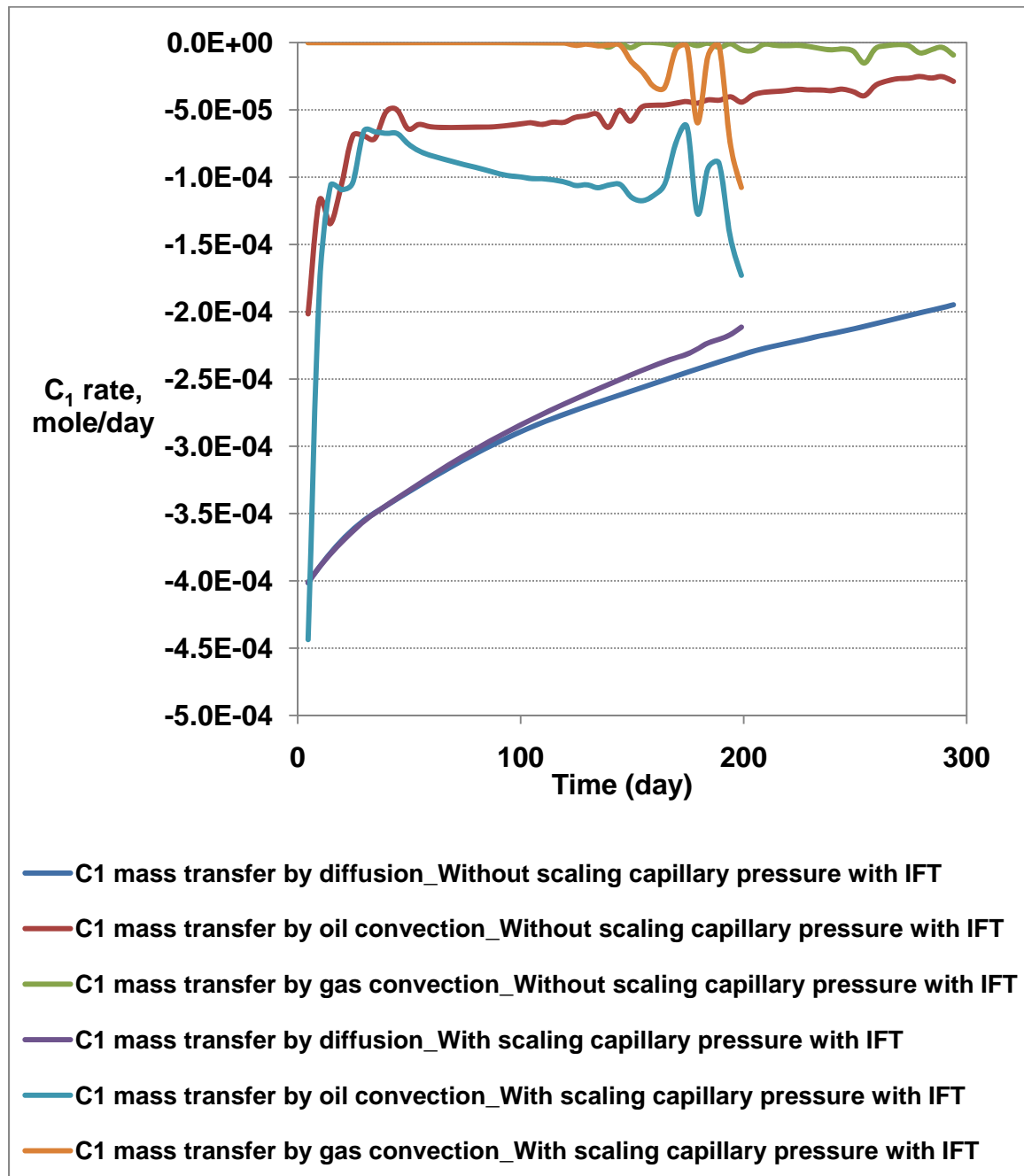
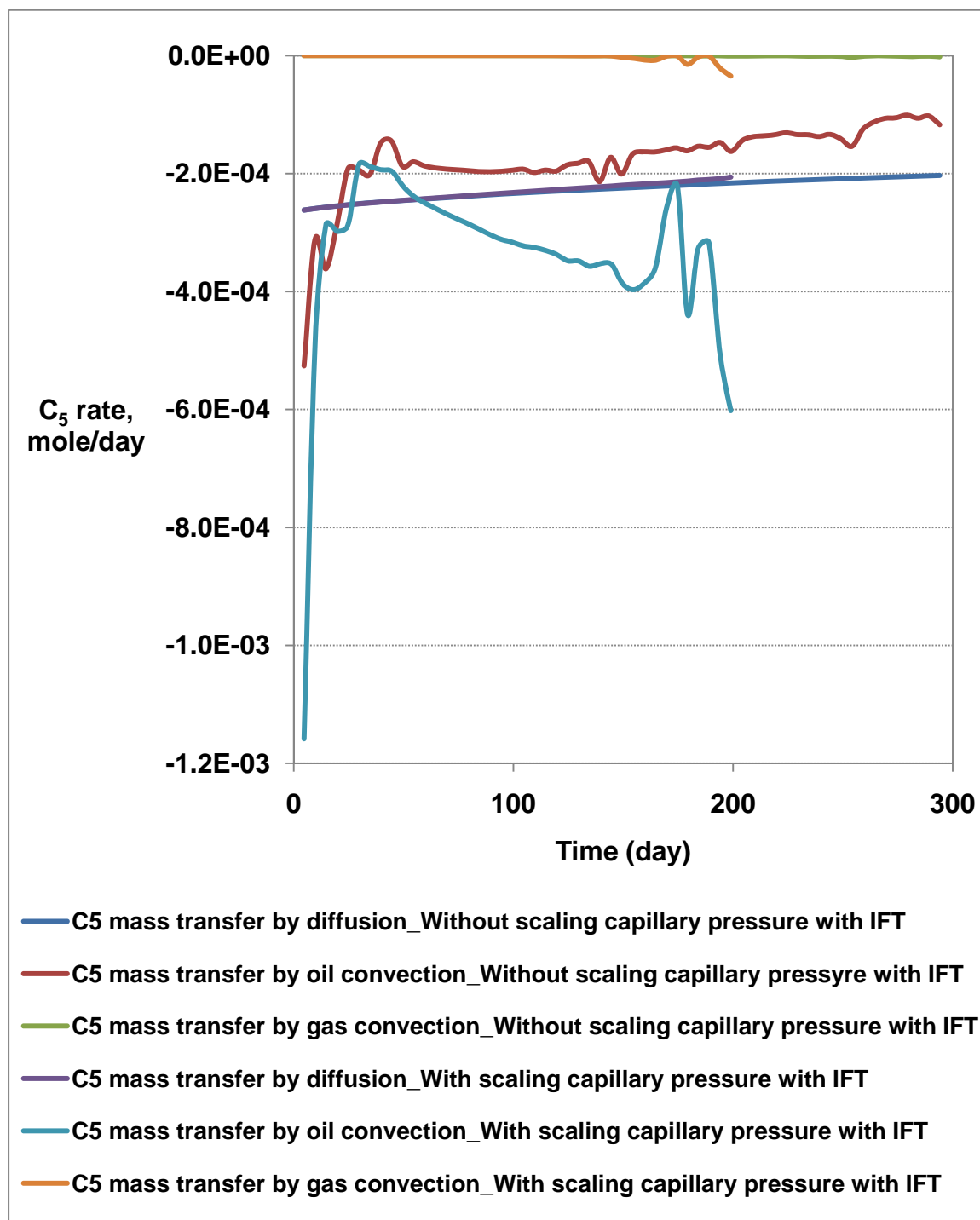


Fig. 7.17: Calculated  $C_5$  mass transfer rates at matrix-fracture surface for Example 2- Case C



## Chapter 8. Conclusions and recommendations

### 8.1. Conclusions

The following conclusions may be drawn from this dissertation:

- The mathematical model calculations matched nitrogen and carbon dioxide injection experimental data including recovery of each component, saturation profiles along the core, and differential pressure.
- Model calculations showed that there is a countercurrent flow inside the core in both nitrogen and carbon dioxide injection experiments. While oil flows from end of the core towards the fracture, gas flows in the opposite direction.
- For both injection experiments, diffusion at the matrix-fracture boundary and inside the core is an important mechanism at early times of the experiments. However, gas convection at the matrix-fracture boundary and also inside the core becomes an important transport mechanism as time advances.
- It was not possible to simulate the carbon dioxide injection experiment without considering convection between fluids (oil and gas) in the matrix and gas in the fracture.



- In the 2-D examples, diffusion at the matrix-fracture surface was an important mechanism in transporting carbon dioxide, methane, and pentane between matrix and fracture.
- The recoveries of methane and pentane were functions of grid size. Recoveries increased by decreasing the grid size in the 2-D examples.
- In the 2-D examples, scaling capillary pressure with interfacial tension enhanced CO<sub>2</sub> mass transfer between matrix and fracture in Example 2.

## 8.2. Recommendations

Recommendations for future research are following:

- The proposed mathematical model for mass-transfer between matrix and fracture can be used to model gas injection in naturally fractured reservoirs by the single porosity model.

## Nomenclatures

$a_i, a_m, a_{ij}$	Equation of state parameters
$A$	Area, $m^2$
$A_m$	Equation of state parameter
$b_i, b_m$	Equation of state parameter
$B_m$	Equation of state parameter
$C$	Concentration, mole/ $m^3$
$c$	Component
$c_\phi$	Pore compressibility, 1/psi
$c_b$	Bulk compressibility, 1/psi
$c_r$	Total rock compressibility, 1/psi
$c_i$	correction factor for component $i$ in SRK EOS, $ft^3/mole$
$D$	Depth, $m$
$D_{c,o}, D_{c,g}$	Diffusion coefficient of component $c$ in oil and gas, $cm^2/s$
$D_{ij}$	Binary diffusion coefficient of components $i$ and $j$ , $cm^2/s$
$D_g$	Gas diffusion coefficient, $cm^2/s$

$D_{e,c}$	Effective diffusion coefficient for component c at matrix-fracture boundary, $\text{cm}^2/\text{s}$
$D_{e,i}$	Effective diffusion coefficient for component i, $\text{cm}^2/\text{s}$
d	Correlation coefficients
e	Correlation coefficients
$f_{o,c}, f_{g,c}$	Fugacity of component c in oil and gas, psi
$f_{m,i}$	Fugacity of component i in phase m, psi
F	Formation resistivity factor
H	Fracture thickness in z-direction, m
k	Permeability, md
$k_c$	Diffusion mass transfer coefficient of component c at matrix-fracture boundary, $\text{mole}/(\text{m}^2 \cdot \text{s})$
$K_c$	Equilibrium ratio of component c
$k_{i,j}$	Binary interaction coefficient
$k_{ro}, k_{rg}, k_{rw}$	Relative permeability of oil, gas, and water

$k_{rgcw}$	Gas relative permeability at connate water
$k_{rocw}$	Oil relative permeability at connate water
$k_{rwro}$	Water relative permeability at residual oil saturation
$L$	Moles of oil per unit mole feed
$l$	Length of fracture, m
$m$	Cementation factor
$MW_i$	Molecular weight of component $i$ , g/gmole
$n_1$	Exponent
$n_c$	Number of components
$N_{c,p}$	Diffusion molar flux of component $c$ at phase $p$ , mole/(m <sup>2</sup> .s)
$n_{og}, n_g, n_w, n_{ow}$	Exponents on relative permeability curves
$P_{cog}, P_{cow}$	Capillary pressure (oil-gas and oil-water), psi
$P_c^0$	Reference capillary pressure at reference interfacial tension, psi
$p$	Pressure, psi
$p_{c,i}$	Critical pressure of component $i$ , psi
$P_i$	Parachor of component $i$

$p_o, p_g, p_w$	Pressure of oil, gas, and water, psi
$p_{ref}$	Reference pressure, psi
$\Delta p$	Pressure gradient, psi/ft
$q_{D, fm, c}$	Diffusion rate of component c at the matrix-fracture boundary, mole/s
$q_{C, fm, c}$	Convection mass transfer rate of component c at the matrix-fracture boundary, mole/s
q	Flow rate, ft <sup>3</sup> /day
R	Universal gas constant, cm <sup>3</sup> MPa/(K. mole)
$S_{gg}$	Geometric mean of matrix and fracture gas saturation
$S_o, S_g, S_w$	Saturation of oil, gas, and water
$S_{gr}$	Residual gas saturation
$S_{org}$	Residual oil saturation to gas
$S_{orw}$	Residual oil saturation to water
$S_{wir}$	Irreducible water saturation
$S_i$	Volume shift parameter in PR EOS

$t$	Time, day
$T$	Temperature, K
$T_{c,i}$	Critical temperature of component $i$ , K
$T_o, T_g, T_w$	Transmissibilities of oil, gas, and water, mole.md/(m <sup>2</sup> .cp)
$T_{o,c}^M, T_{g,c}^M$	Molecular transmissibilities of component $c$ in oil and gas, mole/s
$T_{r,i}$	Reduced temperature of component $i$
$V$	Moles of vapor per unit mole feed
$\bar{v}$	Average gas stream velocity in the fracture, m/s
$v_m$	Molar volume, cm <sup>3</sup> /mole
$V^L$	Molar volume of liquid, ft <sup>3</sup> /mole
$V^V$	Molar volume of vapor, ft <sup>3</sup> /mole
$V_{corr}^L$	Corrected liquid molar volume, ft <sup>3</sup> /mole
$V_{corr}^V$	Corrected gas molar volume, ft <sup>3</sup> /mole
$\bar{v}_o$	Oil bulk velocity, m/s
$\bar{v}_g$	Gas bulk velocity, m/s

$v_x, v_y, v_z$	Fluid bulk velocities in x, y, and z directions, m/s
$V_r$	Bulk volume, m <sup>3</sup>
$V_p$	Pore volume, m <sup>3</sup>
$V_{c,i}$	Critical volume of component i, cm <sup>3</sup> /mole
$W$	Fracture width in y-direction, m
$x,y,z$	Cartesian coordinates
$x_c$	Mole fraction of component c in oil phase
$x_j$	Mole fraction of component j in oil phase
$x_{i,m}, x_{j,m}$	Mole fraction of component i and j in phase m
$y_c$	Mole fraction of component c in gas phase
$y_j$	Mole fraction of component j in gas phase
$y_{c,mf}$	Mole fraction of component c in the gas phase at matrix-fracture boundary
$y_{c,f}$	Mole fraction of component c at the entrance of the fracture
$(y_i)_m, (y_i)_f$	Mole fraction of component i in gas phase in matrix and fracture
$Z_c$	Overall composition of component c

$Z_j$	Overall composition of component j
$Z_o, Z_g, Z_m$	Compressibility factor of oil, gas, and phase m
$z_{ref}$	Reference elevation, m

### Greek

$\alpha$	Equation of state parameter
$\alpha_s$	Factor for considering skin-effect at matrix-fracture boundary
$\Omega_{a,i}, \Omega_{b,i}$	Equation of state parameters for component i
$\Omega_{ij}$	Collision diameter of the Lennard-Jones potential
$\sigma_{ij}$	Collision integral of the Lennard-Jones potential
$\Delta t$	Time step, day
$\Delta x, \Delta y, \Delta z$	Grid cells dimensions, m
$\gamma_o, \gamma_g, \gamma_w$	Specific gravity of oil, gas, and water, psi/ft
$\overline{\gamma_o}, \overline{\gamma_g}, \overline{\gamma_w}$	Average specific weight of oil, gas, and water, psi/ft
$\mu_o, \mu_g, \mu_w$	Viscosity of oil, gas, and water, cp
$\phi$	Porosity



$\phi_0$	Porosity at a reference pressure
$\phi_{o,c}, \phi_{g,c}$	Fugacity coefficient of component c in oil and gas
$\rho_o, \rho_g, \rho_w$	Molar densities of oil, gas, and water, mole/cm <sup>3</sup>
$\rho_r$	Reduced density
$\rho_m$	Mixture molar density, mole/cm <sup>3</sup>
$\rho_{C,c}$	Critical density of component c, mole/cm <sup>3</sup>
$\rho_{mr}$	Reduced density of the mixture
$\sigma$	Interfacial tension, dyne/cm
$\sigma_0$	Initial interfacial tension corresponding to the read-in capillary pressure, dyne/cm
$\tau$	Tortuosity of the porous medium
$\omega_i, \omega_c$	Acentric factor of component i and c

### Subscripts

c	Component
c	Capillary

c	Critical
f	Fracture
g	Gas
i	Component
i	Grid block number in x-direction
j	Grid block number in y-direction
k	Grid block number in z-direction
m	Mixture
m	Phase
m	Matrix block
o	Oil
p	Phase
p	Pore
r	Reduced
ref	Reference
x,y,z	x,y,z directions

w            Water

**Superscript**

*l*            Iteration level

L            Liquid

n            time step

M            Molecular diffusion

v            Vapor

## References

**Amyx , J. W., Bass, D. M., and Whiting, R. L. ;** “Petroleum reservoir engineering : physical properties”, McGraw-Hill, NY, 1960

**Alavian, A. and Whitson, C. H.:** “Modeling CO<sub>2</sub> injection in a fractured chalk experiment”, SPE125362, 2009

**Arana, V. H.;** “Diffusion and convective mixing of components in naturally fractured reservoirs”, PhD thesis, Colorado School of mines, 2002

**Bird, R. B., Stewart, W. E., and Lightfoot, E. N.:** “Transport phenomena”, Second edition, 2002

**Chukwuma, F.:** “Mass transfer of gaseous carbon dioxide into a quiescent liquid hydrocarbon”, PhD thesis, University of Tulsa, 1983

**Coats, K. H.:** “An equation of state compositional modeling”, SPE, Oct. 1980

**Coats, K. H.:**“Implicit compositional simulation of single-porosity and dual-porosity reservoirs”, SPE18427, 1989

**Darvish, G.R., Lindeberg, E., Holt, T., and Utne, S.A.:** “Reservoir-conditions laboratory experiments of CO<sub>2</sub> injection into fractured cores”, SPE99650, 2006

**Da Silva, F.V. and Belery, P.:** “Molecular diffusion in naturally fractured reservoirs: a decisive recovery mechanism”, SPE19672, 1989

**Fayers, F. J. and Lee, S. T.;** “Crossflow mechanisms by gas drive in heterogenous reservoirs”, SPE 24934, 1992

**Firoozabadi, A.:** “Reservoir-fluid phase behavior and volumetric prediction with equations of state”, SPE, April 1988

**Firoozabadi, A.:** “Thermodynamics of hydrocarbon reservoirs”, McGraw-Hill, 1999

**Hashem, Y. Kh.:** “Explicit composition implicit pressure and saturation simulation of dual-porosity/permeability reservoirs”, PhD thesis, Colorado School of Mines, 1998

**Hoteit, H. and Firoozabadi, A.:** “Numerical modeling of diffusion in fractured media for gas injection and recycling schemes”, SPE103292, 2006

**Hua Hu, Whitson, C. H., and Yuanchang Qi:** “A study of recovery mechanism in a nitrogen diffusion experiment”, SPE21893, 1991

**Jhaveri, B. S. and Youngren, G. K.:** “Three-parameter modification of the Peng-Robinson equation of state to improve volumetric predictions”, SPE 13118, 1988

**Karimaie, H.:** “Aspects of water and gas injection in fractured reservoirs”, PhD thesis, Norwegian University of Science and Technology, Dec. 2007

**Lake, L. W., Pope, G. A., Carey, G., and Sepehrnoori, K.:** “Isothermal, multiphase, multicomponent fluid flow in permeable media”, *In Situ*, 8(1), 1-40, 1984

**Langness, G. L., Robertson, J. O., Chilingar, G. V.:** “Secondary recovery and carbonate reservoirs”, Elsevier, New York, 1972

**Le Gallo, Y., Le Romancer, J-F. X., Bourbiaux, B., and Fernandes, G.:** “Mass transfer in fractured reservoirs during gas injection: experimental and numerical modeling”, SPE 38924, 1997

**Lenormand, R., Le Romancer, J-F. X., Le Gallo, Y., and Bourbiaux, B.:** “Modeling the diffusion between matrix and fissure in a fissured reservoir”, SPE49007, 1998

**Le Romancer, J-F. X., Defives, D. F., Kalaydjian, F., and Fernandes, G.:** “Influence of the diffusing gas on the mechanism of oil recovery by gas diffusion in fractured reservoir”, IEA Collaborative Project on Enhanced Oil Recovery Workshop and Symposium, Bergen, Norway, 28-31 August 1994a

**Le Romancer, J-F. X., Defives, D. F., and Fernandes, G.:** “Mechanism of oil recovery by gas diffusion in presence of water”, SPE27746, 1994b

**Lohrenz, J., Bray, B. G., and Clark, C. R.:** “Calculating viscosities of reservoir fluids from their composition”, *JPT, Trans., AIME*, Vol. 225, 177-184, Oct. 1964

**McCain, W. D.:** "Properties of petroleum fluids", PennWell Publishing Company, 1990

**Moortgat, J., Firoozabadi, A., and Morravej, M.:** "A new approach to compositional modeling of CO<sub>2</sub> injection in fractured media compared to experimental data", SPE124918, 2009

**Morel, D., Latil, M., and Borbiaux, B.:** "Diffusion effect in gas flooded light oil fractured reservoirs", SPE20516, 1990

**Peneloux, A., Rauzy, E, and Freze, R.:** "A consistent correction for Redlich-Kwong-Soave volumes", Fluid Phase Equilibria, Vol. 8, p. 7, 1982

**Peng, Ding-Yu and Robinson, D. B.:** "A new two-constant equation of state", Ind. Eng. Chem. Fund., pp59-64, 1976

**Redlich, O. and Kwong, J. N. S.:** "On the thermodynamic of solutions. V-An equation of state. Fugacities of gaseous solutions", Chemical reviews, Vol. 44, pp52-63, 1949

**Reid, R. C., and Sherwood, T. K.:** "The properties of gases and liquids", 3<sup>rd</sup> edition, McGraw-Hill Book Co. Inc., New York, 1977

**Renner, T.A.:** "Measurement and correlation of diffusion coefficients for CO<sub>2</sub> and rich-gas applications", SPE, May 1988

**Reynolds, A. C., Guehria, F. M., and Thompson, L. G.:** "A robust algorithm for determining hydrocarbon PVT properties using a generalized EOS", SPE 21588, 1990

**Riazi, M. R., Whitson, C. H., and Da Silva, F.:** "Modeling of diffusional mass transfer in naturally fractured reservoirs", Journal of Petroleum Science and Engineering, 10, 239-253, 1994

**Robinson, D. B., Peng, D. Y., and Chung, S. Y. K.:** "Development of Peng-Robinson equation and its application to phase equilibrium in a system containing methanol", Fluid Phase Equilibria, Vol. 24, p. 25, 1985

**Sage, B. H. and Lacey, W. N.:** "Thermodynamic properties of the lighter paraffin hydrocarbons and nitrogen", Monograph on API Research Project 37, API, New York, 1950

**Saidi, A. M.:** "Twenty years of gas injection history into well-fractured Haft Kel field (Iran)", SPE35309, 1996

**Saidi, A. M. and Sakthikumar, S.:** "Gas gravity drainage under secondary and tertiary conditions in fractured reservoirs", SPE25614, 1993

**Sigmund, P. M.:** "Prediction of molecular diffusion at reservoir conditions. Part I", The Journal of Canadian Petroleum, 48-57, April 1976

**Sigmund, P. M.:** "Prediction of molecular diffusion at reservoir conditions. Part II- Estimating the effects of molecular diffusion and convective mixing in mutli-



component system”, The Journal of Canadian Petroleum, 48-57, July-September 1976

**Soave, G.:** “Equilibrium constants from a modified Redlich-Kwong equation of state”, Chemical Engineering science, Vol. 27, pp1197-1203, 1972

**Thiebot, B. M. and Sakthikumar, S. S.:** “Cycling fractured reservoirs containing volatile oil: laboratory investigation of the performance lean gas or nitrogen injection”,

SPE 21427, 1991

**Thomas, L. K., Dixon, T. N., Pierson, R. G., and Hermansen, H.:** “Ekofisk nitrogen injection”, SPE, June 1991

**Thomas, L.K., Dixon, T.N., and Pierson, R.G.:** “Fractured reservoir simulation”,

SPE 9305, Volume 23, Number 1, 42-54, 1983

**Wilson,G.:** “A modified Redlich-Kwong equation of state, Application to general physical data calculations”, paper 15C presented at the 1968 AIChE National Meeting, Cleveland, OH, May 4-7

**Yamamoto, R. H., Padgett, J. B., and Ford, W. T.:** “Compositional reservoir simulator for fissured system-The single-block model”, SPE, 113-128, June 1971

**Young, L. C. and Stephenson, R. E.:** “A generalized compositional approach for reservoir simulation”, SPE 10516, 1983

## Appendix A. Derivation of the multiphase flow equations

The multiphase flow equations govern compositional simulation will be derived. Basically these equations are continuity equations for each component  $c$  over a volume element  $\Delta x \Delta y \Delta z$  fixed in the space (Fig. A.1) as following:

(Molar rate of component  $c$  in) - (Molar rate of component  $c$  out) +

(Molar injection rate of component  $c$ ) - (Molar production rate of component  $c$ ) =

(Molar accumulation rate of component  $c$ ) **Eq.(A.1)**

Component  $c$  can be transported across the volume element boundary by two mechanisms: diffusion and convection. These mechanisms, injection rate, production rate, and accumulation rate will be discussed in details next.

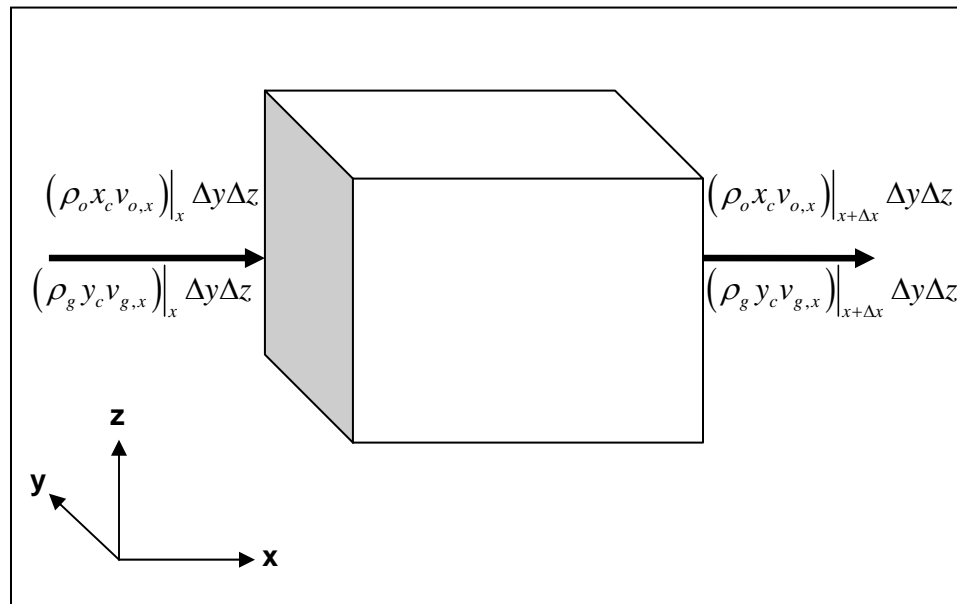


**Fig. A.1: Volume Element for deriving the multiphase flow equations**

### A.1. Convection mechanism

Convective transport is the amount of material carried along by the bulk movement of the fluid. The driving force in convective transport is potential gradient.

The molar rate in minus molar rate out of component  $c$  (mole/time) for  $x$ ,  $y$ , and  $z$  directions due to convective transport in oil and gas phases are:

$$\begin{aligned} & \left( \rho_o x_c v_{o,x} \right) \Big|_x \Delta y \Delta z + \left( \rho_g y_c v_{g,x} \right) \Big|_x \Delta y \Delta z - \left( \rho_o x_c v_{o,x} \right) \Big|_{x+\Delta x} \Delta y \Delta z - \left( \rho_g y_c v_{g,x} \right) \Big|_{x+\Delta x} \Delta y \Delta z + \\ & \left( \rho_o x_c v_{o,y} \right) \Big|_y \Delta x \Delta z + \left( \rho_g y_c v_{g,y} \right) \Big|_y \Delta x \Delta z - \left( \rho_o x_c v_{o,y} \right) \Big|_{y+\Delta y} \Delta x \Delta z - \left( \rho_g y_c v_{g,y} \right) \Big|_{y+\Delta y} \Delta x \Delta z + \\ & \left( \rho_o x_c v_{o,z} \right) \Big|_z \Delta x \Delta y + \left( \rho_g y_c v_{g,z} \right) \Big|_z \Delta x \Delta y - \left( \rho_o x_c v_{o,z} \right) \Big|_{z+\Delta z} \Delta x \Delta y - \left( \rho_g y_c v_{g,z} \right) \Big|_{z+\Delta z} \Delta x \Delta y \end{aligned}$$

**Eq.(A.2)**

where

$$\bar{v}_p = -\frac{kk_{rp}}{\mu_p} \left( \bar{\nabla} p_p - \gamma_p \bar{\nabla} D \right) \quad p = o, g \quad \text{Eq.(A.3)}$$

$\rho_o$  and  $\rho_g$  are the molar densities of oil and gas

$\phi$  is the porosity of the volume element

$x_c$  is the mole fraction of component  $c$  in the oil phase

$y_c$  is the mole fraction of component  $c$  in the gas phase

### A.2. Diffusion (molecular) transport

Molecular transport, or diffusion, can also add material across the faces of the volume element. If  $N_{o,c}$  and  $N_{g,c}$  are the diffusion molar fluxes of component  $c$

(mole c per time per area) in oil and gas phases, these quantities have units of mole per area per time and represents the amount of transport by diffusion. Therefore, following the previous approach, the molar rate in minus molar rate out of component c for x, y, and z directions by diffusion are:

$$\begin{aligned} & \left(N_{c,o,x}\right)\Big|_x \Delta y \Delta z + \left(N_{c,g,x}\right)\Big|_x \Delta y \Delta z - \left(N_{c,o,x}\right)\Big|_{x+\Delta x} \Delta y \Delta z - \left(N_{c,g,x}\right)\Big|_{x+\Delta x} \Delta y \Delta z \\ & + \left(N_{c,o,y}\right)\Big|_y \Delta x \Delta z + \left(N_{c,g,y}\right)\Big|_y \Delta x \Delta z - \left(N_{c,o,y}\right)\Big|_{y+\Delta y} \Delta x \Delta z - \left(N_{c,g,y}\right)\Big|_{y+\Delta y} \Delta x \Delta z \\ & + \left(N_{c,o,z}\right)\Big|_z \Delta x \Delta y + \left(N_{c,g,z}\right)\Big|_z \Delta x \Delta y - \left(N_{c,o,z}\right)\Big|_{z+\Delta z} \Delta x \Delta y - \left(N_{c,g,z}\right)\Big|_{z+\Delta z} \Delta x \Delta y \end{aligned}$$

**Eq.(A.4)**

where

$$N_{c,o} = \phi S_o \rho_o \left( D_{c,o} \nabla x_c \right) \quad \text{Eq.(A.5)}$$

$$N_{c,g} = \phi S_g \rho_g \left( D_{c,g} \nabla y_c \right) \quad \text{Eq.(A.6)}$$

### A.3. Production or injection

Finally, production and/or injection of component c into the volume element are given by:

$$q_{D, fm, c} + q_{C, fm, c} \quad \text{Eq.(A.7)}$$

where  $q_{D, fm}$  and  $q_{C, fm}$  are diffusion and convection mass transfer between matrix and fracture at the matrix-fracture boundary.

#### A.4. Accumulation

The total mole of fluid in the volume element at any time is  $\phi(\rho_o S_o + \rho_g S_g) \Delta x \Delta y \Delta z$ , and the mole of component  $c$  is  $\phi(\rho_o S_o x_c + \rho_g S_g y_c) \Delta x \Delta y \Delta z$ . Therefore, the rate of accumulation of mole of component  $c$  is:

$$\frac{\partial}{\partial t} [\phi(\rho_o S_o x_c + \rho_g S_g y_c)] \Delta x \Delta y \Delta z \quad \text{Eq. (A.8)}$$

#### A.5. Flow equations

The flow equations can be obtained by substituting Eq.(A.2) to Eq.(A.8) into Eq.(A.1). If the resulting equations are divided by volume element  $\Delta x \Delta y \Delta z$  and applying limit when the volume element goes to zero, it becomes:

$$\begin{aligned} & - \left[ \frac{\partial(\rho_o x_c v_{o,x} + \rho_g y_c v_{g,x})}{\partial x} + \frac{\partial(\rho_o x_c v_{o,y} + \rho_g y_c v_{g,y})}{\partial y} + \frac{\partial(\rho_o x_c v_{o,z} + \rho_g y_c v_{g,z})}{\partial z} \right] \\ & - \left[ \frac{\partial(N_{c,o,x} + N_{c,g,x})}{\partial x} + \frac{\partial(N_{c,o,y} + N_{c,g,y})}{\partial y} + \frac{\partial(N_{c,o,z} + N_{c,g,z})}{\partial z} \right] \\ & + q_{D,fm,c} + q_{C,fm,c} = \frac{\partial}{\partial t} [\phi(\rho_o S_o x_c + \rho_g S_g y_c)] \end{aligned} \quad \text{Eq.(A.9)}$$

Or, in vector notation,

$$-\nabla \cdot (\rho_o x_c v_o + \rho_g y_c v_g) - \nabla \cdot (N_{c,o} + N_{c,g}) + q_{D,fm,c} + q_{C,fm,c} = \frac{\partial}{\partial t} [\phi(\rho_o S_o x_c + \rho_g S_g y_c)] \quad \text{Eq.(A.10)}$$

By substituting  $v_o$  and  $v_g$  from Eq. (A.3) and  $N_{c,o}$  and  $N_{c,g}$  from Eq.(A.5) and Eq.(A.6) into Eq. (A.10), it becomes:

$$\begin{aligned} & \nabla \cdot \left( \rho_o x_c \frac{kk_{ro}}{\mu_o} (\bar{\nabla} p_o - \gamma_o \bar{\nabla} D) + \rho_g y_c \frac{kk_{rg}}{\mu_g} (\bar{\nabla} p_g - \gamma_g \bar{\nabla} D) \right) + \\ & \nabla \cdot \left( \phi S_o \rho_o (D_{c,o} \nabla x_c) + \phi S_g \rho_g (D_{c,g} \nabla y_c) \right) + q_{D, fm, c} + q_{C, fm, c} = \frac{\partial}{\partial t} \left[ \phi (\rho_o S_o x_c + \rho_g S_g y_c) \right] \end{aligned}$$

**Eq.(A.11)**

Eq. (A.11) is a general case of compositional multiphase flow through porous media for each component in oil and gas phases.

For the water phase, considering that hydrocarbon phases are immiscible in water, we have,

$$\nabla \cdot \left( \rho_w \frac{kk_{rw}}{\mu_w} (\bar{\nabla} p_w - \gamma_w \bar{\nabla} D) \right) = \frac{\partial}{\partial t} \left[ \phi (\rho_w S_w) \right]$$

**Eq.(A.12)**

## Appendix B. Discretizing the flow equations

The final form of the general hydrocarbon flow equations, as obtained in Appendix A (Eq. A.12), is as follows

$$\begin{aligned} & \nabla \cdot \left( \rho_o x_c \frac{kk_{ro}}{\mu_o} (\bar{\nabla} p_o - \gamma_o \bar{\nabla} D) + \rho_g y_c \frac{kk_{rg}}{\mu_g} (\bar{\nabla} p_g - \gamma_g \bar{\nabla} D) \right)_{i,i,k}^{n+1} + \\ & \nabla \cdot \left( \phi S_o \rho_o (D_{c,o} \nabla x_c) + \phi S_g \rho_g (D_{c,g} \nabla y_c) \right)_{i,j,k}^{n+1} + (q_{D, fm,c} + q_{C, fm,c})_{i,j,k}^{n+1} = \text{Eq. (B.1)} \\ & \frac{\partial}{\partial t} \left[ \phi (\rho_o S_o x_c + \rho_g S_g y_c) \right]_{i,j,k}^{n+1} \end{aligned}$$

where  $c = 1, 2, \dots, n_c$

For simplicity, flow equations are discretized in x-direction only. The same procedure can be applied to y and z directions. Eq.(B.1) in x-direction becomes:

$$\begin{aligned} & \frac{\partial}{\partial x} \left( \rho_o x_c \frac{kk_{ro}}{\mu_o} \left( \frac{\partial p_o}{\partial x} - \gamma_o \frac{\partial D}{\partial x} \right) + \rho_g y_c \frac{kk_{rg}}{\mu_g} \left( \frac{\partial p_g}{\partial x} - \gamma_g \frac{\partial D}{\partial x} \right) \right)_{i,j,k}^{n+1} + \\ & \frac{\partial}{\partial x} \left( \phi S_o \rho_o \left( D_{c,o} \frac{\partial x_c}{\partial x} \right) + \phi S_g \rho_g \left( D_{c,g} \frac{\partial y_c}{\partial x} \right) \right)_{i,j,k}^{n+1} + (q_{D, fm,c} + q_{C, fm,c})_{i,j,k}^{n+1} = \text{Eq. (B.2)} \\ & \frac{\partial}{\partial t} \left[ \phi (\rho_o S_o x_c + \rho_g S_g y_c) \right]_{i,j,k}^{n+1} \end{aligned}$$

### B.1. Discretization oil and gas convective terms in x-direction

Defining oil and gas convective terms as:

$$v_{ox} = \rho_o x_c \frac{k_x k_{ro}}{\mu_o} \left( \frac{\partial p_o}{\partial x} - \gamma_o \frac{\partial D}{\partial x} \right) \quad \text{Eq. (B.3)}$$

$$v_{gx} = \rho_g y_c \frac{k_x k_{rg}}{\mu_g} \left( \frac{\partial p_g}{\partial x} - \gamma_g \frac{\partial D}{\partial x} \right) \quad \text{Eq. (B.4)}$$

Oil convective flux term will be discretized first. By substituting Eq.(B.3) into Eq.(B.2), the oil convective flux term in equation Eq. (B.2) in x-direction becomes:

$$\frac{\partial}{\partial x} \left[ x_c \rho_o \frac{k_x k_{ro}}{\mu_o} \left( \frac{\partial p_o}{\partial x} - \gamma_o \frac{\partial D}{\partial x} \right) \right]_{i,j,k}^{n+1} = \frac{\partial v_{o,x_{i,j,k}}^{n+1}}{\partial x} \quad \text{Eq. (B.5)}$$

Using central finite differences into Eq. (B.5):

$$\frac{\partial v_{o,x_{i,j,k}}^{n+1}}{\partial x} = \frac{v_{o,x_{i+\frac{1}{2},j,k}}^{n+1} - v_{o,x_{i-\frac{1}{2},j,k}}^{n+1}}{\Delta x_{i,j,k}} \quad \Delta x_{i,j,k} = x_{i+\frac{1}{2},j,k} - x_{i-\frac{1}{2},j,k} \quad \text{Eq. (B.6)}$$

where,

$$v_{o,x_{i+\frac{1}{2},j,k}}^{n+1} = \left( \rho_o x_c \frac{k_x k_{ro}}{\mu_o} \right)_{i+\frac{1}{2},j,k}^{n+1} \left[ \frac{p_{o_{i+1,j,k}} - p_{o_{i,j,k}}}{\Delta x_{i+\frac{1}{2},j,k}} - \gamma_{o_{i+\frac{1}{2},j,k}} \frac{D_{i+1,j,k} - D_{i,j,k}}{\Delta x_{i+\frac{1}{2},j,k}} \right]^{n+1} \Delta x_{i+\frac{1}{2},j,k} = x_{i+1,j,k} - x_{i,j,k} \quad \text{Eq. (B.7)}$$

and,

$$v_{o,x_{i-\frac{1}{2},j,k}}^{n+1} = \left( \rho_o x_c \frac{k_x k_{ro}}{\mu_o} \right)_{i-\frac{1}{2},j,k}^{n+1} \left[ \frac{p_{o_{i,j,k}} - p_{o_{i-1,j,k}}}{\Delta x_{i-\frac{1}{2},j,k}} - \gamma_{o_{i-\frac{1}{2},j,k}} \frac{D_{i,j,k} - D_{i-1,j,k}}{\Delta x_{i-\frac{1}{2},j,k}} \right]^{n+1} \Delta x_{i-\frac{1}{2},j,k} = x_{i,j,k} - x_{i-1,j,k} \quad \text{Eq. (B.8)}$$

By substituting Eq. (B.7) and Eq. (B.8) into Eq. (B.5):



$$\frac{\partial v_{ox_{i,j,k}}^{n+1}}{\partial x} = \frac{1}{\Delta x_{i,j,k}} \left[ \left( \frac{\rho_o x_c \frac{k_x k_{ro}}{\mu_o}}{\Delta x} \right)_{i+\frac{1}{2},j,k} \left( p_{o_{i+1,j,k}} - p_{o_{i,j,k}} - \gamma_{o_{i+\frac{1}{2},j,k}} [D_{i+1,j,k} - D_{i,j,k}] \right) \right]^{n+1} - \frac{1}{\Delta x_{i,j,k}} \left[ \left( \frac{\rho_o x_c \frac{k_x k_{ro}}{\mu_o}}{\Delta x} \right)_{i-\frac{1}{2},j,k} \left( p_{o_{i,j,k}} - p_{o_{i-1,j,k}} - \gamma_{o_{i-\frac{1}{2},j,k}} [D_{i,j,k} - D_{i-1,j,k}] \right) \right]^{n+1} \quad \text{Eq. (B.9)}$$

Gas convective flux term can be discretized by the same manner as:

$$\frac{\partial v_{gx_{i,j,k}}^{n+1}}{\partial x} = \frac{1}{\Delta x_{i,j,k}} \left[ \left( \frac{\rho_g y_c \frac{k_x k_{rg}}{\mu_g}}{\Delta x} \right)_{i+\frac{1}{2},j,k} \left( p_{g_{i+1,j,k}} - p_{g_{i,j,k}} - \gamma_{g_{i+\frac{1}{2},j,k}} [D_{i+1,j,k} - D_{i,j,k}] \right) \right]^{n+1} - \frac{1}{\Delta x_{i,j,k}} \left[ \left( \frac{\rho_g y_c \frac{k_x k_{rg}}{\mu_g}}{\Delta x} \right)_{i-\frac{1}{2},j,k} \left( p_{g_{i,j,k}} - p_{g_{i-1,j,k}} - \gamma_{g_{i-\frac{1}{2},j,k}} [D_{i,j,k} - D_{i-1,j,k}] \right) \right]^{n+1} \quad \text{Eq. (B.10)}$$

## B.2. Discretization the oil and gas diffusive flux term in x-direction

Oil diffusive flux term will be discretized first as:

$$\frac{\partial}{\partial x} \left( \phi S_o \rho_o \left( D_{c,o} \frac{\partial x_c}{\partial x} \right) \right)_{i,j,k}^{n+1} = \frac{1}{\Delta x_{i,j,k}} \left[ \left( \phi S_o \rho_o \left( D_{c,o} \frac{\partial x_c}{\partial x} \right) \right)_{i+\frac{1}{2},j,k}^{n+1} - \left( \phi S_o \rho_o \left( D_{c,o} \frac{\partial x_c}{\partial x} \right) \right)_{i-\frac{1}{2},j,k}^{n+1} \right]$$

$$\text{Eq. (B.11)}$$

Expanding the (i+1/2) and (i-1/2) term in Eq. (B.11):

$$\left( \phi S_o \rho_o \left( D_{c,o} \frac{\partial x_c}{\partial x} \right) \right)_{i+\frac{1}{2},j,k}^{n+1} = \left( \frac{\phi S_o \rho_o D_{c,o}}{\Delta x} \right)_{i+\frac{1}{2},j,k}^{n+1} \left( x_{c_{i+1,j,k}} - x_{c_{i,j,k}} \right)^{n+1} \quad \text{Eq. (B.12)}$$

$$\left( \phi S_o \rho_o \left( D_{c,o} \frac{\partial x_c}{\partial x} \right) \right)_{i-\frac{1}{2},j,k}^{n+1} = \left( \frac{\phi S_o \rho_o D_{c,o}}{\Delta x} \right)_{i-\frac{1}{2},j,k}^{n+1} \left( x_{c_{i,j,k}} - x_{c_{i-1,j,k}} \right)^{n+1} \quad \text{Eq. (B.13)}$$

Substituting Eq.(B.12) and Eq.(B.13) in Eq.(B.11):

$$\frac{\partial}{\partial x} \left( \phi S_o \rho_o \left( D_{c,o} \nabla x_c \right) \right)_{i,j,k}^{n+1} = \frac{1}{\Delta x_{i,j,k}} \left[ \left( \frac{\phi S_o \rho_o D_{c,o}}{\Delta x} \right)_{i+\frac{1}{2},j,k}^{n+1} \left( x_{c_{i+1,j,k}} - x_{c_{i,j,k}} \right)^{n+1} - \left( \frac{\phi S_o \rho_o D_{c,o}}{\Delta x} \right)_{i-\frac{1}{2},j,k}^{n+1} \left( x_{c_{i,j,k}} - x_{c_{i-1,j,k}} \right)^{n+1} \right]$$

**Eq. (B.14)**

The same procedure can be used to discretize gas molecular diffusion term as:

$$\frac{\partial}{\partial x} \left( \phi S_g \rho_g \left( D_{c,g} \nabla y_c \right) \right)_{i,j,k}^{n+1} = \frac{1}{\Delta x_{i,j,k}} \left[ \left( \frac{\phi S_g \rho_g D_{c,g}}{\Delta x} \right)_{i+\frac{1}{2},j,k}^{n+1} \left( y_{c_{i+1,j,k}} - y_{c_{i,j,k}} \right)^{n+1} - \left( \frac{\phi S_g \rho_g D_{c,g}}{\Delta x} \right)_{i-\frac{1}{2},j,k}^{n+1} \left( y_{c_{i,j,k}} - y_{c_{i-1,j,k}} \right)^{n+1} \right]$$

**Eq. (B.15)**

### B.3. Discretization the accumulation term

The accumulation term is discretized by using regressive finite differences in time as:

$$\frac{\partial}{\partial t} \left[ \phi (x_c \rho_o S_o + y_c \rho_g S_g) \right]_{i,j,k} = \frac{1}{\Delta t} \left[ \left( \phi x_c \rho_o S_o + \phi y_c \rho_g S_g \right)^{n+1} - \left( \phi x_c \rho_o S_o + \phi y_c \rho_g S_g \right)^n \right]_{i,j,k}$$

Eq. (B.16)

#### B.4. Final form of discretized flow equations

Substituting equations Eq.(B.9), Eq.(B.10), Eq.(B.14), Eq.(B.15), and Eq.(B.16) into equation Eq. (B.2):

$$\begin{aligned} & \frac{1}{\Delta x_{i,j,k}} \left[ \left( \frac{\rho_o x_c \frac{k_x k_{ro}}{\mu_o}}{\Delta x} \right)_{i+\frac{1}{2},j,k} \left( p_{o_{i+1,j,k}} - p_{o_{i,j,k}} - \gamma_{o_{i+\frac{1}{2},j,k}} [D_{i+1,j,k} - D_{i,j,k}] \right) \right]^{n+1} - \\ & \frac{1}{\Delta x_{i,j,k}} \left[ \left( \frac{\rho_o x_c \frac{k_x k_{ro}}{\mu_o}}{\Delta x} \right)_{i-\frac{1}{2},j,k} \left( p_{o_{i,j,k}} - p_{o_{i-1,j,k}} - \gamma_{o_{i-\frac{1}{2},j,k}} [D_{i,j,k} - D_{i-1,j,k}] \right) \right]^{n+1} + \\ & \frac{1}{\Delta x_{i,j,k}} \left[ \left( \frac{\rho_g y_c \frac{k_x k_{rg}}{\mu_g}}{\Delta x} \right)_{i+\frac{1}{2},j,k} \left( p_{g_{i+1,j,k}} - p_{g_{i,j,k}} - \gamma_{g_{i+\frac{1}{2},j,k}} [D_{i+1,j,k} - D_{i,j,k}] \right) \right]^{n+1} - \\ & \frac{1}{\Delta x_{i,j,k}} \left[ \left( \frac{\rho_g y_c \frac{k_x k_{rg}}{\mu_g}}{\Delta x} \right)_{i-\frac{1}{2},j,k} \left( p_{g_{i,j,k}} - p_{g_{i-1,j,k}} - \gamma_{g_{i-\frac{1}{2},j,k}} [D_{i,j,k} - D_{i-1,j,k}] \right) \right]^{n+1} + \\ & \frac{1}{\Delta x_{i,j,k}} \left[ \left( \frac{\phi S_o \rho_o D_{c,o}}{\Delta x} \right)_{i+\frac{1}{2},j,k}^{n+1} \left( x_{c_{i+1,j,k}} - x_{c_{i,j,k}} \right)^{n+1} - \left( \frac{\phi S_o \rho_o D_{c,o}}{\Delta x} \right)_{i-\frac{1}{2},j,k}^{n+1} \left( x_{c_{i,j,k}} - x_{c_{i-1,j,k}} \right)^{n+1} \right] + \\ & \frac{1}{\Delta x_{i,j,k}} \left[ \left( \frac{\phi S_g \rho_g D_{c,g}}{\Delta x} \right)_{i+\frac{1}{2},j,k}^{n+1} \left( y_{c_{i+1,j,k}} - y_{c_{i,j,k}} \right)^{n+1} - \left( \frac{\phi S_g \rho_g D_{c,g}}{\Delta x} \right)_{i-\frac{1}{2},j,k}^{n+1} \left( y_{c_{i,j,k}} - y_{c_{i-1,j,k}} \right)^{n+1} \right] + (q_{D, fm,c} + q_{C, fm,c})_{i,j,k}^{n+1} \\ & = \frac{1}{\Delta t} \left[ \left( \phi x_c \rho_o S_o + \phi y_c \rho_g S_g \right)^{n+1} - \left( \phi x_c \rho_o S_o + \phi y_c \rho_g S_g \right)^n \right]_{i,j,k} \end{aligned}$$

Eq. (B.17)

Multiplying Eq. (B.17) by the volume of the grid cell,  $V_{r,i,j,k} = \Delta y_{i,j,k} \Delta z_{i,j,k} \Delta x_{i,j,k}$ , and rearranging, it becomes:

$$\begin{aligned}
& \left[ \left( \frac{\Delta y_{i,j,k} \Delta z_{i,j,k} \rho_o x_c \frac{k_x k_{ro}}{\mu_o}}{\Delta x} \right)_{i+\frac{1}{2},j,k} \left( p_{o_{i+1,j,k}} - p_{o_{i,j,k}} - \gamma_{o_{i+\frac{1}{2},j,k}} [D_{i+1,j,k} - D_{i,j,k}] \right) \right]^{n+1} - \\
& \left[ \left( \frac{\Delta y_{i,j,k} \Delta z_{i,j,k} \rho_o x_c \frac{k_x k_{ro}}{\mu_o}}{\Delta x} \right)_{i-\frac{1}{2},j,k} \left( p_{o_{i,j,k}} - p_{o_{i-1,j,k}} - \gamma_{o_{i-\frac{1}{2},j,k}} [D_{i,j,k} - D_{i-1,j,k}] \right) \right]^{n+1} + \\
& \left[ \left( \frac{\Delta y_{i,j,k} \Delta z_{i,j,k} \rho_g y_c \frac{k_x k_{rg}}{\mu_g}}{\Delta x} \right)_{i+\frac{1}{2},j,k} \left( p_{g_{i+1,j,k}} - p_{g_{i,j,k}} - \gamma_{g_{i+\frac{1}{2},j,k}} [D_{i+1,j,k} - D_{i,j,k}] \right) \right]^{n+1} - \\
& \left[ \left( \frac{\Delta y_{i,j,k} \Delta z_{i,j,k} \rho_g y_c \frac{k_x k_{rg}}{\mu_g}}{\Delta x} \right)_{i-\frac{1}{2},j,k} \left( p_{g_{i,j,k}} - p_{g_{i-1,j,k}} - \gamma_{g_{i-\frac{1}{2},j,k}} [D_{i,j,k} - D_{i-1,j,k}] \right) \right]^{n+1} + \\
& \left[ \left( \frac{\Delta y_{i,j,k} \Delta z_{i,j,k} \phi S_o \rho_o D_{c,o}}{\Delta x} \right)_{i+\frac{1}{2},j,k} (x_{c_{i+1,j,k}} - x_{c_{i,j,k}})^{n+1} - \left( \frac{\Delta y_{i,j,k} \Delta z_{i,j,k} \phi S_o \rho_o D_{c,o}}{\Delta x} \right)_{i-\frac{1}{2},j,k} (x_{c_{i,j,k}} - x_{c_{i-1,j,k}})^{n+1} \right] + \\
& \left[ \left( \frac{\Delta y_{i,j,k} \Delta z_{i,j,k} \phi S_g \rho_g D_{c,g}}{\Delta x} \right)_{i+\frac{1}{2},j,k} (y_{c_{i+1,j,k}} - y_{c_{i,j,k}})^{n+1} - \left( \frac{\Delta y_{i,j,k} \Delta z_{i,j,k} \phi S_g \rho_g D_{c,g}}{\Delta x} \right)_{i-\frac{1}{2},j,k} (y_{c_{i,j,k}} - y_{c_{i-1,j,k}})^{n+1} \right] + \\
& (q_{D,fm,c} + q_{C,fm,c})_{i,j,k}^{n+1} = \frac{V_{r,i,j,k}}{\Delta t} \left[ (\phi x_c \rho_o S_o + \phi y_c \rho_g S_g)^{n+1} - (\phi x_c \rho_o S_o + \phi y_c \rho_g S_g)^n \right]_{i,j,k}
\end{aligned}$$

**Eq. (B.18)**

Now, defining the transmissibility terms for oil and gas phases as:

$$T_{o,i\pm\frac{1}{2},j,k} = \left[ \frac{\Delta y_{i,j,k} \Delta z_{i,j,k} \rho_o \frac{k_x k_{ro}}{\mu_o}}{\Delta x} \right]_{i\pm\frac{1}{2},j,k} \quad \text{Eq. (B.19)}$$

$$T_{o,i\pm\frac{1}{2},j,k} = \left[ \frac{\Delta y_{i,j,k} \Delta z_{i,j,k} \rho_g \frac{k_x k_{rg}}{\mu_g}}{\Delta x} \right]_{i\pm\frac{1}{2},j,k} \quad \text{Eq. (B.20)}$$

$$T_{o,c,i\pm\frac{1}{2},j,k}^M = \left[ \frac{\Delta y_{i,j,k} \Delta z_{i,j,k} \phi S_o \rho_o D_{c,o}}{\Delta x} \right]_{i\pm\frac{1}{2},j,k} \quad \text{Eq. (B.21)}$$

$$T_{g,c,i\pm\frac{1}{2},j,k}^M = \left[ \frac{\Delta y_{i,j,k} \Delta z_{i,j,k} \phi S_g \rho_g D_{c,g}}{\Delta x} \right]_{i\pm\frac{1}{2},j,k} \quad \text{Eq. (B.22)}$$

Substituting Equations Eq. (B.19) through Eq. (B.22) into Eq. (B.18), it becomes:

$$\begin{aligned} & \left[ (T_o x_c)_{i+\frac{1}{2},j,k} \left( p_{o_{i+1},j,k} - p_{o_{i,j,k}} - \gamma_{o_{i+\frac{1}{2},j,k}} [D_{i+1,j,k} - D_{i,j,k}] \right) \right]^{n+1} - \\ & \left[ (T_o x_c)_{i-\frac{1}{2},j,k} \left( p_{o_{i,j,k}} - p_{o_{i-1},j,k} - \gamma_{o_{i-\frac{1}{2},j,k}} [D_{i,j,k} - D_{i-1,j,k}] \right) \right]^{n+1} + \\ & \left[ (T_g y_c)_{i+\frac{1}{2},j,k} \left( p_{g_{i+1},j,k} - p_{g_{i,j,k}} - \gamma_{g_{i+\frac{1}{2},j,k}} [D_{i+1,j,k} - D_{i,j,k}] \right) \right]^{n+1} - \\ & \left[ (T_g y_c)_{i-\frac{1}{2},j,k} \left( p_{g_{i,j,k}} - p_{g_{i-1},j,k} - \gamma_{g_{i-\frac{1}{2},j,k}} [D_{i,j,k} - D_{i-1,j,k}] \right) \right]^{n+1} + \\ & \left[ (T_{o,c}^M)_{i+\frac{1}{2},j,k}^{n+1} (x_{c_{i+1},j,k} - x_{c_{i,j,k}})^{n+1} - (T_{o,c}^M)_{i-\frac{1}{2},j,k}^{n+1} (x_{c_{i,j,k}} - x_{c_{i-1},j,k})^{n+1} \right] + \\ & \left[ (T_{g,c}^M)_{i+\frac{1}{2},j,k}^{n+1} (y_{c_{i+1},j,k} - y_{c_{i,j,k}})^{n+1} - (T_{g,c}^M)_{i-\frac{1}{2},j,k}^{n+1} (y_{c_{i,j,k}} - y_{c_{i-1},j,k})^{n+1} \right] + \\ & (q_{D,fm,c} + q_{C,fm,c})_{i,j,k}^{n+1} = \frac{V_{r,i,j,k}}{\Delta t} \left[ (\phi x_c \rho_o S_o + \phi y_c \rho_g S_g)^{n+1} - (\phi x_c \rho_o S_o + \phi y_c \rho_g S_g)^n \right]_{i,j,k} \end{aligned} \quad \text{Eq. (B.23)}$$

Eq. (B.23) can also be written as:

$$\Delta \left[ T_o x_c (\Delta p_o - \Delta(\gamma_o D)) \right]_{i,j,k}^{n+1} + \Delta \left[ T_g y_c (\Delta p_g - \Delta(\gamma_g D)) \right]_{i,j,k}^{n+1} + \Delta \left[ T_{o,c}^M \Delta x_c \right]_{i,j,k}^{n+1} + \Delta \left[ T_{g,c}^M \Delta y_c \right]_{i,j,k}^{n+1} + (q_{D,fm,c} + q_{C,fm,c})_{i,j,k}^{n+1} = \frac{V_{r,i,j,k}}{\Delta t} \Delta_t \left[ \phi x_c \rho_o S_o + \phi y_c \rho_g S_g \right]_{i,j,k}$$

**Eq. (B.24)**

Eq. (24) is the final discretized form of the hydrocarbon flow equations in x direction.

Following the same procedure, the discretized water flow equation in x direction becomes:

$$\Delta \left[ T_w (\Delta p_w - \gamma_w \Delta D) \right]_{i,j,k}^{n+1} = \frac{V_{r,i,j,k}}{\Delta t} \Delta_t \left[ \phi \rho_w S_w \right]_{i,j,k} \quad \text{Eq. (B.25)}$$

where

$$T_{w_{i \pm \frac{1}{2}, j, k}} = \left[ \frac{\Delta y_{i,j,k} \Delta z_{i,j,k} \rho_w \frac{k_x k_{rw}}{\mu_w}}{\Delta x} \right]_{i \pm \frac{1}{2}, j, k} \quad \text{Eq. (B.26)}$$

## Appendix C. Newton-Raphson method

The Newton-Raphson method to solve a set of nonlinear equations is described in detail.

The problem consists of solving the following set of non-linear equations:

$$\begin{aligned}
 F_1(x_1, x_2, \dots, x_n) &= 0 \\
 F_2(x_1, x_2, \dots, x_n) &= 0 \\
 &\cdot \\
 &\cdot \\
 &\cdot \\
 F_n(x_1, x_2, \dots, x_n) &= 0
 \end{aligned}
 \tag{C. 1}$$

or,

$$F_i(x) = 0 \tag{C. 2}$$

where  $F_i$ ,  $i=1,2,\dots,n$  are the equations and  $x_1, x_2, \dots, x_n$  are the unknowns. To develop the Newton-Raphson algorithm, all functions are first expressed as a Taylor series expansion about an arbitrary point  $(x_1, x_2, \dots, x_n, F_1, F_2, \dots, F_n)$  as:

$$\begin{aligned}
 F_i(x_1 + \Delta x_1, x_2 + \Delta x_2, \dots, x_n + \Delta x_n) = \\
 F_i(x_1, x_2, \dots, x_n) + \Delta x_1 \frac{\partial F_i}{\partial x_1} + \Delta x_2 \frac{\partial F_i}{\partial x_2} + \dots + \Delta x_n \frac{\partial F_i}{\partial x_n} \quad i = 1, 2, \dots, n \tag{C. 3}
 \end{aligned}$$

The objective is to find the roots of the equations by setting the left-hand sides of these  $n$  equations equal to zero. If initial values of the unknowns are

assumed, the  $n$  equations of Eq.(C.3) can be solved for  $\Delta x_1, \Delta x_2, \dots, \Delta x_n$ . This system of  $n$  equations may also be written as:

$$\begin{aligned} \frac{\partial F_1}{\partial x_1} \Delta x_1 + \frac{\partial F_1}{\partial x_2} \Delta x_2 + \dots + \frac{\partial F_1}{\partial x_n} \Delta x_n &= -F_1 \\ \frac{\partial F_2}{\partial x_1} \Delta x_1 + \frac{\partial F_2}{\partial x_2} \Delta x_2 + \dots + \frac{\partial F_2}{\partial x_n} \Delta x_n &= -F_2 \\ \cdot & \\ \cdot & \\ \cdot & \\ \frac{\partial F_n}{\partial x_1} \Delta x_1 + \frac{\partial F_n}{\partial x_2} \Delta x_2 + \dots + \frac{\partial F_n}{\partial x_n} \Delta x_n &= -F_n \end{aligned} \tag{Eq.(C.4)}$$

Eq. (C.4) can also be expressed in matrix form as:

$$\begin{bmatrix} \frac{\partial F_1}{\partial x_1} & \frac{\partial F_1}{\partial x_2} & \cdot & \cdot & \cdot & \frac{\partial F_1}{\partial x_n} \\ \frac{\partial F_2}{\partial x_1} & \frac{\partial F_2}{\partial x_2} & \cdot & \cdot & \cdot & \frac{\partial F_2}{\partial x_n} \\ \cdot & \cdot & \cdot & \cdot & \cdot & \cdot \\ \cdot & \cdot & \cdot & \cdot & \cdot & \cdot \\ \cdot & \cdot & \cdot & \cdot & \cdot & \cdot \\ \frac{\partial F_n}{\partial x_1} & \frac{\partial F_n}{\partial x_2} & \cdot & \cdot & \cdot & \frac{\partial F_n}{\partial x_n} \end{bmatrix} \begin{bmatrix} \Delta x_1 \\ \Delta x_2 \\ \cdot \\ \cdot \\ \cdot \\ \Delta x_n \end{bmatrix} = - \begin{bmatrix} F_1 \\ F_2 \\ \cdot \\ \cdot \\ \cdot \\ F_n \end{bmatrix} \tag{Eq.(C.5)}$$

Eq. (C.5) can be written as:

$$[J] \Delta x = -F \tag{Eq(C.6)}$$



J is called the Jacobian of the n equations system. The system of Eq.(C.6) can be solved either by Gaussian elimination or by any appropriate procedure. The unknowns  $(x_1, x_2, \dots, x_n)$  are updated after each iteration as:

$$x_i^{l+1} = x_i^l + \Delta x_i^{l+1} \quad i = 1, 2, \dots, n \quad \text{Eq.(C. 7)}$$

where  $l$  is the iteration level.

The iteration is terminated when  $\max(|\Delta x_i|) < tolerance$ .